AEDC-TR-73-2

HYPERSONIC LIFTING BODY WINDWARD SURFACE FLOW-FIELD ANALYSIS FOR HIGH ANGLES OF INCIDENCE

John C. Adams, Jr., and William R. Martindale

ARO, Inc.

February 1973

VON KÁRMÁN GAS DYNAMICS FACILITY
ARNOLD ENGINEERING DEVELOPMENT CENTER
AIR FORCE SYSTEMS COMMAND
ARNOLD AIR FORCE STATION, TENNESSEE

NOTICES

When U. S. Government drawings specifications, or other data are used for any purpose other than a definitely related Government procurement operation, the Government thereby incurs no responsibility nor any obligation whatsoever, and the fact that the Government may have formulated, furnished, or in any way supplied the said drawings, specifications, or other data, is not to be regarded by implication or otherwise, or in any manner licensing the holder or any other person or corporation, or conveying any rights or permission to manufacture, use, or sell any patented invention that may in any way be related thereto.

Qualified users may obtain copies of this report from the Defense Documentation Center.

References to named commercial products in this report are not to be considered in any sense as an endorsement of the product by the United States Air Force or the Government.

HYPERSONIC LIFTING BODY WINDWARD SURFACE FLOW-FIELD ANALYSIS FOR HIGH ANGLES OF INCIDENCE

John C. Adams, Jr., and William R. Martindale

ARO, Inc.

FOREWORD

The work reported herein was conducted by the Arnold Engineering Development Center (AEDC), Air Force Systems Command (AFSC), under Program Element 65802F.

The results of research presented were obtained by ARO, Inc. (a subsidiary of Sverdrup & Parcel and Associates, Inc.), contract operator of AEDC, AFSC, Arnold Air Force Station, Tennessee. The research was conducted from July 1971 until July 1972 under ARO Project No. VW5206, and the manuscript was submitted for publication on August 9, 1972.

The authors wish to acknowledge the contributions of R. H. Eaves, Jr., R. K. Matthews, and L. L. Trimmer, ARO, Inc., who were responsible for the AEDC-von Kármán Gas Dynamics Facility (VKF) test program which provided most of the experimental data used in the present report.

This technical report has been reviewed and is approved.

ELTON R. THOMPSON
Research and
Development Division
Directorate of Technology

ROBERT O. DIETZ
Director of Technology

ABSTRACT

Formulation and application of a windward surface flow-field (inviscid and viscous) analysis is presented for general lifting body configurations at high angles of incidence under hypersonic perfect gas conditions. Primary emphasis is placed on development of an approach which is accurate and easy to use while requiring only modest digital computing facilities. Basically the present technique applies the "strip theory" concept, leading to an infinite extent yawed body treatment applied in the windward surface crossflow plane for both the inviscid and viscous (boundary layer) flow fields. A one-strip integral relations approach is used to determine the spanwise surface pressure distribution at a given body location with all inviscid centerline quantities determined via an inviscid conical flow approach or some alternate technique. The boundary-layer analysis is based on implicit finite-difference integration of the governing equations for infinite-extent, yawed, blunt body boundary layers. Both laminar and turbulent flows are considered using a three-dimensional eddy viscosity-mixing length model of turbulence. Comparisons of the present "strip theory" approach with experimental data on various lifting body configurations (including several NASA Phase B Space Shuttle configurations) are presented in order to ascertain the validity and applicability of the current technique.

CONTENTS

APPENDIXES

NOMENCLATURE

A_*	van Driest damping constant, 26.0
$\bar{A}_n, \bar{B}_n, \bar{C}_n, \bar{D}_n$	Coefficients in finite-difference Eq. (III-36)
a^*	Inviscid sonic velocity
$\bar{a}$	Local speed of sound
a_e	Local edge speed of sound
B_1, B_2, B_3	Wall derivative numerical coefficients defined by Eqs. (III-57, -58, -59)
C_{f_∞}	Local skin-friction coefficient
C_p	Constant pressure specific heat
C_{p_b}	Body surface pressure coefficient defined by Eq. (107)
c	Streamwise velocity ratio, $\bar{w}/W_e$
c′	Streamwise velocity ratio gradient, $\frac{\partial c}{\partial \eta}$
D	Diameter of circular cylinder
D_1, D_2	Coefficients for finite-difference derivatives defined by Eqs. (III-32) and (III-33)
D_i	Trapezoidal rule integration step size defined by Eq. (III-48)
$\frac{dU_e}{dx}$	Inviscid edge crossflow velocity gradient
E_n	Coefficient in finite-difference Eq. (III-41)
e_n	Coefficient in finite-difference Eq. (III-41)

f	Transformed stream function defined by Eq. (37)
f'	Crossflow velocity ratio, $\bar{u}/U_e$
f''	Crossflow velocity gradient, $\partial(u/U_e)/\partial\eta$
$\bar{G}$	Scalar velocity function defined by Eq. (18)
g	Total enthalpy ratio, $\bar{H}/H_e$
g'	Total enthalpy ratio gradient, $\partial g/\partial\eta$
H'	Fluctuating total enthalpy
$\bar{H}$	Mean total enthalpy
h'	Fluctuating static enthalpy
$\bar{h}$	Mean static enthalpy
j	Body-type indicator
K	Variable grid parameter defined by Eq. (III-34)
$\bar{K}$	Hypersonic similarity parameter defined by Eq. (106)
k	Thermal conductivity
k_*	Inner law mixing-length constant, 0.435
L	Reference length
ℓ	Density-viscosity product ratio, $\rho\mu/\rho_e\mu_e$
ℓ_*	Mixing length
ℓ^*	Modified density-viscosity product ratio for use in momentum equation defined by Eq. (46)
ℓ^{**}	Modified density-viscosity product ratio for use in energy equation defined by Eq. (47)
M	Mach number
M_e	Local edge Mach number
$M_{N\infty}$	Component of free-stream Mach number normal to body centerline
M_∞	Free-stream Mach number
N	Total number of grid points
$Nu_{D,\,aw}$	Nusselt number based on diameter D and adiabatic wall temperature

$Nu_{L, aw}$	Local Nusselt number based on reference length L and adiabatic wall temperature
Pr	Laminar Prandtl number, 0.71
Pr_t	Turbulent Prandtl number, 0.90
$\bar{p}$	Static pressure
p_b	Body surface pressure
$p_{\mathfrak{C}\!\!\!/}$	Centerline pressure
p_∞	Free-stream static pressure
$\dot{q}$	Heat flux
$\dot{q}_w$	Wall heat flux
R	Specific gas constant
Re_e	Local Reynolds number based on inviscid edge conditions
$Re_{\infty, D}$	Free-stream Reynolds number based on circular cylinder diameter
$Re_{\infty, L}$	Free-stream Reynolds number based on reference length
r_f	Recovery factor
St_∞	Local Stanton number based on free-stream conditions
$\bar{T}$	Mean static temperature
T_{aw}	Adiabatic wall temperature
T_e	Static temperature at outer edge of boundary layer
$\bar{T}_o$	Mean stagnation temperature
$T_{o, \infty}$	Free-stream stagnation temperature
T_{pc}	Phase-change paint temperature
T_w	Wall temperature
TP	Transition onset parameter defined by Eq. (96)
T_∞	Free-stream static temperature
U_e	Crossflow velocity component at outer edge of boundary layer

u'	Fluctuating crossflow velocity component
$\bar{u}$	Mean crossflow velocity component
$\bar{u}_{s\ell}$	Streamwise velocity in streamline coordinates
V	Combined normal velocity components according to Eq. (6)
V_∞	Free-stream velocity
v'	Fluctuating normal velocity component
$\bar{v}$	Mean normal velocity component
W	Dependent variable in finite-difference Eq. (III-16)
W_e	Streamwise velocity component at outer edge of boundary layer
w'	Fluctuating streamwise velocity component
$\bar{w}$	Mean streamwise velocity component
$\bar{w}_{s\ell, max}$	Maximum crossflow velocity in streamline coordinates
x	Crossflow coordinate normal to body centerline
x^*	Crossflow coordinate distance from body centerline to location of sonic point
y	Coordinate normal to body surface
y_ℓ	Characteristic thickness of boundary layer in Eq. (25)
z	Streamwise coordinate along body centerline
α	Angle of attack
$\alpha_1, \alpha_2, \alpha_3, \alpha_4$	"Standard form" coefficients for parabolic partial differential equation following Eq. (III-16)
β	Inviscid velocity gradient parameter defined by Eq. (48)
γ	Specific heat ratio, 1.40
δ	Boundary-layer thickness
δ^*	Displacement thickness
δ_v	Sharp cone semivertex angle
ϵ	Eddy viscosity

ϵ_i	Eddy viscosity in inner region
ϵ_o	Eddy viscosity in outer region
ζ	Initial (off wall) $\Delta\eta$ step size defined by Eq. (III-35)
θ	Static temperature ratio, $\bar{T}/T_e$, defined by Eq. (52)
θ'	Static temperature gradient, $\partial(\bar{T}/T_e)/\partial\eta$
θ_m	Momentum thickness
θ_{shock}	Shock angle
κ	Eddy thermal conductivity
Λ	Sweep angle
λ	Outer law mixing-length constant, 0.090
μ	Laminar (molecular) viscosity
ξ, η	Transformed coordinates defined by Eqs. (31) and (32)
ρ'	Fluctuating mass density
$\bar{\rho}$	Mean mass density
ρ_e	Mass density at outer edge of boundary layer
ρ_∞	Free-stream mass density
τ	Shear stress
τ_w	Wall shear stress
Φ_*	Sonic angle location on a rounded corner
ϕ	Local ray angle defined on Fig. 5
χ	Crossflow Reynolds number defined by Eq. (97)
ψ	Stream function
Ω	Energy equation term defined by Eq. (49)
Ω'	Energy equation term gradient, $\partial\Omega/\partial\eta$
ω	Local streamline angle
ω^*	Streamline angle at leading edge

SUBSCRIPTS

aw	Adiabatic wall
b	Body

$\mathfrak{C}$	Centerline
c	Corner
D	Based on diameter of circular cylinder
e	Outer edge of boundary layer
I	Initial approximation
L	Based on reference length L
ℓe	Leading edge
o	Stagnation or total
o, ∞	Free-stream stagnation or total
pc	Phase-change paint
ref	Reference
s	Surface
sℓ	Streamline coordinates
turb	Turbulent
w	Wall
x	x-direction
z	z-direction
∞	Free stream

SUPERSCRIPTS

′	Fluctuating quantity or partial derivative with respect to η depending on usage
–	Averaged quantity with respect to time

SECTION I
INTRODUCTION

The successful design and operation of a reusable lifting entry spacecraft depends largely upon the design of the vehicle thermal protection system. In turn, the thermal protection system design depends primarily on the thermodynamic environment. Peak heat-transfer rates, distribution of the heating over the vehicle, and duration of the heating are the most influential thermodynamic parameters. The most important region in the design of a thermal protection system for a lifting entry vehicle is the bottom (windward) surface, which is about 40 percent of the total vehicle surface area for configurations of current interest relative to the National Aeronautics and Space Adminstration (NASA) Space Transportation System (STS), better known as the Space Shuttle (SS). Current state-of-the-art surveys of the aerodynamics and aerodynamic heating technology status for STS applications may be found in Refs. 1 through 5.

The prediction of the thermal environment to be encountered by SS vehicles during entry will require extrapolation of ground test (wind tunnel) data by appropriate theoretical methods. Ideally, this may be accomplished by ensuring that ground test data, taken over appropriate ranges of Mach number and Reynolds number, can be calculated from theory and then extrapolated to flight by applying that theory to flight conditions. Reviews of the aerodynamic heating problems and constraints on lifting entry vehicles have been presented by Schadt (Ref. 6) and Kipp and Masek (Ref. 7) with emphasis on the state-of-the-art aerodynamic heat-transfer-rate prediction methods and experimental techniques for arriving at spacecraft design information. Specific aerodynamic heating problems with direct application to hypersonic lifting body technology have been reported by Guard and Schultz (Ref. 8), Young, Reda, and Roberge (Ref. 9), and Marvin, et al. (Ref. 10); these studies include both analytical and experimental investigations.

The concluding summary on page 255 of Ref. 3 concerning the current status and future needs of flow-field analysis techniques for SS applications states that "the need for a three-dimensional method applicable at high angles of attack is clear." The present report documents one such technique applicable to the windward surface of general lifting body configurations at high angles of incidence under hypersonic perfect gas wind tunnel conditions with primary emphasis placed on development of an engineering-type analysis which is accurate and easy to use, while requiring only modest digital computing facilities for application.

Basically, the present technique applies the "strip theory" concept leading to an infinite extent yawed body analysis applied in the windward surface crossflow plane for both the inviscid and viscous (boundary-layer) flow fields. A NASA-developed one-strip method of integral relations digital computer program is used to calculate the spanwise surface pressure distribution at a given body location with all inviscid centerline quantities determined via an inviscid conical flow approach or some alternate technique. The boundary-layer analysis is based on implicit finite-difference integration of the governing infinite yawed blunt-body boundary-layer equations for both laminar and turbulent flows using a three-dimensional eddy viscosity-mixing length model of turbulence. Full details of both the inviscid and viscous analyses are included in the present report with a source deck listing and sample input-output for the currently developed stagnation line boundary-layer digital computer code included as appendixes. Comparisons of the present "strip theory" approach with experimental data are presented in order to establish and ascertain the validity and applicability of the current technique; included in this data-theory comparison are recent experimental measurements taken during the Arnold Engineering Development Center (AEDC) von Kármán Facility (VKF) hypersonic wind tunnel tests of various NASA Phase B SS configurations under the sponsorship of the NASA Marshall Space Flight Center. *

SECTION II
ANALYTICAL ANALYSIS

2.1 STRIP THEORY PRINCIPLE

The basic aerodynamic concept applied in the present analysis is termed "strip theory," which, according to Section 7 of Chapter 1 in Hypersonic Flow Theory, by Hayes and Probstein (Ref. 11), may be defined in terms of the following aerodynamic principle:

---

*These data were obtained in the VKF Facility of AEDC under a test program identified as STS Heating Test, AEDC Project No. VT1162, sponsored by NASA Defense Purchase Project H-74068A with Mr. John D. Warmbrod, Fluid Mechanics Research Office, Aerophysics Division, Aero-Astrodynamics Laboratory, NASA Marshall Space Flight Center, as the project monitor.

> "If the shape of a body in a given flow field is altered in such a way that a suitably defined aspect ratio (AR) approaches infinity, the flow about the body approaches a state which can be described as independent of the aspect ratio."

This principle applies generally to all nontransonic flows and is especially applicable under hypersonic flow conditions. To illustrate the principle, consider a body of length $\bar{b}$ which lies along a z-axis normal to the undisturbed flow direction, as illustrated below. This coordinate system is chosen in such a manner as to be consistent with the general lifting body coordinate system used in later sections of the present report.

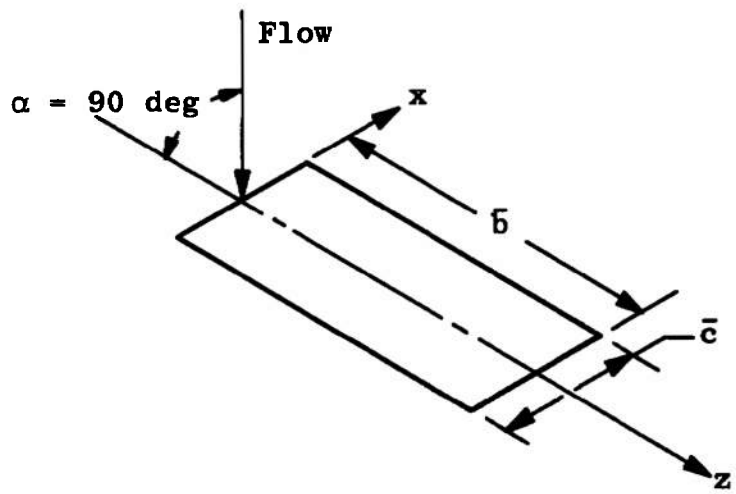

The shape of the body is characterized by the body cross sections normal to the z-axis which are taken to depend smoothly upon only the z-variable. The largest dimension of the cross sections is of the same order of magnitude as a reference span width c, and the aspect ratio (AR) is defined by AR = $\bar{b}/\bar{c}$.

A limiting process is now considered in which $\bar{c}$ is fixed while $b \longrightarrow \infty$ so that AR $\longrightarrow \infty$. In the governing equations of motion for both inviscid and viscous flows, all partial derivative terms in $\partial/\partial z$ become neglibibly small through this limiting process. Physically, this means that the flow (be it inviscid or viscous) locally approaches a two-dimensional flow.

If the aspect ratio is large enough (AR >> 1) so that the flow closely approximates a local two-dimensional flow, it may be considered to be

independent of the actual value of AR. Hayes and Probstein (Ref. 11, p. 27) state this in terms of an independence principle:

> "Local flows at corresponding points in two flows of sufficiently large but different values of AR are not different from each other in any fundamental way."

This independence principle applies with respect to all real-fluid effects such as those attributed to viscosity and equilibrium chemical phenomena.

An immediate generalization of the above principle to windward surface lifting body studies under hypersonic conditions is obtained by allowing the basic z-axis to be pitched at a fixed angle relative to the free-stream direction. The local flow then approaches that about an infinite yawed two-dimensional body under the requirement that the inclination angle α of the z-axis relative to the free-stream direction (i. e., the angle of attack α or the complement of the yaw angle Λ) is not too small, by which is meant AR $\sin \alpha \gg 1$. An additional generalization is obtained by letting the basic z-axis be a space curve with the body described in terms of cross sections locally normal to the z-axis curve. Here the characteristic curvature of the z-axis curve must not be too great. With the curvature of the z-axis curve small enough, the curvature may be simply neglected and the above principle applied locally so that the local flow depends only on the local cross-sectional shape and the angle of attack. Here the important requirement with respect to basic applicability of the principle is that AR $\sin \alpha \gg 1$ as discussed previously. However, as long as AR is finite, there will be some downstream point on the body where the principle will fail and the flow will not behave locally like that on a two-dimensional infinite body. In addition, failure of body smoothness, such as discontinuities in body cross sections, results in a local failure of the principle, which does not generally imply any overall failure of the principle.

The mathematical justification for the above-discussed "strip theory" principle may be found in the generalized hypersonic small-disturbance analysis by Sychev (Ref. 12) as discussed by Hayes and Probstein (Ref. 11, pp. 103-112 and 342-355). The most important feature of Sychev's analysis as it relates to lifting bodies at high angles of attack in a hypersonic flow is that if the angle of attack, α, of the body is large, then the zeroth-order solution of the inviscid small-disturbance equations becomes the solution of a blunt body in the transverse plane based on the component of the free-stream Mach number normal to the body, i. e., $M_\infty \sin \alpha$. Hence, as stated previously, the local flow depends only on

the local cross-sectional shape and the angle of attack. Further, the local flow behavior is independent of flow behavior at other body locations under the restriction of body smoothness discussed above.

The application of the above "strip theory" to the classical cases of infinite yawed cylinder flows and infinite swept wing flows is well known and discussed in such textbooks as Schlichting (Ref. 13, Chapter 10) and Nash and Patel (Ref. 14, Chapter 4). With respect to compressible flows under supersonic and hypersonic conditions, Reshotko and Beckwith (Ref. 15), Beckwith (Refs. 16 and 17), and Kaups and Keltner (Ref. 18) have examined infinite extent yawed cylinder and swept wing flows for the case of a laminar boundary layer; the corresponding turbulent boundary-layer case has been examined by Beckwith and Gallagher (Ref. 19), Fleming and Krauss (Ref. 20), Bradley (Ref. 21), and Hunt, Bushnell, and Beckwith (Ref. 22). Hypersonic laminar boundary-layer flows over slender delta wings at high angles of attack have been analyzed by Bertram, Feller, and Dunavant (Ref. 23), Bertram and Henderson (Ref. 24), Cole and Brainerd (Ref. 25), Bertram and Everhart (Ref. 26), Everhart and Dunavant (Ref. 27), and Whitehead and Dunavant (Ref. 28) on the basis of the above "strip theory" approach. Beckwith and Cohen (Ref. 29) present a method whereby the "strip theory" principle can be applied to arbitrary bodies at incidence in a high-speed flow via locally similar laminar boundary-layer solutions for yawed cylinders of arbitrary cross-sectional shape. The Beckwith and Cohen approach has recently been applied by Pappas (Refs. 30 and 31) for calculation of windward surface laminar heating rates on SS vehicles at high angles of attack. Baranowski (Ref. 32) has applied the same basic Beckwith and Cohen ideas through an approximate technique for analyzing the effects of three-dimensional crossflow on heating rates and boundary-layer transition along the windward centerline of delta planforms and flat plates of finite width under moderate-to-high angle-of-attack hypersonic flow conditions. The present analysis is, to the authors' knowledge, the first to apply the "strip theory" principle to the calculation of both laminar and turbulent boundary-layer flows on arbitrary bodies at moderate-to-high angles of incidence in a hypersonic flow based on implicit finite-difference solution of the reduced ($\partial / \partial z = 0$) governing equations of motion.

2.2 GOVERNING BOUNDARY-LAYER EQUATIONS

The present analysis employs the three-dimensional compressible turbulent boundary-layer equations in terms of time-averaged mean flow quantities as derived by Vaglio-Laurin (Ref. 33). Assuming the ratio of boundary-layer thickness to local surface curvature to be everywhere small, the governing equations of motion, in terms of the orthogonal coordinate system x, y, z illustrated in Fig. 1, Appendix I, reduce to the following (see NOMENCLATURE for terminology):

CONTINUITY

$$\frac{\partial \bar{\rho}\bar{u}}{\partial x} + \frac{\partial \bar{\rho} V}{\partial y} + \cancelto{0}{\frac{\partial \bar{\rho}\bar{w}}{\partial z}} = 0 \tag{1}$$

x-MOMENTUM

$$\bar{\rho}\bar{u}\frac{\partial \bar{u}}{\partial x} + \bar{\rho} V \frac{\partial \bar{u}}{\partial y} + \bar{\rho}\bar{w}\cancelto{0}{\frac{\partial \bar{u}}{\partial z}} = -\frac{\partial \bar{p}}{\partial x} + \frac{\partial}{\partial y}\left[\mu \frac{\partial \bar{u}}{\partial y} - \bar{\rho}\,\overline{u'v'}\right] \tag{2}$$

y-MOMENTUM

$$\frac{\partial \bar{p}}{\partial y} = 0 \tag{3}$$

z-MOMENTUM

$$\bar{\rho}\bar{u}\frac{\partial \bar{w}}{\partial x} + \bar{\rho} V \frac{\partial \bar{w}}{\partial y} + \bar{\rho}\bar{w}\cancelto{0}{\frac{\partial \bar{w}}{\partial z}} = \cancelto{0}{-\frac{\partial \bar{p}}{\partial z}} + \frac{\partial}{\partial y}\left[\mu \frac{\partial \bar{w}}{\partial y} - \bar{\rho}\,\overline{v'w'}\right] \tag{4}$$

ENERGY

$$\bar{\rho}\bar{u}\frac{\partial \bar{H}}{\partial x} + \bar{\rho} V \frac{\partial \bar{H}}{\partial y} + \bar{\rho}\bar{w}\cancelto{0}{\frac{\partial \bar{H}}{\partial z}} = \frac{\partial}{\partial y}\left[\mu\left(\frac{\partial \bar{H}}{\partial y} + \frac{1 - Pr}{Pr}\frac{\partial \bar{h}}{\partial y}\right) - \bar{\rho}\,\overline{v'H'}\right] \tag{5}$$

where

$$V = \bar{v} + \frac{\overline{\rho' v'}}{\bar{\rho}} \tag{6}$$

$$\bar{H} = \bar{h} + \frac{\bar{u}^2 + \bar{w}^2}{2} \tag{7}$$

and the usual expressions for the mean and fluctuating parts of the dependent variables are used; e. g.,

$$\rho = \bar{\rho} + \rho' \tag{8}$$

Implicit in Vaglio-Laurin's derivation of the above equations are the following stipulations:

a. The rates of change of the mean flow properties in the x- and z-directions [$\mathcal{O}(1)$] are smaller than the rates of change in the y-direction [$\mathcal{O}(\delta^{-1})$] by an order of magnitude.

b. Mean squares and products of the turbulent fluctuations are $\mathcal{O}(\delta)$; that is, the turbulent level is small. The terms involving mean squares of the velocity fluctuations are taken to be negligible, which is valid for high Reynolds number flows with a zero or favorable pressure gradient.

c. The time-average molecular transports are approximated by those pertaining to the mean flow properties; indeed, even the latter are negligible, except very near the wall, compared with terms involving the turbulent transports.

Also implicit in the above equations is the requirement of an infinite extent body of the yawed cylinder or yawed wing type, which leads to the term $\partial/\partial z = 0$ as discussed in the first part of the current section.

If subscript w denotes wall and subscript e denotes outer edge of the boundary layer, the associated boundary conditions on the above defined equations are

MOMENTUM

$$\begin{gathered} y = 0: \ \bar{u} = \bar{v} = \bar{w} = \overline{u'v'} = \overline{v'w'} = \overline{\rho'v'} = 0 \\ \text{as } y \to \infty: \ \bar{u} \to U_e, \ \bar{w} \to W_e \\ \overline{u'v'} \to 0, \ \overline{v'w'} \to 0, \ \overline{\rho'v'} \to 0 \end{gathered} \tag{9}$$

ENERGY

$$\begin{gathered} y = 0: \ \bar{H} = H_w = h_w, \ \overline{v'H'} = 0 \\ \text{as } y \to \infty: \ \bar{H} \to H_e, \ \overline{v'H'} \to 0 \end{gathered} \tag{10}$$

which reflect the requirements of no slip and no mass transfer (suction or blowing) at the wall, as well as a prescribed constant wall enthalpy. The y-momentum equation (3) reveals that the static-pressure variation across the boundary layer is negligible, and hence the static pres-

sure, $\bar{p}(x)$, is regarded as an external input to the boundary-layer analysis from a separate inviscid analysis. The outer edge velocities, U_e and W_e, as well as the outer-edge static enthalpy, h_e, must be determined from the inviscid analysis consistent with the imposed static-pressure distribution.

The gas model adopted for the present study is thermally and calorically perfect air or nitrogen having a constant specific heat ratio $\gamma = 1.40$ and obeying the equation of state

$$\bar{p} = \bar{\rho} R \bar{T} \tag{11}$$

where $R = 1716$ ft^2/sec^2-°R for air and $R = 1776$ ft^2/sec^2-°R for nitrogen. Hence, under this assumption the static enthalpy, $\bar{h}$, is given by

$$\bar{h} = C_p \bar{T} \tag{12}$$

where $C_p = 6006$ ft^2/sec^2-°R for air and $C_p = 6216$ ft^2/sec^2-°R for nitrogen. The laminar viscosity, μ, is taken to obey Sutherland's law, which gives for air

$$\mu = \frac{2.270 \times 10^{-8}\ T^{3/2}}{T + 198.6} \frac{\text{lbf-sec}}{\text{ft}^2} \tag{13}$$

and for nitrogen

$$\mu = \frac{2.1996 \times 10^{-8}\ T^{3/2}}{T + 198.6} \frac{\text{lbf-sec}}{\text{ft}^2} \tag{14}$$

where T must have units of °R in the above. The laminar Prandtl number, Pr, is taken to be a constant value of 0.71 across the entire boundary layer for both air and nitrogen.

2.3 TURBULENT TRANSPORT MODEL

Before Eqs. (1), (2), (4), and (5) can be solved, expressions must be supplied for the Reynolds stress or turbulent shear terms in the momentum equations and the turbulent flux of total enthalpy in the energy equation. The approach used in the present analysis is to model these terms as functions of the mean-flow variables following Adams (Refs. 34, 35, and 36), whose studies are based on the original analysis by Hunt, Bushnell, and Beckwith (Ref. 22).

The concept that the Reynolds stress in turbulent flow is proportional to a momentum exchange coefficient times the mean-flow velocity

gradient normal to the surface is well known and commonly used in turbulent boundary-layer analyses. This concept is based on an assumed analogy between the so-called eddy viscosity and the molecular viscosity. The total shear components in the streamwise, z, and crossflow, x, directions are written as

$$\tau_x = \mu \frac{\partial \bar{u}}{\partial y} - \bar{\rho}\,\overline{u'v'} = \mu \frac{\partial \bar{u}}{\partial y} + \epsilon_x \frac{\partial \bar{u}}{\partial y} \tag{15}$$

$$\tau_z = \mu \frac{\partial \bar{w}}{\partial y} - \bar{\rho}\,\overline{v'w'} = \mu \frac{\partial \bar{w}}{\partial y} + \epsilon_z \frac{\partial \bar{w}}{\partial y} \tag{16}$$

where the eddy viscosities ϵ_x and ϵ_z in the x- and z-directions, respectively, might in general be different. Applying the Prandtl mixing-length hypothesis in conjunction with the assumption that the eddy viscosity is a scalar function independent of coordinate direction (which means physically that the turbulent shear stress acts in the mean rate of strain direction) results in an eddy viscosity relationship of the form

$$\epsilon = \epsilon_x = \epsilon_z = \bar{\rho} \ell_*^2 \frac{\partial \bar{G}}{\partial y} \tag{17}$$

where $\bar{G}$ is a scalar velocity function defined by

$$\frac{\partial \bar{G}}{\partial y} = \left[\left(\frac{\partial \bar{u}}{\partial y} \right)^2 + \left(\frac{\partial \bar{w}}{\partial y} \right)^2 \right]^{1/2} \tag{18}$$

The quantity ℓ_* is termed the mixing length and is some characteristic length related to the size or scales of eddies responsible for the flux of momentum in the y-direction. Under the above model the turbulent shear stress in a three-dimensional turbulent boundary layer may be written in the form

$$\tau_{turb} = \bar{\rho} \ell_*^2 \left[\left(\frac{\partial \bar{u}}{\partial y} \right)^2 + \left(\frac{\partial \bar{w}}{\partial y} \right)^2 \right] \tag{19}$$

The complete derivation of Eqs. (17), (18), and (19) is given in Refs. 34, 35, and 36.

The expression for the total heat flux in a turbulent boundary layer may be written in terms of the static enthalpy as

$$\dot{q} = \frac{k}{C_p} \frac{\partial \bar{h}}{\partial y} - \bar{\rho}\,\overline{v'h'} = \frac{k}{C_p} \frac{\partial \bar{h}}{\partial y} + \frac{\kappa}{C_p} \frac{\partial \bar{h}}{\partial y} \tag{20}$$

where k is the laminar (molecular) thermal conductivity and κ is the so-called eddy thermal conductivity. Using the definition of the laminar (molecular) Prandtl number

$$Pr = \frac{C_p \mu}{k} \tag{21}$$

and defining, by analogy, a turbulent Prandtl number (based on the use of static enthalpy) as

$$Pr_t = \frac{C_p \epsilon}{\kappa} \tag{22}$$

with ϵ the eddy viscosity discussed previously, the total heat flux expression (20) may be written in the form

$$\dot{q} = \mu \left[\frac{1}{Pr} + \frac{\epsilon}{\mu} \frac{1}{Pr_t} \right] \frac{\partial \bar{h}}{\partial y} \tag{23}$$

2.4 MIXING-LENGTH MODEL

The turbulent shear stress in a three-dimensional turbulent boundary layer as governed by Eq. (19) is treated herein by the use of a two-layer inner-outer model using Prandtl's mixing-length hypothesis and a modification of van Driest's analysis for the near-wall region. This results in a continuous distribution of the shear stress from the laminar value at the wall, through the fully turbulent region, reaching zero at the outer edge of the boundary layer. The energy transport in a turbulent boundary layer is treated in this work through the incorporation of the eddy conductivity, κ, into the turbulent Prandtl number, Pr_t.

In the manner of Escudier (Ref. 37), Patankar and Spalding (Ref. 38) recommend the following variation of the mixing length, ℓ_*, across the turbulent two-dimensional boundary layer which is adopted for the present three-dimensional case by noting that the scalar properties of a turbulence field are unlikely to be affected by moderate three-dimensionality because turbulence is inherently three-dimensional in nature for even so-called two-dimensional flows:

$$\begin{aligned} \ell_* &= k_* y, \text{ for } 0 < y \leq \lambda y \rho'/k_* \\ \ell_* &= \lambda y \rho', \text{ for } \lambda y \rho'/k_* < y \end{aligned} \tag{24}$$

where the values for the various numerical constants are taken to be $k_* = 0.435$ and $\lambda = 0.09$. The value of y at the point where the velocity in the boundary layer is equal to 0.99 of the velocity at the boundary-layer outer edge is used to define the distance y_ℓ; i. e.,

$$y_\ell = \left\{ \text{y-value where } \frac{\left[(\bar{u})^2 + (\bar{w})^2\right]^{1/2}}{\left[(U_e)^2 + (W_e)^2\right]^{1/2}} = 0.99 \right\} \tag{25}$$

By analogy with Stokes' solution for an infinite flat plate undergoing simple harmonic motion parallel to itself in an infinite fluid, van Driest (Ref. 39) concluded that in the vicinity of a wall the total shear stress in a turbulent two-dimensional fluid should be of the form

$$\tau = \mu \frac{\partial \bar{u}}{\partial y} + \bar{\rho} k_*^2 y^2 \left[1 - \exp\left(\frac{-y\sqrt{\tau_w \bar{\rho}}}{\mu A_*}\right)\right]^2 \left(\frac{\partial \bar{u}}{\partial y}\right)^2 \tag{26}$$

which results in an exponential damping of the turbulent part of the shear stress as the wall is approached and yields exactly the laminar shear stress form, $\tau = \mu(\partial \bar{u}/\partial \bar{y})$, at the wall. Although Eq. (26) was originally developed for incompressible flow, it can be applied to compressible flow by application of the suggestion by Patankar and Spalding (Ref. 38) that the local value of shear stress be used instead of the wall value as originally recommended by van Driest (Ref. 39). Hence, by analogy of Eq. (26) with Eqs. (18) and (19), the relationship for the three-dimensional near-wall shear stress as used in the present analysis is

$$\tau = \mu \frac{\partial \bar{G}}{\partial y} + \bar{\rho} k_*^2 y^2 \left[1 - \exp\left(\frac{-y\sqrt{\tau \bar{\rho}}}{\mu A_*}\right)\right]^2 \left(\frac{\partial \bar{G}}{\partial y}\right)^2 \tag{27}$$

where the constant A_* is taken to be 26.0 following the original van Driest proposal (Ref. 39). Note that the damping term in Eq. (27) reflects the application of the local total shear stress as opposed to the wall shear stress of Eq. (26), as discussed previously.

Based on Eqs. (17), (18), (24), and (27), the eddy viscosity expression for the inner region is

$$\epsilon_i = \bar{\rho} k_*^2 y^2 \left[1 - \exp\left(\frac{-y\sqrt{\tau \bar{\rho}}}{\mu A_*}\right)\right]^2 \frac{\partial \bar{G}}{\partial y} \tag{28}$$

and for the outer region

$$\epsilon_o = \bar{\rho}\lambda^2 y_\ell^2 \frac{\partial \bar{G}}{\partial y} \tag{29}$$

with the constants k_*, A_*, λ, and y_ℓ defined previously. The constraint used to define the end of the inner region and the beginning of the outer region is the continuity of the eddy viscosity. From the wall outward, the expression for the inner eddy viscosity applies until $\epsilon_i = \epsilon_o$, from which point the outer eddy viscosity is used. A schematic of this variation in terms of the mixing lengths is shown below.

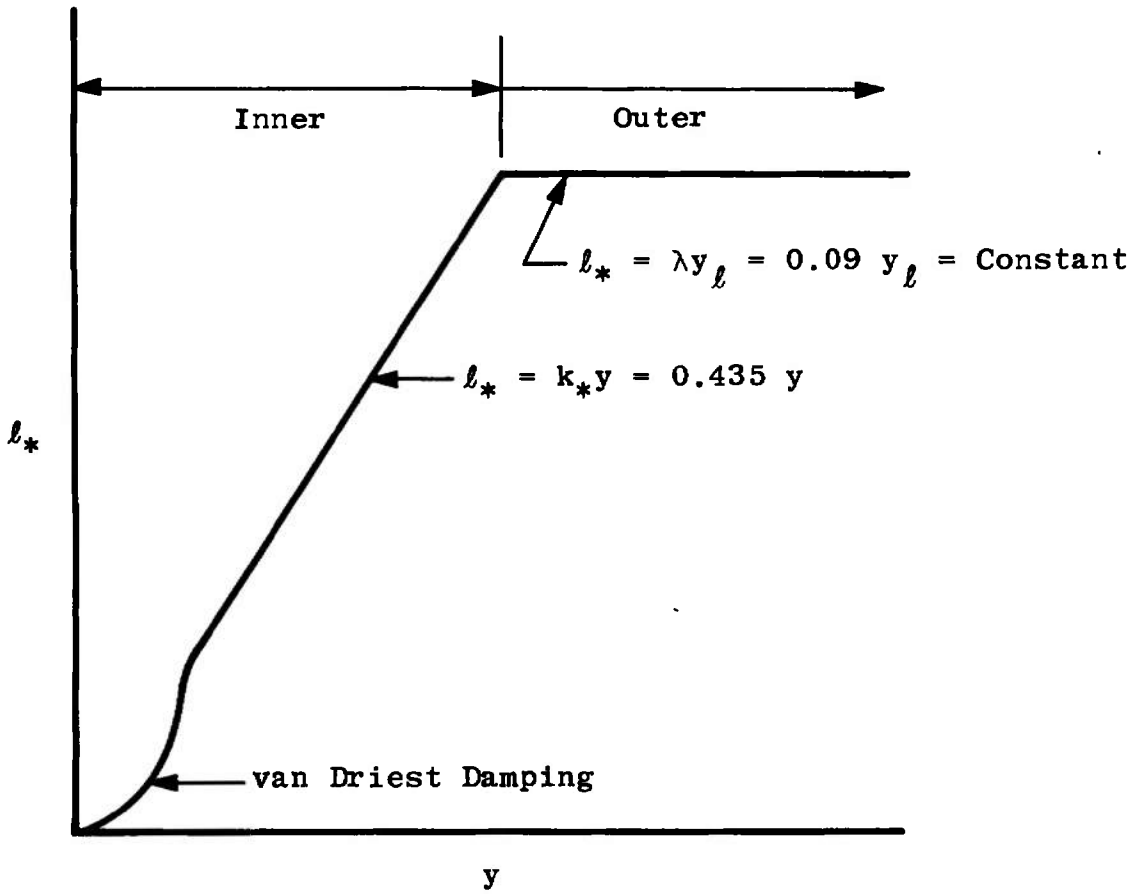

The turbulent Prandtl number (based on the static enthalpy definition of the turbulent heat flux) as given by Eq. (22) is physically a measure of the ratio of the turbulent transport of momentum to the turbulent transport of heat. For the present work, the turbulent Prandtl number

defined by Eq. (22) is taken to remain constant at the value 0.90 across the entire boundary layer as recommended by Patankar and Spalding (Ref. 38) for two-dimensional turbulent boundary layers.

For the case of purely laminar flow in the present analysis, the inner and outer eddy viscosities defined by Eqs. (28) and (29) are both set identically equal to zero so that the governing turbulent boundary-layer equations reduce to their laminar counterpart.

2.5 ALTERNATE FORM OF ENERGY EQUATION

To apply the eddy viscosity-eddy thermal conductivity model discussed above to the present work, the energy equation (5) must be rewritten to replace the total turbulent energy flux $\bar{\rho}\,\overline{v'H'}$ in terms of static quantities. By following the steps outlined on pages 176-183 in Dorrance (Ref. 40), one can see that the energy equation (5) may be written in the equivalent form

$$\bar{\rho}\bar{u}\frac{\partial \bar{H}}{\partial x} + \bar{\rho}\bar{v}\frac{\partial \bar{H}}{\partial y} + \bar{\rho}\bar{w}\cancelto{0}{\frac{\partial \bar{H}}{\partial z}} = \frac{\partial}{\partial y}\left\{\frac{\mu}{Pr}\left(1+\frac{\epsilon}{\mu}\frac{Pr}{Pr_t}\right)\frac{\partial \bar{H}}{\partial y} + \mu\left[\frac{Pr-1}{Pr} + \frac{\epsilon}{\mu}\frac{Pr_t-1}{Pr_t}\right]\left[\bar{u}\frac{\partial \bar{u}}{\partial y} + \bar{w}\frac{\partial \bar{w}}{\partial y}\right]\right\} \quad (30)$$

based on the definitions of the scalar eddy viscosity and the turbulent Prandtl number given in Section 2.3 of the present report. Equation (30) is to be regarded as the three-dimensional analog of Eq. (7-31) on page 182 in Dorrance (Ref. 40) for a two-dimensional turbulent boundary layer. Implicit in the derivation of Eq. (30) is the neglect of terms involving mean squares of the velocity fluctuations, which is consistent with Vaglio-Laurin's derivation of the governing equations as discussed previously in Section 2.2.

2.6 COORDINATE TRANSFORMATION

To facilitate numerical integration of the governing boundary-layer equations (1), (2), (4), and (30), it is convenient to transform them to a coordinate system that removes the mathematical singularity at $x = 0$ and stretches the coordinate normal to the surface, as is usually done in two-dimensional laminar flow analyses. The coordinate transfor-

mation used in the present work is the well-known Illingworth-Levy (Ref. 40, p. 30) transformation. The new independent variables introduced are

$$\xi(x) = \int_o^x \rho_e \mu_e U_e dx \tag{31}$$

$$\eta(x,y) = \frac{\rho_e U_e}{\sqrt{2\xi}} \int_o^y \frac{\bar{\rho}}{\rho_e} dy \tag{32}$$

so that the transformed streamwise and normal derivatives become

$$\frac{\partial}{\partial x} = \rho_e \mu_e U_e \frac{\partial}{\partial \xi} + \frac{\partial \eta}{\partial x} \frac{\partial}{\partial \eta} \tag{33}$$

$$\frac{\partial}{\partial y} = \frac{\bar{\rho} U_e}{\sqrt{2\xi}} \frac{\partial}{\partial \eta} \tag{34}$$

Define a so-called stream function, $\psi(x, y)$, in such a manner as to identically satisfy the continuity equation (1); i. e.,

$$\bar{\rho}\bar{u} = \frac{\partial \psi}{\partial y} \tag{35}$$

$$\bar{\rho}\bar{v} = -\frac{\partial \psi}{\partial x} \tag{36}$$

and introduce a nondimensional stream function $f(\xi, \eta)$ such that

$$\psi(\xi,\eta) = \sqrt{2\xi}\, f(\xi,\eta) \tag{37}$$

so that the governing boundary-layer equations (2), (4), and (30) become, in the transformed (ξ, η) coordinates:

CROSSFLOW (x) MOMENTUM

$$(\ell^* f'')' + f f'' + \beta[\theta - (f')^2] = 2\xi \left[f' \frac{\partial f'}{\partial \xi} - f'' \frac{\partial f}{\partial \xi} \right] \tag{38}$$

STREAMWISE (z) MOMENTUM

$$(\ell^* c')' + f c' = 2\xi \left[f' \frac{\partial c}{\partial \xi} - c' \frac{\partial f}{\partial \xi} \right] \tag{39}$$

ENERGY

$$\left(\frac{\ell^{**}}{Pr}\, g'\right)' + fg' + \Omega' = 2\xi\left[f'\frac{\partial g}{\partial \xi} - g'\frac{\partial f}{\partial \xi}\right] \tag{40}$$

with the new dependent variables

$$f'(\xi,\eta) = \frac{\bar{u}}{U_e} \tag{41}$$

$$c(\xi,\eta) = \frac{\bar{w}}{W_e} \tag{42}$$

$$g(\xi,\eta) = \frac{\bar{H}}{H_e} \tag{43}$$

The following definitions apply to the above equations:

$$\theta = \frac{\rho_e}{\bar{\rho}} = \frac{\bar{T}}{T_e} \tag{44}$$

$$\ell = \frac{\bar{\rho}\mu}{\rho_e \mu_e} \tag{45}$$

$$\ell^* = \ell\left[1 + \frac{\epsilon}{\mu}\right] \tag{46}$$

$$\ell^{**} = \ell\left[1 + \frac{\epsilon}{\mu}\frac{Pr}{Pr_t}\right] \tag{47}$$

$$\beta = \frac{2\xi}{U_e}\frac{dU_e}{d\xi} \tag{48}$$

$$\Omega = \ell\left[\frac{\epsilon}{\mu}\left(1 - \frac{1}{Pr_t}\right) + \left(1 - \frac{1}{Pr}\right)\right]\left[\frac{U_e^2}{H_e} f'f'' + \frac{W_e^2}{H_e} cc'\right] \tag{49}$$

where the inviscid x-momentum equation evaluated on the body surface

$$\frac{d\bar{p}}{dx} + \rho_e U_e \frac{dU_e}{dx} = 0 \tag{50}$$

has been used to relate the inviscid velocity, U_e, to the imposed inviscid static pressure, $\bar{p}$. In the transformed governing equations, primes

denote partial differentiation with respect to the η-coordinate; i. e.,

$$\left.\begin{aligned} f' &= \frac{\partial f}{\partial \eta} \\ f'' &= \frac{\partial^2 f}{\partial \eta^2} \end{aligned}\right\} \tag{51}$$

An expression for the static temperature ratio, θ, of Eq. (44) can be found by application of Eq. (7) to yield

$$\theta = \frac{\overline{T}}{T_e} = \frac{\overline{h}}{h_e} = \frac{\overline{H} - \left(\frac{\overline{u}^2 + \overline{w}^2}{2}\right)}{h_e} \tag{52}$$

which can be written in the form, using Eqs. (41), (42), and (43),

$$\theta = \frac{H_e}{h_e} g - \frac{1}{2}\left[\frac{U_e^2}{h_e}(f')^2 + \frac{W_e^2}{h_e}(c)^2\right] \tag{53}$$

The physical boundary conditions given by Eqs. (9) and (10) become, in terms of the transformed vairables,

MOMENTUM

$$\left.\begin{aligned} f(\xi,\eta = 0) &= 0 \\ f'(\xi,\eta = 0) &= 0 \\ c(\xi,\eta = 0) &= 0 \\ \lim_{\eta\to\infty} f'(\xi,\eta) &= 1 \\ \lim_{\eta\to\infty} c(\xi,\eta) &= 1 \end{aligned}\right\} \tag{54}$$

ENERGY

$$\left.\begin{aligned} g(\xi,\eta = 0) &= \frac{H_w}{H_e} = \frac{h_w}{H_e} = g_w \\ \lim_{\eta\to\infty} g(\xi,\eta) &= 1 \end{aligned}\right\} \tag{55}$$

2.7 BOUNDARY-LAYER PARAMETERS

Given the numerical solution to the governing equations of motion (Eqs. (38), (39), and (40)) following the integration procedure of Appendix III, the associated local boundary-layer parameters at a given body station may be determined as follows. The local convective heat flux at the body surface (y = 0) is given by the well-known Fourier law,

$$\dot{q}_w = -k_w\left(\frac{\partial \bar{T}}{\partial y}\right)_w = \frac{-k_w}{c_p}\left(\frac{\partial \bar{h}}{\partial y}\right)_w \tag{56}$$

which can be written in the equivalent form

$$\dot{q}_w = -\frac{\mu_w}{Pr}\left(\frac{\partial \bar{H}}{\partial y}\right)_w \tag{57}$$

through use of Eqs. (7) and (21) with

$$\left(\frac{\partial \bar{H}}{\partial y}\right)_w = \left(\frac{\partial \bar{h}}{\partial y}\right)_w + \left[\cancelto{0}{\bar{u}}\frac{\partial \bar{u}}{\partial y} + \cancelto{0}{\bar{w}}\frac{\partial \bar{w}}{\partial y}\right]_w \tag{58}$$

through application of $\bar{u} = 0$ and $\bar{w} = 0$ at the wall, as given by Eq. (9). In terms of the transformed (ξ, η) coordinates, Eq. (57) becomes

$$\dot{q}_w = \frac{-\ell_w \rho_e \mu_e U_e H_e}{Pr\sqrt{2\xi}}\, g'(\xi,\eta = 0) \tag{59}$$

where

$$\ell_w = \frac{\bar{\rho}_w \mu_w}{\rho_e \mu_e} \tag{60}$$

In a similar manner, the local wall shearing stress in the x- and z-directions may be written in terms of the transformed coordinates as

$$\tau_{w,x} = \mu_w \left(\frac{\partial \bar{u}}{\partial y}\right)_w = \frac{\ell_w \rho_e \mu_e U_e^2}{\sqrt{2\xi}} f''(\xi,\eta = 0) \tag{61}$$

$$\tau_{w,z} = \mu_w \left(\frac{\partial \bar{w}}{\partial y}\right)_w = \frac{\ell_w \rho_e \mu_e U_e W_e}{\sqrt{2\xi}} c'(\xi,\eta = 0) \tag{62}$$

Physical height in the boundary layer is determined from the y-transformation relationship, Eq. (34), as

$$y = \frac{\sqrt{2\xi}}{\rho_e U_e} \int_o^\eta \theta \, d\eta \tag{63}$$

For the case of three-dimensional boundary-layer flow, two lengths characterizing mass-flow defect may be defined in terms of the profiles of the two velocity components in the x- and z-directions

$$\delta_x^* = \int_o^\infty \left(1 - \frac{\bar{\rho}\bar{u}}{\rho_e U_e}\right) dy \tag{64}$$

$$\delta_z^* = \int_o^\infty \left(1 - \frac{\bar{\rho}\bar{w}}{\rho_e W_e}\right) dy \tag{65}$$

and it is not clear which, if either, defines a displacement thickness properly describing the extent to which the nonviscous flow is deflected by the boundary layer. Moore (Ref. 41) has considered this problem in great detail relative to the proper definition of a three-dimensional displacement surface, and the interested reader is referred to this source for further discussion of the subject. In terms of the transformed (ξ, η) coordinates, the two mass-flow defect lengths may be written as

$$\delta_x^* = \frac{\sqrt{2\xi}}{\rho_e U_e} \int_o^\infty (\theta - f') \, d\eta \tag{66}$$

$$\delta_z^* = \frac{\sqrt{2\xi}}{\rho_e U_e} \int_o^\infty (\theta - c) \, d\eta \tag{67}$$

In a similar manner, the momentum thicknesses in the x- and z-directions may be written as

$$\theta_{m,x} = \int_o^\infty \frac{\bar{\rho}\,\bar{u}}{\rho_e U_e}\left(1 - \frac{\bar{u}}{U_e}\right)dy \tag{68}$$

$$= \frac{\sqrt{2\xi}}{\rho_e U_e}\int_o^\infty f'(1 - f')\,d\eta \tag{69}$$

and

$$\theta_{m,z} = \int_o^\infty \frac{\bar{\rho}\,\bar{w}}{\rho_e W_e}\left(1 - \frac{\bar{w}}{W_e}\right)dy$$

$$= \frac{\sqrt{2\xi}}{\rho_e U_e}\int_o^\infty c(1 - c)\,d\eta \tag{70}$$

Along the stagnation or attachment line (centerline) of an infinite extent yawed blunt body where $\xi = 0$ since $x = 0$ (see Fig. 1 for clarification), the above equations reduce to the following limiting forms (under the restriction that $U_e \approx \left[\frac{dU_e}{dx}\right]_{x=0} x$ near $x = 0$ so that $\xi \approx \frac{1}{2}\rho_e \mu_e \left[\frac{dU_e}{dx}\right]_{x=0} x^2$ near $x = 0$):

$$[\dot{q}_w]_{x=0} = \frac{-\ell_w H_e}{Pr}\sqrt{\rho_e\mu_e\left[\frac{dU_e}{dx}\right]_{x=0}}\,g'(\xi,\eta = 0) \tag{71}$$

$$\left.\begin{aligned}[\tau_{w,x}]_{x=0} &= 0\\ [\tau_{w,z}]_{x=0} &= \ell_w W_e\sqrt{\rho_e\mu_e\left[\frac{dU_e}{dx}\right]_{x=0}}\,c'(\xi,\eta = 0)\end{aligned}\right\} \tag{72}$$

$$[y]_{x=0} = \sqrt{\frac{\mu_e}{\rho_e\left[\frac{dU_e}{dx}\right]_{x=0}}}\int_o^\eta \theta\,d\eta \tag{73}$$

$$[\delta_x^*]_{x=0} = \sqrt{\frac{\mu_e}{\rho_e\left[\frac{dU_e}{dx}\right]_{x=0}}}\int_o^\infty (\theta - f')\,d\eta \tag{74}$$

$$[\delta_z^*]_{x=0} = \sqrt{\frac{\mu_e}{\rho_e\left[\frac{dU_e}{dx}\right]_{x=0}}}\int_o^\infty (\theta - c)\,d\eta \tag{75}$$

$$[\theta_{m,x}]_{x=0} = \sqrt{\frac{\mu_e}{\rho_e \left[\frac{dU_e}{dx}\right]_{x=0}}} \int_0^\infty f'(1-f')\,d\eta \tag{76}$$

$$[\theta_{m,z}]_{x=0} = \sqrt{\frac{\mu_e}{\rho_e \left[\frac{dU_e}{dx}\right]_{x=0}}} \int_0^\infty c(1-c)\,d\eta \tag{77}$$

Furthermore, the pressure gradient parameter, β, defined by Eq. (48) assumes the value $\beta \equiv 1$ on the stagnation or attachment line (centerline) under the above restriction on U_e and ξ near $x = 0$.

Various quantities of interest are defined as follows:

FREE-STREAM REYNOLDS NUMBER BASED ON REFERENCE LENGTH L

$$Re_{\infty,L} = \frac{\rho_\infty V_\infty L}{\mu_\infty} \tag{78}$$

LOCAL UNIT REYNOLDS NUMBER BASED ON INVISCID EDGE CONDITIONS

$$Re_{e,x}/ft = \frac{\rho_e U_e}{\mu_e} \tag{79}$$

$$Re_{e,z}/ft = \frac{\rho_e W_e}{\mu_e} \tag{80}$$

LOCAL MOMENTUM THICKNESS REYNOLDS NUMBER BASED ON INVISCID EDGE CONDITIONS

$$Re_{e,\theta_{m,x}} = \frac{\rho_e U_e \theta_{m,x}}{\mu_e} \tag{81}$$

$$Re_{e,\theta_{m,x}} = \frac{\rho_e W_e \theta_{m,z}}{\mu_e} \tag{82}$$

FREE-STREAM MACH NUMBER

$$M_\infty = \frac{V_\infty}{\sqrt{\gamma R T_\infty}} \tag{83}$$

LOCAL MACH NUMBER BASED ON INVISCID EDGE CONDITIONS

$$M_{e,x} = \frac{U_e}{\sqrt{\gamma R T_e}} \tag{84}$$

$$M_{e,z} = \frac{W_e}{\sqrt{\gamma R T_e}} \tag{85}$$

LOCAL ANGULAR DIRECTION OF A STREAMLINE RELATIVE TO THE Z-AXIS DIRECTION

$$\omega = \arctan\left[\frac{U_e f'(\xi,\eta)}{W_e c(\xi,\eta)}\right] \tag{86}$$

which becomes at the outer edge

$$\omega_e = \arctan\left[\frac{U_e}{W_e}\right] \tag{87}$$

and at the body surface

$$\omega_s = \arctan\left[\frac{U_e f''(\xi,\eta=0)}{W_e c'(\xi,\eta=0)}\right] \tag{88}$$

LOCAL STANTON NUMBER BASED ON FREE-STREAM CONDITIONS

$$St_\infty = \frac{-\dot{q}_w}{\rho_\infty V_\infty C_p (T_{o,\infty} - T_w)} \tag{89}$$

LOCAL NUSSELT NUMBER BASED ON REFERENCE LENGTH L AND ADIABATIC WALL TEMPERATURE

$$Nu_{L,aw} = \frac{-\dot{q}_w L}{k_\infty (T_{aw} - T_w)} \tag{90}$$

where for yawed cylinder flow the adiabatic wall temperature is given by (see p. 8, Ref. 19)

$$\frac{T_{aw}}{T_{o,\infty}} = r_f\left(1 - \frac{T_e}{T_{o,\infty}}\right) + \frac{T_e}{T_{o,\infty}} \tag{91}$$

with

$$r_f = \sqrt{Pr} = \sqrt{0.71} = 0.843 \tag{92}$$

for laminar boundary layers and

$$r_f = \sqrt[3]{Pr} = \sqrt[3]{0.71} = 0.892 \tag{93}$$

for turbulent boundary layers with Pr = 0.71, as previously specified in Section 2.2.

LOCAL SKIN-FRICTION COEFFICIENT BASED ON FREE-STREAM CONDITIONS

$$C_{f_{\infty,x}} = \frac{\tau_{w,x}}{\frac{1}{2}\rho_\infty V_\infty^2} \tag{94}$$

$$C_{f_{\infty,z}} = \frac{\tau_{w,z}}{\frac{1}{2}\rho_\infty V_\infty^2} \tag{95}$$

2.8 BOUNDARY-LAYER TRANSITION CORRELATION PARAMETERS

In the NASA Phase A Space Shuttle studies, the various contractors used a number of criteria for predicting the onset of boundary-layer transition. These were based either on local boundary-layer edge Reynolds number or on more complex criteria such as a local Reynolds number based on the laminar boundary-layer momentum thickness. By detailed evaluation of existing delta wing centerline transition data at various angles of incidence in hypersonic wind tunnel flows, Masek (Ref. 42) proposed an onset to transition correlation parameter of the form

$$TP = \left[\frac{Re_{e,\theta_{m,z}}/M_{e,z}}{[Re_{e,z}/ft]^{0.2}}\right]_{x=0} \tag{96}$$

applicable only along the windward centerline. The transition onset parameter, TP, was shown to have a value of approximately 10 at angles of attack below 35 deg, rising to slightly above 20 at 60-deg angle of attack (see Fig. 8 in Ref. 7 for clarification). This transition onset correlation has recently been shown to be also applicable to space shuttle configurations at incidence under hypersonic wind tunnel conditions, as can be seen by reference to Fig. 11 in Matthews, et al. (Ref. 43) as well as Fig. 16a in Marvin, et al. (Ref. 10). All of the

quantities necessary to compute the transition correlation parameter of Eq. (96) are derived as part of the present inviscid-viscous analysis. It is to be noted that Masek (Ref. 42) determined the momentum thickness, $\theta_{m,z}$, from incompressible flat plate-reference enthalpy relations with an approximate correction for flow divergence. The momentum thickness in the present analysis is exact in the sense that it is a result of numerical solution to the laminar boundary-layer equations allowing thermodynamic property variations across the layer, as well as flow divergence influence on the resultant velocity profiles.

Another type of (three-dimensional) boundary-layer transition which has received little attention to date relative to space-shuttle-type configurations is the so-called crossflow-induced transition first observed by Owen and Randall (Ref. 44) and Chapman (Ref. 45) in swept-wing flows. A general discussion of the basic phenomenon and its three-dimensional nature may be found in the recent report by Adams (Ref. 46). Briefly, three-dimensional crossflow has an adverse effect on laminar boundary-layer stability in that a system of streamwise vortices contained within the boundary layer may be formed, apparently because of the inflection point in the rotated crossflow velocity profile illustrated in Fig. 2, which is unstable to small disturbances. This vortex formation apparently signals the onset to three-dimensional crossflow-induced transition of the boundary layer from laminar to turbulent flow.

The exact location at which the above-discussed vortex system will originate cannot be determined from classical boundary-layer stability theory for three-dimensional flows such as that presented by Gregory, Stuart, and Walker (Ref. 47). Instead, the abrupt formation of these vortices and also the development of complete turbulence, i. e., transition, in a three-dimensional boundary layer can apparently be correlated with a so-called maximum local crossflow Reynolds number, χ, defined (Refs. 44, 45, and 46) as

$$\chi = \frac{\rho_e \, \bar{w}_{s\ell,max} \, \delta}{\mu_e} \tag{97}$$

where $\bar{w}_{s\ell,\,max}$ is the maximum crossflow velocity in the streamline coordinates of Fig. 2, and δ is the boundary-layer thickness defined as the normal distance from the surface where the total resultant velocity

$$\sqrt{\bar{u}^2 + \bar{w}^2}$$

reaches 0.995 of the total resultant inviscid edge velocity

$$\sqrt{U_e^2 + W_e^2} \quad ;$$

ρ_e and μ_e are the values of density and viscosity, respectively, evaluated at the inviscid edge conditions. Owen and Randall (Ref. 44) found the critical value of crossflow Reynolds number for vortex formation and for crossflow-induced transition to be 125 and 175, respectively, based on the leading edge of swept wings at subsonic speeds. The work by Chapman (Ref. 45) on swept cylinders at supersonic speeds (free-stream Mach numbers up to seven) indicates that

$$\chi < 100 \longrightarrow \text{Laminar Boundary Layer}$$

$$100 \leqq \chi \leqq 200 \longrightarrow \text{Vortex Formation and Transitional Boundary Layer}$$

$$\chi > 200 \longrightarrow \text{Turbulent Boundary Layer}$$

which means that the crossflow stability criterion of Owen and Randall may apparently be expected to apply without change on cylindrical leading edges for both subsonic and supersonic flows. Chapman's work further showed that the amount of crossflow needed to induce crossflow instability downstream of the leading edge was very small - on the order of one to five percent of the inviscid edge velocity for the conditions observed. This means physically that on delta wing and space shuttle configurations at incidence with large spanwise pressure gradients, boundary-layer transition may more likely be caused by instability of the crossflow than by instability of the streamwise velocity profile (i.e., Tollmien-Schlichting instability) because of the extremely small amount of crossflow needed to cause transition at small values of the local crossflow Reynolds number.

It should be noted that Eq. (96) is a centerline transition parameter, whereas Eq. (97) is a transition parameter for the spanwise (crossflow) direction off the centerline. Hence, the possibility exists of boundary-layer transition at some spanwise location off the centerline while the centerline itself remains laminar. Along the centerline, classical Tollmien-Schlichting-type instability is expected to be the dominant mode leading to boundary-layer transition. Off the centerline at some spanwise location, crossflow-type instability may become the dominant mode leading to boundary-layer transition. A clear and basic understanding of these instabilities and which ones may be expected to be dominant under what conditions remains to be achieved.

It should be noted that the oil-flow investigations of both Marvin, et al. (Ref. 10) and Cleary (Ref. 48) reveal an accumulation of oil in chordwise streaks on the swept wing of typical space shuttle configurations under hypersonic wind tunnel conditions. This accumulation is believed to be caused by the entrained vortices that form in three-dimensional boundary-layer flows as discussed above. As indicated by Marvin, et al. (Ref. 10, Fig. 12), these vortices result in irregular heating patterns which cause severe lateral gradients in heating rates.

2.9 NUMERICAL SOLUTION OF THE GOVERNING BOUNDARY-LAYER EQUATIONS

In the present study of infinite extent yawed body boundary-layer flows, numerical solution of the governing nonlinear, parabolic, partial differential equations (Eqs. (38), (39), and (40)) is performed by obtaining linear finite-difference equivalents of the equations and solving these using an iterative, marching, implicit finite-difference integration technique involving inversion of tridiagonal matrices. Full details of this numerical approach are given in Appendix III.

The digital computer code is written in FORTRAN 63 for use on a CDC 1604-B digital computer. Solution time (including on-line printing) is approximately seven to eight minutes on the 1604-B machine for a body divided into 40 spanwise stations. Approximately 0.5 minutes of this time are required to generate a laminar stagnation or attachment line solution, whereas a corresponding turbulent solution requires about 1.5 minutes because of the larger number of iterations needed for convergence in the turbulent case. No numerical stability problems have been encountered with the present finite-difference approach because of its implicit nature.

A CDC FORTRAN 63 source deck listing of Program SLYBBCBL (Stagnation Line Yawed Blunt-Body Compressible Boundary Layer) is given in Appendix IV. Sufficient comment cards are inserted at key locations in the program to enable the potential user to follow the basic program logic. All of the associated inviscid and viscous theory aspects of the analysis are contained in the present report; the numerical analysis aspects of the solution technique are fully documented in Appendix III of the present report. It should be noted that the digital computer code is written in a very general and compact manner so that any number of coupled, ordinary, linear or nonlinear, variable or constant coefficient, second-order differential equations with two-point (split-end) boundary conditions of the function type can be solved simply by chang-

ing the number-of-equations indicator (NEQ) and redefining the necessary ALPHA-coefficients in Subroutine ABCD. In addition, an auxiliary subroutine (such as VISC in the present program) may have to be written to evaluate some of the variable coefficients in the governing differential equations. Furthermore and obviously, the input and output aspects of the code need modification for application to a new problem. The basic and important point is that the solution technique itself is coded in a general manner so that no changes as to overall program logic are required to adapt the present approach to new questions involving boundary-value problems governed by second-order ordinary differential equations.

Examples of input and output to Program SLYBBCBL are given in Appendix V for practical cases of aerodynamic interest, some of which are included in Section III of the present report. A written description of the input data is also included in Appendix V to provide the potential user with an understanding of the various input options for different-type analyses. For the reader interested in using Program SLYBBCBL for applications similar to those of the present report, it is suggested that a thorough study of the example input data and resulting program output relative to the program source deck listing will be most informative toward gaining a clear understanding of how the various types of analyses are coded into the program, as well as how the program output may be interpreted relative to the input data.

Program SLYBBCBL requires approximately 16,500 core storage locations on the CDC 1604-B digital computer (which has a maximum available core storage of approximately 32,000 locations). The CDC 1604-B digital computer has a 48-bit word length which results in approximately 11-significant-decimal-digit accuracy in single precision. All of the present calculations have been performed using single precision arithmetic. As mentioned previously, a laminar boundary-layer stagnation line solution using Program SLYBBCBL requires about 0.5 minutes on the CDC 1604-B digital computer; corresponding time for a turbulent boundary-layer stagnation line solution using Program SLYBBCBL is approximately 1.5 minutes. These quoted computation times for the CDC 1604-B digital computer can be reduced by a factor of approximately 12 to 15 through use of a CDC 6600 or UNIVAC 1108 machine.

A FORTRAN source deck listing of Program SIYBBCBL (Spanwise Infinite Yawed Blunt-Body Compressible Boundary Layer) which performs the marching-type numerical integration necessary for a nonsimilar boundary-layer analysis in the spanwise direction at a given

axial body station is not presented in the present report because of its length and complexity. Program SIYBBCBL includes Program SLYBBCBL as part of its internal structure, since a stagnation line solution must initially be generated to start the spanwise marching-type integration technique. A careful examination of Subroutine VISC in Program SLYBBCBL of Appendix IV will reveal that the three-dimensional invariant model of turbulence is coded in a general form suitable for application in Program SIYBBCBL. In fact, Program SLYBBCBL of Appendix IV has been obtained from the more general Program SIYBBCBL by suitable deletion of portions of the spanwise analysis not needed for a stagnation line solution in conjunction with the addition of certain internal options (such as the inviscid centerline flow parameters) necessary to make Program SLYBBCBL execute as a "stand-alone" or "load-and-go" program.

2.10 INVISCID FLOW FIELD

The inviscid flow-field quantities needed for input to the present boundary-layer analysis (such as U_e, W_e, $\bar{p}$, etc.) are herein determined in a simplified manner consistent with the "strip theory" principle of Section 2.1. Stagnation or attachment line ($x = 0$) parameters are used in conjunction with an analysis of a local cross-sectional body cut in a plane normal to the stagnation or attachment line axis (which physically coincides with the z-coordinate). The details of this approach are presented below.

2.10.1 Inviscid Supersonic and Hypersonic Flow Past a Yawed Cylinder

For the case of inviscid supersonic or hypersonic flow past an infinite yawed cylinder, simple inviscid sweep theory following Reshotko and Beckwith (Ref. 15) is used in the following manner to determine the inviscid stagnation line parameters. Consider the infinite yawed circular cylinder illustrated in Fig. 3 under the restriction that the chordwise component of the free-stream velocity be supersonic, i.e., $M_\infty \cos \Lambda > 1$. When the chordwise component of the free-stream velocity is supersonic, the wall pressure at the stagnation line is that which would be sensed by a pitot tube placed normal to the shock. This pressure is related to the free-stream static pressure by the Rayleigh pitot formula as

$$\frac{[p_b]_{x=0}}{p_\infty} = \left(\frac{\gamma+1}{2} M_{N\infty}{}^2\right)^{\frac{\gamma}{\gamma-1}} \left[\frac{\gamma+1}{2\gamma M_{N\infty}{}^2 - \gamma + 1}\right]^{\frac{1}{\gamma-1}} \tag{98}$$

where

$$M_{N\infty} = M_\infty \cos \Lambda \tag{99}$$

and M_{N_∞} must be greater than unity. Since the shock is parallel to the yawed cylinder, the z-direction inviscid surface velocity is simply

$$[W_e]_{x=0} = V_\infty \sin \Lambda \tag{100}$$

Since the x-direction inviscid surface velocity, U_e, is zero at the stagnation line, the inviscid static temperature, T_e, may be determined from conservation of total energy which gives, for a perfect gas,

$$[T_e]_{x=0} = T_{o,\infty} - \frac{[W_e{}^2]_{x=0}}{2C_p} \tag{101}$$

As discussed in Refs. 15 and 19, the surface pressure distribution around the front half of a yawed circular cylinder may be well represented through modified Newtonian theory as

$$\frac{\bar{p}(x)}{[p_b]_{x=0}} = \left(1 - \frac{p_\infty}{[p_b]_{x=0}}\right) \cos^2\left(\frac{2x}{D}\right) + \frac{p_\infty}{[p_b]_{x=0}} \tag{102}$$

where $[p_b]_{x=0}$ is given by Eq. (98). Experimental data indicate that M_{N_∞} should be greater than approximately two for Eq. (102) to apply. The inviscid stagnation line velocity gradient, $\left[\frac{dU_e}{dx}\right]_{x=0}$, based on the pressure distribution of Eq. (102) is given by

$$\left[\frac{dU_e}{dx}\right]_{x=0} = \frac{2}{D}\sqrt{\frac{2\{[p_b]_{x=0} - p_\infty\}}{[\rho_e]_{x=0}}} \tag{103}$$

where, for a perfect gas,

$$[\rho_e]_{x=0} = \frac{[p_b]_{x=0}}{[R\,T_e]_{x=0}} \tag{104}$$

Note that Eq. (103) is simply the classical Newtonian velocity gradient expression. Based on the above discussion, M_{N_∞} should be greater than approximately two in order for the inviscid stagnation line velocity gradient given by Eq. (103) to apply.

With the inviscid stagnation line (x = 0) quantities determined per the above discussion, all inviscid surface quantities at any x-location around the front half of the yawed cylinder can be determined through application of an isentropic expansion from the stagnation line conditions to the desired x-location surface pressure as determined from Eq. (102). Constancy of total energy is used to determine the x-direction component of velocity, $U_e(x)$, knowing the value of the static temperature $T_e(x)$ from an isentropic expansion and the fact that $W_e(x)$ remains constant at its stagnation line value given by Eq. (100) because of the shock's being parallel with the body.

It should be mentioned in closing this discussion of inviscid yawed cylinder flows that Ref. 15 also considers the case of subsonic chordwise flow where M_{N_∞} is less than unity. Such flows will not be considered in the present report.

2.10.2 Delta Wing and General Lifting Body Stagnation or Attachment Line Inviscid Flow Parameters

For the case of hypersonic flow past the windward surface of a slender, sharp-nosed delta wing at moderate-to-high angles of incidence, much experimental evidence exists to show that along the windward centerline (which is the z-axis in the present nomenclature and corresponds to the stagnation or attachment line along which x = 0) the inviscid flow parameters are essentially conical and well-represented by inviscid-sharp-cone-at-zero-yaw (tangent cone) values where the sharp cone half-angle is taken to be equal to the total flow deflection angle of the delta wing, i. e., the delta wing's angle of attack relative to the free-stream direction. Proof of the above statement may be found in the delta wing experimental studies of Barber (Ref. 49) and Nagel, Fitssimmons, and Doyle (Ref. 50). The recent experimental investigations by Matthews, et al. (Ref. 43) and Ashby (Ref. 51) show that a locally applied tangent-cone approximation (up to shock detachment) is applicable and accurate for calculation of the windward surface centerline inviscid flow parameters on space shuttle orbiter configurations at moderate-to-high angles of attack in a hypersonic flow. Further, at moderate-to-high incidence angles, nose bluntness effects disappear within a maximum distance of 5 to 10 nose radii from the nose stagnation

point, as can be seen from the windward centerline surface pressure results presented in Figs. 6 and 7 of Ref. 52, which are for a 75-deg-sweep blunted delta wing at 20- and 40-deg angles of attack in a Mach 8 hypersonic flow.

Based on the above evidence, all of the present windward surface inviscid parameters along the centerline of either delta wings or space shuttle orbiter configurations are herein calculated from tangent-cone theory applied locally unless otherwise noted (such as for the case of 60-deg angle of attack, where tangent-cone theory predicts shock detachment). The particular form of tangent-cone theory applied in the present analysis is based on a simple approximate solution for the hypersonic small-disturbance form of the Van Dyke stream function equation (Ref. 53) as developed by Rasmussen (Ref. 54). From Eq. (16) in Rasmussen, the surface pressure on an unyawed sharp cone in hypersonic perfect gas flow is given by

$$\frac{C_{p_b}}{\sin^2 \delta_v} = 1 + \left\{ \left[\frac{(\gamma + 1)\bar{K}^2 + 2}{(\gamma - 1)\bar{K}^2 + 2} \right] \ln \left(\frac{\gamma + 1}{2} + \frac{1}{\bar{K}^2} \right) \right\} \tag{105}$$

where

$$\bar{K} = M_\infty \sin \delta_v \tag{106}$$

is the hypersonic similarity parameter (HSP) and

$$C_{p_b} = \frac{2(p_b - p_\infty)}{\gamma p_\infty M_\infty^2} = \frac{2\left(\frac{p_b}{p_\infty} - 1\right)}{\gamma M_\infty^2} \tag{107}$$

with the sharp cone nomenclature shown below.

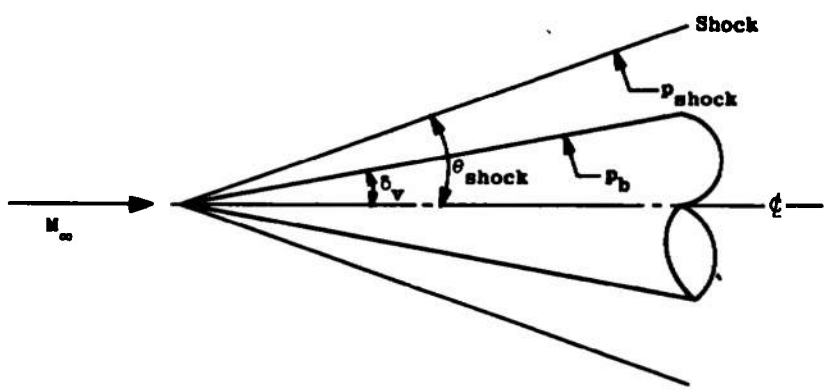

The shock angle, θ_{shock}, is related to the cone half-angle, δ_v, by Eq. (15) in Rasmussen (Ref. 54), which gives

$$\frac{\sin \theta_{shock}}{\sin \delta_v} = \left[\frac{\gamma + 1}{2} + \frac{1}{\bar{K}^2}\right]^{1/2} \tag{108}$$

With the shock angle known from Eq. (108) and the surface pressure determined from Eq. (105), all other inviscid quantities on the cone surface can be determined by crossing the conical shock using oblique shock relations followed by isentropic compression to surface conditions.

For the hypersonic limiting conditions as $\bar{K} \longrightarrow \infty$, Eqs. (105) and (108) reduce to the limiting forms

$$\left[\frac{C_{p_b}}{\sin^2 \delta_v}\right]_{\bar{K} \to \infty} \to 1 + \left(\frac{\gamma + 1}{\gamma - 1}\right) \ln \left(\frac{\gamma + 1}{2}\right) \tag{109}$$

$$\left[\frac{\sin \theta_{shock}}{\sin \delta_v}\right]_{\bar{K} \to \infty} \to \left[\frac{\gamma + 1}{2}\right]^{1/2} \tag{110}$$

which are in excellent agreement with the curves for $M_\infty = \infty$ in Charts 5 and 6, pp. 48-51, of NACA Report 1135 (Ref. 55) for the case $\gamma = 1.40$. Further note that Eq. (109) gives the proper Newtonian limit ($\gamma \longrightarrow 1$, $M_\infty \longrightarrow \infty$, δ_v fixed) for all δ_v; i. e.,

$$\left[C_{p_b}\right]_{\text{Newtonian Limit}} \to 2 \sin^2 \delta_v \tag{111}$$

For the case of finite but hypersonic Mach number flow past a sharp cone, Table I (Appendix II) presents a comparison of hypersonic small-disturbance (HSD) calculations following the above approach by Rasmussen (Ref. 54) relative to the conical flow tables of Sims (Ref. 56), which are based on numerical solution of the inviscid conical flow equations for a $\gamma = 1.40$ perfect gas. The case considered is for a 30-deg half-angle sharp cone to assess the accuracy of the HSD approach under conditions typical for application to lifting body studies. In general, the agreement of the HSD technique with the Sims tables is excellent for all parameters in the Mach number range considered. Whittliff (Ref. 57)

has also noted the basic applicability of the above HSD technique under flow conditions such that $\bar{K} = M_\infty \sin \delta_V > 1$.

For flow deflection angles greater than approximately 50 deg, and where the exact inviscid conical flow theory predicts that shock detachment will occur for free-stream Mach numbers greater than approximately three (see Chart 5 in Ref. 55), the present analysis utilizes the findings of Fig. 6 in the paper by Matthews, et al. (Ref. 43) that a reasonable approximation to the local shock angle may be obtained by simply adding from five to eight degrees to the local total flow deflection angle. Such a procedure is also valid for delta wings at high incidence, as shown in Fig. 21 in Bertram and Henderson (Ref. 24). With the shock angle determined in the above manner, the surface pressure may be calculated by use of classical Newtonian theory evaluated at the local total flow deflection angle

$$\frac{p_b}{p_\infty} = 1 + \gamma M_\infty^2 \sin^2 \delta_v \tag{112}$$

which is applicable at high angles of incidence in a hypersonic flow as shown by Bertram and Henderson (Ref. 24), as well as Barber (Ref. 49). Other approximate techniques, such as modified Newtonian theory, may be used for determination of the surface pressure based on the preference of the individual analyst. With both the shock angle and surface pressure determined per the above discussion, all other inviscid surface quantities can be determined by crossing the prescribed shock using oblique shock relations followed by isentropic compression to surface conditions. Needless to say, this approach is applicable to any streamline tracing-type analysis.

2.10.3 Delta Wing and General Lifting Body Inviscid Crossflow Parameters

Application of the "strip theory" principle discussed previously in Section 2.1 to the determination of the inviscid flow parameters for a body cross-sectional cut in a plane normal to the z-axis (which physically corresponds to the stagnation or attachment line) leads to an inviscid flow-field model of the type discussed in Appendix B of the report by Thomas and Perlbachs (Ref. 58) for the case of delta wings at high angles of incidence in a hypersonic flow. A similar model has been proposed by Nagel, Fitzsimmons, and Doyle (Ref. 50) for delta wing flows. Basically, these two approaches are as follows.

Consider a sharp, flat delta wing at an angle of attack, α, which generates a shock wave at an angle, θ_{shock}, to the free-stream flow as illustrated in Fig. 4. Now assume that the lower surface velocity, W_e, in the streamwise z-direction is constant across any cross-sectional cut of the body at a value equal to that at the centerline, $W_{e_{\mathbb{C}}}$, which is determined from the stagnation or attachment line inviscid analysis discussed in the previous subsection. Further, assume that the inviscid flow in the plane normal to the lower surface at the leading edge is sonic and directed outward in the x-direction. Such a model is very reasonable at high angles of attack in a hypersonic flow where the delta wing resembles a blunt body in the plane normal to the wing surface, as can be seen by a careful study of the work by Kennet (Ref. 59) and Pearce (Ref. 60) for the windward side of a thin, pointed, lifting delta wing with the shock attached at the vertex but detached at the leading edge. The key concept in this model is the sonic and outward flow condition at the leading edge of the delta wing caused by the detached leading-edge shock.

Based on the above inviscid model's having a forced sonic condition at the leading edge, the present analysis utilizes the one-strip method of integral relations digital computer code developed by South (Ref. 61) to calculate the x-direction surface pressure distribution over a body cross-sectional cut in a plane normal to the z-axis. Basically, the South analysis involves numerical calculation of perfect gas, inviscid, supersonic, or hypersonic flow past axisymmetric blunt bodies with forced sonic corners based on fourth-order Runge-Kutta numerical integration of a system of ordinary, nonlinear, differential equations derived from application of the one-strip method of integral relations approach attributed to Dorodnitsyn and Belotserkovskii (Ref. 11, pp. 407-438). The complete derivation of the governing one-strip method of integral relations equations as used by South (Ref. 61) may be found in the report by Xerikos and Anderson (Ref. 62), together with papers (Refs. 63 and 64) by the same two authors. The "entropy-continuity" formulation, so-called by Xerikos and Anderson (Ref. 63), is used by South (Ref. 61) instead of the alternate "pure-continuity" formulation because the former gives somewhat better results than the latter in the first (one-strip) approximation. The basic South digital computer code (Ref. 61) includes the following body geometry options:

a. Circular disk normal to flow.

b. Spherical cap convex or concave to flow.

c. Spherically blunted cones of large half-angle at zero angle of attack.

In all cases the location of the singular sonic transition is forced at the sharp corner of the body. A rough, but general, requirement for the occurrence of the sonic point at the corner is that the local surface inclination should be everywhere greater than that at the regular sonic point of a full hemisphere.

For application in the present study, the basic digital computer code of South (Ref. 61) has been modified in the following manner:

1. The term $\frac{\delta \sin \theta}{r_o}$ in Eqs. (2) and (3) on page 4 of South's report (Ref. 61) has been multiplied by a body-type indicator, j, where j = 1 for an axisymmetric body and j = 0 for a two-dimensional body. For the two-dimensional case with j = 0, the initial guess for the stagnation point shock standoff is taken as three times the axisymmetric (j = 1) value built into the original code. A derivation and discussion of this modification may be found in Ref. 62.

2. Capabilities for a body geometry consisting of a flat-faced disk (j = 1) or flat-faced strip (j = 0) having a rounded corner or shoulder have been added to the original geometry options listed above. A sketch of the flat-faced body with rounded corners is shown below for an axisymmetric body.

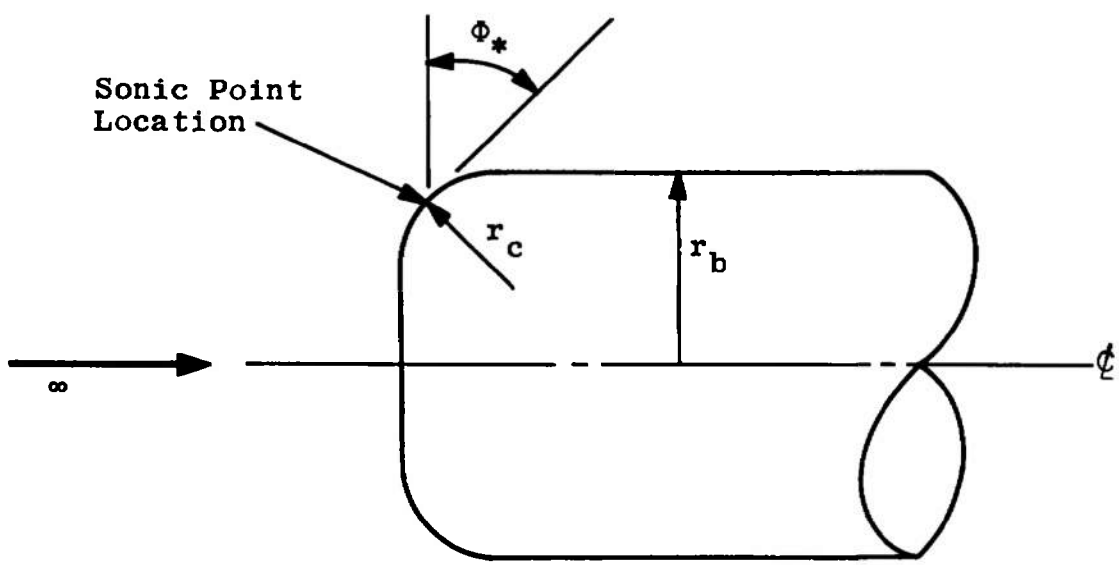

The location of the (natural) sonic point on the rounded shoulder is determined from Fig. 5 in the report by Kaattari (Ref.

65), which gives the sonic angle ratio $\Phi_*/\Phi_{*,\,sphere}$ as a function of corner radius ratio r_c/r_b for any axisymmetric flat-faced disk with a rounded shoulder under supersonic or hypersonic perfect gas flow conditions. The sonic angle $\Phi_{*,\,sphere}$ for a hemisphere is given by Clark in Ref. 66, Eq. (2) as

$$\Phi_{*,sphere} = 41.44 + \frac{23.82}{M_\infty{}^2} \tag{113}$$

where $\Phi_{*,\,sphere}$ has units of degrees. Equation (113) is based upon correlation of experimental data on hemispheres in the free-stream Mach number range from 2 to 20. All of the experimental results are within 5 percent of the value given by Eq. (113) for a common Mach number. For truncated flat-faced bodies with rounded corners, a check is made in the program to see if the truncated corner location precedes the predicted natural sonic point determined by the above procedure. If so, the program uses the truncated corner location as a fixed sonic point; if not, the program uses the predicted natural sonic point location. The same procedure is used for a two-dimensional body as for the axisymmetric case because of a lack of corresponding information and experimental data for a two-dimensional flow. Obviously such a procedure is not strictly correct, and more work needs to be done in the two-dimensional area.

3. It has been shown by numerous authors that the shock shape and body pressure distributions obtained by the method of integral relations first-approximation (one-strip) compare excellently with both experimental and more exact solutions; however, the stagnation point velocity gradient ($\frac{dU_e}{dx}$ evaluated at $x = 0$ in the present nomenclature) is considerably higher than other predictions (see Refs. 67 and 68 for further discussion of this point). Since the above-discussed inviscid stagnation point velocity gradient is directly used in the calculation of the stagnation or attachment line (the z-axis along which $x = 0$) boundary-layer parameters of Section 2.7, an alternate method of calculating the inviscid stagnation point velocity gradient has been developed for application in the present work. Based on the inviscid x-direction momentum equation evaluated on the body surface ($y = 0$) with the additional restriction from the "strip theory" principle of Section 2.1 that $\frac{\partial U_e}{\partial z} = 0$, the so-

called inviscid crossflow velocity , $U_e(x)$, distribution is determined from

$$\rho_e U_e \frac{dU_e}{dx} + \frac{d\bar{p}}{dx} = 0 \tag{114}$$

At the stagnation or attachment line ($x = 0$) where $U_e(x = 0) = 0$ and $\frac{dp}{dx}(x = 0) = 0$, the limiting form of Eq. (114) reduces to

$$\left[\frac{dU_e}{dx}\right]_{x=0} = \sqrt{\left[\frac{-1}{\rho_e}\frac{d^2\bar{p}}{dx^2}\right]_{x=0}} \tag{115}$$

The term ρ_e at $x = 0$ in Eq. (115) is herein evaluated based on the inviscid approach of Section 2.10.2. The derivative term $\frac{d^2\bar{p}}{dx^2}$ at $x = 0$ is evaluated via numerical differentiation of the pressure distribution obtained from the South one-strip method of integral relations with allowance for the fact that the pressure distribution is symmetric about the point $x = 0$; a centered five-point equally spaced Δx-increment numerical differentiation formula

$$\left[\frac{d^2\bar{p}}{dx^2}\right]_{x=0} = \frac{-\bar{p}_{-2} + 16\bar{p}_{-1} - 30\bar{p}_o + 16\bar{p}_{+1} - \bar{p}_{+2}}{12(\Delta x)^2} \tag{116}$$

is herein used following the schematic diagram shown below:

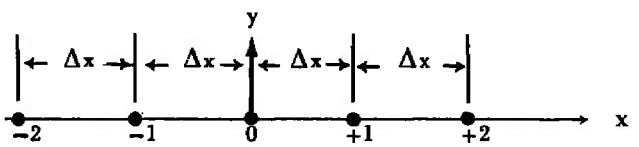

Because of the symmetry of the pressure distribution about $x = 0$, $\bar{p}_{-1} \equiv \bar{p}_{+1}$ and $\bar{p}_{-2} \equiv \bar{p}_{+2}$ so that Eq. (116) becomes

$$\left[\frac{d^2\bar{p}}{dx^2}\right]_{x=0} = \frac{-\bar{p}_{+2} + 16\bar{p}_{+1} - 15\bar{p}_o}{6(\Delta x)^2} \tag{117}$$

which is the final form of the numerical derivative as used in the present work. It should be noted that the above procedure is not the only manner in which the inviscid stagnation point velocity gradient can be computed; Refs. (67) and (68) present some alternate methods which may be just as acceptable as the above technique. Furthermore, the above procedure is used only for external applications; all internal calculations in the South program (Ref. 61) are self-consistent with the one-strip method of integral relations formalism.

Application of the above-discussed techniques to calculating the inviscid flow field on a lifting body at incidence in a hypersonic perfect gas flow proceeds in the following manner. For a given z-station location on the body, a cross-sectional cut in the x-direction (normal to the z-axis) is performed. The resulting cross-sectional body geometry is fitted with the most appropriate South program geometry option having either natural or forced sonic corners with, in either instance, the program being "told" where the sonic corner is located. A choice of either axisymmetric or two-dimensional body type is made, and a one-strip method of integral relations solution is obtained based on the component of the free-stream Mach number normal to the body centerline; i.e., in the negative y-direction at the desired z-location. The resulting numerical solution is used only to provide the surface pressure distribution along the cross-sectional cut in a normalized manner; i.e., $\bar{p}(x)/p_{\mathfrak{C}}$ where $p_{\mathfrak{C}}$ is the inviscid centerline value ($p_{\mathfrak{C}} = \bar{p}(x = 0)$) determined via the inviscid conical flow approach of Section 2.10.2 or some other treatment such as Newtonian theory. With the inviscid centerline (x = 0) quantities determined in accordance with Section 2.10.2, all inviscid surface quantities at any x-location along the cross-sectional cut can be determined through application of an isentropic expansion from the centerline conditions to the desired x-location pressure. Constancy of total energy is used to determine the x-direction component of velocity, $U_e(x)$, knowing the value of the static temperature, $T_e(x)$, from an isentropic expansion and the fact that $W_e(x)$ is assumed to remain constant at the centerline value across the entire cross-sectional cut; i.e., $W_e(x) \equiv W_e(x = 0)$. The inviscid centerline velocity gradient is determined from the numerical differentiation procedure developed in the previous paragraph.

For the case of a blunt-nosed lifting body at incidence, the effects of nose bluntness should be included in the inviscid analysis used to determine the inviscid surface quantities for input to a boundary-layer analysis. Such would be a very difficult task that would require the

coupling of a complete three-dimensional inviscid analysis, such as that reported by Thomas, et al. (Ref. 69) for blunt delta bodies, with a complete three-dimensional boundary-layer analysis. From the practical point of view adopted in the present work of applying the present inviscid techniques to determination of outer edge conditions for input to the infinite-type body boundary-layer analysis, it must be realized and acknowledged that there is some location on the body downstream of which the inviscid bluntness effects are confined to a layer, the so-called entropy layer, which is thinner than the viscous boundary-layer; i. e., the boundary layer is said to have "swallowed" the inviscid entropy layer. Beyond this location the boundary-layer edge conditions are those of a sharp-pointed body and the results of the present analysis are applicable and accurate. The physical location of this "swallowing" point depends on the angle of attack and the nose radius, being closer to the nose for high angles of incidence and small nose radius. Implicit in the use of the present inviscid and viscous analysis techniques is the assumption that the boundary layer has completely "swallowed" the inviscid entropy layer; therefore, no explicit consideration of nose bluntness and entropy layer "swallowing" is included in the present work. Comparisons of the present inviscid treatment with more exact analyses and experimental data will be presented in Section III of the present report.

As should be obvious from the above discussion, the present analysis technique is restricted to the region $0 \leqq x \leqq x^*$ where x^* is the physical x-location at which the inviscid surface flow becomes sonic. To extend the present analysis beyond the sonic point location, the simple Newtonian-type $\sin^2$-deficiency method described by Love, et al. (Ref. 70) can be used. Application of the Love, et al. technique to lifting bodies of the type under present consideration has been reported by Pappas (Refs. 30 and 31). No attempt has been made in the present work to extend the numerical calculations past the sonic point location.

It should also be noted that other analyses are currently available for determination of the inviscid centerline parameters on lifting body geometries at incidence which may be more applicable and accurate than the present tangent-cone approach under certain conditions. The reports by Kaattari (Refs. 71, 72, and 73) present simple methods for calculation of the shock inclination and surface pressure distribution along the windward centerline of a space shuttle orbiter at incidence. Even if one does choose to use the Kaattari approach over the present tangent-cone approximation, the basic concept of the present type of analysis using the South integral relations code requires no change; only the inviscid centerline quantities are different.

2.11 RANGE OF APPLICABILITY OF STRIP THEORY

A representation of the flow-field regimes on the windward surface of sharp-edged delta wings at incidence in hypersonic flow is given in Fig. C6, page 115, of the report by Thomas and Perlbachs (Ref. 58) and is reproduced in the present report as Fig. 5. Strip theory as descirbed in Section 2.1 of the present report is basically applicable in the region bordered by $(\frac{d\omega}{d\phi})_{\phi=0} = 1$ and $M_S = 1$, i.e., region 6 in Fig. 5, which physically encompasses the flow regime in which the dividing streamline and the body centerline coincide at some angle of attack (mathematically represented by the condition $(\frac{d\omega}{d\phi})_{\phi=0} = 1$) to a sufficiently large angle of incidence that the windward surface inviscid streamwise-directed flow becomes subsonic (mathematically represented by the condition $M_S = 1$).

A correlation equation for $(\frac{d\omega}{d\phi})_{\phi=0}$ based on high angle-of-incidence hypersonic flow results obtained using the method of integral relations analysis by Kennet (Ref. 59) is given by Eq. (B16) on page 94 of Ref. 58 as

$$\left(\frac{d\omega}{d\phi}\right)_{\phi=0} = 0.53\left(\frac{1.4}{\gamma}\right)^{1/3}\left[\frac{a^*_{\ell e}}{U_{e,\mathfrak{L}}}\sec\Lambda\right] \tag{118}$$

where $a^*_{\ell e}$ is the inviscid sonic velocity at the leading edge, $U_{e,\mathfrak{L}}$ is the inviscid centerline velocity, Λ is the delta wing sweep angle, and γ is the ratio of specific heats. Noting that for a perfect gas with constant specific heats undergoing an isentropic expansion,

$$U_{e,\mathfrak{L}} = M_{e,\mathfrak{L}}\, a_{e,\mathfrak{L}} \tag{119}$$

$$\frac{a^*_{\ell e}}{a_{e,\mathfrak{L}}} = \left(\frac{p^*_{\ell e}}{p_{\mathfrak{L}}}\right)^{\frac{\gamma-1}{2\gamma}} = (0.528)^{\frac{\gamma-1}{2\gamma}} \tag{120}$$

and upon setting $(\frac{d\omega}{d\phi})_{\phi=0} = 1$, Eq. (118) becomes (for a $\gamma = 1.40$ perfect gas)

$$\left[M_{e,\mathcal{L}}\right]\left(\frac{d\omega}{d\phi}\right)_{\phi=0} = 1 = \frac{\sec \Lambda}{2.067} \tag{121}$$

which physically gives the minimum inviscid centerline Mach number for a given sweep angle, Λ, at which "strip theory" should be applicable. By use of the inviscid tangent-cone flow theory of Section 2.10.2, the above minimum inviscid centerline Mach number can be related to an angle of attack, α, by matching the Mach number from Eq. (121) to the inviscid surface Mach number on a sharp cone of half-angle α at zero angle of incidence. The results of such a procedure are presented in Fig. 6, which may be interpreted as defining the lower limit of angle of attack for which "strip theory" is applicable to sharp-edged-delta-wing-at-incidence flows under hypersonic conditions. Note that three free-stream Mach number conditions are shown in Fig. 6 to illustrate that the lower limit of angle of attack is a weak function of free-stream Mach number under hypersonic conditions.

Also shown in Fig. 6 is the approximate perfect gas upper limiting angle of attack curve for which "strip theory" is strictly valid. This upper limit curve was obtained from Curve 1 (perfect gas, $\gamma = 1.40$, $M_\infty \longrightarrow \infty$) of Fig. 2, page 10, in the recent report by Pearce (Ref. 60). Above this upper limit angle of attack the shock detaches from the apex of the wing and becomes curved. This results in axial gradients along the wing which are not taken into account by the present "strip theory".

Analytical analysis defining the lower angle-of-attack limit for the validity of "strip theory" on delta planforms having general cross-sectional shapes are not currently available. Available experimental surface pressure and oil flow data for such bodies indicate that windward surface curvature may reduce the lower angle-of-attack limit below that shown in Fig. 6. The present "strip theory" analysis is thus expected to be applicable for delta planforms of general cross sections down to at least the sharp-edged delta wing lower angle-of-attack limit and probably below this value.

An excellent example of how one may use surface oil flow data obtained via hypersonic wind tunnel testing of complicated lifting body configurations at high angles of incidence to indicate the body regions in which the present "strip theory" approach is expected to be applicable may be illustrated by examination of Fig. 7 taken from Fig. 9c in the report by Seegmiller (Ref. 74). The body here is the North American Rockwell (NAR) Delta Wing Orbiter Configuration 129 as tested at 30-

deg angle of attack in the NASA-Ames 3.5-Foot Hypersonic Wind Tunnel at a Mach number of 7.4 and a free-stream Reynolds number of two million per foot. As is clearly seen from Fig. 7, the forward one-third of the windward surface on the NAR Orbiter Configuration 129 is covered with a smoothly expanding flow of relatively uniform divergence with the surface flow emanating from the stagnation line (centerline). The presence of the wing leading edge starting about half-way aft on the body causes a turning and compression of the expanding flow which becomes nearly two-dimensional in appearance over the rear of the body. Although the fuselage-wing leading edge juncture is smoothly faired, it is seen from Fig. 7 that a rather complex flow exists over the aft delta wing portion of the present body which is directly related to the turning and compression of the expanding flow by the juncture of the wing leading edge and fuselage. A better idea of the details of surface flow turning near the fuselage-wing leading edge juncture may be gained from the oblique view of the windward surface presented in Fig. 8 as taken from Fig. 4b in the recent report by Cleary (Ref. 75), documenting wind tunnel tests of the NAR Orbiter Configuration 134 in the same NASA-Ames 3.5-Foot Hypersonic Wind Tunnel described above. Note that the flow over the aft delta wing portion of the 134 configuration in Fig. 8 is much smoother than the complex aft flow over the 129 configuration in Fig. 7; this is a direct result of different lower surface spanwise contours on the two configurations.

The important point from examination of the above-discussed photographs relative to the applicability of the present "strip theory" approach to general lifting body configurations, keeping in mind the criterion for delta wing flows delineated earlier in this subsection, may be simply stated as follows:

> Strip theory applied to the windward surface of general lifting body configurations at high angles of incidence in a hypersonic flow may be expected to be applicable in the body areas free of external flow interference (such as shock interference) and where the body planform width varies slowly and smoothly. The angle of attack must be sufficiently large that the surface flow emanates from the stagnation line (centerline) of the body and flows smoothly outward in a downstream direction over the windward surface.

The assumption made in Section 2.2 of an infinite extent yawed cylinder-type turbulent boundary-layer analysis in which the eddy vis-

cosity is evaluated at the local flow condition appears very questionable for application to general three-dimensional turbulent flows because of the failure to include details of upstream boundary-layer "history." With respect to details of the turbulent motion, the primary restriction imposed by the above "local evaluation" assumption is that the characteristics of the turbulent motion be controlled mainly by the immediate environment. The time and length scales of the turbulent flow may vary slowly downstream, but if the turbulence time scales are small enough to permit adjustment to the gradually changing environment, it is possible to assume that the turbulence is dynamically similar everywhere if nondimensionalized with local length and time scales; such has been done in the present analysis (clarify Sections 2.3 and 2.4 concerning the turbulent transport and mixing-length models). The physical body requirement for applicability of the present "strip theory" approach as presented in the previous paragraph, namely that the body planform width must vary slowly and smoothly, is essential for satisfaction of the above slowly varying time and length scale criterion. The high angle-of-attack requirement for applicability of the present "strip theory", namely that the surface flow must emanate from the stagnation line (centerline) of the body and flow smoothly outward over the downstream windward surface, is responsible for the turbulent motion's being controlled mainly by the local environment providing the boundary layer is in a fully turbulent state. Examples which verify the foregoing proposed criterion for basic applicability of the "strip theory" approach, as well as the "local evaluation" turbulence treatment, will be given in Section III of the present report. Similar "local evaluation" arguments have been advanced by Adams (Refs. 35 and 36) relative to analysis of the three-dimensional turbulent boundary layer on a sharp cone at incidence under supersonic and hypersonic flow conditions.

SECTION III
RESULTS AND DISCUSSION

Presentation and comparison of results from the present three-dimensional inviscid and viscous "strip theory" analysis technique relative to hypersonic wind tunnel experimental data will be given in this section. Both laminar and turbulent three-dimensional boundary-layer flows will be considered for various body geometries (yawed cylinders, delta wings, and NASA Phase B SS configurations) at high angles of incidence. Assessment of the presently proposed inviscid flow-field analysis will also be included.

3.1 YAWED CIRCULAR CYLINDER FLOWS

Certainly one of the simplest of all infinite yawed body flows is the classical yawed cylinder case. The present subsection will consider application of the current laminar and turbulent boundary-layer analysis to yawed circular cylinder flows under supersonic and hypersonic flow conditions. The yawed circular cylinder geometry and nomenclature are illustrated in Fig. 3.

The cylindrically blunted leading edge of a sharp-prow delta wing at zero angle of attack is effectively the same as the stagnation or attachment line of a yawed circular cylinder whose yaw angle is equal to the sweep angle of the delta wing. Presented in Fig. 9 is a comparison of the present laminar boundary-layer theory relative to the experimental data of Everhart and Dunavant (Ref. 27) for the cylindrically blunted leading edge of a 70-deg sweep delta wing at zero angle of attack under hypersonic conditions. The agreement between theory and experiment is excellent for this laminar flow condition. Other comparisons, not presented herein, of similar laminar boundary-layer flows on yawed cylinders and cylindrically blunted swept leading edge wings indicate that the present laminar boundary-layer theory is applicable and accurate under supersonic and hypersonic flow conditions which satisfy the inviscid requirement of Section 2.10.1 that $M_{N_\infty} = M_\infty \cos \Lambda > 2$.

With respect to analysis of the turbulent boundary layer on yawed cylinders under hypersonic conditions, Figs. 10, 11, and 12 present comparisons of calculated and experimental surface pressure and heat-transfer distributions. As shown in the top portion of Fig. 10, the Newtonian theory given by Eq. (102) in the present report appears very acceptable for determination of the surface pressure distribution over the front half of a yawed cylinder in hypersonic flow. Further, the calculated turbulent heat-transfer-rate distribution shown in Fig. 10 over the front half of the yawed cylinder is in excellent agreement with the experimental measurements of Bushnell (Ref. 76). However, note that the heat-transfer calculations of Fig. 10 are based on the use of a value $\lambda = 0.05$ for the outer mixing-length constant in the present three-dimensional eddy viscosity model of turbulence. The results of Fig. 11 also indicate that λ must assume a value of approximately 0.05 for the calculated heat-transfer rates to agree with the experimental heat-transfer measurements of Fleming and Krauss (Ref. 20) for the stagnation or attachment line of a yawed cylinder in hypersonic flow. Hunt, Bushnell, and Beckwith (Ref. 22) reached the same conclusion regarding the value of $\lambda = 0.05$ for agreement of theory and experiment on a yawed

cylinder-slab under hypersonic conditions. It should be noted here for future reference that all of the foregoing discussion of yawed cylinder turbulent boundary-layer flows has been concerned with hypersonic conditions in which the free-stream Reynolds number based on cylinder diameter is in the range $2.55 \times 10^5 \leqq Re_{\infty, D} \leqq 8.5 \times 10^5$.

For the highest Reynolds number condition examined by Beckwith and Gallagher (Ref. 19), namely $Re_{\infty, D} = 3.5 \times 10^6$, Fig. 12 shows that the present calculated heat-transfer rates using the value $\lambda = 0.09$ as formulated in Section 2.4 for fully turbulent boundary-layer flows are in good agreement with the experimental measurements as well as the turbulent theory developed by Beckwith and Gallagher in Appendix A of Ref. 19. These findings suggest a free-stream Reynolds number effect on yawed cylinder turbulent boundary-layer flow development under supersonic and hypersonic conditions which is in agreement with the incompressible flow studies of Cumpsty and Head (Refs. 77 and 78), who found that the stagnation or attachment line flow on a yawed cylinder bears strong similarity in its behavior to fully developed flow in pipes. In neither case does there appear to be any instability to small disturbances. To produce a turbulent boundary-layer flow there must be a sufficient disturbance and the Reynolds number, $Re_{\infty, D}$, must be large enough. In each case the flow a sufficient distance downstream from the disturbance is independent of the nature of the disturbance. Hence, the turbulent boundary layers in Figs. 10 and 11 are probably in some sort of a transitional state possessing low levels of turbulence intensity. As the free-stream Reynolds number, $Re_{\infty, D}$, is increased, the turbulent boundary-layer intensity level will also increase until the boundary layer reaches a fully turbulent state in which the appropriate outer mixing-length constant is the value $\lambda = 0.09$ recommended in Section 2.4 for fully turbulent boundary-layer flows.

The variation of fully turbulent heat-transfer rate with increasing yaw angle, as shown in Fig. 12, illustrates an interesting point concerning the use of adiabatic wall temperature in the definition of a heat-transfer coefficient such as $Nu_{D, aw}$. Note that the fully turbulent Stanton number, St_∞, based on the flow stagnation temperature, attains a maximum value at a yaw angle of approximately 30 deg. However, the Nusselt number, $Nu_{D, aw}$, based on the adiabatic wall temperature, does not attain a maximum value until a yaw angle of approximately 40 deg. This discrepancy is caused by the variation of adiabatic wall temperature with yaw angle, as shown in the middle of Fig. 12. Hence, one must be careful in the physical interpretation of yawed cylinder heat-transfer coefficients based on adiabatic wall temperature; such coefficients may

give erroneous information as to the yaw angle at which maximum turbulent heating is to be expected.

As is well known and as is clearly shown in Fig. 12, one method of reducing the level of aerodynamic heating to cylindrically blunted leading edge wings and fins in the case of a laminar boundary layer is to sweep the leading edge rearward. For the case of a turbulent boundary layer, however, Fig. 12 shows that the level of aerodynamic heating increases with sweep up to an angle of approximately 30 deg and then decreases. Thus, if the occurrence of turbulent boundary layers is anticipated, heating can be reduced through use of small sweep angles or of sweep angles considerably in excess of 30 deg (note that the turbulent heating rates at a sweep angle of 0 and 58 deg are identical in Fig. 12). For control surfaces the latter approach, involving large sweep angles, is obviously preferable to the aerodynamic design since axial drag is also reduced.

Another interesting point to observe from the top of Fig. 12 is that the present turbulent heat-transfer calculations correctly approach the calculated laminar values as the yaw angle of the cylinder approaches zero. Further note that for a sweep or yaw angle of 70 deg, the laminar adiabatic wall temperature is almost equal to the value for the physical wall temperature used in all the present calculations (a constant value of 560°R). The calculated laminar Stanton number distribution at the top of Fig. 12 reflects this approach to an adiabatic wall condition as the sweep angle is increased. However, for a sweep or yaw angle of 70 deg, note that $M_{N_\infty} = 4.15 \cos 70 \text{ deg} = 1.42$ so that the criterion of $M_{N_\infty} > 2$ for the applicability of the inviscid yawed cylinder theory presented in Section 2.10.1 is violated.

Illustrations of how to apply Program SLYBBCBL to both laminar and turbulent boundary layers on the attachment or stagnation line of a yawed cylinder under hypersonic conditions are given in Appendix V. Since, in succeeding sections, Program SLYBBCBL will be applied to calculation of the attachment or stagnation line flows on more general lifting body configurations, it is well to end this present section with a short discussion of the physical nature of yawed cylinder flows, which is important for an understanding of attachment-line flows in general. The attachment or stagnation line flow on a yawed cylinder is a special case of the more general plane-of-symmetry flows discussed in Chapter 4 of Nash and Patel (Ref. 14) and is characterized by the divergence of the streamlines on either side of the plane of symmetry (see Fig. 13 for clarification). This streamline divergence removes fluid from the

region adjacent to the plane of symmetry at precisely the rate necessary to offset its retardation caused by the shear-stress gradient. As a result, all the properties of the boundary layer, including its thickness, are invariant with distance along the attachment line, i. e., invariant in the local direction of flow.

3.2 DELTA WING CONFIGURATIONS

3.2.1 Inviscid Flows

The most successful calculations of inviscid hypersonic flow past the lower surface of a delta wing at high angles of incidence with a detached shock have been reported by Kennet (Ref. 59) and Pearce (Ref. 60), with Pearce's analysis representing an extension to real gases of Kennet's earlier perfect gas work. Kennet (Ref. 59) applied the one-strip method of integral relations to a reduced set of ordinary differential equations derived from the complete governing Euler equations of inviscid motion. Upon replacing one of the momentum equations by an equation expressing the constancy of entropy on the wing surface, Kennet (Ref. 59) started his outward numerical integration from the wing centerline with the correct value for the centerline shock standoff distance determined by requiring that the sonic singular point occur at the leading edge through an iterative procedure.

As discussed in Sections 2. 10. 2 and 2. 10. 3, the present work utilizes an approximate technique based on the "strip theory" approach to calculate the inviscid quantities required for input as edge conditions to the present boundary-layer analysis. Recall from Section 2. 10. 2 that inviscid centerline quantities are determined from application of either inviscid conical flow theory (applied in a tangent-cone sense) or some other approach. The South one-strip method of integral relations analysis (Ref. 61) is used to determine the spanwise pressure distribution over a body cross section normal to the centerline with the normal (to the body) component of the free-stream Mach number being used as an "effective" free-stream Mach number which, of course, is a function of body angle of attack. With the spanwise pressure distribution known (in the normalized form $\bar{p}/p_{\mathfrak{C}}$), as well as the centerline inviscid properties determined via tangent-cone theory or otherwise, an isentropic expansion in conjunction with constancy of total energy is used to calculate all of the required inviscid properties over the body cross section of interest. It is now in order to evaluate this approximate technique applied to sharp-leading-edge-delta-wing-at-incidence flows rela-

tive to the more exact analyses by Kennet (Ref. 59) and Pearce (Ref. 60), as well as experimental data in the form of spanwise pressure distribution.

Presented in Fig. 14 is a comparison of the present approximate inviscid analysis technique for calculation of the surface pressure distribution relative to both experiment and theory as taken from Fig. 5 in the paper by Kennet (Ref. 59) for Mach 6.08 hypersonic flow past the windward surface of an 80-deg sweep sharp-leading-edge delta wing at 60-deg angle of attack. Calculated results for both an axisymmetric (j = 1) flat-faced disk and a two-dimensional (j = 0) flat-faced strip are included in order to assess which type body is most applicable to delta wing flows. As can be seen from Fig. 14, the present approximate "strip theory" analysis using South's method of integral relations program (Ref. 61) is in excellent agreement with both experiment and Kennet's theoretical caluclations, providing the body is taken to be axisymmetric (j = 1), i.e., a flat-faced disk approximation. A two-dimensional (j = 0) flat-faced strip body approximation results in a somewhat lower value for the surface pressure over the majority of the wing's span, as shown in Fig. 14. It is to be noted that the calculated centerline surface pressure used in the present treatment is based upon application of classical Newtonian theory for this 60-deg angle-of-attack condition. The important conclusion from Fig. 14 is that an axisymmetric-type body approximation, i.e., a flat-faced disk, appears to be the more appropriate body choice when used in conjunction with the South one-strip method of integral relations for determination of the spanwise pressure distribution on sharp-edged delta wings at high angles of incidence in a hypersonic flow.

Further evidence that the flat-faced disk (axisymmetric body) is the more appropriate type of body approximation is given in Fig. 15 based on comparison of calculated spanwise shock shapes on a 75-deg sweep sharp-leading-edge delta wing at 60-deg angle of incidence in a Mach 9.6 hypersonic flow. The flat-faced disk shock shape based on application of South's one-strip method of integral relations (Ref. 61) is seen to be in good agreement with the shock shape from Kennet's delta wing analysis (Ref. 59) over most of the span. Also shown in Fig. 15 for comparison is the shock shape from the Newtonian-type analysis by Cole and Brainerd (Ref. 25). The two-dimensional-type body approximation used in conjunction with the South method of integral relations analysis results in a substantially larger shock stand-off distance (an increase of almost a factor of two) compared with the axisymmetric body approximation, as can be seen from Fig. 15.

Additional comparisons of the present approximate "strip theory" approach toward calculation of delta-wing-at-incidence inviscid flow fields relative to the more exact analysis by Pearce (Ref. 60) are presented in Figs. 16 and 17. For the 75-deg sweep sharp-edged delta wing at 60-deg angle of attack shown in Fig. 16, the present flat-faced disk approximation is in good agreement with the numerical results from Fig. 20 in the report by Pearce (Ref. 60) with respect to spanwise surface pressure and density distributions; the streamwise-directed velocity (W_e) distribution is also in reasonable agreement between the two analyses. The most significant discrepancy is seen in the crossflow velocity (U_e) distribution, with the present flat-faced-disk approximation yielding a slightly higher velocity than the more exact results of Pearce. It should be noted, however, that there are small inconsistencies in the surface coordinate system used by Pearce (Ref. 60) and the present work, which will influence the strict relative interpretation of Figs. 16 and 17. It should also be noted that the present approximate "strip theory" calculations presented in Fig. 16 are based on the use of classical Newtonian theory for the centerline pressure, as well as on the use of a centerline shock angle of 67.5 deg to calculate the inviscid centerline density and streamwise-directed velocity.

Similar comparisons are presented in Fig. 17 for the case of an 85-deg sweep sharp-leading-edge delta wing at 30-deg angle of attack in a Mach 7.4 flow. As shown in Fig. 13 on page 29 of the report by Pearce (Ref. 60), the centerline shock angle for this particular highly swept delta wing at 30 deg angle of attack is about 32.5 deg, whereas inviscid conical flow (tangent-cone theory) gives a value of approximately 34 deg. Hence, the "strip theory" calculations presented in Fig. 17 are based on the following two assumptions as to the type of presently applied inviscid centerline analysis:

1. Inviscid conical flow (tangent-cone) analysis.
2. Assumption of shock parallel with surface in conjunction with classical Newtonian surface pressure.

By this choice of analyses the centerline shock angle of 32.5 deg as reported by Pearce (Ref. 60) is bracketed; i.e., the centerline shock angle is 30 deg under the parallel shock assumption and approximately 34 deg under the inviscid conical flow tangent-cone assumption. The comparisons of Fig. 17 indicate that the analysis by Pearce (Ref. 60) is indeed bracketed by the present approximate "strip theory" approach with respect to the spanwise surface pressure distribution and the

streamwise-directed velocity, W_e. However, the crossflow velocity, U_e, for both of the present "strip theory" treatments is slightly larger than the value reported by Pearce (Ref. 60) at a common span location. The mismatch in surface coordinates between the present work and that of Pearce is very small for this particular case because of the large sweep angle of the delta wing. The following subsection on viscous delta wing flows will present heat-transfer results for this particular delta wing configuration and flow conditions in which the effects of the above two assumptions as to the type of inviscid centerline flow will be ascertained as to their effect on calculated heat-transfer rates.

One of the most important inviscid centerline quantities required for input to the present stagnation line boundary-layer analysis (Program SLYBBCBL in Appendix IV) is the inviscid stagnation line velocity gradient $\left[\frac{dU_e}{dx}\right]_{x=0}$, which can be numerically evaluated following the numerical differentiation procedure of Section 2. 10. 3 based on the flat-faced-disk approximation for calculation of the sharp leading edge delta wing spanwise pressure distribution. The classic paper by Bertram and Henderson (Ref. 24) suggests that the stagnation line inviscid velocity gradient for sharp-edged delta wing flows at high angles of incidence under hypersonic conditions be represented by the equation

$$\left[\frac{dU_e}{dx}\right]_{x=0} = \frac{0.745\, a_{e,\mathfrak{C}}}{2x^*} \tag{122}$$

where $a_{e,\mathfrak{C}}$ is the local speed of sound based on the local inviscid centerline temperature; i. e., for a perfect gas,

$$a_{e,\mathfrak{C}} = \sqrt{\gamma R T_{e,\mathfrak{C}}} \tag{123}$$

and x^* is the local spanwise distance from the delta wing centerline to the sharp leading edge at the axial body location of interest as sketched below.

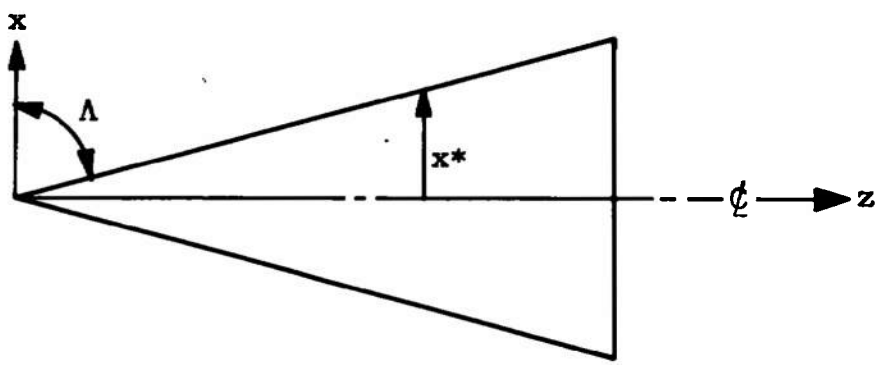

The justification for the use of Eq. (122) to represent the stagnation line inviscid velocity gradient is based on the earlier work of Bertram, Feller, and Dunavant (Ref. 23), who arrived at this expression by correlating the inviscid velocity distributions on flat-faced cylinders as calculated from experimental pressure distributions. References 23 and 24 also indicate that the effects of corner roundings, i.e., a flat-faced cylinder with rounded shoulders, can be well-approximated by adding another term representing the rounding to the right-hand side of Eq. (122).

For the present work based on application of South's one-strip method of integral relations applied to flat-faced disk flows for caluclation of the spanwise pressure distribution on sharp-leading-edge delta wings at high angles of incidence, it has been found (based on analysis of a large number of hypersonic flow calculations) that the constant 0.745 in Eq. (122) should be changed slightly to the value 0.78; i.e.,

$$\left[\frac{dU_e}{dx}\right]_{x=0} = \frac{0.78\sqrt{\gamma R\, T_{e,\mathfrak{L}}}}{2x^*} \tag{124}$$

It should be noted that the value 0.78 is based on the use of a constant $\gamma = 1.40$ perfect gas model in the South one-strip method of integral relations analysis (Ref. 61); use of a different γ, say $\gamma = 1.20$ for "faked" real gas flows, will result in a different numerical value for the constant term in question. It should be further noted that the numerical value 0.78 is based on the free-stream Mach number range $10 \leqq M_\infty \leqq 20$ and angle-of-attack range 30 to 50 deg using inviscid conical flow (tangent-cone) centerline parameters following Section 2.10.2. For a free-stream Mach number of 5 at 50-deg angle of attack, the South analysis indicates that the numerical constant should be approximately 0.75, which is in excellent agreement with the value 0.745 proposed by Refs. 23 and 24. In this connection the experimental data used by Bertram, Feller, and Dunavant (Ref. 23) to evaluate their constant 0.745 is based on the free-stream Mach number range $3.55 \leqq M_\infty \leqq 6.2$, as shown in Fig. 20 of Ref. 23. Hence, it may be recommended that the numerical value 0.745, as in Eq. (122), be used for low hypersonic Mach number flows, whereas the constant 0.78, as in Eq. (124), should be used for high Mach number flows; in both cases the flow must be a $\gamma = 1.40$ perfect gas flow. Equation (124) for high Mach number flows is built into Program SLYBBCBL of Appendix IV as one of the stagnation line inviscid velocity gradient input options. No attempt has been made in the current work to modify Eq. (124) to reflect corner rounding as discussed

in the previous paragraph relative to the analyses of Refs. 23 and 24. However, note the possibility of using an "effective" x^* value in Eq. (124); more will follow on this subject relative to application of Eq. (124) to general lifting body geometries.

3.2.2 Boundary-Layer Flows

In the current subsection comparisons will be made between surface heat-transfer rate and surface flow angle calculations based on the present three-dimensional boundary-layer analysis relative to experimental measurements taken on various delta wing geometries at incidence in hypersonic wind tunnel flows. The range of delta wing sweep angle covered is 73 to 85 deg with both laminar and turbulent boundary-layer flows being considered.

Experimental centerline heating rates for an 85-deg sweep sharp-edged delta wing at various angles of incidence in a Mach number 7.4 flow are shown in Fig. 18. These data were obtained from Fig. 8 in the report by Lockman (Ref. 79) and were taken in the NASA-Ames 3.5-Foot Hypersonic Wind Tunnel over the free-stream unit Reynolds number range from one million to six million per foot. Also shown in Fig. 18 are laminar heating rate calculations based on the present three-dimensional laminar boundary-layer theory using the two different inviscid flow models relative to Fig. 17 discussed in the previous subsection. Over the angle-of-attack range from 15 to 70 deg, the calculations based on the Newtonian pressure - parallel shock inviscid flow model are in excellent agreement with the experimental data; calculations based on the conical inviscid flow model fall toward the upper limit of the data spread band. Note particularly from Fig. 18 that the present "strip theory" approach appears to yield accurate and applicable results over the entire angle-of-attack range from 15 to 60 deg. Comparison of these results with the expected range of validity for "strip theory" application on an 85-deg sweep delta wing as given in Fig. 6 (which is based on the discussion in Section 2.11 of the current report) indicates that Fig. 6 can be applied with some confidence to highly swept-delta-wing-at-incidence flows.

Spanwise heating rate data for the 50-deg angle-of-attack condition in the above-referenced experimental investigation by Lockman (Ref. 79) are compared in Fig. 19 with results from the present three-dimensional laminar spanwise boundary-layer analysis. The identical centerline inviscid flow models of Figs. 17 and 18 are used in conjunction with a flat-faced-disk spanwise pressure distribution following Fig. 17

for inviscid input to the boundary-layer analysis. Good agreement between the present "strip theory" approach and experiment is shown in Fig. 19 with the calculated results assuming the Newtonian pressure-parallel shock model in best agreement with the experimental data.

Comparisons of experimental (oil flow) spanwise surface flow angles from Ref. 79 are presented in Fig. 20 relative to calculated surface flow angles from the present three-dimensional laminar boundary-layer analysis for the same 50-deg angle-of-attack condition as that of the above spanwise heating comparison. As is obvious from examination of Fig. 20, the experimental data are in best agreement with the calculated results assuming the Newtonian pressure-parallel shock model. It is interesting to observe from Fig. 20 that over the 10- to 90-percent semispan region, the calculated surface flow angle, ω_s, is approximately a factor of two larger than the calculated inviscid edge angle, ω_e, based on a common semispan location and inviscid flow model.

One of the more complete experimental investigations into the effects of angle of attack on boundary-layer transition for the case of hypersonic flow past an 80-deg sweep delta wing has been documented by Stultz and Fehrman (Ref. 80) in the form of a detailed data report. The test series was conducted in the AEDC-VKF Hypersonic Wind Tunnel (B) at a free-stream Mach number of 8 under high Reynolds number conditions. To provide sufficient coverage of the three-dimensional transition patterns, the phase-change paint technique for determination of the local heat-transfer rate was used for all tests. The basic shape tested was the delta planform with an 80-deg sweep angle as mentioned above; the nose and leading edges of the wing were very slightly blunted and for practical purposes may be considered sharp. Further details of the test program and model geometry may be found in Ref. 80. Presented in Fig. 21 is a comparison of calculated centerline heat-transfer rates based on the present three-dimensional laminar and turbulent boundary-layer analysis (using the "strip theory" approach in conjunction with inviscid conical flow edge conditions) relative to the experimental measurements as tabulated in Appendix A of Ref. 80. For the 30-deg angle-of-attack condition, boundary-layer transition occurs over the front one-third of the body, with fully turbulent flow over the aft section. As can be seen from Fig. 21, the present "strip theory" approach for a fully turbulent ($\lambda = 0.09$) boundary layer and the experimental data from Group 44 of Ref. 80 are in excellent agreement. For the 50-deg angle-of-attack condition in Fig. 21, note that natural boundary-layer transition occurred for the Group 54 condition, whereas the Group 55 data (which was a repeat run) appeared to be "tripped" at approximately 8 in.

from the apex. A complete discussion of boundary-layer "tripping" under high angle-of-attack conditions will be given later in the present report. Suffice it to say for the present that, because of its thinness, the three-dimensional laminar boundary layer is extremely easy to "trip" under high angle-of-attack conditions; a paint speck or model joint provides sufficient roughness for "tripping," as will be demonstrated later in this report. Relative to the natural transition results for Group 54 in Fig. 21, note that centerline boundary-layer transition started at the location $z \approx 12.5$ in., with fully turbulent heating rates (which indicates the end of transition) attained at the location $z \approx 22$ in. The ratio of z-distance for inception of fully developed turbulent flow to the z-distance for transition onset based on the above results yields a value slightly less than two, which is in good agreement with the suggestion by Masaki and Yakura (Ref. 81) that a value of two appears reasonable under supersonic and hypersonic flow conditions; this length factor ratio is a function of the local edge Reynolds number at onset of transition and appears to decrease as the onset Reynolds number increases, as shown in Fig. 9 of the recent paper by Kipp and Masek (Ref. 7). Returning to further discussion of Fig. 21 in the present report, the present three-dimensional laminar and turbulent boundary-layer calculations are in excellent agreement with the experimental data, both laminar and turbulent, for the 50-deg angle-of-attack condition. Note that, for example, at the $z = 10.0$-in. centerline location the calculated turbulent heat-transfer rate is a factor of three greater than the corresponding laminar value, which clearly justifies the vehicle designer's concern over the exact body location where boundary-layer transition begins under high angle-of-attack conditions.

With respect to centerline location of the onset to boundary-layer transition, Section 2.8 of the present report discusses the windward centerline onset to transition correlation parameter (TP) proposed by Masek (Ref. 42) based on examination of existing delta-wing-at-incidence transition data from hypersonic wind tunnel tests. Presented in Fig. 22 is the calculated Masek transition parameter variation along the windward centerline of the present 80-deg sweep delta wing at 50 deg angle of attack based on the current three-dimensional laminar boundary-layer "strip theory" approach. As shown previously in Fig. 21, natural transition onset occurred at the centerline location $z \approx 12.5$ in. for the present flow condition. From Fig. 22 the numerical value of the calculated transition parameter at $z = 12.5$ in. is approximately 16.5, which is in reasonable agreement with the 50-deg angle-of-attack transition parameter value from the correlation curve given in Fig. 8 of Ref. 7.

One of the now classical sources of information concerning delta-wing-at-incidence flows under hypersonic conditions is the NASA report by Nagel, Fitzsimmons, and Doyle (Ref. 50), which contains both experimental data and theoretical calculations obtained during the X-20 (Dyna-Soar) program. Reference 50 includes surface pressure, heat-transfer, oil flow, and shock angle measurements taken in various hypersonic wind tunnel facilities, as well as calculated laminar and turbulent boundary-layer results based on the so-called Boeing $\rho_r\mu_r$ three-dimensional boundary-layer theory developed by Richard A. Hanks of The Boeing Company in the course of the X-20 program. Full documentation of the $\rho_r\mu_r$ approach may be found in Refs. 50, 82, and 83, which include comparisons with experimental data. These references establish that the $\rho_r\mu_r$ method for estimating both laminar and turbulent heating rates is well substantiated by experimental data obtained on several body configurations for a wide range of test conditions. Figure 23 presents a comparison of the present three-dimensional turbulent boundary-layer approach relative to results from the Boeing turbulent $\rho_r\mu_r$ method for the case of a 73-deg-sweep delta wing at 40-deg angle of attack in a Mach 7, high Reynolds number flow. Also included in Fig. 23 are experimental data from Fig. 51f in Ref. 50. Since the delta wing under examination has cylindrically blunted leading edges of diameter 0.332 in., the present calculations using the "strip theory" approach are based on a flat-faced-disk-with-rounded-corners approximation using the South one-strip method of integral relations to determine the spanwise pressure distribution for a given centerline location per the approach of Section 2.10.3 in the current report; inviscid centerline quantities are based on the use inviscid conical flow theory for the present 40-deg angle-of-attack condition. As can be seen from Fig. 23, the present three-dimensional turbulent boundary-layer calculation (using $\lambda = 0.09$) is in good agreement with the Boeing turbulent $\rho_r\mu_r$ method and both are in reasonable agreement with the experimental data (note that the experimental data has been obtained by "tripping" the boundary layer.)

Corresponding spanwise surface flow angle results for a slightly larger (leading edge diameter of 0.90 in.) 73-deg-sweep delta wing at 45-deg angle of attack under the same free-stream conditions as above are presented in Fig. 24. The experimentally determined surface flow angles are based on oil flow results with the boundary layer "tripped" to turbulent flow near the apex of the wing. Note from Fig. 24 that the spanwise station of interest is at a centerline location ($z/D = 6.71$) which should be sufficiently aft of the "trip" location to remove any "trip" effect on the data. As can be seen from Fig. 24, the present three-dimensional turbulent boundary-layer calculation is in good agree-

ment with the oil flow measurements over the entire span up to and including the leading edge shoulder. Using the 80-percent semispan location as an example, observe from Fig. 24 that the calculated surface flow angle, ω_s, based on the present three-dimensional turbulent boundary-layer "strip theory" approach yields a value of approximately 13 deg, whereas the corresponding calculated external flow angle, ω_e, at the edge of the boundary layer is about 10 deg. These results illustrate quite clearly that the amount of turning by the three-dimensional turbulent boundary layer relative to the inviscid outer edge flow direction is nowhere near as large as for the case of a laminar boundary layer such as that previously presented in Fig. 20 of the present report. It should be noted that the method of calculation used for the above-discussed example is identical in all respects to the method described in the previous paragraph, i. e., the spanwise pressure distribution determined from the South one-strip method of integral relations for a flat-faced disk with rounded corners in conjunction with inviscid conical flow values for the inviscid centerline parameters.

An example of how to apply Program SLYBBCBL of Appendix V to the case of a fully turbulent boundary layer at the centerline location $z/D = 12.5$ on the 73-deg-sweep delta wing of Fig. 23 at 40-deg angle of attack is given in Appendix V. For purposes of illustration the delta wing has been assumed to have sharp leading edges so that Eq. (124) of the previous subsection can be used for calculation of the inviscid stagnation line velocity gradient; such is a good approximation since the delta wing of Fig. 23 is only very slightly blunted (leading edge diameter of 0.332 in.). Comparison of the present output with the more exact calculation in Fig. 23 shows almost identical agreement, which illustrates that for slightly blunted leading edge delta wings at incidence application of Program SLYBBCBL as if the body had sharp leading edges will yeild very acceptable results. Such usage is very beneficial for engineering studies, since the intermediate step of determining a spanwise pressure distribution based on the South one-strip method of integral relations is hereby eliminated.

A recent investigation performed in the AEDC-VKF Hypersonic Wind Tunnel B at Mach 8 was concerned with location of three-dimensional boundary-layer transition fronts on a blunt-nosed 75-deg-sweep delta wing at high angles of attack based on heat-transfer measurements via the phase-change paint technique. The results of this investigation (which was sponsored by NASA as part of the Phase B SS program) are fully documented in Ref. 84, which includes data for 20-, 40-, and 60-deg angle-of-attack conditions, as well as two different free-stream

Reynolds number conditions. The particular delta configuration was designed by the NASA Langley Research Center and is designated in Ref. 84 as the NASA LRC-DB; full details of the model are given in Fig. 1 of Ref. 84. For the present it should be noted that the delta wing was blunt-nosed with cylindrically blunted leading edges of radius 0.675 in. Comparisons between the present three-dimensional laminar and turbulent boundary-layer analysis based on the "strip theory" approach relative to the experimental measurements of Ref. 84 for the 40-deg-angle-of-attack, high Reynolds number condition (Group 348 in Ref. 84) are presented in Fig. 25. As is obvious from the figure, agreement between the present three-dimensional boundary-layer theory and experiment is excellent for both the centerline and spanwise (body location $z/L = 0.5$) heating rate distributions. Note that the approximate factor of two between end of transition and onset of transition distances as discussed previously with respect to the 80-deg-sweep delta wing of Fig. 21 is also applicable for the present 75-deg blunted delta, as can be seen from the centerline heat-transfer distribution in Fig. 25. Further note the different character of a spanwise turbulent heat-transfer distribution (heating rate constant over the majority of the span and decreasing as the leading edge is approached) as shown in Fig. 25 and a spanwise laminar heat-transfer distribution (fairly constant heating rate near the centerline but increasing as the leading edge is approached) as presented previously in Fig. 19. This behavior is due to the difference in flow acceleration effects on the three-dimensional laminar and turbulent boundary layer in regions of strong favorable pressure gradient such as near the leading edge of a delta wing.

Examples of how to apply Program SLYBBCBL of Appendix IV to the 75-deg swept delta wing flow of Fig. 25 for a laminar boundary layer at the centerline location $z/L = 0.2$ and a turbulent boundary layer at the centerline location $z/L = 0.5$ are given in Appendix V. All of the necessary inviscid input has been calculated based on use of the South one-strip method of integral relations for a flat-faced disk with rounded corners having a natural sonic point in conjunction with inviscid conical flow values for all the necessary inviscid centerline parameters. Note that the example for a laminar boundary layer is at a 60-deg angle-of-attack condition, whereas the turbulent boundary-layer example corresponds to the 40-deg, $z/L = 0.5$ centerline location in Fig. 25.

3.3 NORTH AMERICAN ROCKWELL (NAR) DELTA WING ORBITER CONFIGURATION 161B

One of the NASA Phase B SS designs tested extensively in the AEDC-VKF Hypersonic Wind Tunnel (B) at Mach 8 was the North American Rockwell (NAR) Delta Wing Orbiter Configuration 161B (0.009 scale). A side and windward planform view of this configuration is shown in Fig. 26; more complete details of the body geometry can be found in Refs. 85 and 86, which document the data taken during the AEDC wind tunnel tests. A recent report by Lockman and DeRose (Ref. 87) documenting the NASA-Ames Research Center wind tunnel tests on the same configuration includes detailed body cross sections at various z/L locations along the body. As can be seen from Fig. 3d of Ref. 87, the NAR Orbiter Configuration 161B windward surface cross-sectional shapes can be well represented in the axial coordinate range $0.1 < z/L < 0.5$ by a flat-faced body with rounded shoulders having a natural sonic point; between $z/L = 0.5$ and $z/L = 0.7$, a flat-faced body with rounded shoulders approximation having a forced sonic point at the leading edge appears reasonable. For $z/L > 0.7$ the delta wing is sweeping out from the body and the "strip theory" approach of the present analysis is not applicable as discussed in the following paragraph.

With reference to the NAR Orbiter Configuration 161B windward planform geometry shown in Fig. 26, note that in the range $0.1 < z/L < 0.6$ the planform is essentially a highly swept delta wing of sweep angle 81.5 deg. For $z/L > 0.6$ the planform is a delta wing of 60-deg sweep. At a z/L location of approximately 0.6 there is a discontinuity in body planform geometry. With respect to the "strip theory" principle discussed in Section 2.1 of the present report, an aspect ratio (AR) typical of the forward delta planform ($z/L < 0.6$) may be defined as

$$AR \approx \frac{20}{4} = 5$$

where the number 20 is the approximate total length (in inches) of the model and the number 4 is the approximate planform width (in inches) of the model at the $z/L = 0.6$ station. Furthermore, the forward delta planform ($z/L < 0.6$) satisfies the body smoothness criterion of Section 2.1 in that the body planform depends smoothly on the z-coordinate in the range $0.1 < z/L < 0.6$. Since $AR \gg 1$ and $AR \sin \alpha \gg 1$ (providing the angle of attack, α, is greater than about 25 deg, as shown in Fig. 6 for applicability of "strip theory" to an 81.5-deg sweep delta wing) in conjunction with the body smoothness property, it is to be expected that

the "strip theory" approach is applicable to the windward surface NAR Orbiter Configuration 161B in the axial coordinate region $0.1 < z/L < 0.6$ under hypersonic flow conditions. With the discontinuity in body planform at $z/L \approx 0.6$ to a delta wing of 60-deg sweep which has a minimum aspect ratio of

$$AR \approx \frac{20}{12} = 1.67$$

based on the maximum width of the model, the "strip theory" approach is not expected to "work" for the present configuration in the region $z/L \gtrsim 0.7$. As discussed previously in Section 2.11 with respect to delta wing flows in general, the "strip theory" approach is not expected to be applicable to a 60-deg sweep delta wing under hypersonic conditions except at extremely high angles of attack approaching 60 to 70 deg. Hence, all of the suceeding analysis of the NAR Orbiter Configuration 161B will be restricted to the region $0.1 \leqq z/L \leqq 0.7$, where it is believed that "strip theory" should be applicable, providing the angle of attack is greater than about 25 deg.

To assess the accuracy and applicability of the inviscid centerline theories presented in Section 2.10.2 for application to lifting body configurations using flow concepts, Fig. 27 shows a comparison of both inviscid tangent-cone and classical Newtonian theories relative to the experimental centerline pressure measurements of Ref. 85 on the NAR Orbiter Configuration 161B in the angle-of-attack range 20 deg $\leqq \alpha \leqq$ 50 deg under Mach 8 hypersonic flow conditions. At the lower angles of attack, inviscid tangent-cone theory is in good agreement with the experimental data. At the highest angle of attack (50 deg), the experimental measurements are approximately five percent above the inviscid tangent-cone theory and about ten percent above classical Newtonian theory. These results indicate that inviscid tangent-cone theory is indeed adequate for estimation of windward centerline pressure on lifting body geometries such as the NAR configuration in the angle-of-attack range from 20 to 50 deg under hypersonic conditions. As shown by Fig. 28, inviscid tangent-cone theory is also adequate for estimation of windward centerline shock angles on the present NAR configuration in the angle-of-attack range from 20 to 50 deg. This means that inviscid tangent-cone theory should, in general, provide reasonable estimates of the windward centerline inviscid flow-field parameters needed for input to the present boundary-layer analysis in the angle-of-attack range from 20 to 50 deg under hypersonic conditions.

To calculate heating rate distributions on the NAR configuration, body cross-sectional cuts were made at $z/L = 0.3$, 0.5, and 0.7, and the spanwise pressure distribution at these locations was determined via the method of Section 2.10.3. Figure 29 shows the results of this approach for the body station $z/L = 0.3$ on the NAR Orbiter Configuration 161B at 30-deg angle of attack in a Mach 8 hypersonic flow. Note from Fig. 29 that the windward cross-sectional shape has been approximated by a flat-faced body with rounded corners having a natural sonic point location determined per Section 2.10.3 for an axisymmetric body, i.e., a flat-faced disk with rounded shoulders. Further note from Fig. 29 that the discontinuity in body cross-sectional curvature at the flat-corner juncture point is reflected in the pressure distribution as a discontinuity in the pressure gradient $\frac{d\bar{p}}{dx}$. It should be noted that the spanwise pressure distributions at $z/L = 0.3$ for both the 40- and 50-deg angle-of-attack cases are almost identical with the 30-deg case of Fig. 29. The x^* location of the sonic point is shifted slightly upstream as the angle of attack is increased because of the change in the normal (to the body) component of the free-stream Mach number, which becomes the "effective" free-stream Mach number for purposes of the calculation procedure. No experimental spanwise pressure distributions were reported in Ref. 85 for the NAR Orbiter Configuration 161B, and, to the author's knowledge, no experimental spanwise pressure distribution data exist in the literature for this body.

Heating rate distributions calculated from the present three-dimensional laminar and turbulent boundary-layer analysis (using inviscid tangent-cone theory for the determination of windward centerline inviscid flow parameters in conjunction with the spanwise pressure distribution determined as discussed in the previous paragraph) are presented in Figs. 30 and 31 relative to the experimental measurements of Ref. 86 for the NAR Orbiter Configuration 161B. Figure 30 gives the windward centerline Stanton number distributions for both laminar and turbulent boundary layers at 30-, 40-, and 50-deg angles of attack under AEDC-VKF Tunnel B high Reynolds number conditions. The turbulent data (shown as closed or darkened symbols) were obtained using carborundum grit placed on the windward surface to "trip" the boundary layer; see Ref. 86 for a discussion of this technique. All of the experimental heat-transfer data of Ref. 86 were taken using the thin-skin thermocouple technique under relatively cold wall ($T_w/T_{o,\infty} \approx 0.4$) conditions. The calculations were performed for the $z/L = 0.3$, 0.5, and 0.7 stations discussed in the previous paragraph, and the theoretical lines shown in Fig. 30 are fairing through the three calculated values. In general, good-

to-excellent agreement between theory and experiment is observed for the windward centerline heat-transfer distributions at all three angle-of-attack conditions and both laminar and turbulent boundary layers. Note that boundary-layer transition occurred rather abruptly between $z/L = 0.55$ and 0.60 in both the 40- and 50-deg angle-of-attack cases. A model joint existed at $z/L = 0.57$, and although no measurements were obtained to quantify the amount of body mismatch at this location, it can be surmised that boundary-layer transition was promoted by the joint. Furthermore, it should be noted that all turbulent boundary-layer calculations are based on the use of an outer mixing-length constant $\lambda = 0.09$, i.e., a fully turbulent boundary layer.

The spanwise Stanton number distributions for both laminar and turbulent boundary layers at the body station location $z/L = 0.3$ on the NAR Orbiter Configuration 161B at 30-, 40-, and 50-deg angles of attack under AEDC-VKF Tunnel B high Reynolds number conditions are given in Fig. 31. Note that this body location corresponds to the spanwise pressure distribution of Fig. 29 discussed previously. As can be seen from Fig. 31, good-to-excellent agreement between the present three-dimensional boundary-layer theory and the experimental measurements of Ref. 86 is observed for the case of a fully turbulent boundary layer at all three angle-of-attack conditions. In addition, the agreement between the present three-dimensional laminar boundary-layer theory and experiment is excellent for the 50-deg angle-of-attack case. For the 30- and 40-deg angle-of-attack conditions, the laminar theory is in good agreement with experiment on the body centerline and at the spanwise location $x/x^* \approx 0.4$; at $x/x^* \approx 0.65$ the measured heat-transfer rate is some 15 to 25 percent greater than the corresponding calculated laminar value. Reference to the bottom portion of Fig. 31 shows that the crossflow Reynolds number, χ, is in the range $100 < \chi < 200$ at the spanwise location $x/x^* \approx 0.65$ for both the 30- and 40-deg angle-of-attack conditions; $\chi \approx 90$ for the 50-deg angle-of-attack case. As discussed in Section 2.8 of the present report concerning crossflow-dominated three-dimensional boundary-layer transition,

$$\chi < 100 \longrightarrow \text{Laminar Boundary Layer}$$

$$100 \leqq \chi \leqq 200 \longrightarrow \text{Vortex Formation and Transitional Boundary Layer}$$

$$\chi > 200 \longrightarrow \text{Turbulent Boundary Layer}$$

Hence, the boundary layer at the spanwise location $x/x^* \geqq 0.65$ for both the 30- and 40-deg angle-of-attack conditions may be in a transitional state because of three-dimensional crossflow-dominated laminar bound-

ary-layer instability. At 50-deg angle of attack the laminar boundary layer remains stable to three-dimensional disturbances and does not undergo crossflow-dominated transition. Further observe from the lower portion of Fig. 31 that for a given spanwise location, increasing the body angle of attack serves to decrease the crossflow Reynolds number, χ, which means physically that crossflow-dominated boundary-layer transition is more likely to occur in the lower angle-of-attack range for lifting bodies at incidence under hypersonic conditions.

Note from Fig. 31 for the 30-deg angle-of-attack condition that $\chi \approx 200$ at $x/x^* \approx 0.65$ with a corresponding experimental Stanton number approximately 25 percent above the calculated laminar value. The χ criterion of Section 2.8, as repeated above, suggests that the boundary layer should be in a fully turbulent state for $\chi > 200$. Such is obviously not the case in Fig. 31. To understand why a fully turbulent condition is not attained, examine the inviscid velocity gradient parameter β distribution as shown in the bottom portion of Fig. 31 along with the χ curve. As can be seen, the boundary layer is being substantially accelerated at the spanwise station of interest, $x/x^* \approx 0.65$. The discontinuity in the β curve slope at $x/x^* \approx 0.5$ is a direct reflection of the discontinuity in the pressure gradient caused by the discontinuity in surface curvature at the flat-corner juncture, as discussed previously in connection with Fig. 29.

From studies such as Refs. 88, 89, and 90 it is now well known that a fully turbulent boundary layer may undergo reverse transition toward a laminar boundary layer, sometimes referred to as laminarization, under high acceleration flow conditions such as nozzle flows. In this process the boundary layer becomes laminar-like near the wall, presumably because of a loss of near-wall turbulent transport, and the wall skin-friction and heat-transfer rate are correspondingly less than that associated with a turbulent boundary layer. It is also well known from classical boundary-layer stability theory for a two-dimensional incompressible, laminar boundary layer that a favorable pressure gradient can have a strong stabilizing effect on small disturbances. This conclusion may be deduced from the fact that the value of the minimum critical Reynolds number for neutrally damped disturbances increases rapidly with increasing favorable pressure gradient, as can be seen from Figs. 17.2 and 17.3 on pages 413 and 414, respectively, in Schlichting (Ref. 13). Similar findings apply to high-speed compressible boundary layers, as discussed by Morkovin (Ref. 91) and Mack (Ref. 92). Hence it appears reasonable to postulate that for the present lifting body at incidence boundary-layer flow, three-dimensional cross-

flow tends to promote laminar boundary-layer instability and transition at the same time that the flow acceleration tends to stabilize the boundary layer. This is what the heat-transfer results of Fig. 31 tend to indicate if one accepts the above postulate as being correct; three-dimensional boundary-layer instability and transition tend to increase the surface heat-transfer rate, and the flow acceleration tends to result in transition laminarization and stability. Much more work remains to be done in this relatively unexplored area of fluid mechanics before this phenomenon will be fully understood.

One of the more significant results of the recent study by Snedeker (Ref. 93) was the discovery that even a highly accelerated two-dimensional incompressible laminar boundary layer can be made turbulent if disturbances of sufficient magnitude are introduced in the right manner. Similar conclusions have also been reached by Morkovin (Ref. 91). The importance of these findings with respect to lifting body hypersonic flows is that the three-dimensional laminar boundary layer in the above-discussed stable-unstable spanwise mode may be "tripped" to a fully turbulent state by a sufficient disturbance. An excellent example of such "tripping" may be found by examination of the phase-change paint results from Group 54, page 128, of Ref. 80, which is for a 50-deg angle-of-attack flow condition over the windward surface of the 80-deg sweep delta wing discussed previously in Section 3.2.2 with respect to centerline heat transfer. A summary of these results for the body station $z = 9.28$ in., as taken from Appendix A-42, page 178, of Ref. 80, is shown in Fig. 32 relative to the present spanwise boundary-layer theory. Observe from Fig. 32 that at the spanwise location $x/x^* = 0.75$ the right-hand side heat-transfer coefficient is approaching the calculated fully turbulent level, while the left-hand side value is only slightly above the calculated laminar level. The corresponding crossflow Reynolds number, shown in the lower portion of Fig. 32, indicates that crossflow transition could indeed occur ($\chi \approx 160$ at $x/x^* = 0.75$) based on the criterion of Section 2.8. Note also from Fig. 32 that the boundary layer is being substantially accelerated for $x/x^* \gtrsim 0.5$, as can be seen from the inviscid crossflow velocity gradient β distribution. For values of $x/x^* \leq 0.5$ where $\chi < 100$, both the right- and left-hand side heat-transfer coefficients are in excellent agreement with the calculated laminar values. All of the above indicates that under a flow condition where boundary-layer transition could occur because of three-dimensional crossflow instability, transition may or may not actually occur. It has been the author's experience that small amounts of surface roughness, such as paint specks in phase-change paint, are sufficient to "trip" the three-dimensional laminar boundary layer on lifting body geometries at

high angles of incidence because of the extreme thinness of the laminar boundary layer; see Refs. 94 and 95 for a further discussion of this topic. Hence, it is surmised that the asymmetric heat-transfer results presented in Fig. 32 are probably caused by "surface roughness tripping" of the three-dimensional laminar boundary layer on the right-hand side of the delta wing, while the high boundary-layer acceleration stabilized the left-hand side in the absence of roughness. Such "tripping" is a very interesting fluid mechanics phenomenon which has been observed to occur during AEDC-VKF hypersonic wind tunnel phase-change paint tests on other lifting body configurations (not included in the present report) at high angles of incidence.

Two examples of how to apply Program SLYBBCBL for both laminar and turbulent boundary layers at the $z/L \approx 0.3$ location (Station 840) on the centerline of the NAR Orbiter Configuration 161B at 40-deg angle of incidence under cold wall, high Reynolds number, AEDC-VKF Tunnel B conditions are given in Appendix V. For these illustrative examples both the windward centerline pressure and velocity (as computed from the inviscid conical flow theory of Section 2.10.2) and the inviscid stagnation or attachment line velocity gradient (computed according to Section 2.10.3, using the South one-strip method of integral relations for a flat-faced body with rounded corners) are card input values to the program.

3.4 NASA-LANGLEY RESEARCH CENTER STRAIGHT BODY (NASA LRC-SB) DELTA WING CONFIGURATION

Another of the NASA configurations tested intensively in the AEDC-VKF Hypervelocity Wind Tunnel (F) at nominal Mach number 10.5 using nitrogen gas was the NASA-Langley Research Center Straight Body (NASA LRC-SB) Delta Wing. Side, rear, and windward planform views of this configuration are shown in Fig. 33; more complete details of the body geometry can be found in Ref. 96, which documents the data taken during the AEDC wind tunnel tests. As can be seen from Fig. 33, the NASA LRC-SB planform configuration for x/L locations greater than 0.32 is simply a flat-faced strip with cylindrically rounded edges; the forebody planform is a 75-deg sweep blunt-nosed delta wing with cylindrically blunted leading edges. With respect to the "strip theory" principle of Section 2.1, an aspect ratio (AR) typical of the aft NASA LRC-SB planform ($z/L > 0.32$) may be defined as

$$AR \approx \frac{25}{5} = 5$$

where the number 25 is the approximate total length (in inches) of the model, and the number 5 is the approximate planform width (in inches) of the aft planform of the model. Restricting attention solely to the aft planform, the above equation indicates that "strip theory" should be applicable to this configuration at high angles of incidence in a hypersonic flow. Furthermore, note the similarity between a flat-faced strip at incidence and a yawed cylinder flow.

To illustrate some of the salient features of very high angle-of-attack hypersonic flows, attention will be resticted in the present consideration to one angle-of-attack condition, namely 60 deg, for the NASA LRC-SB configuration. The specific AEDC-VKF Tunnel F conditions to be used correspond to time points of 60 and 136 msec for Run Number 3648 on page 38 of Ref. 96. Note that the AEDC-VKF Tunnel F gas media is nitrogen. Full details of the model instrumentation for this test may be found in Ref. 96.

To assess the accuracy and validity of classical Newtonian theory under high angle-of-attack conditions where inviscid tangent-cone theory is not applicable (see Section 2.10.2 for discussion of these theories), Fig. 34 shows a comparison of classical Newtonian theory relative to the windward centerline pressure measurements of Ref. 96 for the NASA LRC-SB configuration at 60-deg angle of attack. On the aft section of the body ($z/L \gtrsim 0.4$) classical Newtonian theory is in reasonable agreement with the experimental measurements for both time points; note that the tunnel conditions corresponding to these time points are given on the top of the figure. Over the forebody (delta) section ($z/L < 0.4$) the blunted nose influence on the pressure distribution is quite substantial, even though the body is at 60-deg angle of attack. These results indicate that classical Newtonian theory should, in general, provide reasonable estimates of the windward centerline pressure on delta forebody-strip afterbody configurations at high angle of attack in a hypersonic flow provided the region of interest is sufficiently far downstream of a blunted nose for the pressure distribution to attain a constant level.

The spanwise pressure distribution at the body location $z/L = 0.74$ on the strip afterbody of the NASA LRC-SB configuration at 60-deg angle of attack is shown in the lower portion of Fig. 34. The windward cross-sectional shape at this body location is a flat-faced body with rounded corners, as shown by Fig. 33. Hence, the South one-strip method of integral relations for an axisymmetric body (a flat-faced disk with rounded shoulders having a natural sonic point location determined per

Section 2.10.3 of the present report) has been used to calculate the theoretical spanwise pressure distribution shown in Fig. 34. The experimental measurements shown as circles in Fig. 34 represent both time points in that there is very little difference between the individual time point values when interpreted in terms of the ratio $\bar{p}/p_{\mathfrak{L}}$. In general, the agreement between theory and experiment is excellent for the spanwise pressure distribution on this particular body and flow condition.

One could possibly question the use of an axisymmetric body (flat-faced disk with rounded corners) to approximate the strip afterbody; a two-dimensional flat-faced strip with rounded corners appears a more reasonable choice of physical bodies to use in the one-strip method of integral relations treatment. As discussed in Section 2.10.3 of the present report, the South digital computer code of Ref. 61 has been modified to consider both axisymmetric and two-dimensional bodies as part of the current study. The results of applying this analysis to the present NASA LRC-SB flat-faced body with rounded corners having a natural sonic point location in both a two-dimensional (j = 0) and an axisymmetric (j = 1) sense are presented in Fig. 35 for the 60-deg angle of attack, free-stream Mach Number 10.7 condition of current interest. The calculated spanwise pressure distributions are very similar, with the two-dimensional case having a slightly higher pressure than the axisymmetric case in the region near the flat-corner juncture. In the centerline region of the body both analyses are in excellent agreement with each other; essentially identical stagnation line inviscid velocity gradients are obtained from both analyses upon application of the numerical differentiation procedure of Section 2.10.3. Observe from Fig. 35 that the discontinuity in the pressure gradient at the flat-corner juncture is more severe for the two-dimensional flow condition. Upon comparison of Figs. 34 and 35, where Fig. 34 includes the experimental pressure measurements of Ref. 96, the axisymmetric-type analysis appears the more reasonable choice for this type body and flow condition. Similar conclusions have been reached by the present authors based on comparisons (not presented herein) of the South one-strip method of integral relations analysis in a two-dimensional and axisymmetric sense applied to Configurations C2, C3, and C4 of Bertin, et al. (Ref. 97), which are strip-type bodies at incidence under hypersonic conditions. For other body configurations, however, the two-dimensional-type analysis may be more appropriate for determination of the spanwise pressure distribution, and it is recommended by the present authors that the decision as to which type analysis is most applicable to a given geometry and flow condition be made relative to comparison of theory and experiment, if possible.

One of the more interesting aerodynamic phenomena of the delta forebody-strip afterbody configuration at incidence in a hypersonic flow is the physical behavior of the windward centerline shock shape distribution. As shown on the top portion of Fig. 36 for the NASA LRC-SB delta wing at 60-deg angle of attack under AEDC-VKF Tunnel F conditions, there is an inflection in the shock shape between the body locations $z/L = 0.4$ and 0.6. The shock angle on the delta forebody ($\theta_{shock} \approx 68$ deg) is in good agreement with the results of Fig. 21 in Bertram and Henderson (Ref. 24) for a 75-deg-sweep delta wing at 60-deg angle of incidence in a Mach 9.6 airflow. Over the rear of the afterbody strip section, the shock angle approaches the angle of attack; i.e., the shock becomes essentially parallel with the body, just as in a yawed cylinder flow. Hence, one would perhaps expect the flow over the rearward portion of the strip body ($z/L > 0.6$) to behave similarly to flow over a yawed cylinder; both the surface pressure and the shock shape approach constant values in conjunction with no change in the body contour for z/L locations greater than 0.32. The region $z/L = 0.32$ to $z/L = 0.6$ may be regarded physically as a transition region from a blunted delta wing flow to a yawed-cylinder-type flow.

Restricting attention solely to the region $z/L > 0.5$ on the afterbody strip section of the NASA LRC-SB configuration at 60-deg angle of incidence, it is not clear what is the appropriate shock angle for use in determining the inviscid outer edge conditions for input to a centerline boundary-layer analysis following the procedure outlined at the conclusion of Section 2.10.2 in the present report. To assess the effects of shock angle on calculated boundary-layer behavior, the lower portion of Fig. 36 presents calculated centerline turbulent heat-transfer rates based on four different assumed values for the shock angle ($\theta_{shock} = 60.0$, 62.5, 65.0, and 67.5 deg; experimental heat-transfer-rate measurements from the AEDC-VKF Tunnel F Run Number 3648 at two time points (shown on the figure with the corresponding free-stream conditions) are also included for comparison. The spanwise pressure distribution of Fig. 34 is used to determine the stagnation or attachment line inviscid velocity gradient following the numerical differentiation procedure of Section 2.10.3; classical Newtonian theory as shown at the top of Fig. 34 is used to determine the centerline pressure, which remains constant for a given time point, even though the shock angle may change. The boundary-layer calculations are for a fully turbulent ($\lambda = 0.09$) boundary layer having a constant wall temperature of 540°R because of the impulse-type flow character of AEDC-VKF Tunnel F. Note from Fig. 36 that a shock angle of approximately 65 deg results in reasonable agreement between theory and experiment for both time

points. Further note from Fig. 36 that the parallel shock assumption (θ_{shock} = 60.0 deg) results in a calculated turbulent heat rate some 10 to 15 percent above the experimental measurements for both time points. Further illustrations of the effects of shock angle on various inviscid edge parameters, as well as turbulent boundary-layer parameters, are given in Tables II and III. Observe from Table III that increasing the shock angle serves to decrease all of the centerline turbulent boundary-layer parameters. Table II shows that increasing the shock angle results in a decrease in inviscid centerline density, velocity, and velocity gradient with a corresponding increase in centerline inviscid static temperature. Note that the change in some of these parameters is on the order of 30 to 40 percent between shock angles of 60.0 and 67.5 deg.

As shown in Fig. 36, the calculated turbulent heat-transfer rates are constant in the region $0.5 \leqq z/L \leqq 1.0$ based on the present "strip theory" approach. This is a direct consequence of the constant width strip afterbody which, as discussed previously, is very similar in flow behavior to a yawed cylinder under the present high angle-of-attack condition. This means that all the boundary-layer parameters remain constant along the strip afterbody for the present body and flow condition. Such a condition is not immediately apparent to the aerodynamicist accustomed to two-dimensional flat-plate-type boundary layers where the boundary-layer parameters vary with distance along the plate. The important and basic difference here is in the three-dimensional stagnation or attachment line character of the present flow (see the end of Section 2.10.1 for a physical description of this type flow).

As tabulated in Fig. 36 for the centerline heat-transfer-rate distribution on the NASA LRC-SB delta wing at 60-deg angle of attack under AEDC-VKF Tunnel F conditions, the reference heat flux, $\dot{q}_{ref}$, is a calculated value for a 0.675-in.-radius sphere based on the laminar stagnation point boundary-layer theory of Fay and Riddell (Ref. 98) evaluated for the particular tunnel free-stream conditions of interest. Hence, the ratio $\dot{q}_w/\dot{q}_{ref}$ in Fig. 36 represents a turbulent boundary-layer heat flux divided by a laminar boundary-layer heat flux, with the laminar value being used as a reference quantity. As shown by Widhopf (Ref. 99), the turbulent heat-transfer formulation derived by Vaglio-Laurin (Ref. 33) based on inviscid streamline spreading for bodies at incidence in a hypersonic flow in conjunction with a laminar sphere stagnation point reference value computed from the Fay and Riddell theory (Ref. 98) leads to a free-stream unit Reynolds number effect on the turbulent heat-transfer rate in the form (see Eq. (6) of Ref. 99)

$$\frac{\dot{q}_{\text{Turbulent}}}{\dot{q}_{\text{Laminar, Fay and Riddell}}} \propto [\text{Re}_\infty/\text{ft}]^{3/10} \tag{125}$$

This theoretical 3/10-power dependence on the free-stream unit Reynolds number was experimentally verified by Widhopf (Ref. 99) based upon earlier turbulent boundary-layer heat-transfer measurements on a 9-deg half-angel spherically blunted cone at angles of attack up to 20 deg under AEDC-VKF Tunnel F conditions; see Ref. 100 for complete documentation of the experimental investigation. That this 3/10-power dependence of the free-stream unit Reynolds number on turbulent heat-transfer rate is also applicable to lifting body configurations at high angles of incidence can be seen upon careful examination of the experimental data for the two time points presented in Fig. 36. Note the factor-of-two difference in free-stream unit Reynolds number at the two time points, with the free-stream Mach number remaining essentially the same value. Upon application of Eq. (125) to the conditions of Fig. 36,

$$\frac{[\dot{q}_w/\dot{q}_{ref}]_{60\ \text{msec}}}{[\dot{q}_w/\dot{q}_{ref}]_{136\ \text{msec}}} = \left[\frac{10.16 \times 10^6}{5.11 \times 10^6}\right]^{3/10} = 1.23$$

which is in reasonable agreement with a mean fairing of the experimental measurements for the two time points. Further, note that the calculated turbulent heat-transfer rates based on the present eddy viscosity model of turbulence also follow the 3/10-power unit Reynolds number dependence. Using the 65-deg shock angle values of Fig. 36 as an example,

$$\frac{[\dot{q}_w/\dot{q}_{ref}]_{60\ \text{msec}}}{[\dot{q}_w/\dot{q}_{ref}]_{136\ \text{msec}}} = \frac{0.78}{0.615} = 1.27$$

which is in excellent agreement with the above value of 1.23 based on the 3/10 power of the unit Reynolds number. Hence, for a common free-stream Mach number, the ratio of turbulent heat-transfer rate to a reference laminar heat-transfer rate appears to scale as the 3/10 power of the free-stream unit Reynolds number even at high angle-of-attack conditions typical of lifting entry vehicles. If both the free-stream Mach number and unit Reynolds number are considered as parameters, then the above simple 3/10-power scaling is no longer applicable, since Mach number is also variable (see Eq. (6) in Ref. 99 for consideration of Mach number effects).

An examination into the effects of the discontinuity in surface curvature at the flat-corner juncture point on the afterbody section of the NASA LRC-SB configuration as it relates to surface heat-transfer rate and boundary-layer flow direction is presented in Fig. 37. The pressure distribution for this particular flow has been given previously in Figs. 34 and 35, where it was shown that the discontinuity in surface curvature at the flat-corner juncture results in a discontinuity in the pressure gradient at this location. As shown at the top of Fig. 37, this discontinuity in surface curvature has little or no effect on the calculated turbulent boundary-layer heat-transfer distribution for this particular high angle-of-attack flow condition corresponding to the high Reynolds number time point of the AEDC-VKF Tunnel F Run Number 3648 of current interest. The calculated spanwise turbulent heat-transfer rate is in good agreement with the experimental measurements of Ref. 96 at the body location $z/L = 0.74$. As shown at the bottom of Fig. 37, the calculated inviscid edge direction angle, ω_e, as well as the turbulent boundary-layer surface flow direction angle, ω_s, has a discontinuity in both the first and second derivatives at the flat-corner juncture which is a direct reflection of the pressure gradient discontinuity at this location. Note that at the flat-corner juncture point ($x/x_{max} \approx 0.74$) the boundary-layer surface flow angle, ω_s, is approximately 30 deg, while the inviscid edge flow angle is about 23.5 deg. This means physically that the turbulent boundary layer has "turned" an additional 6.5 deg under the outer edge inviscid streamline at this location. On the rounded corner portion of the body ($x/x_{max} > 0.74$), note from Fig. 37 that the calculated turbulent heat-transfer rate reaches a maximum and then decreases rapidly, following the surface pressure level variation shown in Figs. 34 and 35.

3.5 MCDONNELL-DOUGLAS (MDAC) DELTA WING ORBITER CONFIGURATION

The only NASA Phase B SS design tested extensively in both the AEDC-VKF Hypersonic Wind Tunnel (B) at Mach 8 and the AEDC-VKF Hypervelocity Wind Tunnel (F) at nominal Mach Number 10.5 was the McDonnell-Douglas (MDAC) Delta Wing Orbiter configuration (0.011 scale). Side and windward planform views of this configuration are shown in Fig. 38; more complete details of the body geometry can be found in Refs. 101 and 102, which document the data taken during the AEDC wind tunnel tests. As can be seen from Fig. 4 of Ref. 102, the MDAC Orbiter configuration windward surface cross-sectional shapes can be well represented in the axial coordinate range $0.1 < z/L < 0.4$

by a swung-arc body having a forced sonic point at the leading edge; between $z/L = 0.4$ and $z/L = 0.7$, a flat-faced body with rounded shoulders approximation having a forced sonic point at the leading edge appears reasonable. For $z/L > 0.6$, the aft delta wing is sweeping out from the body and the "strip theory" approach of the present analysis is not applicable as discussed in the following paragraph.

With reference to the MDAC Orbiter windward planform geometry shown in Fig. 38, note that in the range $0.1 < z/L < 0.6$ the planform is essentially a highly swept delta wing of sweep angle approximately 81.5 deg. For $z/L > 0.6$, the planform is similar to a delta wing of 55-deg sweep. Note the similarity between the MDAC orbiter planform geometry of Fig. 38 and the NAR Orbiter Configuration 161B presented previously in Fig. 26. All of the arguments presented in Section 3.3 relative to applicability of the present "strip theory" to the NAR Orbiter Configuration 161B also directly apply to the MDAC Orbiter of current interest. Just as in Section 3.3, the succeeding analysis of the MDAC Orbiter configuration will be restricted to the range $0.1 \leqq z/L \leqq 0.7$, where it is believed that "strip theory" should be applicable providing the angle of attack is greater than about 25 deg.

As shown by Figs. 6, 7, and 9 in the recent paper by Matthews, et al. (Ref. 43), inviscid tangent-cone theory applied locally following Section 2.10.2 in the present report is in good agreement with experimental data for the MDAC Orbiter windward centerline pressure distribution, shock angle, and edge Mach number in the angle-of-attack range $30 \text{ deg} \leqq \alpha \leqq 50$ deg under Mach 8 hypersonic flow conditions. This means that inviscid tangent-cone theory should, in general, provide reasonable estimates of the windward centerline inviscid flow-field parameters needed for input to the present boundary-layer analysis in the angle-of-attack range of 30 to 50 deg under hypersonic conditions.

To calculate heating rate distributions on the MDAC configuration, body cross-sectional cuts were made at $z/L = 0.3$, 0.5, and 0.7, and the spanwise pressure distributions at these locations were determined via the method of Section 2.10.3. Figure 39 shows the results of this approach for the body station $z/L = 0.5$ on the MDAC Orbiter configuration at 30-deg angle of attack in a Mach 8 hypersonic flow. Note from Fig. 39 that the windward cross-sectional shape has been approximated by a flat-faced body with rounded corners having a forced sonic point location determined per Section 2.10.3 for an axisymmetric body, i.e., a flat-faced disk with rounded shoulders. Further note from the insert in Fig. 39 that the discontinuity in body cross-sectional curvature at the

flat-corner juncture point is reflected in the pressure distribution as a slight discontinuity in the pressure gradient $\frac{d\bar{p}}{dx}$. It should be noted that the spanwise pressure distributions at z/L = 0.5 for both the 40- and the 50-deg angle-of-attack cases are almost identical with the 30-deg case of Fig. 39 because the location of the forced sonic point is fixed by the body geometry irrespective of the angle of attack. Also shown in Fig. 39 are experimental spanwise surface pressure measurements taken in the VKF Tunnel F as reported for Run Number 3653 in Ref. 102. Even though these measurements were taken in a nominal Mach 10.5 flow, the pressure distribution in the form $\bar{p}/p_{\infty}$ should be relatively insensitive to Mach number changes, providing the flow is hypersonic. The reasonable agreement between theory and experiment observed in Fig. 39 indicates that the current "strip theory" approach applied locally is indeed applicable for calculation of surface pressure under the present flow conditions and body geometry.

Heating rate distributions calculated from the present three-dimensional laminar and turbulent boundary-layer analysis (using inviscid tangent-cone theory for the determination of windward centerline inviscid flow parameters in conjunction with the spanwise pressure distribution determined as discussed in the previous paragraph) are presented in Figs. 40 and 41 relative to the experimental measurements of Ref. 101 for the MDAC Orbiter configuration. Figure 40 gives the windward centerline Stanton number distributions for both laminar and turbulent boundary layers at 30-, 40-, and 50-deg angles of attack under AEDC-VKF Tunnel B high Reynolds number conditions. The turbulent data (shown as closed or darkened symbols) were obtained using carborundum grit placed on the windward surface to "trip" the boundary layer (see Ref. 101 for a discussion of this technique). All of the experimental heat-transfer data of Ref. 101 were determined by the phase-change paint technique employing 0.011-scale Stycast® models using Tempilaq® as the surface temperature indicator. Full details of the AEDC-VKF phase-change paint data reduction technique are presented in the Data Reduction Section of Ref. 101. The calculations were performed for the z/L = 0.3, 0.5, and 0.7 stations of the previous paragraph, and the theoretical lines shown in Fig. 40 are fairings through the three calculated values. In general, good-to-excellent agreement between theory and experiment is observed for the windward centerline heat-transfer distributions at all three angle-of-attack conditions and both laminar and turbulent boundary layers. It should be noted that all turbulent boundary-layer calculations are based on the use of an outer mixing-length constant $\lambda = 0.09$ (i.e., a fully turbulent boundary layer).

The spanwise Stanton number distributions for both laminar and turbulent boundary layers at the body station location $z/L = 0.5$ on the MDAC Orbiter configuration at 30-, 40-, and 50-deg angles of attack under AEDC-VKF Tunnel B high Reynolds number conditions are given in Fig. 41. Note that this body location corresponds to the spanwise pressure distribution of Fig. 39 discussed previously. As can be seen from Fig. 41, good-to-excellent agreement between the present three-dimensional boundary-layer theory and the experimental measurements of Ref. 101 is observed for the case of a fully turbulent boundary layer at all three angle-of-attack conditions. The key point of interest in Fig. 41 is the extremely clear indication of laminar boundary-layer crossflow transition beginning at a spanwise location where the crossflow Reynolds number, χ, reaches a value of approximately 100. (See Section 2.8 for a discussion of crossflow transition and the crossflow Reynolds number.) The present MDAC Orbiter results are in direct agreement with the crossflow transition results of Section 3.3 for the NAR Orbiter Configuration 161B under identical hypersonic, high Reynolds number conditions so that all comments, discussion, and conclusions regarding crossflow transition, as well as flow acceleration resulting in transition laminarization, presented in Section 3.3 apply without change to the present case. The 30-deg angle-of-attack condition of Fig. 41 indicates that crossflow transition may be completed near the sonic point location, i.e., that it is a fully turbulent boundary layer, while at and near the centerline the boundary layer remains in a laminar state. It should be noted that for the 30- and 40-deg angle-of-attack cases in Fig. 40, proper interpretation of the laminar phase-change paint data (shown as the O symbol) indicates that boundary-layer transition did not occur anywhere along the model centerline; the 50-deg angle-of-attack data in Fig. 40 show centerline boundary-layer transition to begin somewhere around $z/L \approx 0.5$ to 0.6 for the present high Reynolds number flow condition.

As discussed in Section 3.3 relative to crossflow transition on the NAR Orbiter Configuration 161B, transition may or may not actually occur under a flow condition where three-dimensional crossflow instability theory indicates that transition could occur. Small amounts of surface roughness, such as paint specks in phase-change paint, have been observed to "trip" the three-dimensional laminar boundary layer on lifting body geometries at high angles of incidence because of the extreme thinness of the laminar boundary layer. By a careful observation of Fig. 41 it may be noted that, for all three angle-of-attack conditions, the increase in heating rate denoting the onset of crossflow transition starts immediately downstream of the flat-corner juncture location

on the body surface. Hence, it is reasonable to surmise that the flat-corner discontinuity may, in some unknown manner, "trip" the boundary layer and trigger the start of transition in a three-dimensional laminar boundary layer which is already unstable to small disturbances because of the three-dimensional crossflow instability mode (note that $90 < \chi < 200$ at the flat-corner juncture in Fig. 41 for all three angles of attack). Such may also well be the case for the NAR Orbiter Configuration 161B as given by Fig. 31, but it is difficult to discern here since only one thermocouple is located downstream of the flat-corner juncture location.

One very important clue as to the behavior of the three-dimensional laminar boundary layer at the flat-corner juncture location can be seen from comparison of Figs. 31 and 41 for the NAR Orbiter Configuration 161B and the MDAC Orbiter, respectively, at 50-deg angle of attack under the same high Reynolds number hypersonic flow condition. Note that at the flat-corner juncture location, $\chi \approx 60$ for the NAR Orbiter, whereas $\chi \approx 95$ for the MDAC Orbiter. The NAR Orbiter heat rate measurements indicate that the boundary layer remained laminar downstream of the flat-corner juncture, whereas the MDAC Orbiter paint data indicate that boundary-layer transition began immediately downstream of the flat-corner juncture location. These findings strongly suggest that the level of the crossflow Reynolds number, χ, must be on the order of 100 or greater for a small disturbance to trigger the crossflow instability mechanism leading to boundary-layer transition in a three-dimensional sense for hypersonic lifting bodies at high angles of incidence. The possibility of suitably designing the cross-sectional contour of the body to keep the crossflow Reynolds number, χ, at as small a value as possible deserves future attention.

A comparison of both calculated and experimental results for windward centerline Stanton number distributions on the MDAC Orbiter configuration at 50-deg angle of attack under both AEDC-VKF Tunnel B and F conditions is given in Fig. 42. The AEDC-VKF Tunnel B experimental data shown in this figure are taken from Run 174 of Ref. 101, and the AEDC-VKF Tunnel F data are taken from Run 3659, time points 71 and 135 msec, of Ref. 102. In general, the present three-dimensional fully turbulent boundary-layer calculations are in good agreement with the experimental results from both tunnels. Note from the top of Fig. 42, which gives the tabulated free-stream flow conditions, that the AEDC-VKF Tunnel F late time point (135 msec) has approximately the same free-stream unit Reynolds number as the AEDC-VKF Tunnel B condition. However, the free-stream Mach number, M_∞, and the wall

temperature ratio, $T_w/T_{o,\infty}$, are both different between the two tunnel flows, especially for the wall temperature ratio ($T_w/T_{o,\infty} = 0.20$ for the AEDC-VKF Tunnel F flow, whereas $T_w/T_{o,\infty} = 0.64$ for the AEDC-VKF Tunnel B flow). Recall that the AEDC-VKF Tunnel B test used a phase-change paint technique (which for the present 50-deg angle-of-attack high Reynolds number flow employed a 400°F phase-change paint temperature), whereas the AEDC-VKF Tunnel F test was conducted under cold wall ($T_w = 540°R$) conditions because of the impulse nature of the flow. A complete examination of the effects of varying wall temperature ratio on both the laminar and turbulent three-dimensional boundary-layer parameters will be presented in a following paragraph. Suffice it to say for the present Fig. (Fig. 42) that a large part of the observed difference between the essentially common Reynolds number AEDC-VKF Tunnels B and F results, both experimental and calculated, is due to the difference in wall temperature ratio between the two flows.

The effects of change in the free-stream Reynolds number at an essentially common free-stream Mach number and wall temperature ratio can be seen from the two AEDC-VKF Tunnel F time point results on Fig. 42. Note from the top part of Fig. 42 that the free-stream Reynolds number decreases by approximately a factor of three between the 61- and 135-msec time points. As discussed previously in Section 3.4, the turbulent-to-laminar reference heat-transfer ratio should theoretically have a 3/10-power dependence on the free-stream unit Reynolds number (assuming the free-stream Mach number fixed). For the present AEDC-VKF Tunnel F flow conditions, Eq. (125) in Section 3.4 of the present report gives

$$\frac{\left[St_\infty/St_{\infty,ref}\right]_{61\ msec}}{\left[St_\infty/St_{\infty,ref}\right]_{135\ msec}} = \left[\frac{12.65 \times 10^6}{4.16 \times 10^6}\right]^{3/10} = 1.40$$

which is in reasonable agreement with a mean fairing of the experimental measurements for the two time points. Further note that the calculated turbulent heat-transfer rates based on the present eddy viscosity model of turbulence also follow the 3/10-power unit Reynolds number dependence. Using the calculated $z/L = 0.5$ Stanton number values in Fig. 42 as an example,

$$\frac{\left[St_\infty/St_{\infty,ref}\right]_{61\ msec}}{\left[St_\infty/St_{\infty,ref}\right]_{135\ msec}} = \frac{0.40}{0.28} = 1.43$$

which is in excellent agreement with the above value of 1.40 based on the 3/10 power of the unit Reynolds number. The combined results of Section 3.4 and the present MDAC Orbiter strongly indicate that, for a common free-stream Mach number and wall temperature, the ratio of turbulent heat-transfer rate to a reference laminar heat-transfer-rate scales as the 3/10 power of the free-stream unit Reynolds number for high angle-of-attack conditions typical of lifting entry vehicles. If the free-stream Mach number and unit Reynolds number, as well as the wall temperature, are considered as parameters, then the above 3/10-power scaling is no longer applicable, and recourse to Eq. (6) in Ref. 99 must be taken for investigation of the combined effects.

The influence of wall temperature ratio on the windward centerline laminar and turbulent boundary-layer parameters for the body location $z/L = 0.5$ on the MDAC Orbiter configuration at 30-deg angle of attack under AEDC-VKF Tunnel B high Reynolds number conditions is given in Tables IV, V, and VI, as well as in Figs. 43, 44, and 45. Several very interesting observations concerning the relative behavior of three-dimensional laminar and turbulent boundary layers with respect to wall temperature changes can be made upon comparison of Tables IV and V. Note that while increasing the wall temperature results in an increase in the laminar boundary layer skin-friction coefficient $C_{f_{\infty,z}}$, increasing the wall temperature decreases the turbulent boundary layer skin-friction coefficient. The three-dimensional turbulent boundary-layer thickness, δ_z, is a factor of 5 to 6 times larger than the corresponding wall temperature three-dimensional laminar boundary layer thickness. Especially note the thinness of the three-dimensional laminar boundary layer on the windward centerline for this flow condition and body location (i.e., $\delta_z \approx 0.02$ to 0.03 in.). This is a clear indication of why even what may be termed "small roughness" can successfully "trip" the three-dimensional laminar boundary layer. As discussed on page 3 of Ref. 86, No. 46 grit on glue (0.025-in. mean total height) distributed over the lower surface of the NAR Orbiter Configuration 161B was sufficient to "trip" the three-dimensional laminar boundary layer under conditions similar to those of present interest. Further observe that although the turbulent Stanton number percentage change between $T_w/T_{o,\infty}$ values of 0.2 and 0.5 is on the order of 15 percent, the laminar Stanton number changes only about 6 percent for the same wall temperature ratio increase. This indicates clearly that the three-dimensional turbulent boundary layer is more sensitive to wall temperature effects reflected in the Stanton number than is the three-dimensional laminar boundary layer.

As shown in Table VI, increasing the wall temperature on the three-dimensional laminar boundary layer decreases the numerical value of the MDAC transition onset parameter defined and discussed in Section 2.8 of the present report. The reason for this behavior can be seen from examination of Table IV with respect to the three-dimensional laminar boundary-layer momentum thickness, $\theta_{m,z}$; an increase in wall temperature decreases the laminar boundary-layer momentum thickness. The implication of Table VI as it relates to lifting body centerline boundary-layer transition is that, for a given flow condition and angle of attack, the colder the wall, the earlier (with respect to surface distance from the nose of the body) centerline transition may be expected to begin adopting the MDAC transition criterion as given in Fig. 8 of Ref. 7 as a valid indicator of boundary-layer transition onset.

The calculated effects of wall temperature on spanwise boundary-layer parameters (heat-transfer rate, surface flow angle direction, and crossflow Reynolds number) are presented in Figs. 43, 44, and 45 for the axial location $z/L = 0.5$ on the MDAC Orbiter configuration at 30-deg angle of attack under AEDC-VKF Tunnel B high Reynolds number Mach 8 flow conditions. Essentially the same trends observed previously in Tables IV and V with respect to effects of wall temperature on the centerline Stanton number apply without change to the spanwise heat-transfer coefficient distributions shown in Fig. 43. The three-dimensional turbulent boundary-layer heat-transfer coefficient in the spanwise direction is more sensitive (with respect to percentage change) to increase in the wall temperature ratio from $T_w/T_{o,\infty} = 0.2$ to 0.5 than the corresponding three-dimensional laminar boundary layer under the same flow conditions.

With respect to wall temperature influence on the boundary-layer surface flow angle, ω_s, Fig. 44 shows that, in general, the hotter the wall, the greater the turning effect on the hypersonic three-dimensional laminar and turbulent boundary layer attributable to crossflow. At the $x = x^*$ span location, Fig. 44 reveals the following variation with wall temperature of the boundary-layer surface flow angle, ω_s:

	ω_s, deg	
$T_w/T_{o,\infty}$	Laminar	Turbulent
0.2	35.0	23.5
0.5	41.5	26.5
0.8	46.0	29.5

The corresponding inviscid edge flow angle for this $x = x^*$ location is $\omega_e = 16.0$ deg. Hence, the maximum laminar boundary-layer turning angle ($\omega_s = 46.0$ deg for the $T_w/T_{o,\infty} = 0.8$ condition) is approximately a factor of three greater than the inviscid flow turning angle, ω_e; the maximum turbulent boundary-layer turning angle (for the same $T_w/T_{o,\infty} = 0.8$ condition) is slightly less than a factor of two greater than the corresponding inviscid value. These findings confirm the statement by Vaglio-Laurin (Ref. 33) that "due to the larger shearing stress, smaller three-dimensional effects can be expected for turbulent layers as compared with laminar layers subject to the same boundary conditions" for the case of lifting body configurations at angle of attack in a hypersonic flow. Similar findings and conclusions have been reported by Adams (Ref. 36) for the case of sharp cones at incidence in a hypersonic flow. See pages 30 and 31 in Ref. 46 for a discussion concerning proper interpretation of hot wall ($T_w/T_{o,\infty} \approx 0.8$) ground test (force) measurements on bodies at incidence under hypersonic conditions relative to cold wall ($T_w/T_{o,\infty} < 0.2$) flight conditions for aerodynamic parameters where the boundary-layer flow direction is important.

One important facet of the crossflow instability phenomenon discussed in Section 2.8 leading to three-dimensional laminar boundary-layer transition is the influence of wall temperature level on the magnitude of the calculated crossflow Reynolds number, χ. As shown very clearly in Fig. 45 for the present MDAC Orbiter at incidence flow condition, increasing wall temperature level at a given spanwise location increases the value of χ and, hence, makes the three-dimensional laminar boundary layer more susceptible to crossflow instability leading to vortex formation and transition. It can be shown by examination of the calculated three-dimensional laminar boundary-layer profiles that the increase of the crossflow Reynolds number with wall temperature level at a given spanwise location, as shown in Fig. 45, is totally due to the sensitivity of the three-dimensional laminar boundary-layer crossflow velocity profile and boundary-layer thickness to changes in the wall temperature level. In general, the hotter the wall, the greater the crossflow velocity and boundary-layer thickness, which leads to greater instability (attributable to increasing crossflow effects) in the three-dimensional laminar boundary layer. As discussed by Adams (Ref. 46), transition contours based on ground testing in hypersonic wind tunnels under hot wall conditions on bodies at incidence may not be totally applicable to cold wall flight conditions at the same free-stream Mach and Reynolds number conditions because of the crossflow instability phenomenon's being enhanced by the hot wall condition which, in turn, can result in premature transition of the three-dimensional laminar boundary layer to turbulent flow.

The recent NASA report by Mellenthin, Hamilton, and Zoerner (Ref. 103) documents excellent oil flow visualization photographs for the MDAC Orbiter configuration at various angles of attack based on wind tunnel tests in the NASA-Ames 3.5-Foot Hypersonic Wind Tunnel at a free-stream Mach number of 7.4 and free-stream unit Reynolds numbers from about 1 million to about 6 million per foot. Figure 46 presents a comparison of calculated spanwise surface flow angles based on the present three-dimensional laminar boundary-layer analysis relative to the experimentally determined oil flow results of Fig. 23c in Ref. 103 for the nose region of the MDAC Orbiter at 50-deg angle of attack. The body station of interest here is at the axial location z/L = 0.2 with the body cross-sectional shape approximated as an axisymmetric (j = 1) swung arc with a forced sonic corner (physically a spherical cap convex to stream) for determination of the spanwise surface pressure distribution using the South one-strip method of integral relations per the discussion of Section 2.10.3 in the present report. Since the wall temperature was not directly measured in the experiments of Ref. 103, two different wall temperature ratios ($T_w/T_{o,\infty}$ = 0.4 and 0.8) representative of the lower and upper experimentally permissible values for the NASA-Ames tests have been used for the calculations shown in Fig. 46. As can be seen from Fig. 46, the present three-dimensional laminar boundary-layer calculation for the $T_w/T_{o,\infty}$ = 0.8 wall temperature ratio is in excellent agreement with the experimental oil flow results. The wall temperature ratio of $T_w/T_{o,\infty}$ = 0.8 is surmised by the present authors to be more representative for the present case than the $T_w/T_{o,\infty}$ = 0.4 value because of the high angle-of-attack condition (50 deg) in conjunction with the nose region location (z/L = 0.2) on the body.

Further comparisons of calculated laminar and turbulent surface flow angles based on the present three-dimensional boundary-layer analysis are presented in Fig. 47 relative to the experimental oil flow results from Fig. 23a in Ref. 103 for the same 50-deg angle-of-attack condition of the previous paragraph. The particular spanwise body station of interest is at the axial location z/L = 0.5, which has been discussed previously in this subsection relative to the spanwise pressure distribution of Fig. 39. As can be seen from Fig. 47, the calculated surface flow angle distribution assuming a fully turbulent boundary layer having a wall temperature ratio of $T_w/T_{o,\infty}$ = 0.8 is in excellent agreement with the experimental oil flow results over the outer 50 percent of the span; for the inner region between the body centerline to approximately the flat-corner juncture location, the experimental oil flow results are in best agreement with the calculated surface flow angle

distribution assuming a fully turbulent boundary layer having a wall temperature ratio of $T_w/T_{o,\infty} = 0.4$. However, for this particular angle of attack and flow condition, the calculated value of the windward centerline transition onset parameter (TP) following Eq. (96) in Section 2.8 of the current report yields a value TP ≈ 12, based on the present three-dimensional laminar boundary-layer theory in conjunction with a wall temperature ratio of $T_w/T_{o,\infty} = 0.4$. Such a low value for the transition onset parameter indicates that the boundary layer should be laminar at this body station, flow condition, and angle of attack, based on a value of TP ≈ 15 for transition onset at 50-deg angle of attack from Fig. 8 in Ref. 7. As can be seen from careful examination of the photographs presented in Figs. 48 and 49 (which are taken from Figs. 23a and c of Ref. 103 and correspond to the photographs used to obtain the experimental oil flow data on Figs. 46 and 47 of the current report), there is a somewhat rough-appearing model joint at the body location $z/L \approx 0.3$ which, in the opinion of the present authors, may be sufficient to "trip" the extremely thin laminar boundary layer to a turbulent state as indicated by the comparisons of Fig. 47 discussed previously. As shown in the recent work of Seegmiller (Ref. 94) based on wind tunnel tests in the NASA-Ames 3.5-Foot Hypersonic Wind Tunnel using models of the North American Rockwell 134B Delta Wing Shuttle configuration with simulated panel joints, a raised joint having a height of less than one-half the thickness of a human hair (about one-thousandth of an inch) is sufficient to "trip" the laminar boundary layer and initiate transition under high angle-of-attack flow conditions similar to those of present interest relative to the MDAC Orbiter.

Another possible interpretation of the comparison shown in Fig. 47 between calculated surface flow angles and experimental oil flow results is that, for the particular body station of current interest ($z/L = 0.5$), the boundary layer is indeed laminar, as indicated by the value of the transition onset parameter discussed in the previous paragraph. As shown in Section 2.11 of the present report relative to the oil flow results of Fig. 7, the proximity of the downstream delta wing may have an effect on upstream three-dimensional boundary-layer development. Such an argument can explain why the experimentally observed turning angles are not as large as the calculated values, assuming that the boundary-layer state is indeed laminar. Which of the above two conjectures is the correct interpretation of Fig. 47 remains an open question at the present time.

As noted at the conclusion of Section 3.2.1 in the present report, it is possible to use an "effective" x^* value in Eq. (124) for calculation of

the stagnation line inviscid velocity gradient. Such is indeed an attractive possibility when used in conjunction with Program SLYBBCBL of Appendix IV for parametric studies of body curvature effects on, say, the centerline turbulent boundary layer. For the present MDAC Orbiter configuration under AEDC-VKF Tunnels B and F flow conditions, the following table of x^* values at selected body locations has been obtained by substituting the value of the stagnation line inviscid velocity gradient determined per the South one-strip method of integral relations following Section 2.10.3 in conjunction with inviscid conical flow tangent-cone centerline properties determined following Section 2.10.2 into Eq. (124) and calculating the resulting x^* value.

z/L	x^*, ft
0.3	0.08
0.5	0.13
0.7	0.185

These x^* values represent a sort of mean average over the angle-of-attack range from 30 to 50 deg under both the AEDC-VKF Tunnel B Mach 8 condition and the Tunnel F Mach 10.5 condition. Examples of how to apply Program SLYBBCBL of Appendix IV for calculation of both the laminar and turbulent boundary layer at the $z/L = 0.3$ station on the centerline of the MDAC Orbiter under AEDC-VKF Tunnel F conditions (nitrogen gas) using the above determined x^* value are given as the last four sample cases in Appendix V.

SECTION IV
CONCLUDING SUMMARY

The present report has documented an inviscid and viscous analysis technique applicable to the windward surface of general lifting body configurations at high angles of incidence under hypersonic perfect gas wind tunnel conditions with primary emphasis placed on development of an engineering-type approach which is accurate and easy to use, while requiring only modest digital computing facilities for application. Basically, the present technique applied the "strip theory" concept leading to an infinite extent yawed body analysis applied in the windward surface crossflow plane for both the inviscid and viscous (boundary-layer) flow fields. A one-strip method of integral relations approach has been used

to determine the spanwise surface pressure distribution at a given body location with all inviscid centerline quantities determined via an inviscid conical flow approach or some alternate technique. The boundary-layer analysis has been based on implicit finite-difference integration of the governing yawed blunt-body boundary-layer equations for both laminar and turbulent flows using a three-dimensional eddy viscosity-mixing-length model of turbulence. Complete details of both the inviscid and viscous analyses have been included in the present report with a source deck listing and sample input-output for the currently developed stagnation line boundary-layer digital computer code included as appendixes.

Comparisons of the present "strip theory" approach with hypersonic wind tunnel data on yawed cylinders, delta wings, and NASA Phase B SS configurations have been presented to establish and ascertain the basic validity and applicability of the current technique. Under conditions where the basic requirements for applicability of "strip theory" are satisfied, the present analytical approach yielded accurate estimates of wall measurable flow parameters such as surface pressure, surface heat transfer, surface streamline direction, etc., for all configurations considered. One of the more important results of the current study was the tentative identification of spanwise crossflow-induced boundary-layer transition and laminarization on SS configurations at high incidence angles. Other significant findings include the 3/10-power scaling of turbulent boundary-layer heat-transfer rate with respect to changes in the free-stream Reynolds number, as well as shock angle and wall temperature effects on both laminar and turbulent boundary-layer parameters.

To the author's knowledge there are no three-dimensional boundary-layer profile measurements on lifting body configurations at high angles of incidence under hypersonic wind tunnel conditions currently available in the literature which can be used for comparison purposes with the present "strip theory" boundary-layer analysis. As the current investigation has shown, the three-dimensional turbulent boundary layer under such conditions is of sufficient thickness to enable detailed probe measurements, providing a sufficiently large model is used in conjunction with rather specialized probe instrumentation (for example, the miniature combined temperature and pressure probe designed by Meier (Ref. 104) and used by Meier and Rotta (Ref. 105) to investigate supersonic and hypersonic turbulent boundary-layer structure). Such a future experimental investigation would be of great value in assessing the present three-dimensional model of invariant turbulence under hypersonic conditions.

REFERENCES

1. Anon. "Space Transportation System Technology Symposium. I - Aerothermodynamics and Configurations." NASA TM X-52876, Vol. I, July 1970.

2. Anon. "NASA Space Shuttle Technology Conference. Vol. I - Aerothermodynamics, Configurations, and Flight Mechanics." NASA TM X-2272, April 1971.

3. Anon. "Space Shuttle Aerothermodynamics Technology Conference. Vol I - Flow Fields." NASA TM X-2506, February 1972.

4. Anon. "Space Shuttle Aerothermodynamics Technology Conference. Vol. II - Heating." NASA TM X-2507, February 1972.

5. Anon. "Space Shuttle Aerothermodynamics Technology Conference. Vol. III - Aerodynamics." NASA TM X-2508, February 1972.

6. Schadt, G. H. "Aerodynamic Heating Problems and Their Influence on Earth Orbit Lifting Entry Spacecraft." AIAA Paper No. 68-1126 presented at the AIAA 5th Annual Meeting and Technical Display, Philadelphia, Pennsylvania, October 21-24, 1968.

7. Kipp, H. W. and Masek, R. V. "Aerodynamic Heating Constraints on Space Shuttle Vehicle Design." ASME Paper No. 70-HT/SpT-45 presented at the Space Technology and Heat Transfer Conference, Los Angeles, California, June 21-24, 1970.

8. Guard, F. L. and Schultz, H. D. "Space Shuttle Aerodynamic Heating Considerations." ASME Paper No. 70-HT/SpT-16 presented at the Space Technology and Heat Transfer Conference, Los Angeles, California, June 21-24, 1970.

9. Young, C. H., Reda, D. C., and Roberge, A. M. "Hypersonic Transitional and Turbulent Flow Studies on a Lifting Entry Vehicle." AIAA Paper No. 71-100 presented at the AIAA 9th Aerospace Sciences Meeting, New York, New York, January 25-27, 1971.

10. Marvin, J. G., Seegmiller, H. L., Lockman, W. K., Mateer, G. G., Pappas, C. C., and DeRose, C. E. "Surface Flow Patterns and Aerodynamic Heating on Space Shuttle Vehicles." AIAA Paper No. 71-594 presented at the AIAA 4th Fluid and Plasma Dynamics Conference, Palo Alto, California, June 21-23, 1971.

11. Hayes, W. D. and Probstein, R. F. Hypersonic Flow Theory, Vol. I, Inviscid Flows. Academic Press, Inc., New York, 1966. (Second Edition)

12. Sychev, V. V. "Three-Dimensional Hypersonic Gas Flow Past Slender Bodies at High Angles of Attack." J. Appl. Math. Mech. (Prikl. Mat. Mekh.), Vol. 24, 1960, pp. 296-306.

13. Schlichting, H. Boundary Layer Theory. McGraw-Hill, Inc. New York, 1960. (Fourth Edition)

14. Nash, J. F. and Patel, V. C. Three-Dimensional Turbulent Boundary Layers. SBC Technical Books, Scientific and Business Consultants, Inc., Atlanta, Georgia, 1972.

15. Reshotko, E. and Bechwith, I. E. "Compressible Laminar Boundary Layer over a Yawed Infinite Cylinder with Heat Transfer and Arbitrary Prandtl Number." NACA Report 1379, 1958.

16. Beckwith, I. E. "Similar Solutions for the Compressible Boundary Layer on a Yawed Cylinder with Transpiration Cooling." NASA TR R-42, 1959.

17. Beckwith, I. E. "Similarity Solutions for Small Cross Flows in Laminar Compressible Boundary Layers." NASA TR R-107, 1961.

18. Kaups, K. and Keltner, G. "Laminar Compressible Boundary Layer on a Yawed Infinite Wing." Douglas Aircraft Company Report No. LB 32706, March 1967.

19. Beckwith, I. E. and Gallagher, J. J. "Local Heat Transfer and Recovery Temperatures on a Yawed Cylinder at a Mach Number of 4.15 and High Reynolds Numbers." NASA TR R-104, 1961.

20. Fleming, W. J., Jr. and Krauss, W. E. "Aerodynamic Heating from Turbulent Boundary Layers to Swept Surfaces." Proceedings of the 3rd International Heat Transfer Conference, Vol. II, August 1966, pp. 102-112.

21. Bradley, R. G. "Approximate Solutions for Compressible Turbulent Boundary Layers in Three-Dimensional Flow." AIAA J., Vol. 6, No. 5, May 1968, pp. 859-864.

22. Hunt, J. L., Bushnell, D. M., and Beckwith, I. E. "The Compressible Turbulent Boundary Layer on a Blunt Swept Slab with and without Leading-Edge Blowing." NASA TN D-6203, March 1971.

23. Bertram, M. H., Feller, W. V., and Dunavant, J. C. "Flow Fields, Pressure Distributions, and Heat Transfer for Delta Wings at Hypersonic Speeds." NASA TM X-316, September 1960.

24. Bertram, M. H. and Henderson, A., Jr. "Recent Hypersonic Studies of Wings and Bodies." ARS J., Vol. 31, No. 8, August 1961, pp. 1129-1139.

25. Cole, J. D. and Brainerd, J. J. "Slender Wings at High Angles of Attack in Hypersonic Flows." Hypersonic Flow Research, Edited by F. R. Riddell, Academic Press, Inc., New York, 1962, pp. 321-343.

26. Bertram, M. H. and Everhart, P. E. "An Experimental Study of the Pressure and Heat-Transfer Distribution of a 70° Sweep Slab Delta Wing in Hypersonic Flow." NASA TR R-153, December 1963.

27. Everhart, P. E. and Dunavant, J. C. "Heat-Transfer Distribution of 70° Swept Slab Delta Wings at a Mach Number of 9.86 and Angles of Attack up to 90°." NASA TN D-2302, October 1964.

28. Whitehead, A. H., Jr. and Dunavant, J. C. "A Study of Pressure and Heat Transfer over an 80° Sweep Slab Delta Wing in Hypersonic Flow." NASA TN D-2708, March 1965.

29. Beckwith, I. E. and Cohen, N. B. "Application of Similar Solutions to Calculation of Laminar Heat Transfer on Bodies with Yaw and Large Pressure Gradients in High-Speed Flow." NASA TN D-625, January 1961.

30. Pappas, C. C. "Windward Body Surface Study for Laminar Heating of Space Shuttle Vehicles at High Angle of Attack." NASA TM X-62,075, October 1971.

31. Pappas, C. C. "Calculation of Laminar Heat Transfer to the Windward Surfaces of Straight Wing Shuttle Vehicles at High Angle of Attack and with Yaw." NASA TN D-6614, May 1972.

32. Baranowski, L. C. "Influence of Cross-Flow on Windward Centerline Heating." Report MDC E0535, December 1971.

33. Vaglio-Laurin, R. "Turbulent Heat Transfer on Blunt-Nosed Bodies in Two-Dimensional and General Three-Dimensional Hypersonic Flow." WADC Technical Note 58-301, September 1958. See also J. Aeron. Sci., Vol. 27, No. 1, January 1960, pp. 27-36.

34. Adams, J. C., Jr. "Implicit Finite-Difference Analysis of Compressible Laminar, Transitional, and Turbulent Boundary Layers along the Windward Streamline of a Sharp Cone at Incidence." AEDC-TR-71-235 (AD734535), December 1971.

35. Adams, J. C., Jr. "Finite-Difference Analysis of the Three-Dimensional Turbulent Boundary Layer on a Sharp Cone at Angle of Attack in a Supersonic Flow." AIAA Paper No. 72-186 presented at the AIAA 10th Aerospace Sciences Meeting, San Diego, California, January 1972.

36. Adams, J. C., Jr. "Analysis of the Three-Dimensional Compressible Turbulent Boundary Layer on a Sharp Cone at Incidence in Supersonic and Hypersonic Flow." AEDC-TR-72-66 (AD743003), June 1972.

37. Escudier, M. P. "The Distribution of the Mixing Length in Turbulent Flows Near Walls." Mechanical Eng. Dept. Report TWF/TN/1, Imperial College, London, March 1965.

38. Patankar, S. V. and Spalding, D. B Heat and Mass Transfer in Boundary Layers. CRC Press, Cleveland, Ohio, 1968.

39. van Driest, E. R. "On Turbulent Flow Near a Wall." J. Aeron. Sci., Vol. 23, No. 11, November 1956, pp. 1007-1011, 1036.

40. Dorrance, W. H. Viscous Hypersonic Flow. McGraw-Hill, Inc., New York, 1962.

41. Moore, F. K. "Displacement Effect of a Three-Dimensional Boundary Layer." NACA TN 2722, June 1952.

42. Masek, R. V. "Boundary Layer Transition on Lifting Entry Vehicle Configurations at High Angle-of-Attack." NASA TM X-52876, Vol. 1, July 1970, pp. 445-462.

43. Matthews, R. K., Buchanan, T. D., Martindale, W. R., and Warmbrod, J. D. "Experimental and Theoretical Aerodynamic Heating and Flow Field Analysis of a Space Shuttle Orbiter." NASA TM X-2507, February 1972, pp. 261-296.

44. Owen, P. R. and Randall, D. G. "Boundary Layer Transition on a Swept-Back Wing." RAE TM Aero. 277, June 1952.

45. Chapman, G. T. "Some Effects of Leading-Edge Sweep on Boundary Layer Transition at Supersonic Speeds." NASA TN D-1075, September 1961.

46. Adams, J. C., Jr. "Three-Dimensional Laminar Boundary-Layer Analysis of Upwash Patterns and Entrained Vortex Formation on Sharp Cones at Angle of Attack." AEDC-TR-71-215 (AD736880), December 1971.

47. Gregory, N., Stuart, J. T., and Walker, N. S. "On the Stability of Three-Dimensional Boundary Layers with Application to the Flow Due to a Rotating Disk." Trans. Roy. Soc. (London), Series A, Vol. 248, No. 943, July 1955, pp. 155-199.

48. Cleary, J. W. "Experimental Surface Flow Patterns and Flow-Field Phenomena of a Delta-Wing Space-Shuttle Orbiter." NASA TM X-62, 113, February 1972.

49. Barber, E. A. "Some Experiments on Delta Wings in Hypersonic Flow." AIAA J., Vol. 4, No. 1, January 1966, pp. 72-83.

50. Nagel, A. L., Fitzsimmons, H. D., and Doyle, L. B. "Analysis of Hypersonic Pressure and Heat Transfer Tests on Delta Wings with Laminar and Turbulent Boundary Layers." NASA CR-535, August 1966.

51. Ashby, G. C., Jr. "Experimental Boundary-Layer Edge Mach Numbers for Two Space Shuttle Orbiters at Hypersonic Speeds." NASA TN D-6574, February 1972.

52. Lordi, J. A., Vidal, R. J., and Johnson, C. B. "Chemical Nonequilibrium Effects on the Flow in the Windward Plane of Symmetry of a Blunted Delta Orbiter." NASA TM X-2506, February 1972, pp. 185-238.

53. Van Dyke, M. D. "A Study of Hypersonic Small-Disturbance Theory." NACA Report 1194, 1954.

54. Rasmussen, M. L. "On Hypersonic Flow Past an Unyawed Cone." AIAA J., Vol. 5, No. 8, August 1967, pp. 1495-1497.

55. Anon. "Equations, Tables, and Charts for Compressible Flow." NACA Report 1135, 1953.

56. Sims, J. L. "Tables for Supersonic Flow around Right Circular Cones at Zero Angle of Attack." NASA SP-3004, 1964.

57. Wittliff, C. E. "Correlation of Drag Coefficients for Sharp Cones." AIAA J., Vol. 6, No. 7, July 1968, pp. 1430-1431.

58. Thomas, A. C. and Perlbachs, A. "Application of Ground Test Data to Reentry Vehicle Design." AFFDL-TR-66-229, January 1967.

59. Kennet, H. "The Inviscid Hypersonic Flow on the Windward Side of a Delta Wing." IAS Paper No. 63-55 presented at the IAS 31st Annual Meeting, New York, January 1963.

60. Pearce, B. E. "Hypersonic Flow of a Real Gas on the Windward Side of a Delta Wing." Aerospace Report No. TR-0059(6770-03)-1, April 1971.

61. South, J. C., Jr. "Calculation of Axisymmetric Supersonic Flow Past Blunt Bodies with Sonic Corners, Including a Program Description and Listing." NASA TN D-4563, May 1968.

62. Xerikos, J. and Anderson, W. A. "A Critical Study of the Direct Blunt Body Integral Method." Douglas Aircraft Company Report SM-42603, December 1962.

63. Xerikos, J. and Anderson, W. A. "An Experimental Investigation of the Shock Layer Surrounding a Sphere in Supersonic Flow." AIAA J., Vol. 3, No. 3, March 1965, pp. 451-457.

64. Xerikos, J. and Anderson, W. A. "Blunt-Body Integral Method for Air in Thermodynamic Equlibrium." AIAA J., Vol. 3, No. 8, August 1965, pp. 1531-1533.

65. Kaattari, G. E. "A Method for Predicting Shock Shapes and Pressure Distributions for a Wide Variety of Blunt Bodies at Zero Angle of Attack." NASA TN D-4539, April 1968.

66. Clark, E. L. "Aerodynamic Characteristics of the Hemisphere at Supersonic and Hypersonic Mach Numbers." AIAA J., Vol. 7, No. 7, July 1969, pp. 1385-1386.

67. Kuby, W. C. "Use of the Method of Integral Relations for the Determination of the Convective Heat Flux to a Re-Entry Body." AIAA J., Vol. 4, No. 5, May 1966, pp. 947-949.

68. Kuby, W. C., Foster, R. M., Byron, S. R., and Holt, M. "Symmetrical, Equilibrium Flow Past a Blunt Body at Superorbital Re-Entry Speeds." AIAA J., Vol. 5, No. 4, April 1967, pp. 610-617.

69. Thomas, P. D., Vinokur, M., Bastianon, R., and Conti, R. J. "Numerical Solution for the Three-Dimensional Hypersonic Flow Field of a Blunt Delta Body." AIAA Paper No. 71-596 presented at the AIAA 4th Fluid and Plasma Dynamics Conference, Palo Alto, California, June 1971.

70. Love, E. S., Woods, W. C., Rainey, R. W., and Ashby, G. C., Jr. "Some Topics in Hypersonic Body Shaping." AIAA Paper No. 69-181 presented at the AIAA 7th Aerospace Sciences Meeting, New York, January 1969.

71. Kaattari, G. E. "A Method for Predicting Pressures on Elliptic Cones at Supersonic Speeds." NASA TN D-5952, August 1970.

72. Kaattari, G. E. "Estimation of Shock Layer Thickness and Pressure Distribution on a Delta Wing-Body Space Shuttle Orbiter." NASA TM X-62, 031, May 1971.

73. Kaattari, G. E. "Prediction of Centerline Shock-Layer Thickness and Pressure Distribution on Delta Wing-Body Configurations." NASA TN D-6550, October 1971.

74. Seegmiller, H. L. "Surface-Flow Visualization Investigation of a Delta Wing Shuttle Configuration at a Mach Number of 7.4 and Several Reynolds Numbers." NASA TM X-62, 036, June 1970.

75. Cleary, J. W. "Experimental Surface Flow Patterns and Flow-Field Phenomena of a Delta-Wing Space Shuttle Orbiter." NASA TM X-62, 113, February 1972.

76. Bushnell, D. M. "Interference Heating on a Swept Cylinder in Region of Intersection with a Wedge at Mach Number 8." NASA TN D-3094, December 1965.

77. Cumpsty, N. A. and Head, M. R. "The Calculation of Three-Dimensional Turbulent Boundary Layers. Part II: Attachment-Line Flow on an Infinite Swept Wing." Aeronaut. Quart., Vol. XVIII, May 1967, pp. 150-164.

78. Cumpsty, N. A. and Head, M. R. "The Calculation of the Three-Dimensional Turbulent Boundary Layer. Part III: Comparison of Attachment-Line Calculations with Experiment." Aeronaut. Quart., Vol. XX, May 1969, pp. 99-113.

79. Lockman, W. K. "Transition Reynolds Numbers, Convective Heating Distributions, and Surface-Flow Patterns for a Flat-Surfaced Pyramid Model at Angle of Attack." NASA SSPD-9, June 1970.

80. Stultz, J. W. and Fehrman, A. L. "AFFDL Temperature Sensitive Heat Transfer Test on an 80° Delta Wing." Report MDC E0276, December 1970.

81. Masaki, M. and Yakura, J. K. "Transitional Boundary Layer Considerations for the Heating Analysis of Lifting Re-Entry Vehicles." J. Spacecraft and Rockets, Vol. 6, No. 9, September 1969, pp. 1048-1053.

82. Hanks, R. A. and Savage, R. T. "Thermal Design Methods for Recoverable Launch Vehicles with Consideration of Arbitrary Wall Temperatures and Surface Conditions." NASA CR-74714, August 1965.

83. Savage, R. T. and Jaeck, C. L. "Investigation of Turbulent Heat Transfer at Hypersonic Speeds. Volume I. Analytical Methods." AFFDL-TR-67-144, December 1967.

84. Matthews, R. K., Martindale, W. R., Warmbrod, J., and Johnson, C. B. "Heat Transfer Investigation of Langley Research Center Transition Models at a Mach Number of 8." NASA CR-120,045, March 1972.

85. Matthews, R. K., Martindale, W. R., and Warmbrod, J. D. "Surface Pressure and Inviscid Flow Field Properties of the North American Rockwell Delta-Wing Orbiter for Nominal Mach Number of 8." NASA CR-120,046, March 1972.

86. Warmbrod, J. D., Martindale, W. R., and Matthews, R. K. "Heat Transfer Rate Measurements on North American Rockwell Orbiter (161B) at Nominal Mach Number of 8." NASA CR-120,029, December 1971.

87. Lockman, W. K. and DeRose, C. E. "Aerodynamic Heating Distributions on a Space Shuttle Delta-Wing Orbiter." NASA TM X-62,114, March 1972.

88. Launder, B. E. "Laminarization of the Turbulent Boundary Layer by Acceleration." Massachusetts Institute of Technology Gas Turbine Laboratory Report No. 77, November 1964.

89. Boldman, D. R., Schmidt, J. F., and Gallagher, A. K. "Laminarization of a Turbulent Boundary Layer as Observed from Heat Transfer and Boundary-Layer Measurements in Conical Nozzles." NASA TN D-4788, September 1968.

90. Back, L. H., Cuffel, R. F., and Massier, P. F. "Laminarization of a Turbulent Boundary Layer in Nozzle Flow." AIAA J., Vol. 7, No. 4, April 1969, pp. 730-733.

91. Morkovin, M. V. "Critical Evaluation of Transition from Laminar to Turbulent Shear Layers with Emphasis on Hypersonically Traveling Bodies." AFFDL-TR-68-149, March 1969.

92. Mack, L. M. "Boundary Layer Stability Theory." JPL/CIT 900-277 Rev. A, November 1969.

93. Snedeker, R. S. "Experimental Study of Transition Induced in an Accelerated Boundary Layer at Low Reynolds Number." A. R. A. P. Report No. 168, October 1971.

94. Seegmiller, H. L. "Effects of Roughness on Heating and Boundary-Layer Transition. Part I - Effects of Simulated Panel Joints on Boundary-Layer Transition." NASA TM X-2507, February 1972, pp. 375-393.

95. Mateer, G. C. "Effects of Roughness on Heating and Boundary-Layer Transition. Part II - Effects of Discrete Roughness on Heating." NASA TM X-2507, February 1972, pp. 395-411.

96. Eaves, R. H., Buchanan, T. D., Warmbrod, J. D., and Johnson, C. B. "Heat Transfer Investigation of Two Langley Research Center Delta Wing Configurations at a Mach Number of 10.5." NASA CR-120, 036, March 1972.

97. Bertin, J. J., Lamb, J. P., Center, K. R., and Graumann, B. W. "Flow Field Measurements for Cylindrical Configurations in a Hypersonic Wind Tunnel: Windward and Leeward Flow Fields." University of Texas at Austin Aerospace Engineering Report 71007, December 1971.

98. Fay, J. A. and Riddell, F. R. "Theory of Stagnation Point Heat Transfer in Dissociated Air." J. Aeron. Sci., Vol. 25, No. 2, February 1958, pp. 73-85, 121.

99. Widhopf, G. F. "Heat Transfer Correlations for Blunt Cones at Angle of Attack." Aerospace Report No. TR-0172(S2816-63)-1, July 1971. See also J. Spacecraft and Rockets, Vol. 8, No. 9, September 1971, pp. 1002-1004.

100. Widhopf, G. F. "Turbulent Heat Transfer Measurements on a Blunt Cone at Angle of Attack." Aerospace Report No. TR-0059 (S6816-66)-1, February 1971. See also AIAA J., Vol. 9, No. 8, August 1971, pp. 1574-1580.

101. Matthews, R. K., Martindale, W. R., and Warmbrod, J. D. "Heat Transfer Rate Distributions on McDonnell-Douglas Delta Wing Orbiter Determined by Phase-Change Paint Technique for Nominal Mach Number of 8." NASA CR-120, 025, Revised July 1972.

102. Eaves, R. H., Buchanan, T. D., and Warmbrod, J. D. "Heat Transfer Investigation of the McDonnell-Douglas Delta Wing Orbiter at a Nominal Mach Number of 10.5." NASA CR-120, 024, May 1972.

103. Mellenthin, J. A., Hamilton, R. K., and Zoerner, G. D. "Aerodynamic Force Characteristics and Oil Flow Studies of a Delta Winged Space Shuttle Orbiter." NASA TM X-62, 108, December 1971.

104. Meier, H. U. "A Combined Temperature and Pressure Probe for Compressible Flow." AIAA J., Vol. 7, No. 3, March 1969, pp. 529-530.

105. Meier, H. U. and Rotta, J. C. "Temperature Distributions in Supersonic Turbulent Boundary Layers." AIAA J., Vol. 9, No. 11, November 1971, pp. 2149-2156.

106. Blottner, F. G. "Finite Difference Methods of Solution of the Boundary Layer Equations." AIAA J., Vol. 8, No. 2, February 1970, pp. 193-205.

107. Davis, R. T. "Numerical Solution of the Hypersonic Viscous Shock-Layer Equations." AIAA J., Vol. 8, No. 5, May 1970, pp. 843-851.

108. Richtmyer, R. D. and Morton, K. W. Difference Methods for Initial-Value Problems. Interscience Publishers, New York, 1967. (Second Edition)

109. Flügge-Lotz, I. and Blottner, F. G. "Computation of the Compressible Laminar Boundary-Layer Flow Including Displacement Thickness Interaction Using Finite-Difference Methods." Stanford University Division of Engineering Mechanics Report No. 131, Stanford, California, January 1962.

110. Smith, A. M. O. and Cebeci, T. "Numerical Solution of the Turbulent Boundary-Layer Equations." Douglas Aircraft Division Report 33735, May 1967.

111. Conte, S. D. Elementary Numerical Analysis. McGraw-Hill, Inc., New York, 1965.

APPENDIXES

I. ILLUSTRATIONS
II. TABLES
III. IMPLICIT FINITE-DIFFERENCE SOLUTION OF GOVERNING BOUNDARY-LAYER EQUATIONS
IV. FORTRAN 63 SOURCE DECK LISTING OF STAGNATION LINE YAWED BLUNT-BODY COMPRESSIBLE BOUNDARY-LAYER PROGRAM SLYBBCBL
V. SAMPLE INPUT-OUTPUT DATA FOR PROGRAM SLYBBCBL

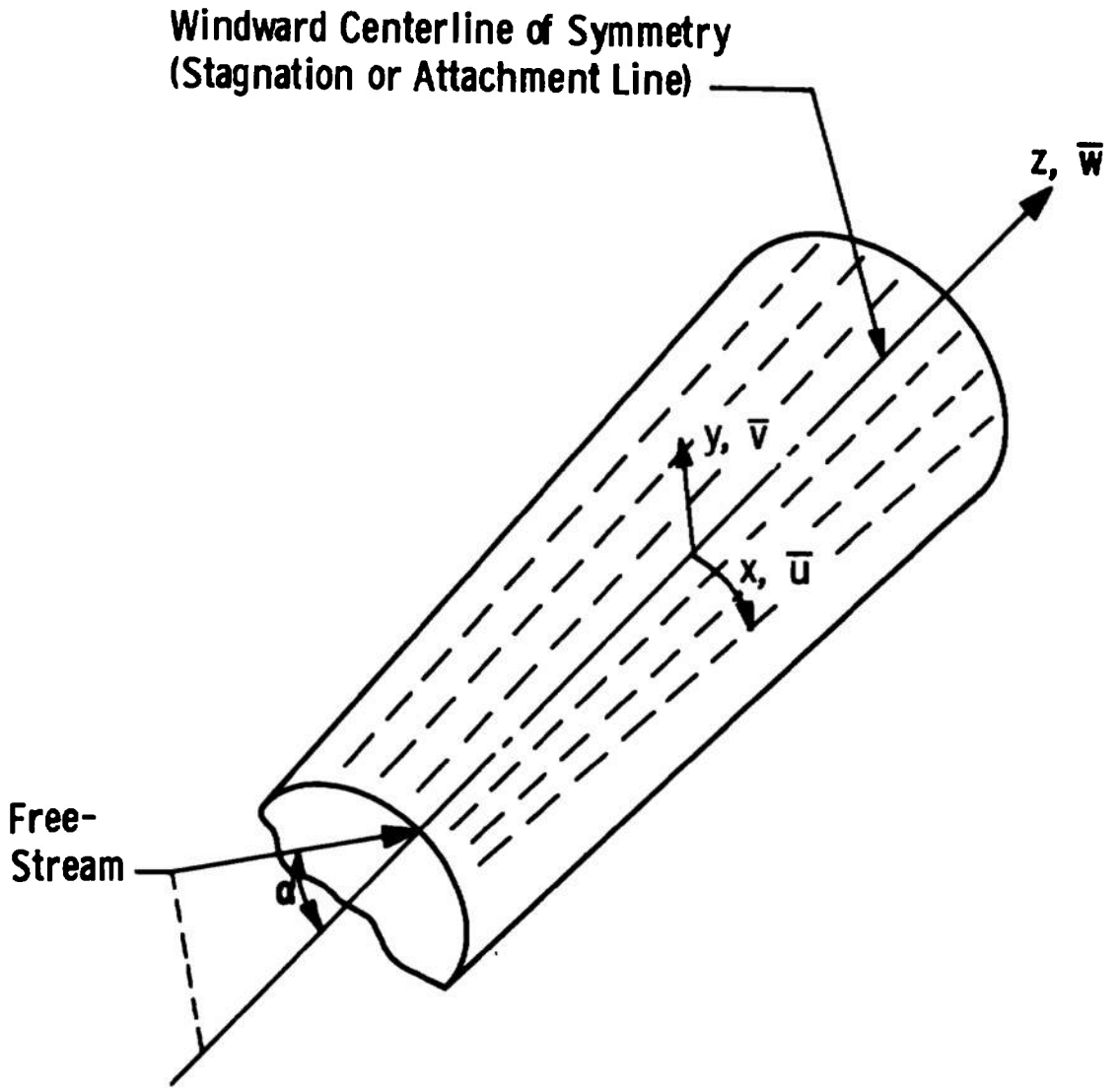

Fig. 1 Windward Surface Orthogonal Coordinate System for General Lifting Body Configurations at Incidence

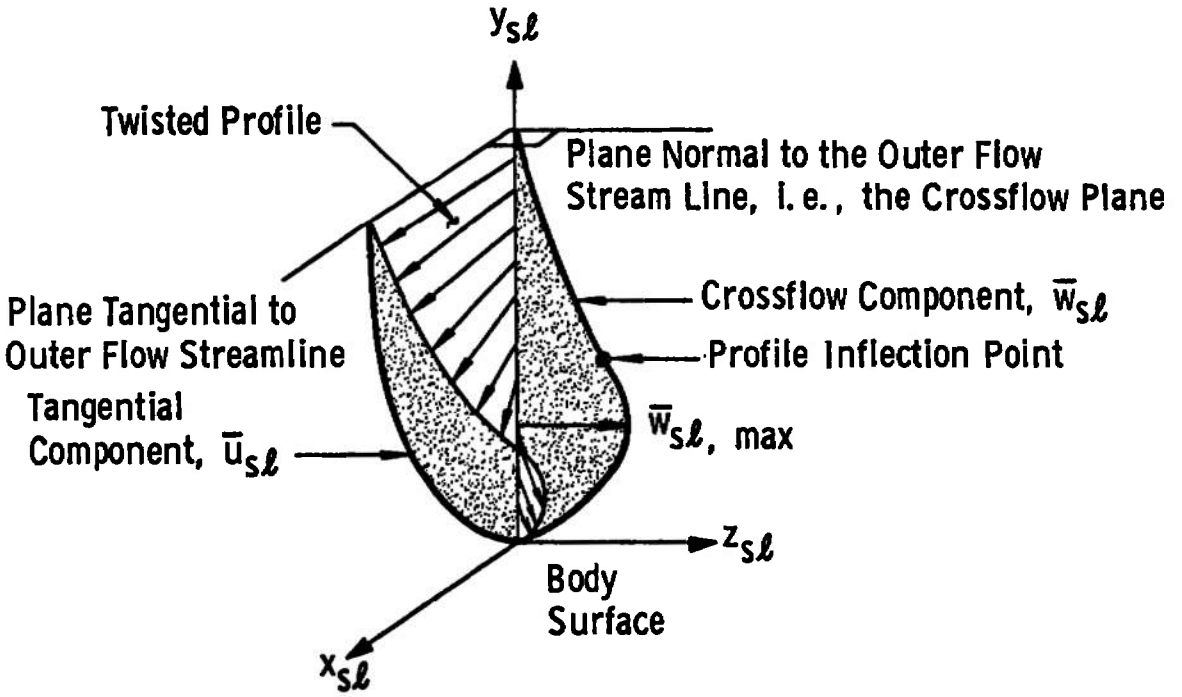

Fig. 2 Three-Dimensional Boundary-Layer Velocity Profiles in Streamline Coordinates

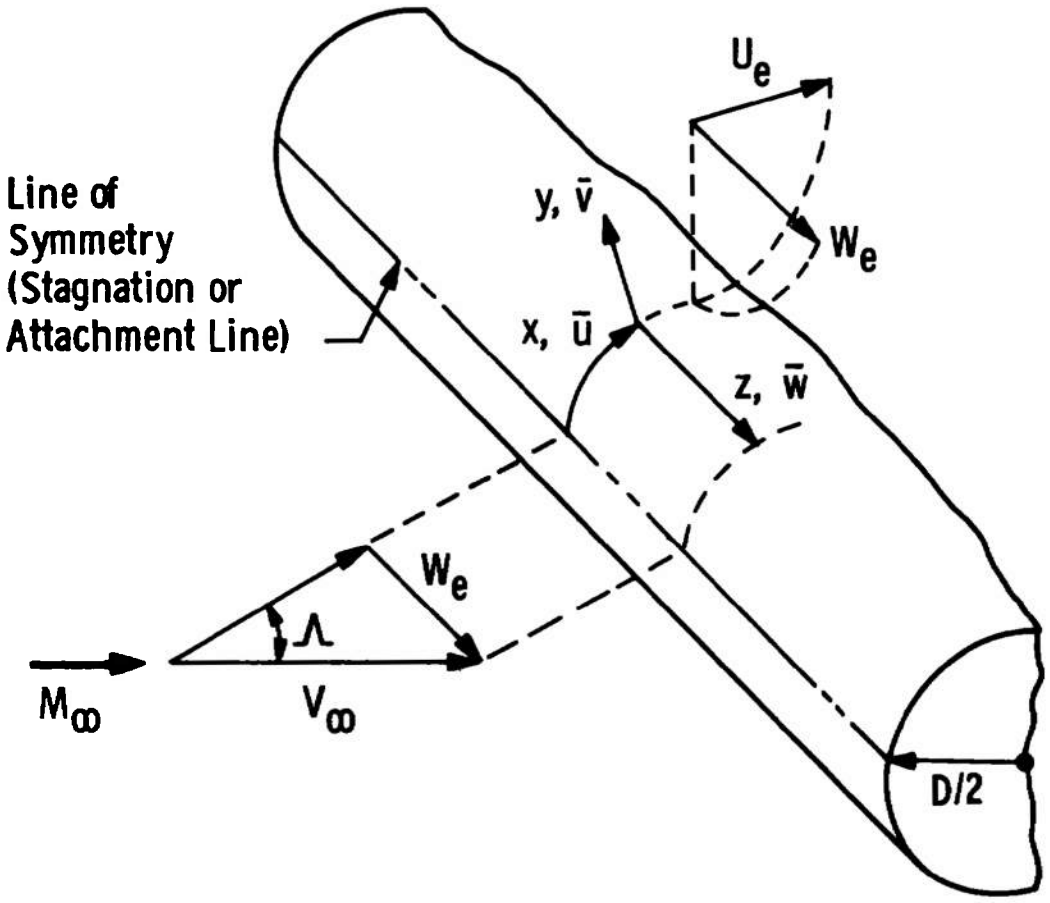

Fig. 3 Coordinate System for Flow over an Infinite Yawed Circular Cylinder

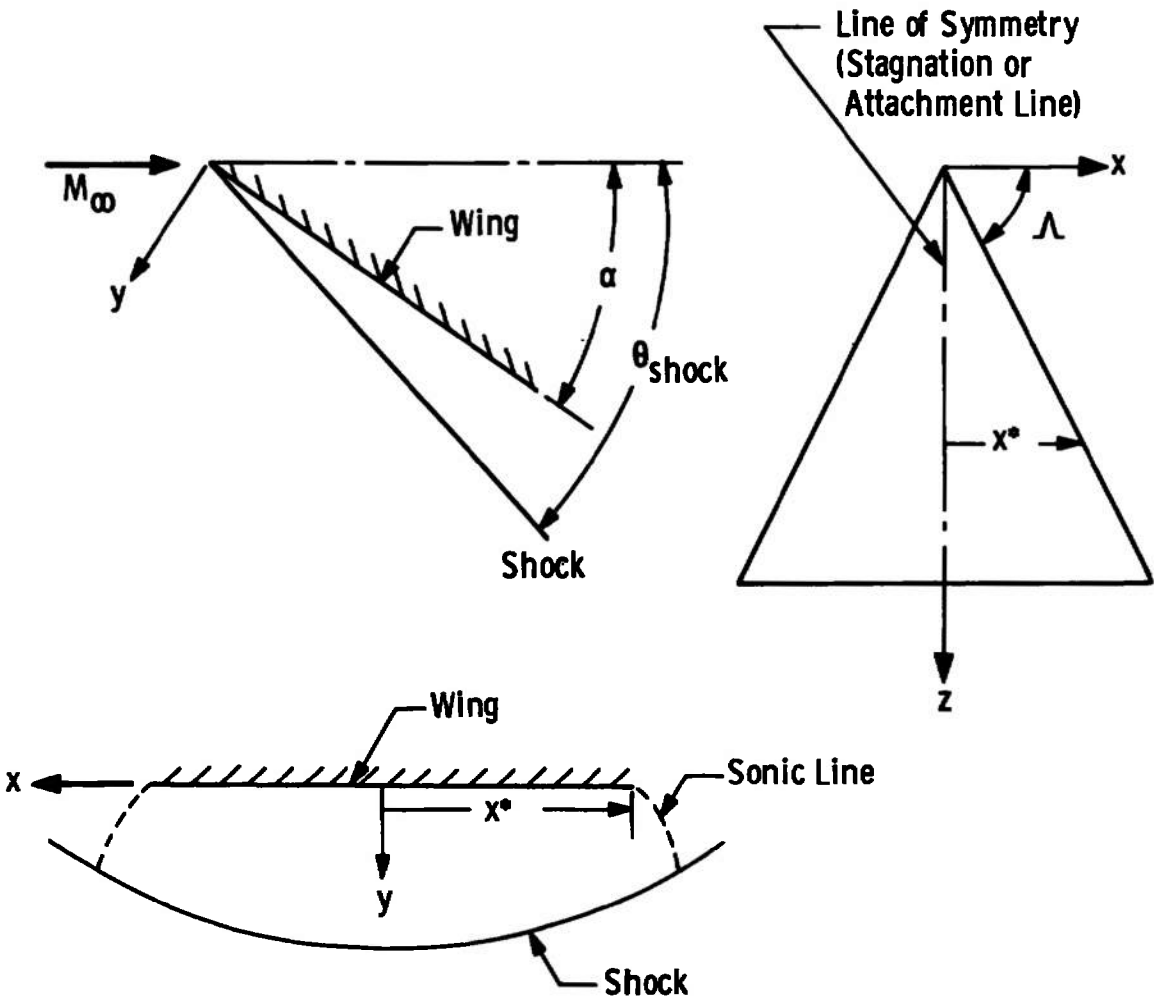

Fig. 4 Coordinate System for Hypersonic Flow Past a Sharp-Leading-Edge Delta Wing at High Angles of Incidence

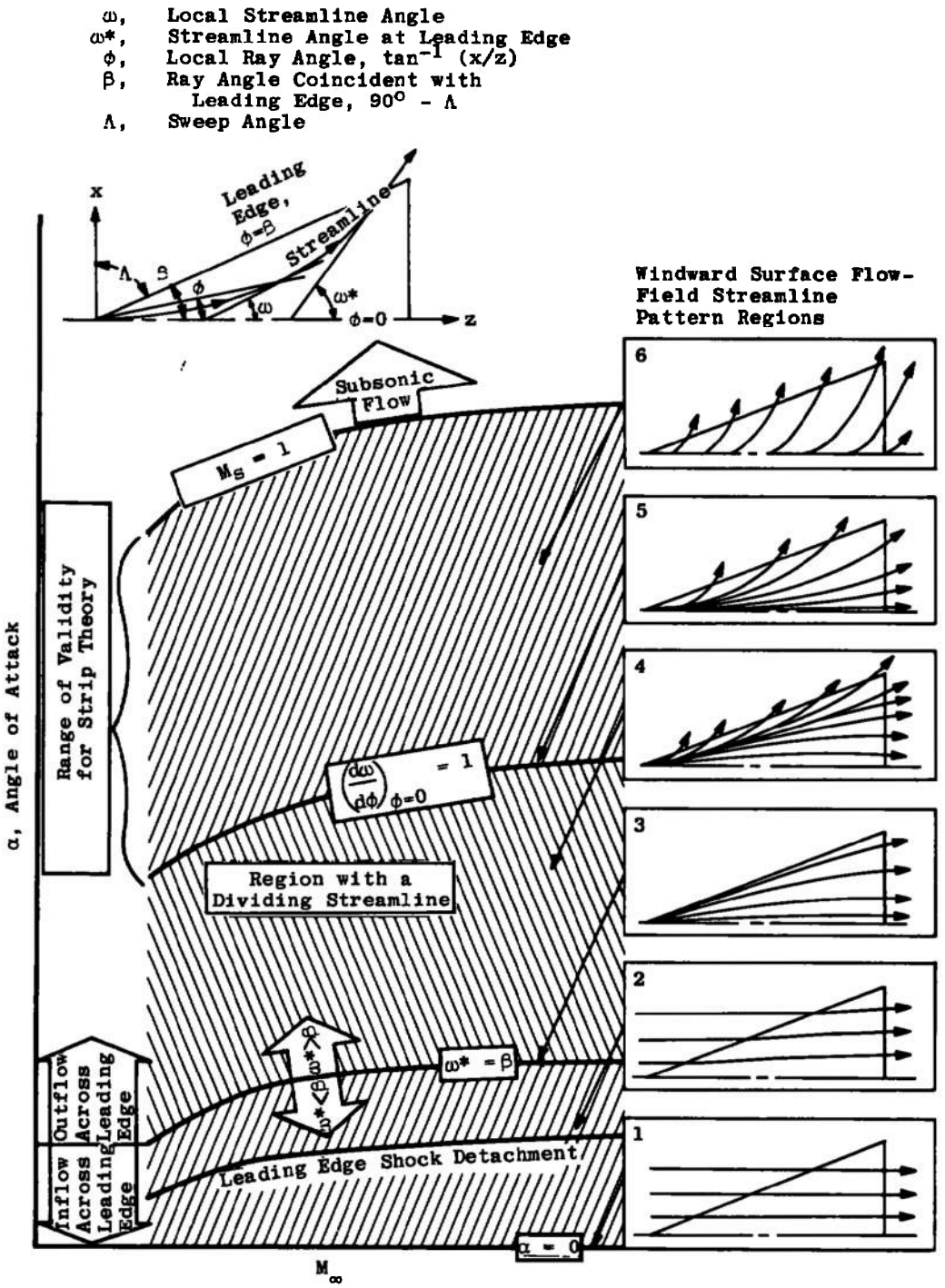

Fig. 5 Schematic of Windward Surface Flow-Field Regimes for Sharp-Edged Delta Wings at Incidence under Hypersonic Conditions as Taken from Fig. C6 in Appendix C of Thomas and Perlbachs (Ref. 58)

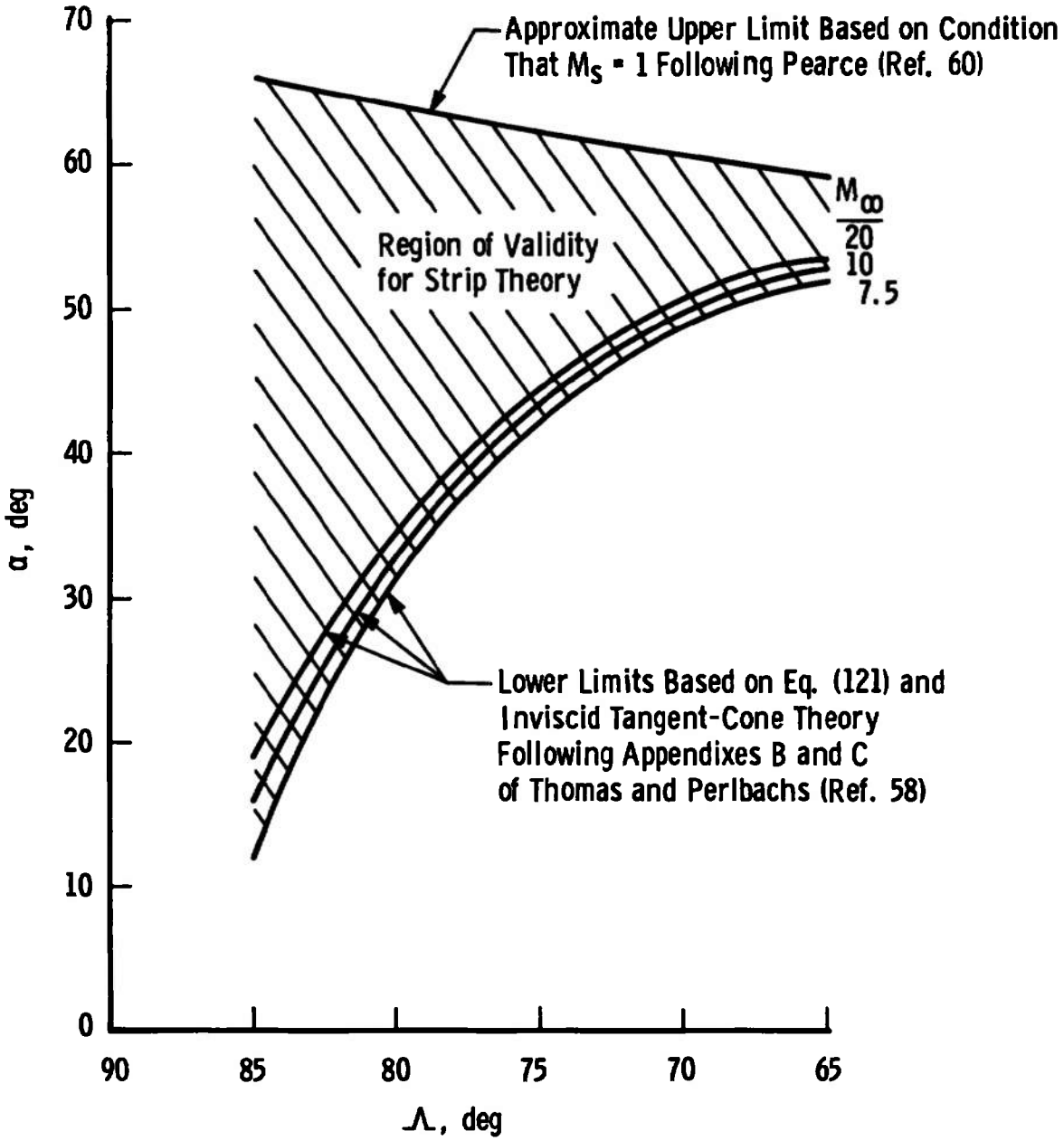

Fig. 6 Range of Applicability of Strip Theory for Sharp-Edged Delta Wings at Incidence under Hypersonic Conditions

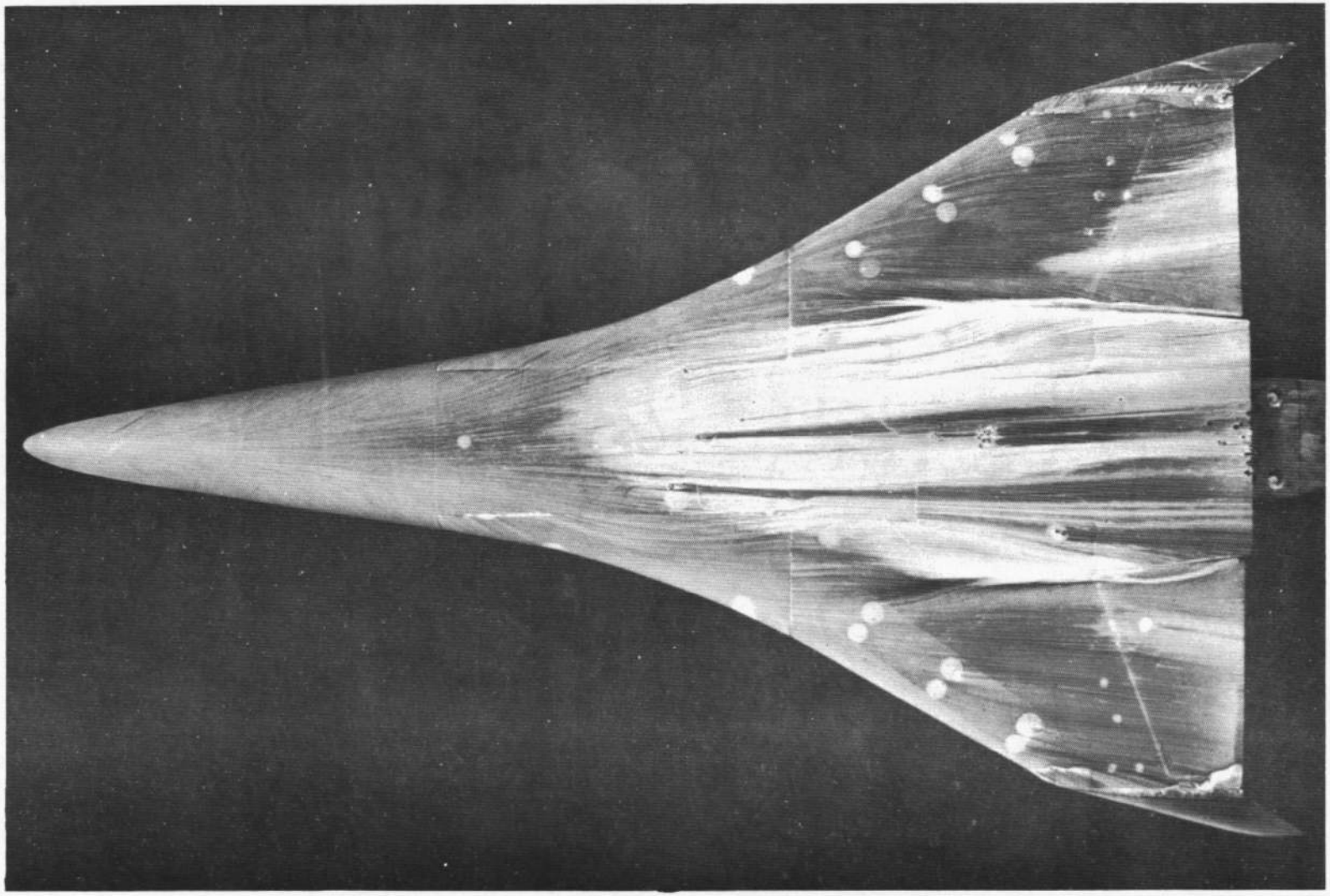

Fig. 7 Windward Surface Flow Visualization Photograph of the NAR Delta Wing Orbiter Configuration 129 at 30-deg Angle of Attack as Taken from Fig. 9c in Seegmiller (Ref. 74)

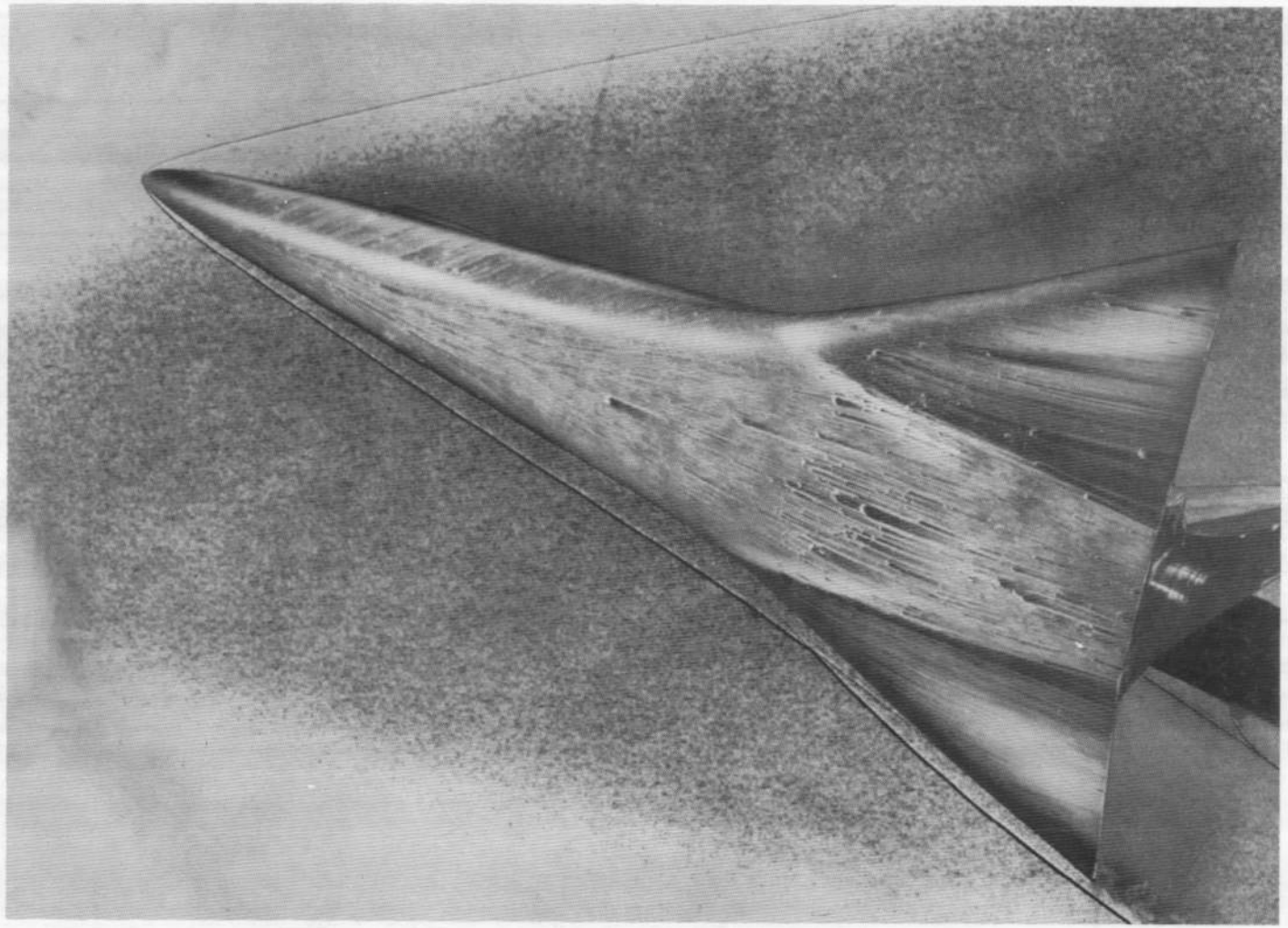

Fig. 8 Oblique View Windward Surface Flow Visualization Photograph of the NAR Delta Wing Orbiter Configuration 134 at 30-deg Angle of Attack as Taken from Fig. 4b in Cleary (Ref. 75)

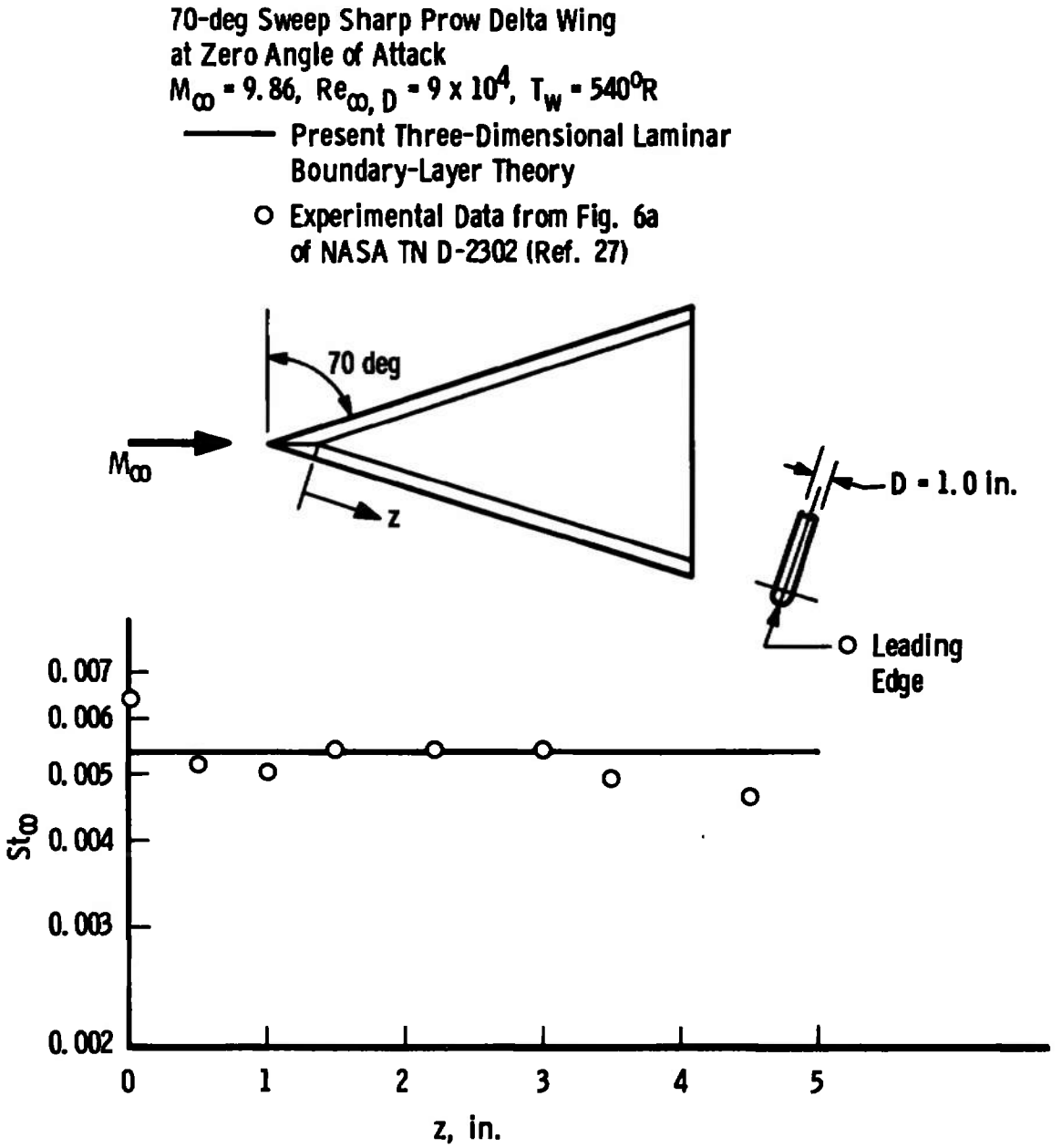

Fig. 9 Comparison of Laminar Heat-Transfer Results for the Cylindrically Blunted Leading Edge of a Sharp-Prow Delta Wing at Zero Angle of Attack

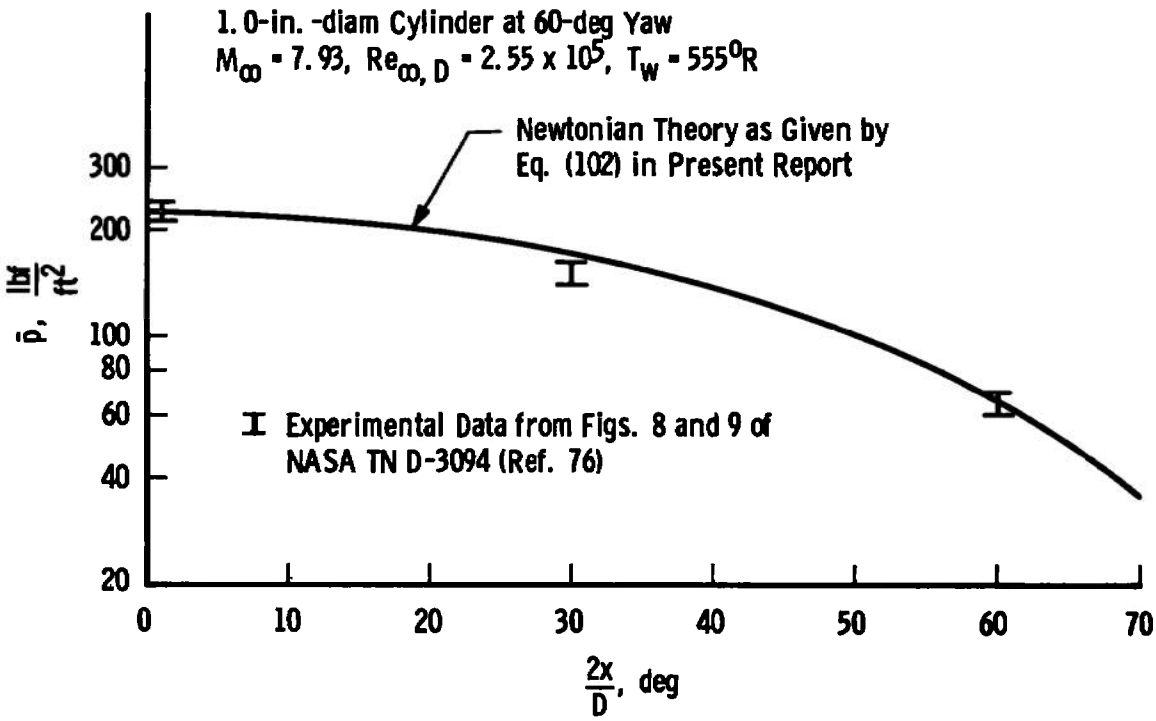

a. Circumferential Pressure Distribution

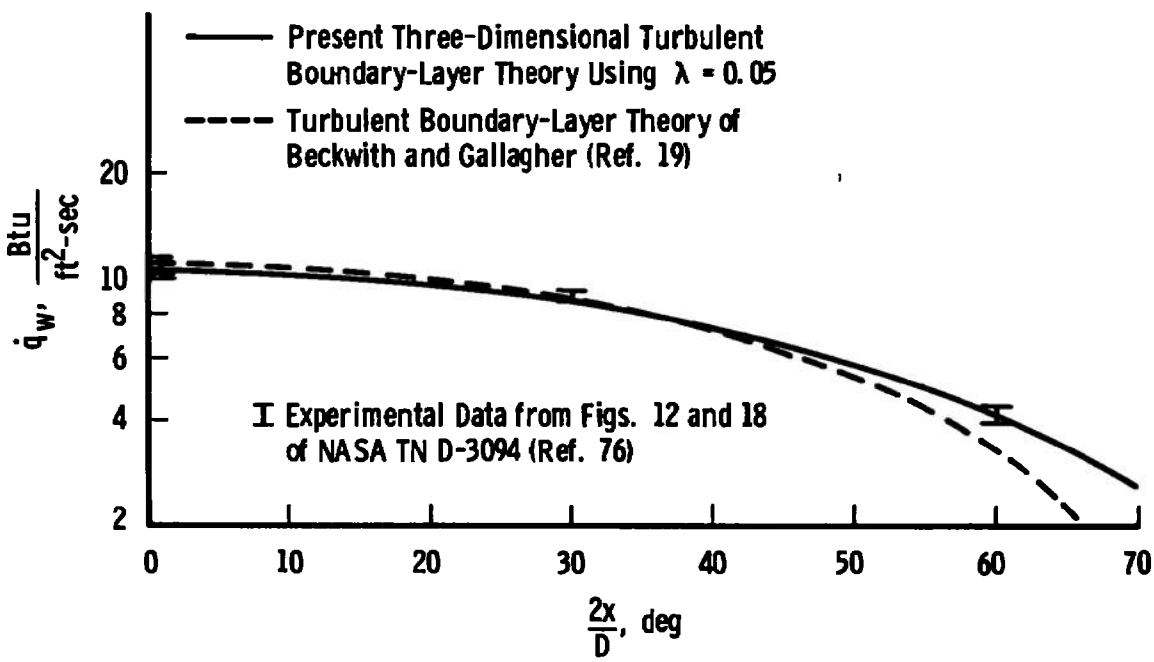

b. Circumferential Heat-Transfer-Rate Distribution

Fig. 10 Comparisons of Pressure and Heat-Transfer-Rate Distributions on a Yawed Cylinder

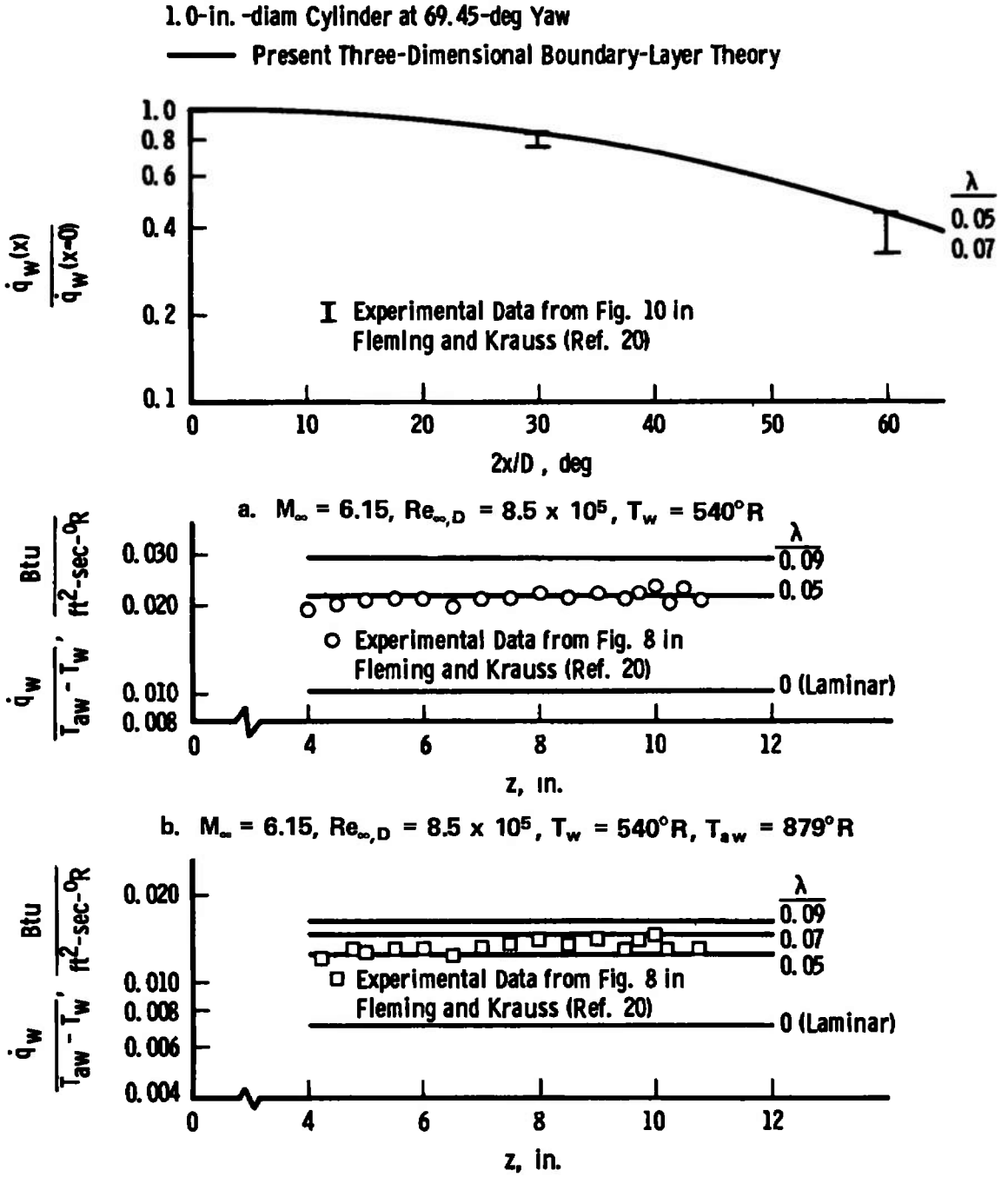

c. M_∞ = 6.12, $Re_{\infty,D}$ = 4.1 x 10^5, T_w = 540°R, T_{aw} = 846°R

Fig. 11 Effects of Outer Mixing-Length Constant λ on Yawed Cylinder Heat Transfer

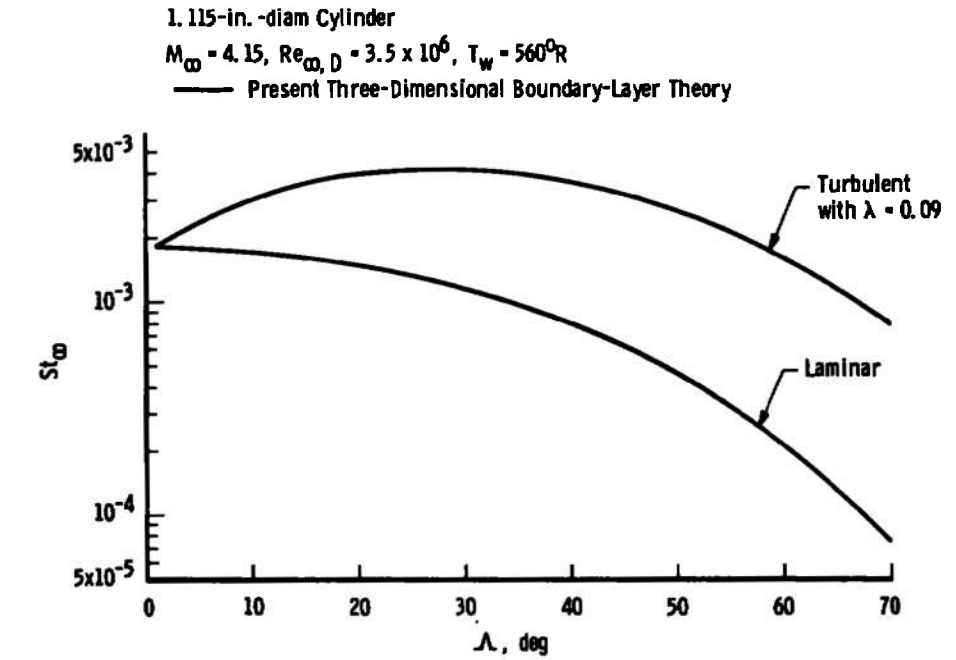

a. Stanton Number Variation with Yaw Angle

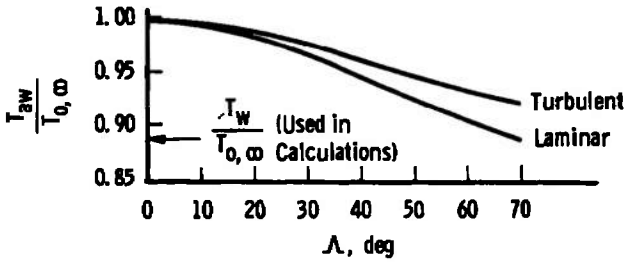

b. Adiabatic Wall Temperature Variation with Yaw Angle

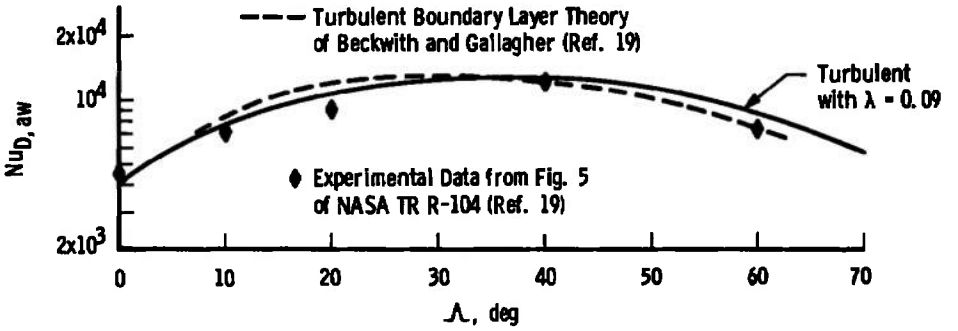

c. Nusselt Number Variation with Yaw Angle

Fig. 12 Effects of Yaw Angle on Yawed Cylinder Stagnation or Attachment Line Laminar and Turbulent Heat Transfer

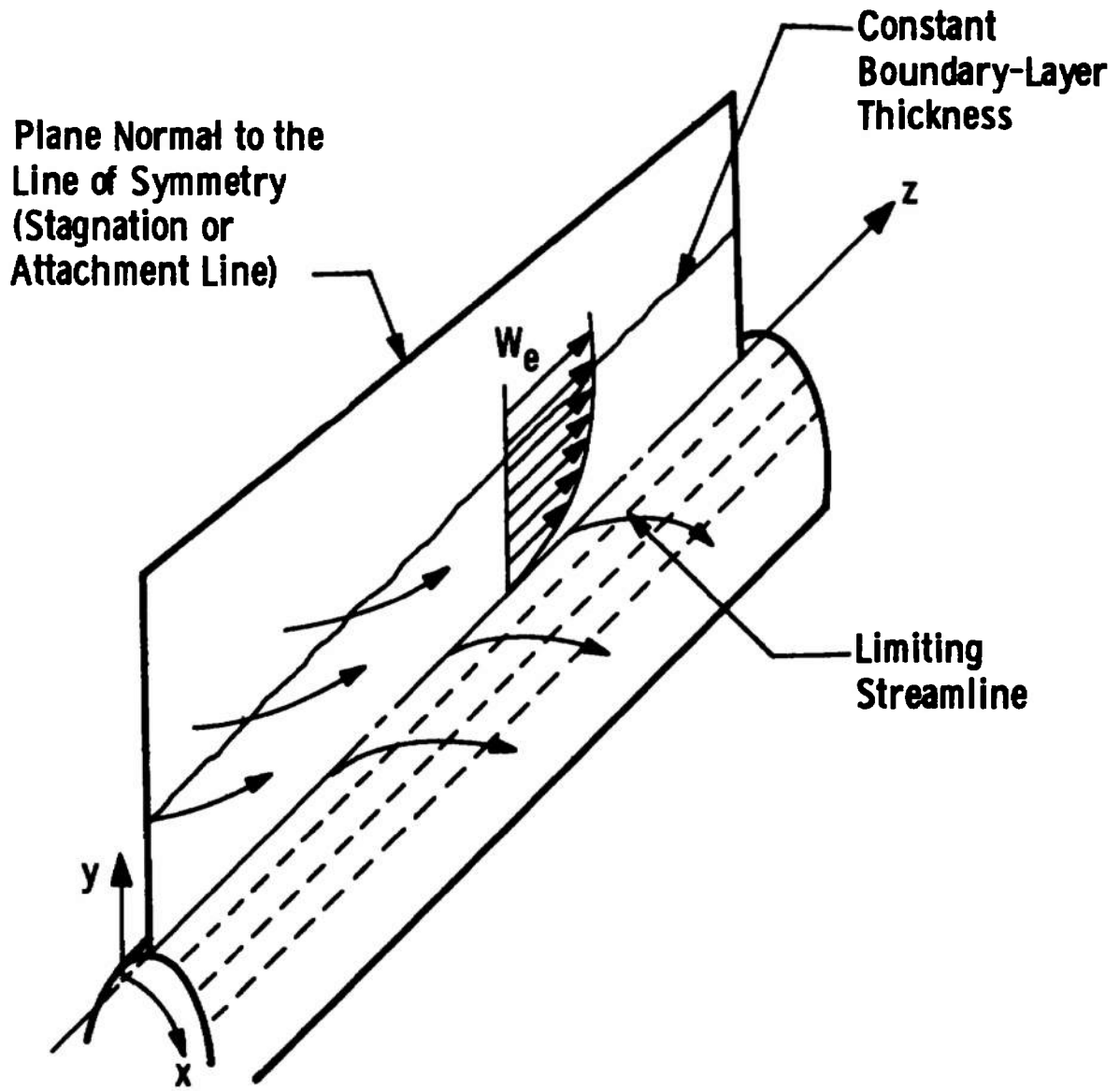

Fig. 13 Schematic of Stagnation or Attachment Line Flow over an Infinite Extent Yawed Circular Cylinder

80-deg Sweep Sharp Leading Edge Delta Wing
at α = 60 deg with M_∞ = 6.08

O Experimental Data from Fig. 5 of IAS Paper No. 63-55 (Kennet, Ref. 59)

South One-Strip Method of Integral Relations for a Flat-Faced Body (Ref. 61)

× Numerical Calculation Following Kennet as Taken from Fig. 5 of IAS Paper No. 63-55 (Ref. 59)

Note: Centerline Pressure Determined from Classical Newtonian Theory

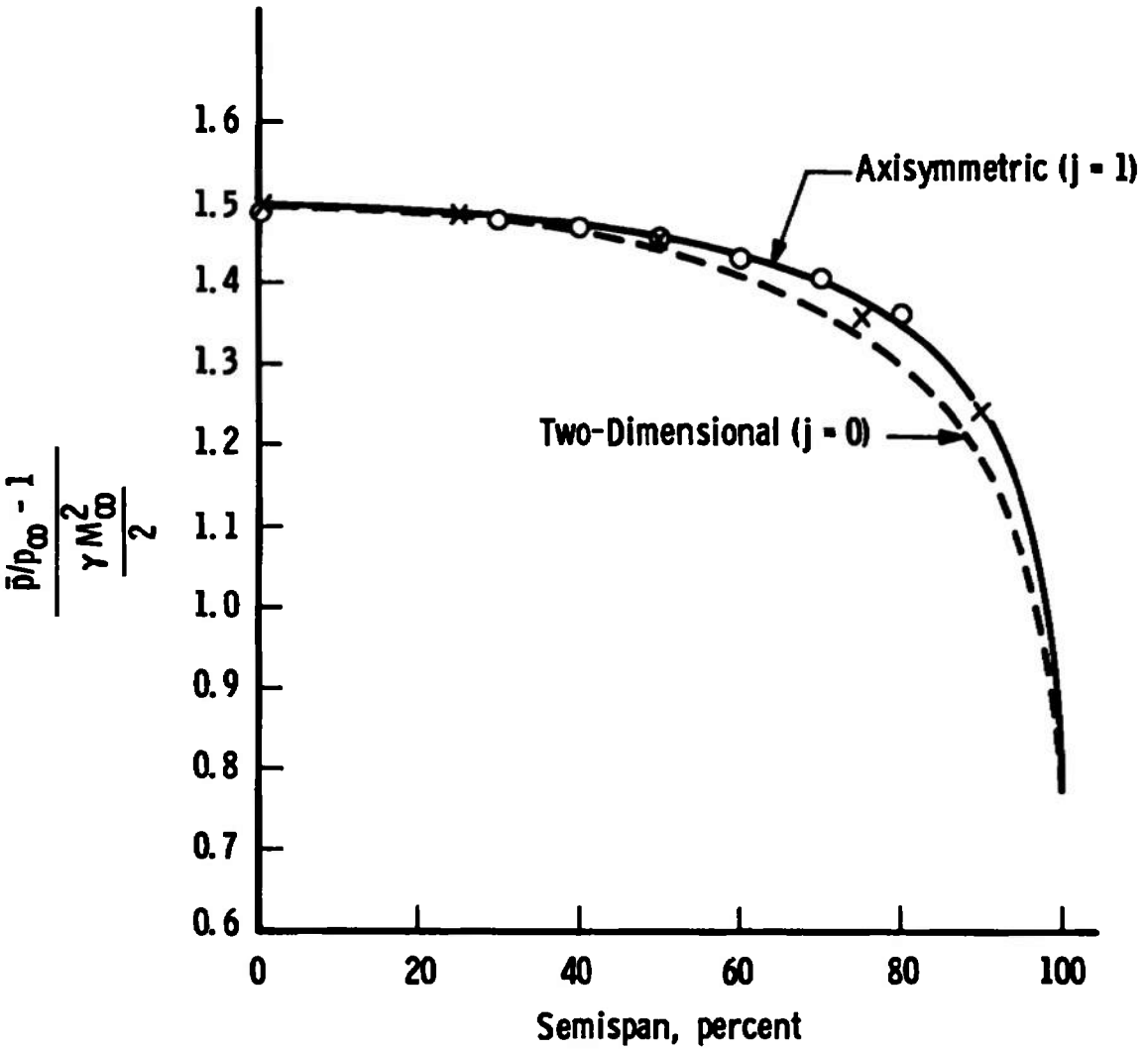

Fig. 14 Spanwise Surface Pressure Distribution on a Sharp-Leading-Edge Delta Wing at High Incidence

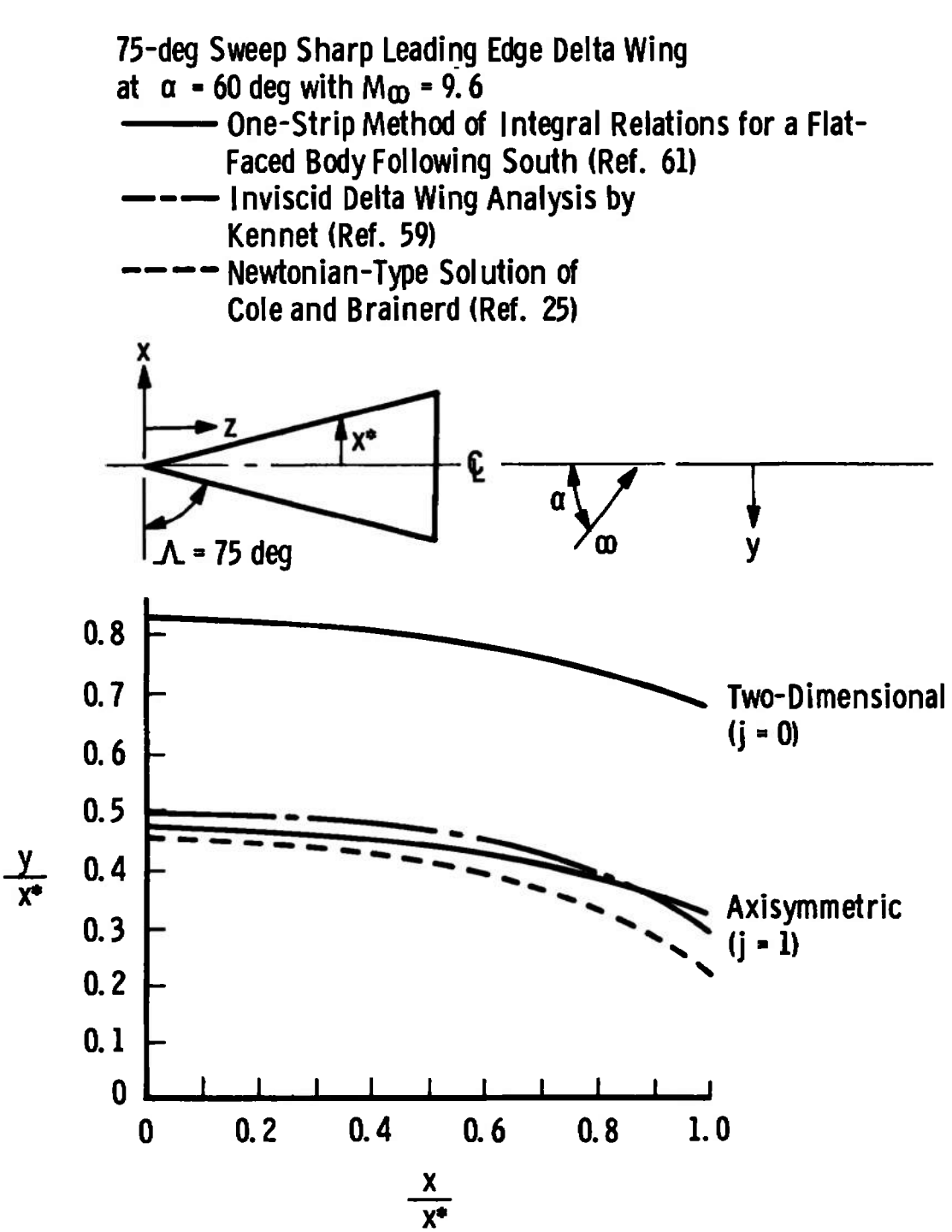

Fig. 15 Comparison of Calculated Spanwise Shock Shape on a Delta Wing at High Incidence

75-deg Sweep Sharp Leading Edge Delta Wing
at α = 60 deg with M_∞ = 9.6

——— One-Strip Method of Integral Relations for a Flat-Faced Disk Following South (Ref. 61)

—·— Inviscid Delta Wing Analysis by Pearce (Ref. 60)

Note: Centerline Pressure Determined from Classical Newtonian Theory with Centerline Shock Angle Set at 67.5 deg

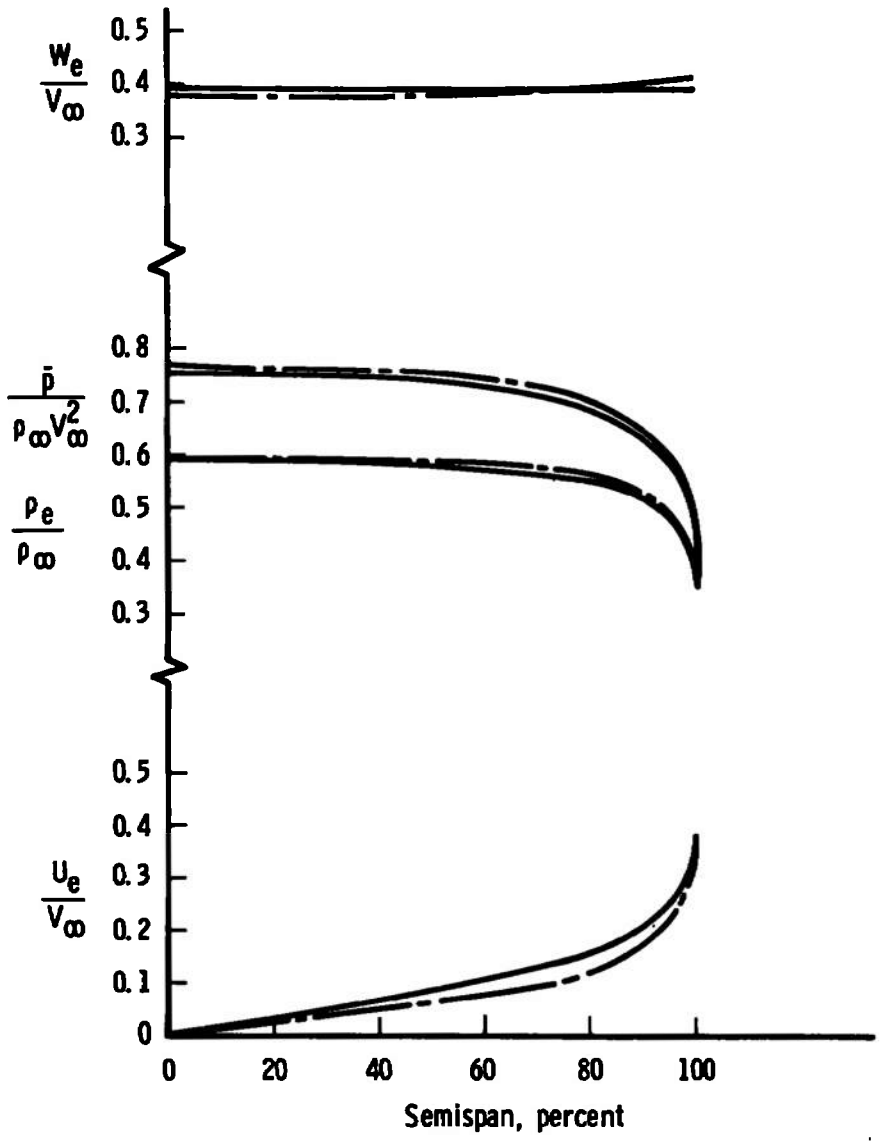

Fig. 16 Spanwise Inviscid Flow Parameters on a Sharp-Leading-Edge Delta Wing at High Incidence

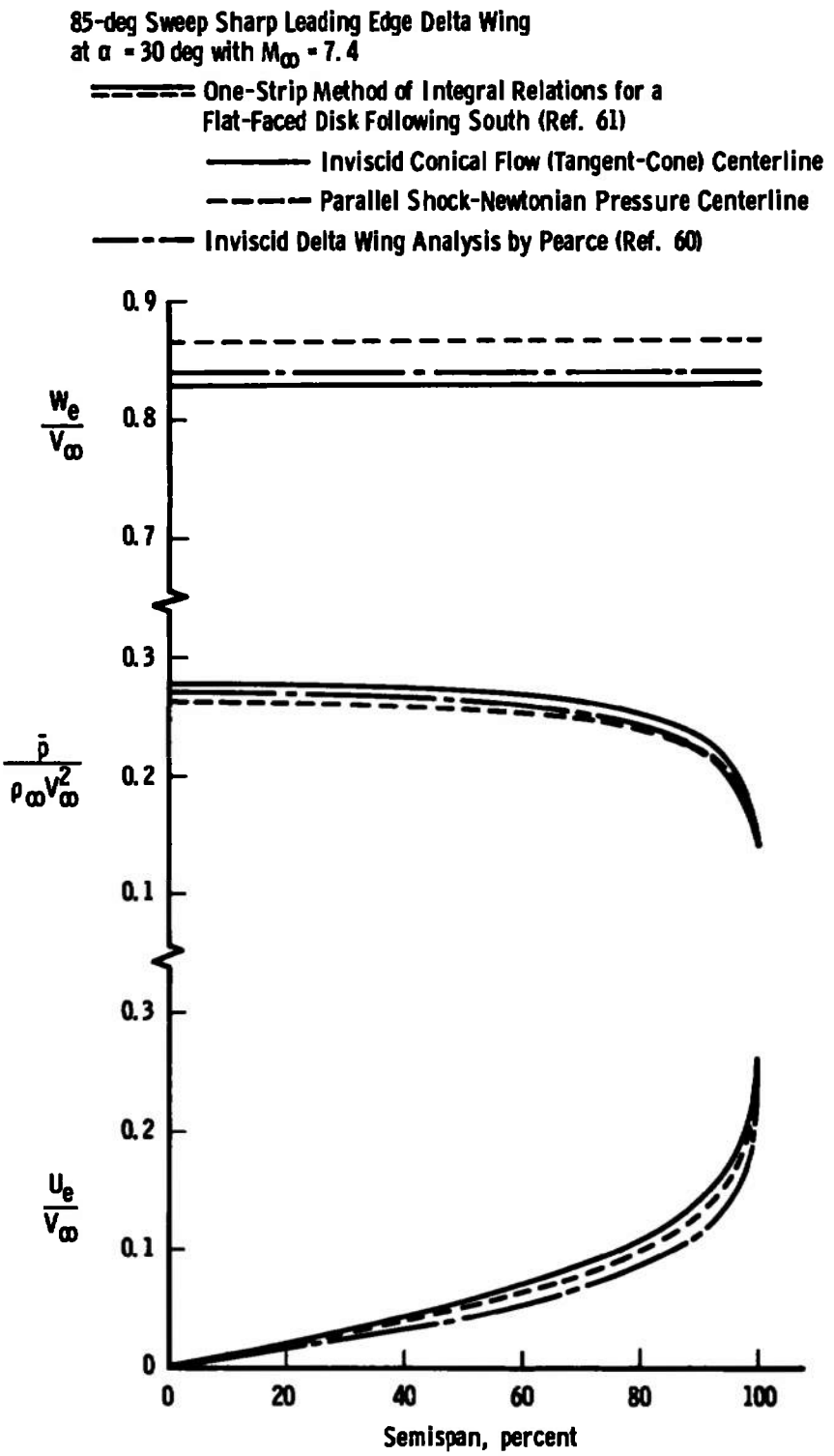

Fig. 17 Spanwise Inviscid Flow Parameters on a Sharp-Leading-Edge Delta Wing at Moderate Incidence

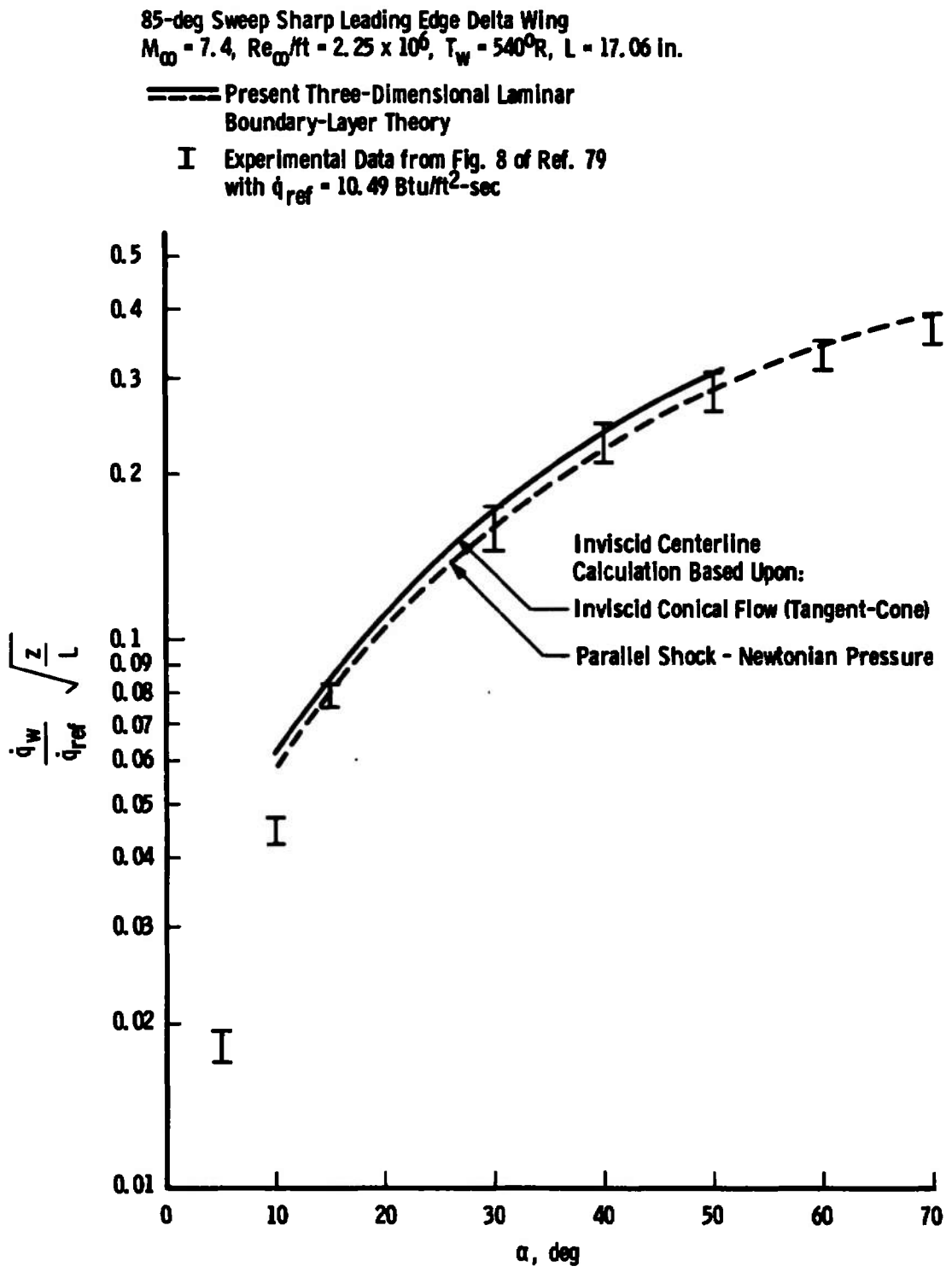

Fig. 18 Angle-of-Attack Effects on Centerline Laminar Heat Transfer

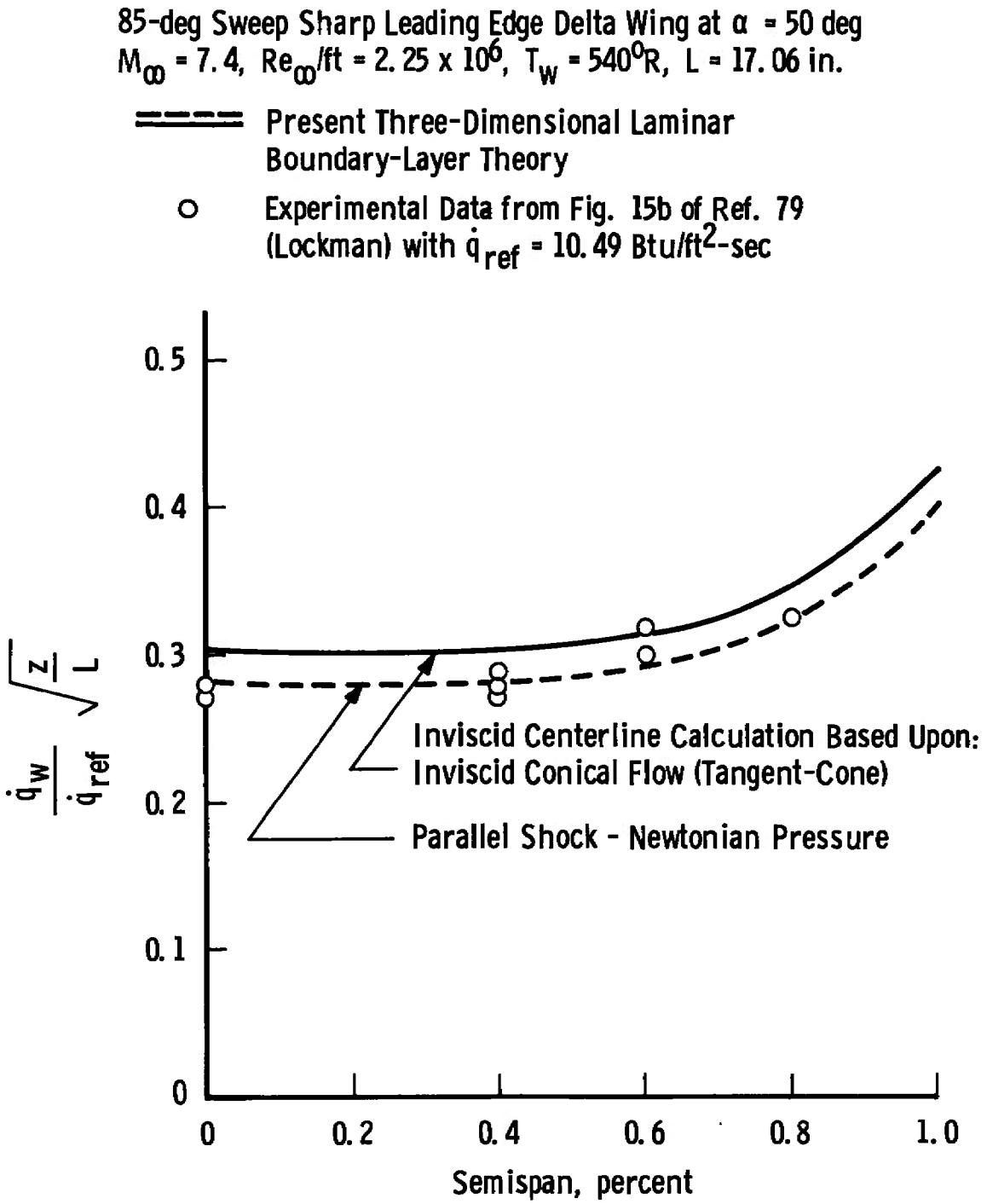

Fig. 19 Spanwise Laminar Heat-Transfer Distribution at a High Incidence Angle

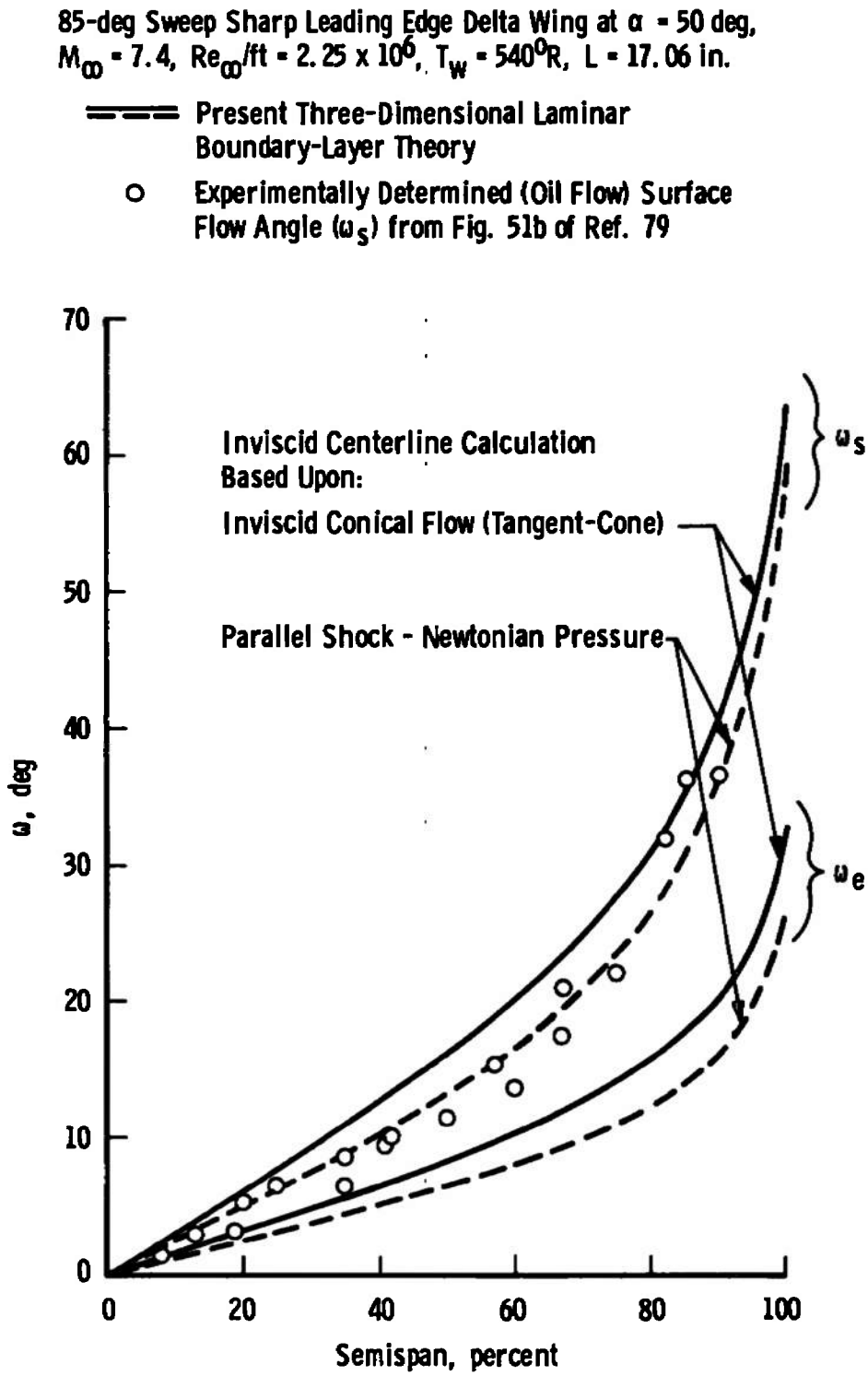

Fig. 20 Spanwise Laminar Surface Flow Angle and Inviscid Edge Flow Angle Distribution at a High Incidence Angle

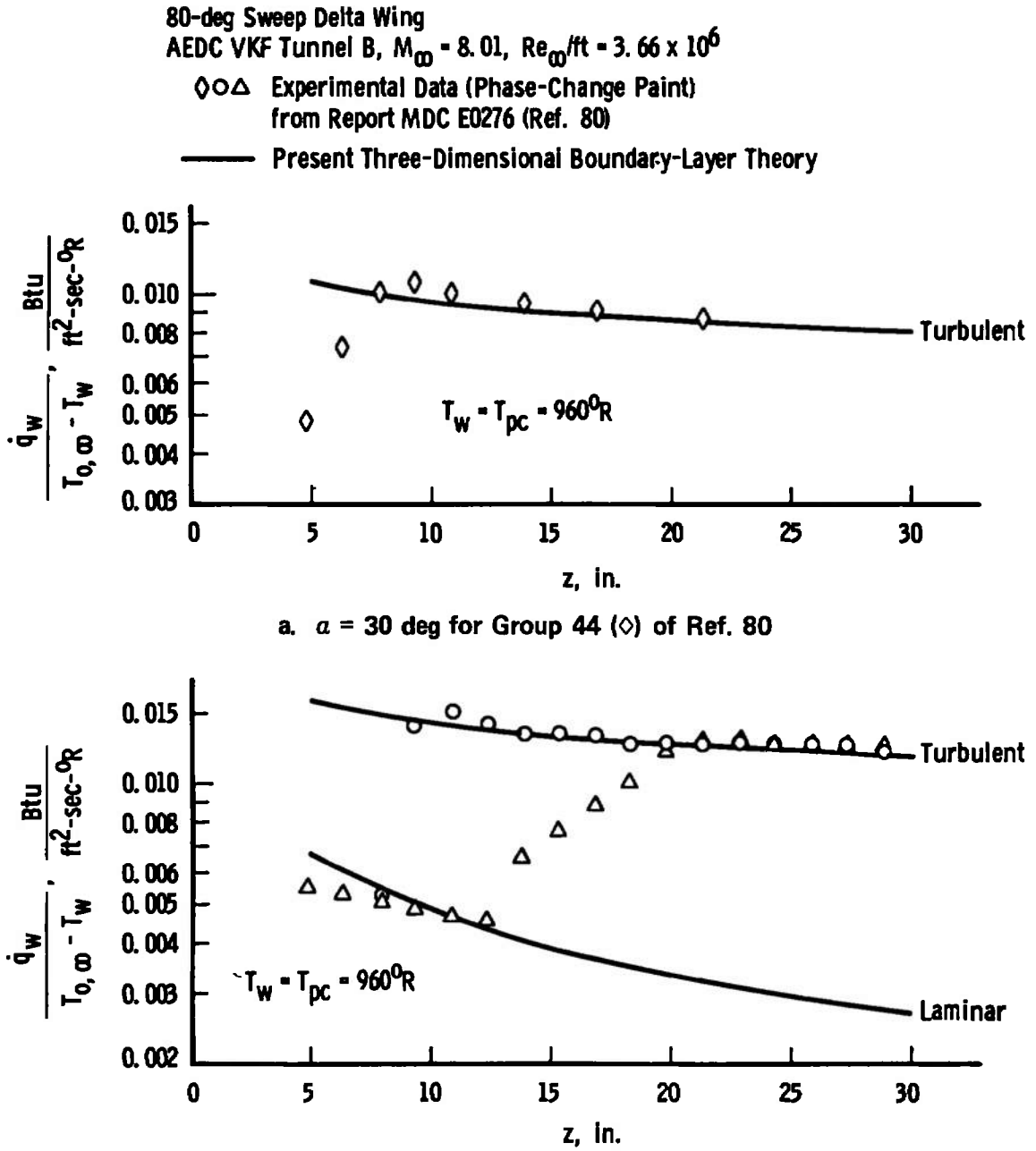

a. α = 30 deg for Group 44 (◇) of Ref. 80

b. α = 50 deg for Group 54 (△) and Group 55 (○) of Ref. 80

Fig. 21 Centerline Laminar, Transitional, and Turbulent Heat Transfer on a Highly Swept Delta Wing at Moderate to High Angles of Incidence

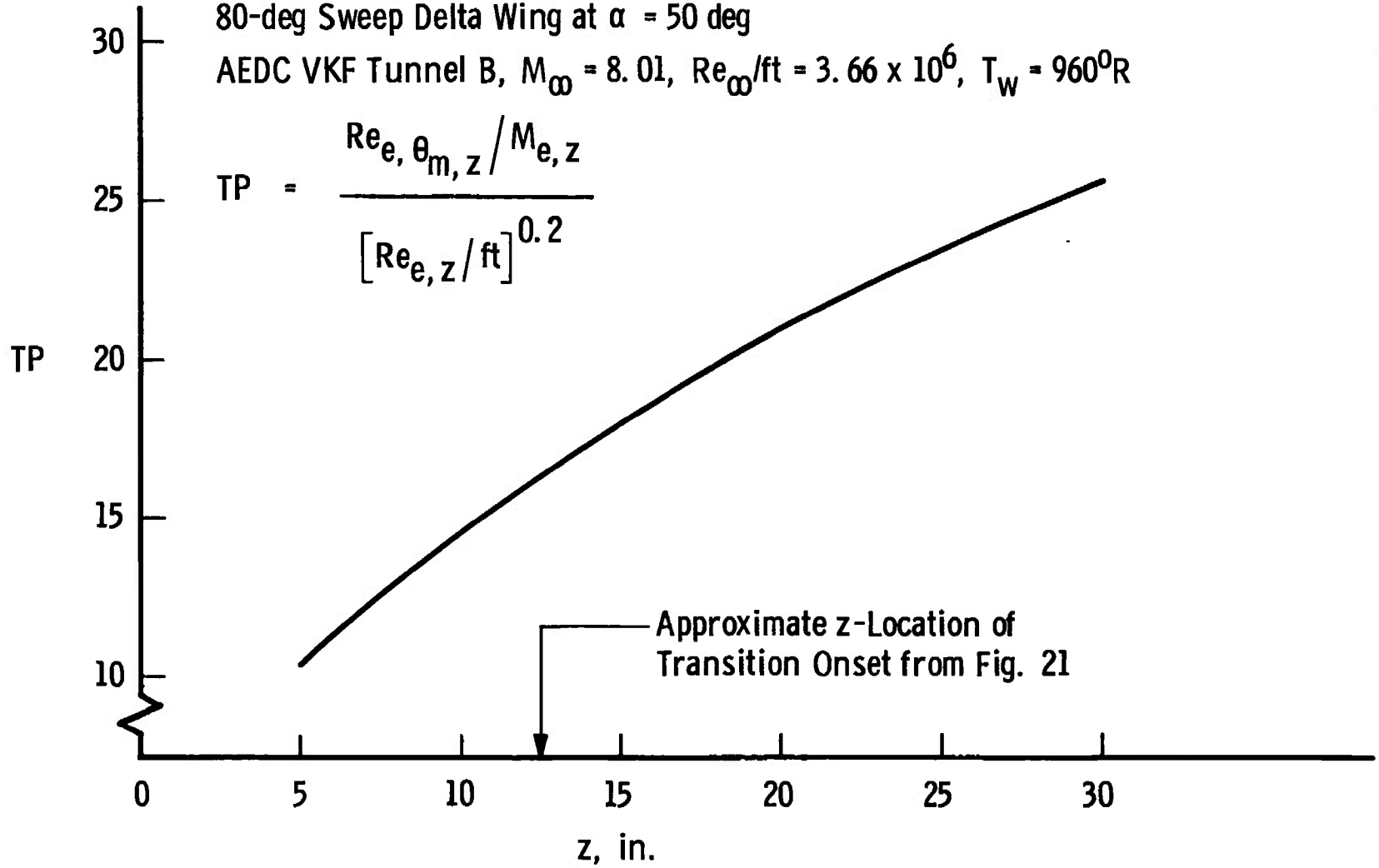

Fig. 22 Centerline Transition Onset Parameter Distribution on a Delta Wing at High Incidence

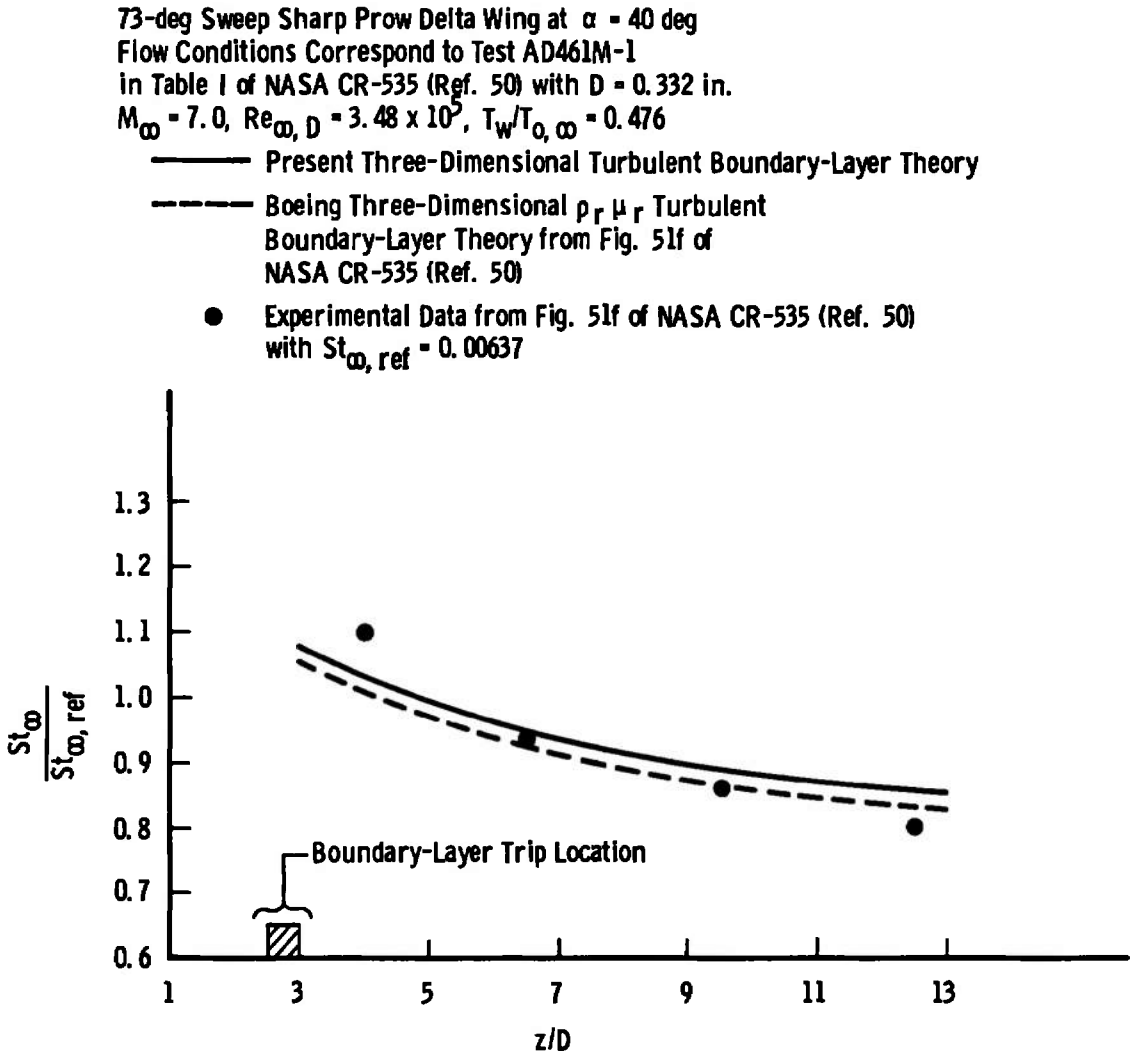

Fig. 23 Comparison of Present Three-Dimensional Turbulent Boundary-Layer Theory with Boeing $\rho_r\mu_r$ Approach along Delta Wing Centerline

73-deg Sweep Delta Wing at α = 45 deg

Test AD461M-1 Model W_2 of NASA CR-535 (Ref. 50)

M_∞ = 7.0, $Re_{\infty, D}$ = 9.45 x 10^5, $T_w/T_{o,\infty}$ = 0.476

D = 0.90 in., z/D = 6.71

O Experimentally Determined (Oil Flow) Surface Flow Angle (ω_s) from Fig. 41c of NASA CR-535 (Ref. 50)

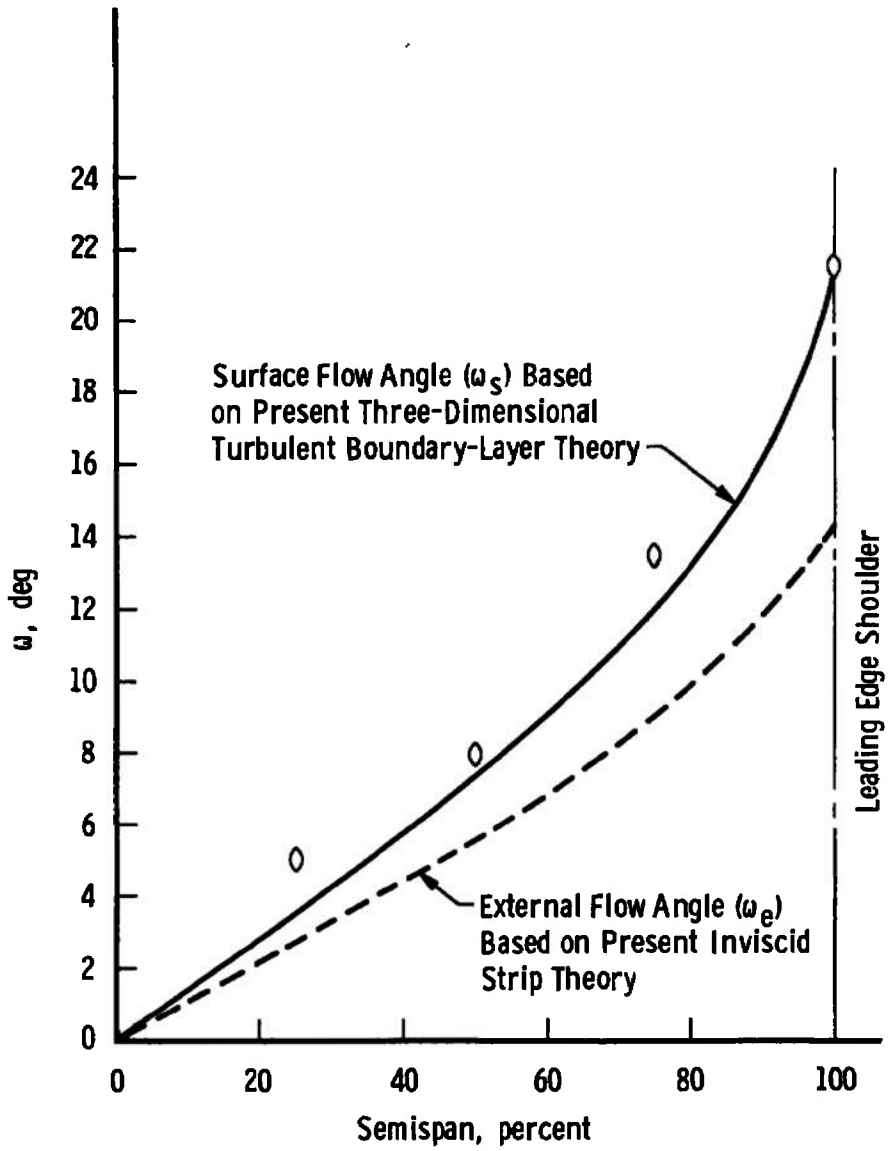

Fig. 24 Spanwise Turbulent Surface Flow Angle and Inviscid Edge Flow Angle Distribution at a High Incidence Angle

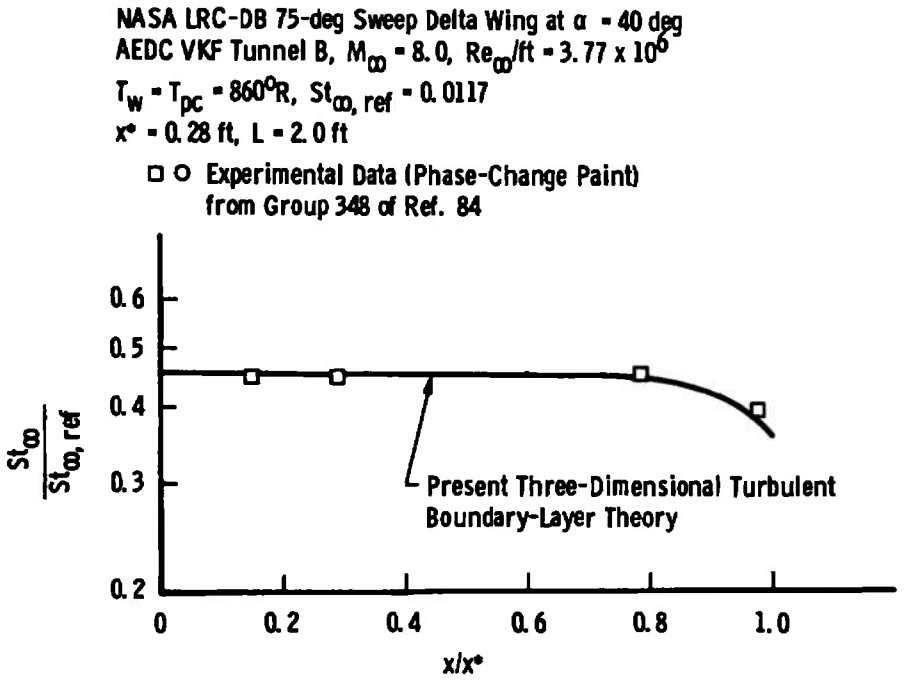

a. Spanwise Heat Transfer Distribution at Body Location z/L = 0.5

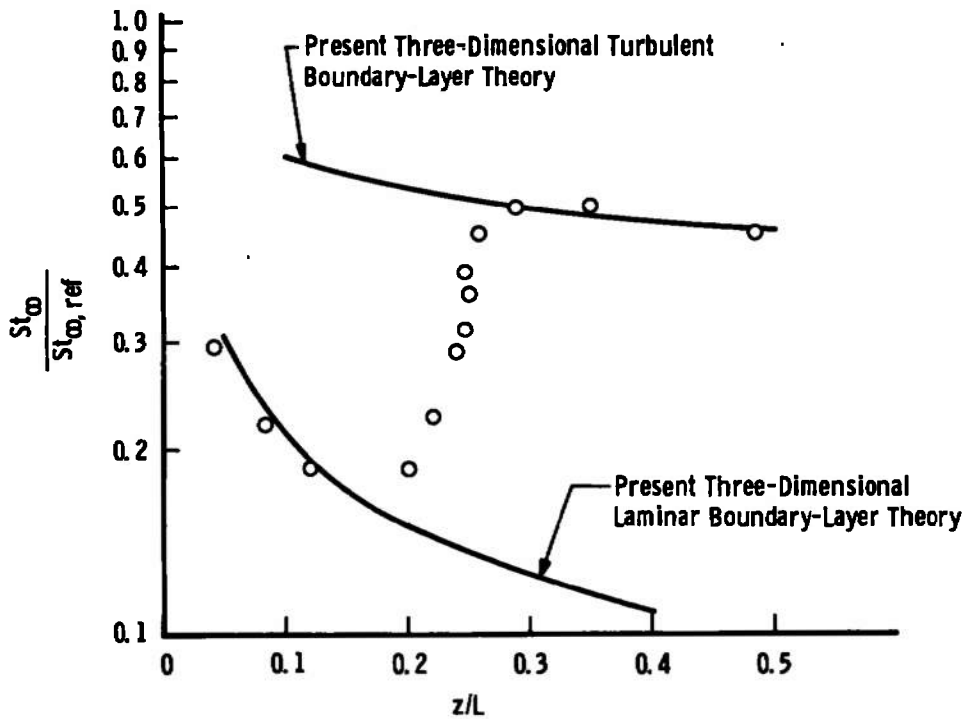

b. Centerline Heat Transfer Distribution

Fig. 25 Centerline and Spanwise Heat-Transfer Distributions on a Delta Wing at Incidence

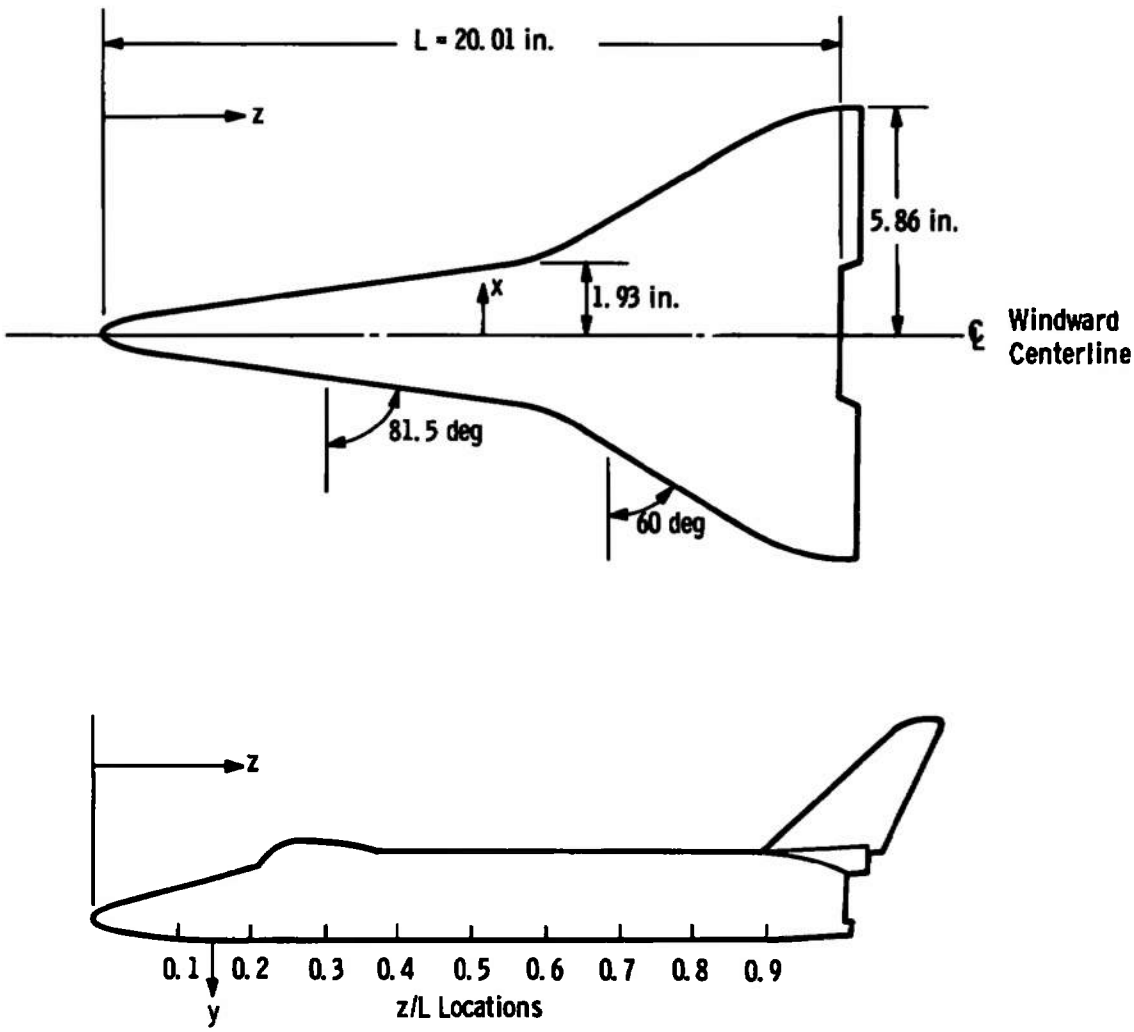

Fig. 26 North American Rockwell (NAR) Delta Wing Orbiter Configuration 161B (0.009-Scale)

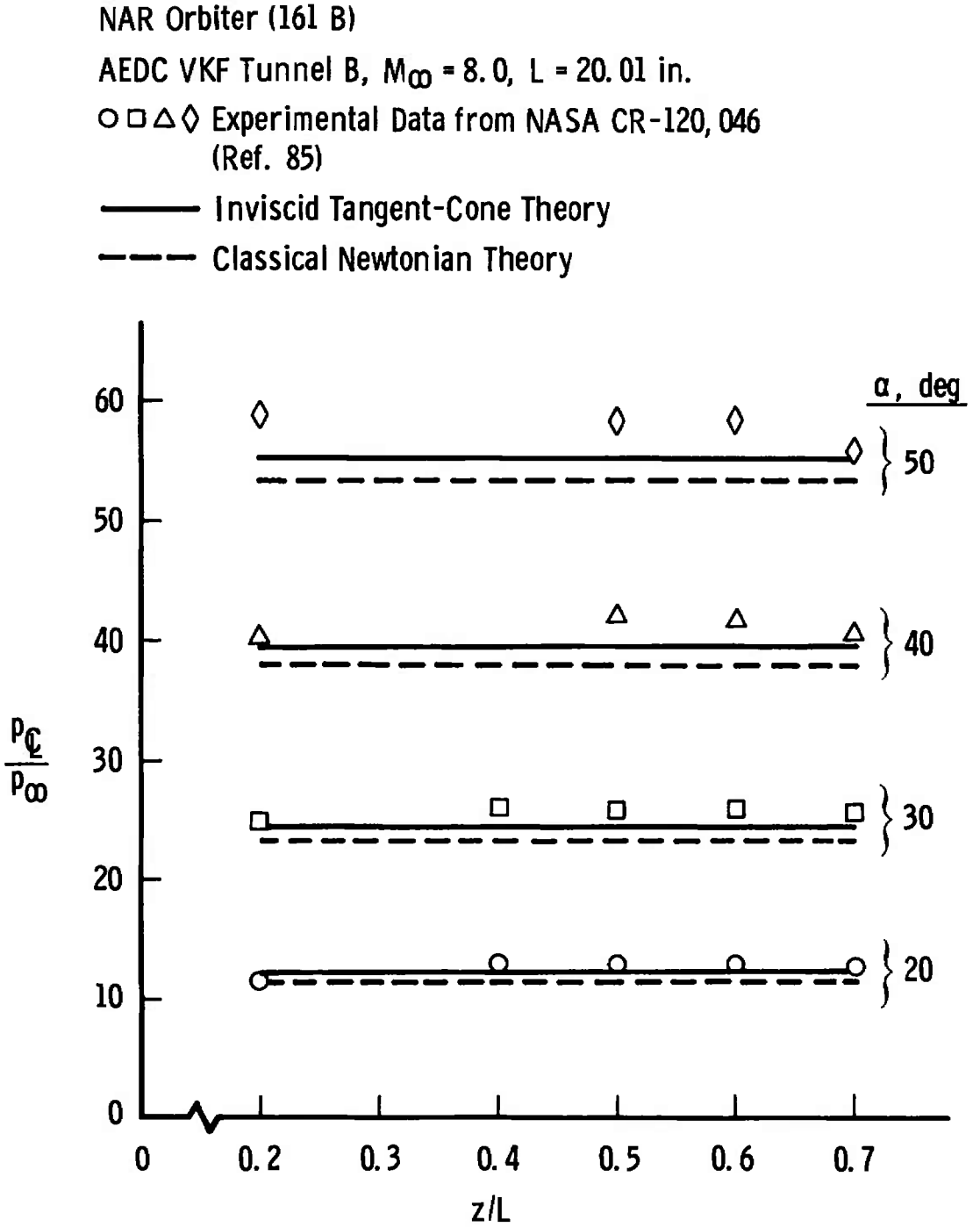

Fig. 27 Centerline Pressure Distribution on the NAR Orbiter at Incidence

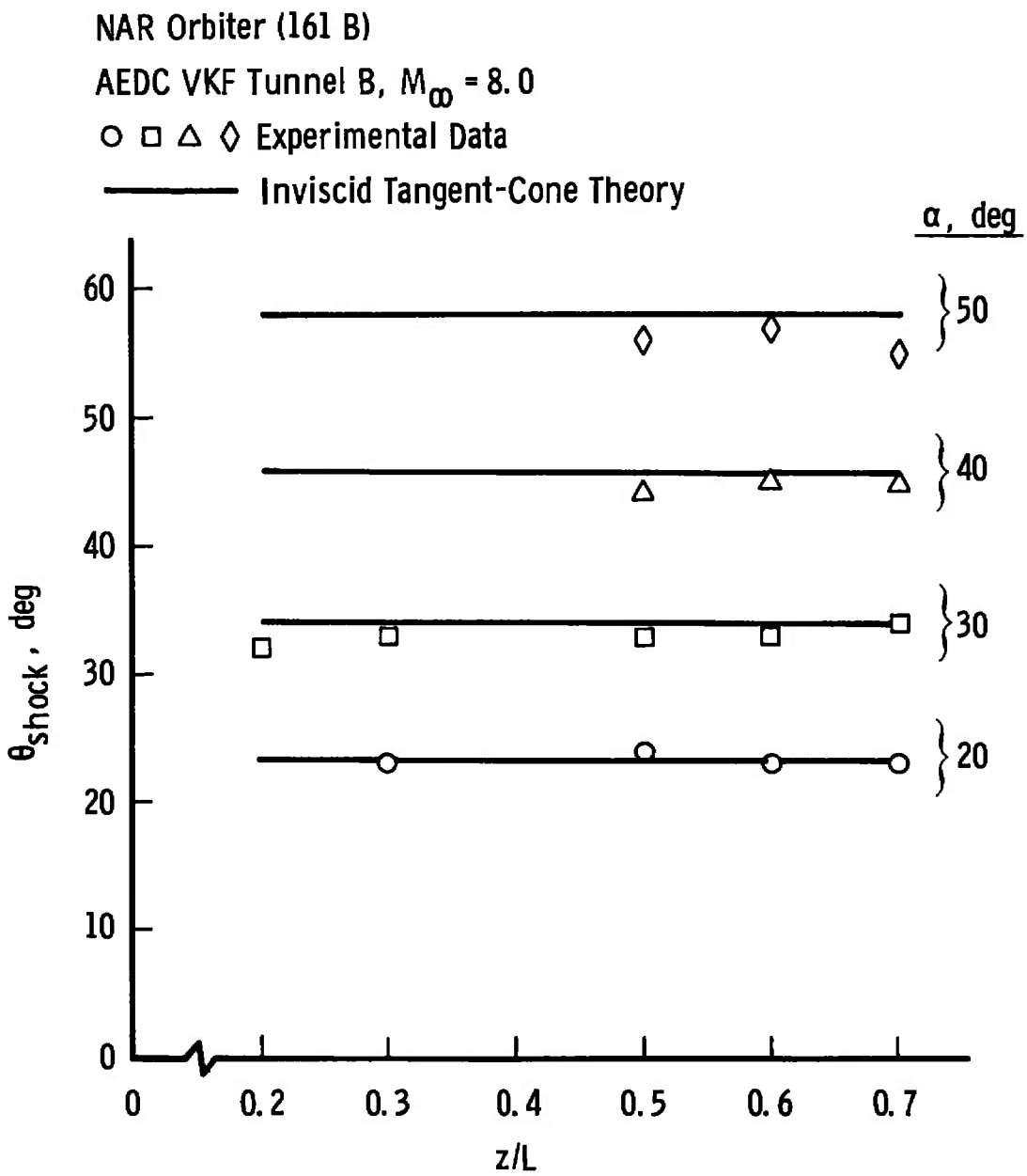

Fig. 28 Centerline Shock Angle Distribution on the NAR Orbiter at Incidence

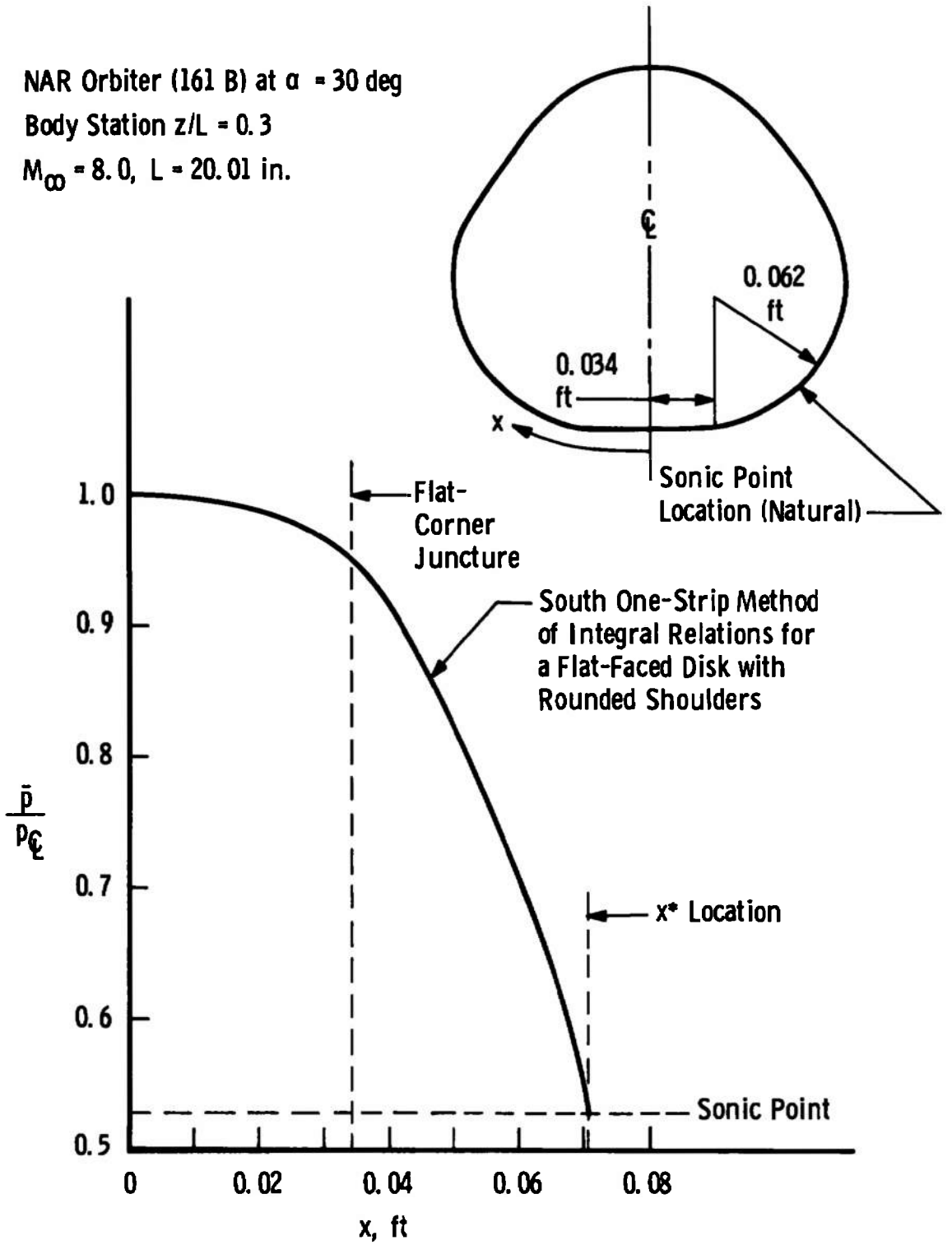

Fig. 29 Spanwise Pressure Distribution on the NAR Orbiter at Incidence

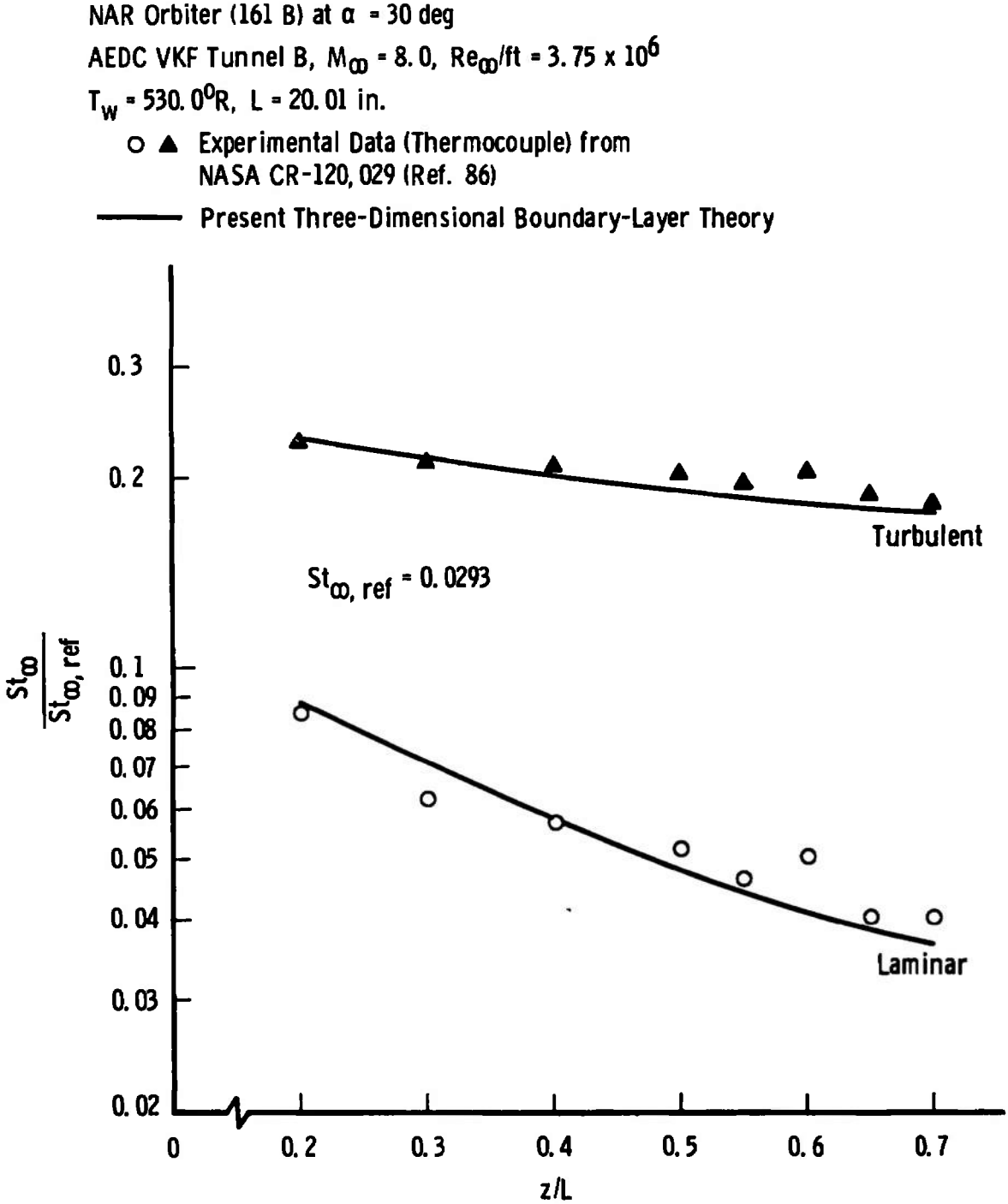

a. 30-deg Angle of Attack

Fig. 30 Windward Centerline Stanton Number Distributions on the NAR Orbiter under AEDC-VKF Tunnel B Conditions

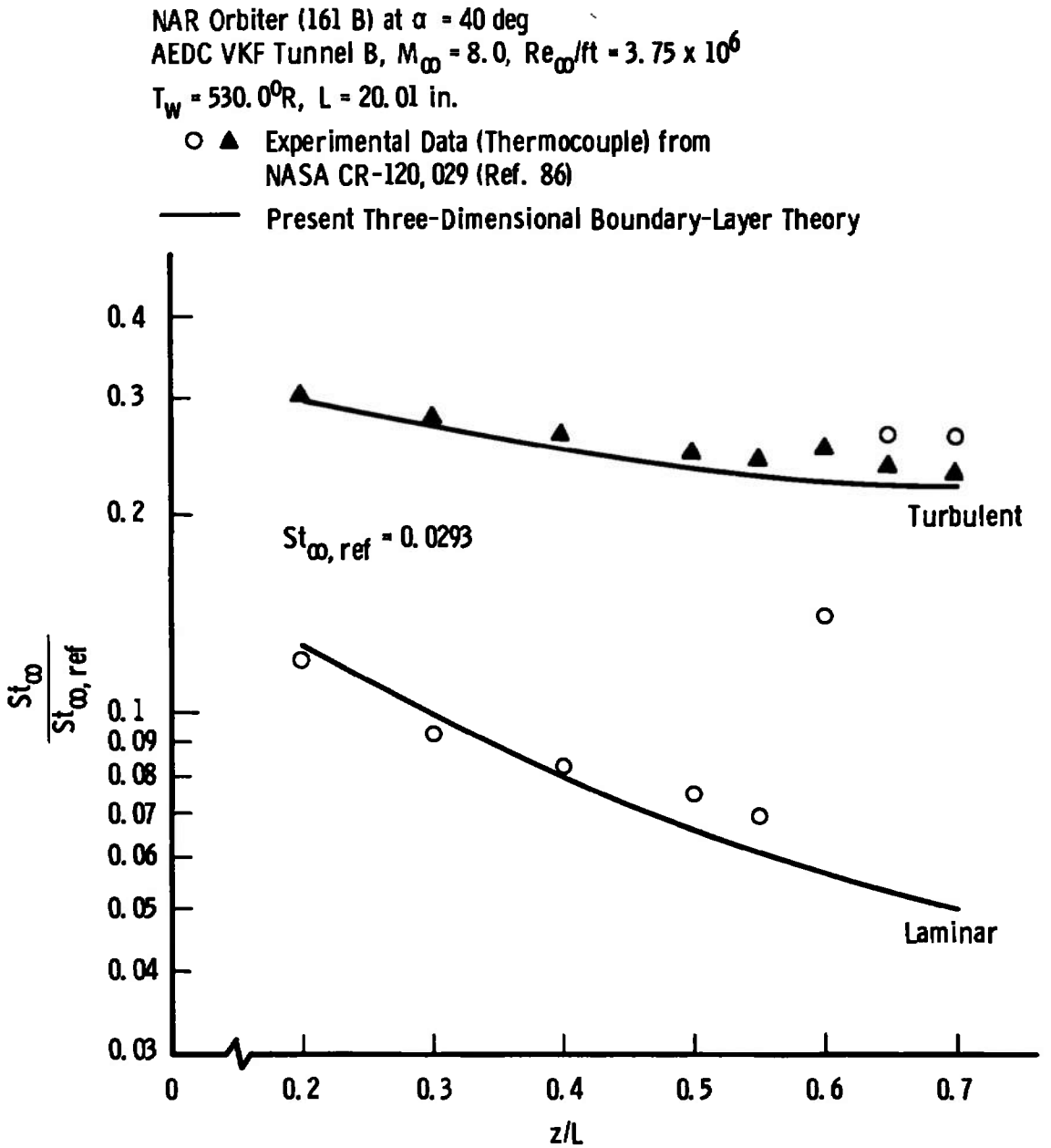

b. 40-deg Angle of Attack
Fig. 30 Continued

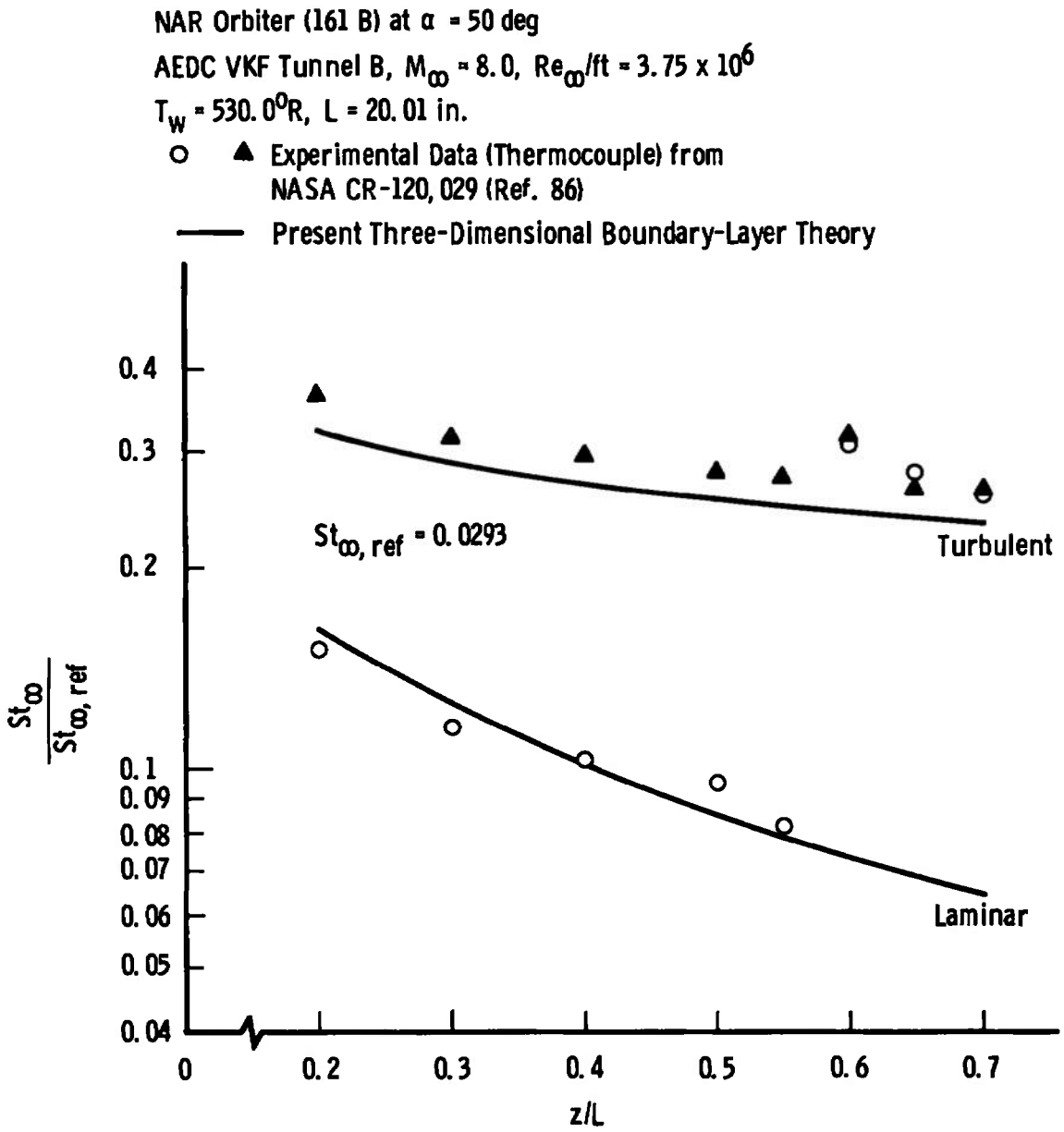

c. 50-deg Angle of Attack
Fig. 30 Concluded

NAR Orbiter (161 B) at α = 30 deg
Body Station Location z/L = 0.3
AEDC VKF Tunnel B, M_∞ = 8.0, Re_∞/ft = 3.75 x 10^6
T_w = 530.0°R, L = 20.01 in.
○ ▲ Experimental Data (Thermocouple) from NASA CR-120,029 (Ref. 86)
═══ Present Three-Dimensional Boundary-Layer Theory

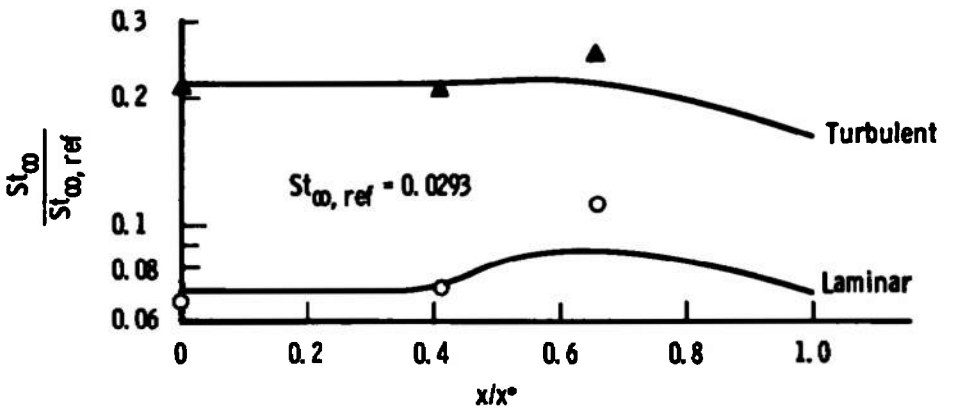

a. Spanwise Stanton Number Distribution

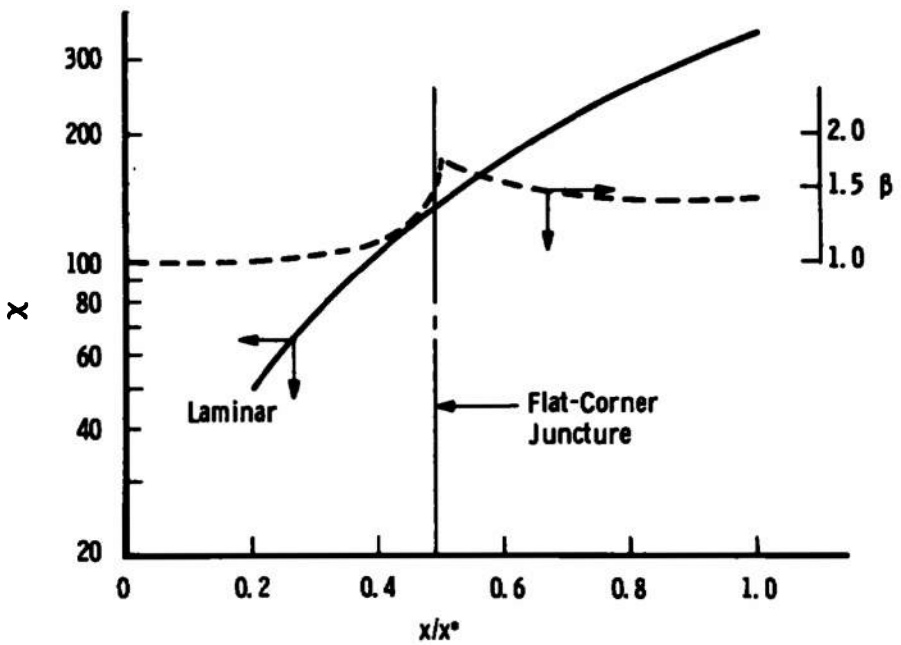

b. Spanwise Crossflow Reynolds Number and Inviscid Velocity Gradient Parameter Distributions

Fig. 31 Spanwise Stanton Number, Crossflow Reynolds Number, and Inviscid Velocity Gradient Parameter Distributions on the NAR Orbiter under AEDC-VKF Tunnel B Conditions

NAR Orbiter (161 B) at α = 40 deg
Body Station Location z/L = 0.3
AEDC VKF Tunnel B, M_∞ = 8.0, Re_∞/ft = 3.75 x 10^6
T_w = 530.0°R, L = 20.01 in.
○ ▲ Experimental Data (Thermocouple) from NASA CR-120,029 (Ref. 86)
═══ Present Three-Dimensional Boundary-Layer Theory

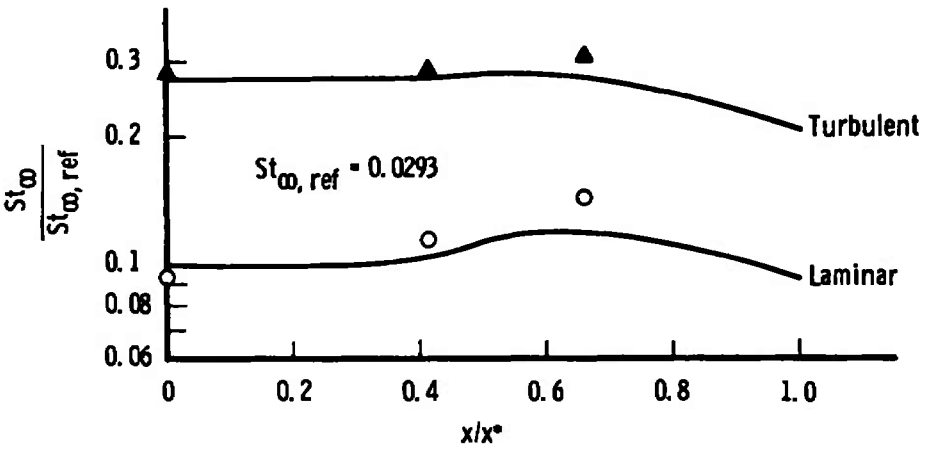

c. Spanwise Stanton Number Distribution

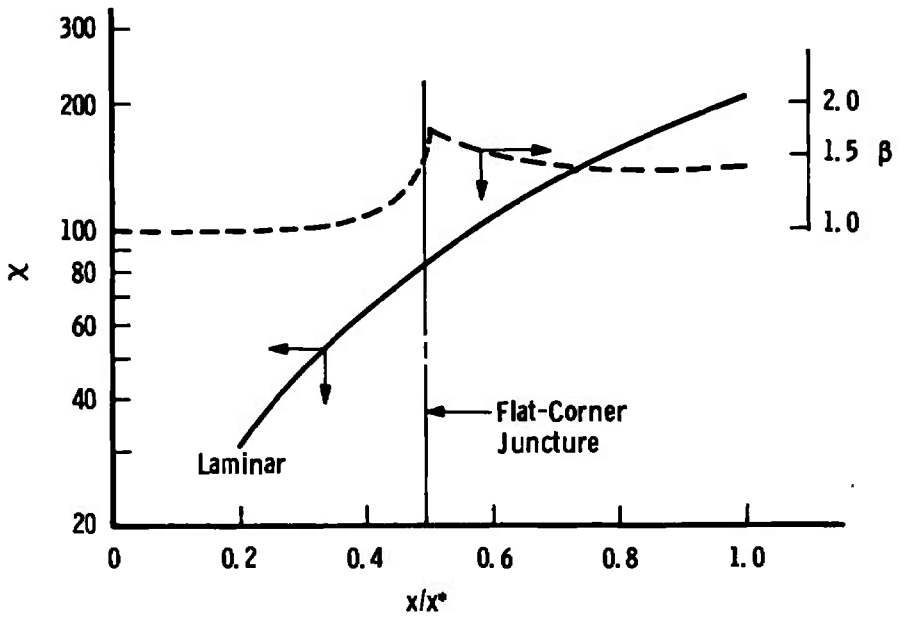

d. Spanwise Crossflow Reynolds Number and Inviscid Velocity Gradient Parameter Distributions

Fig. 31 Continued

NAR Orbiter (161 B) at α = 50 deg
Body Station Location z/L = 0.3
AEDC VKF Tunnel B, M_∞ = 8.0, Re_∞/ft = 3.75×10^6
T_w = 530.0°R, L = 20.01 in.
○▲ Experimental Data (Thermocouple) from NASA CR-120,029 (Ref. 86)
Present Three-Dimensional Boundary-Layer Theory

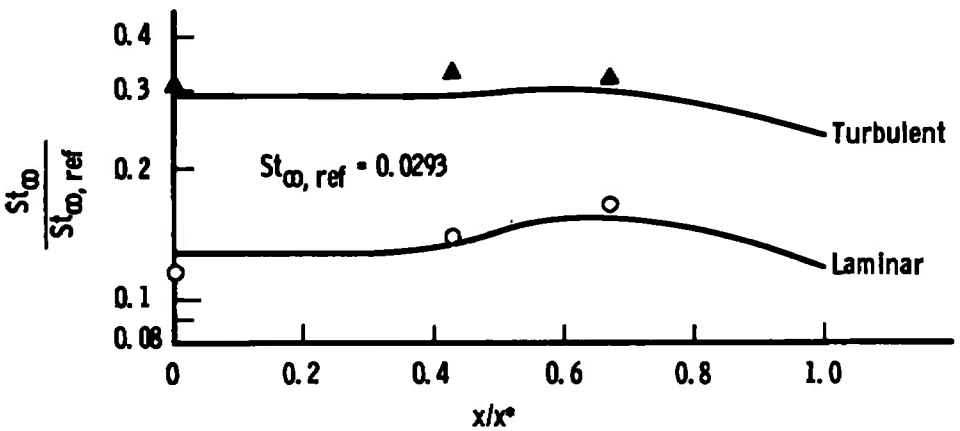

e. Spanwise Stanton Number Distribution

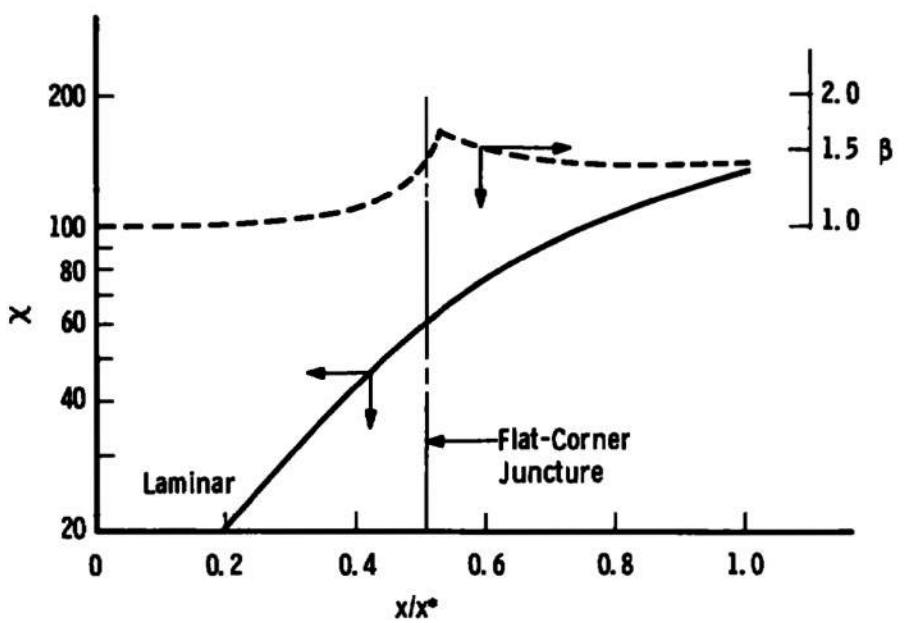

f. Spanwise Crossflow Reynolds Number and Inviscid Velocity Gradient Parameter Distributions

Fig. 31 Concluded

80-deg Sweep Delta Wing at α = 50 deg

M_∞ = 8.0, Re_∞/ft = 3.7 x 10^6, $T_w = T_{pc}$ = 960°R, z = 9.28 in.

◊ □ Experimental Data (Phase-Change Paint) from Appendix A-42 (Group 54) of Report MDC E0276 (Ref. 80)

◊ Right-Hand Side of Wing from Front

□ Left-Hand Side of Wing from Front

Present Three-Dimensional Boundary-Layer Theory

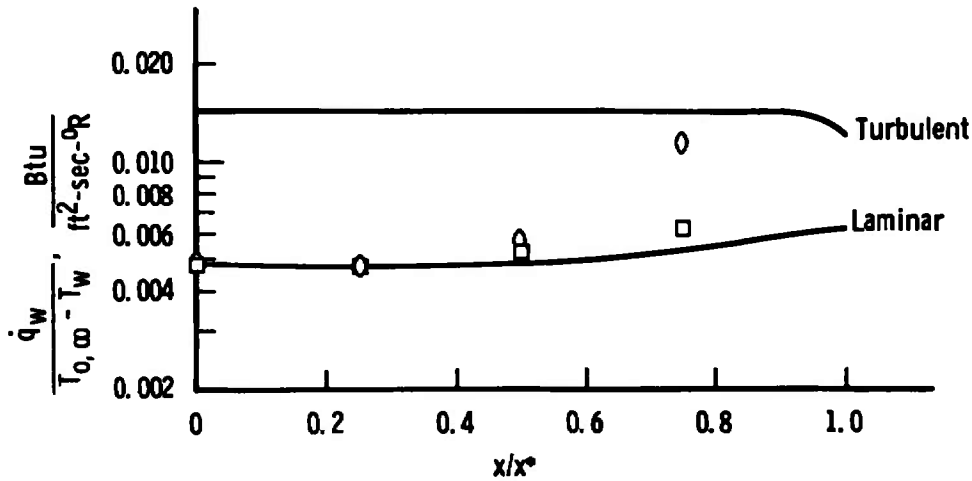

a. Spanwise Heat Transfer Distribution

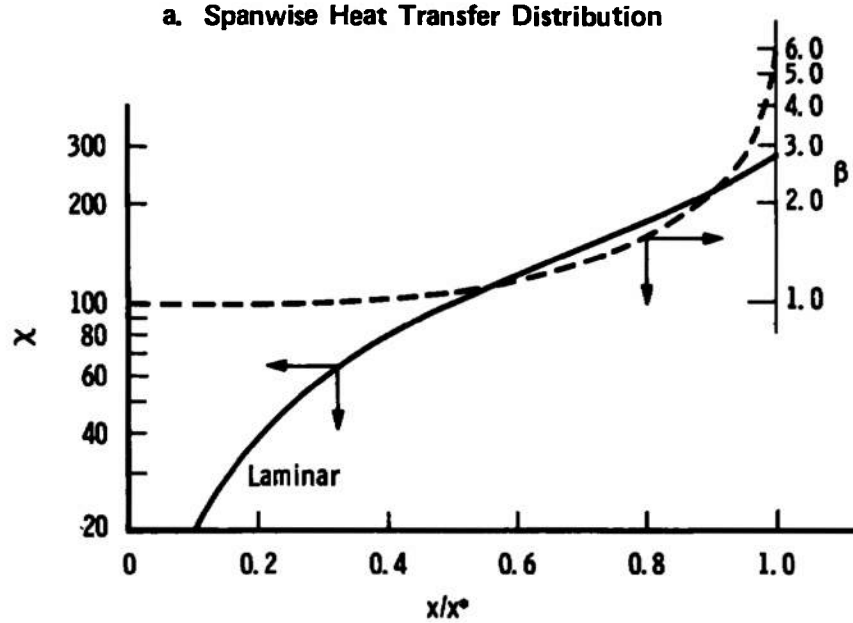

b. Spanwise Crossflow Reynolds Number and Inviscid Velocity Gradient Parameter Distributions

Fig. 32 Illustration of Surmised Spanwise Crossflow Tripping on a Delta Wing at High Incidence

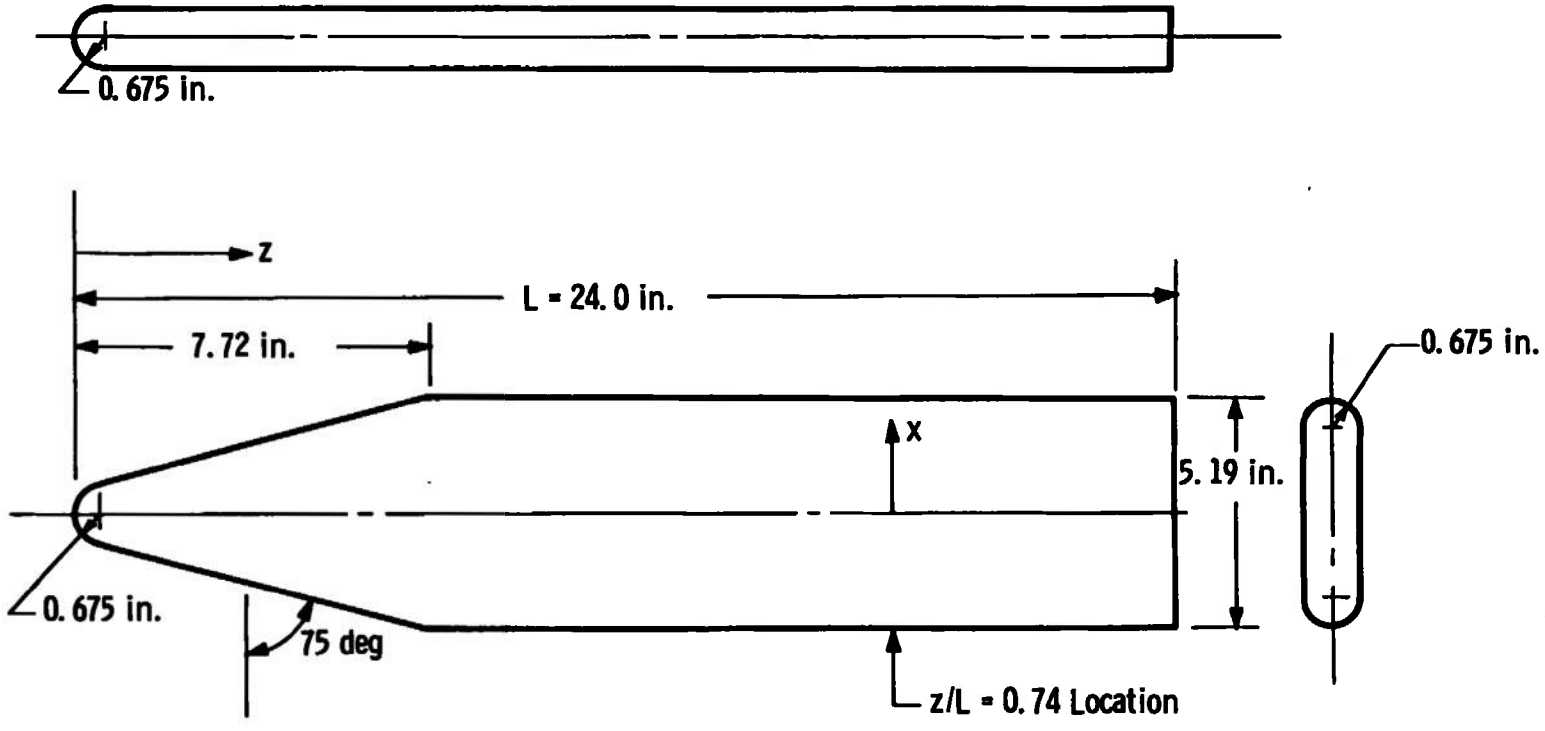

Fig. 33 NASA-Langley Research Center Straight Body (NASA LRC-SB) Delta Wing Configuration

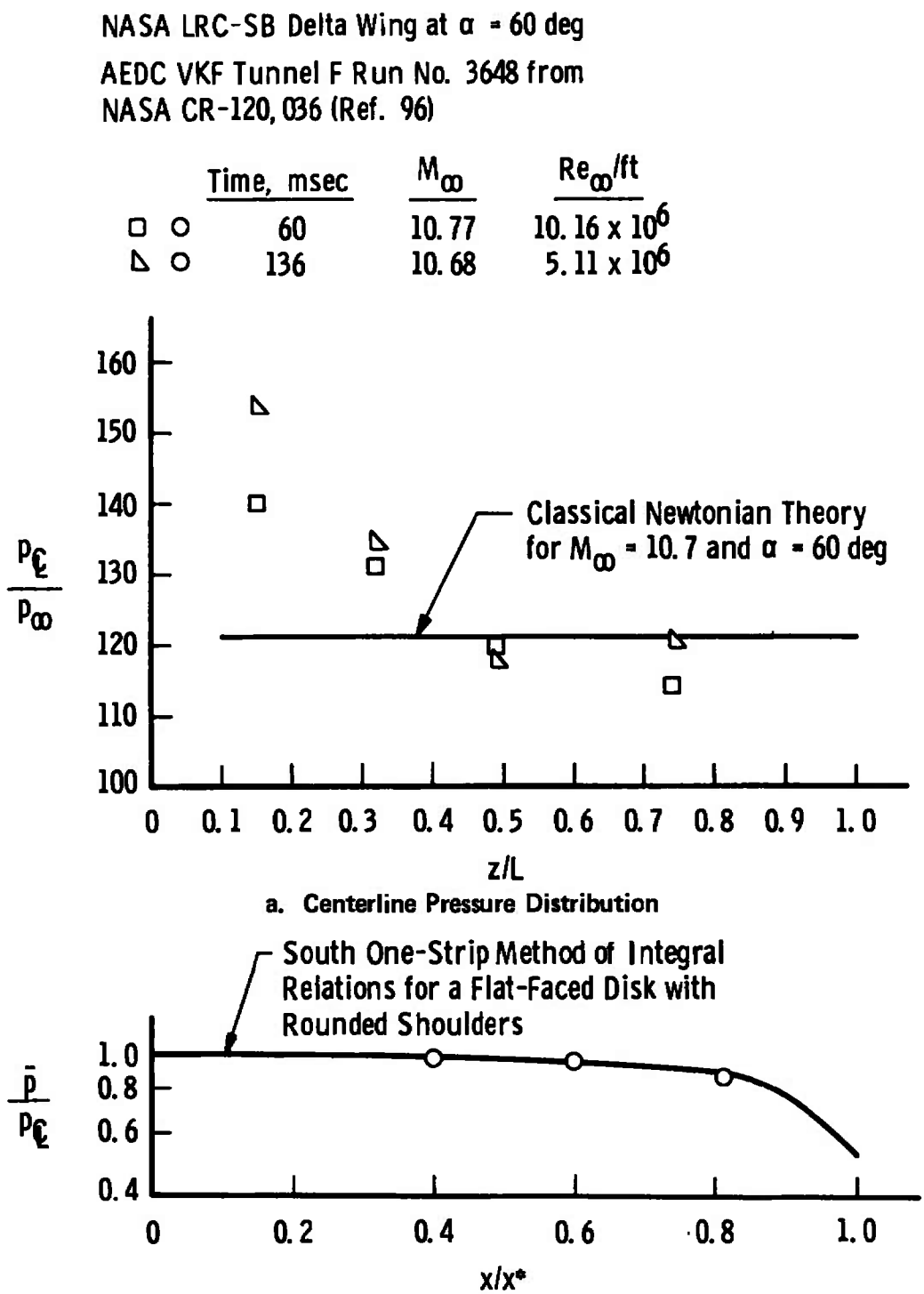

a. Centerline Pressure Distribution

b. Spanwise Pressure Distribution for Body Location z/L = 0.74

Fig. 34 Centerline and Spanwise Pressure Distributions on the NASA LRC-SB at High Incidence

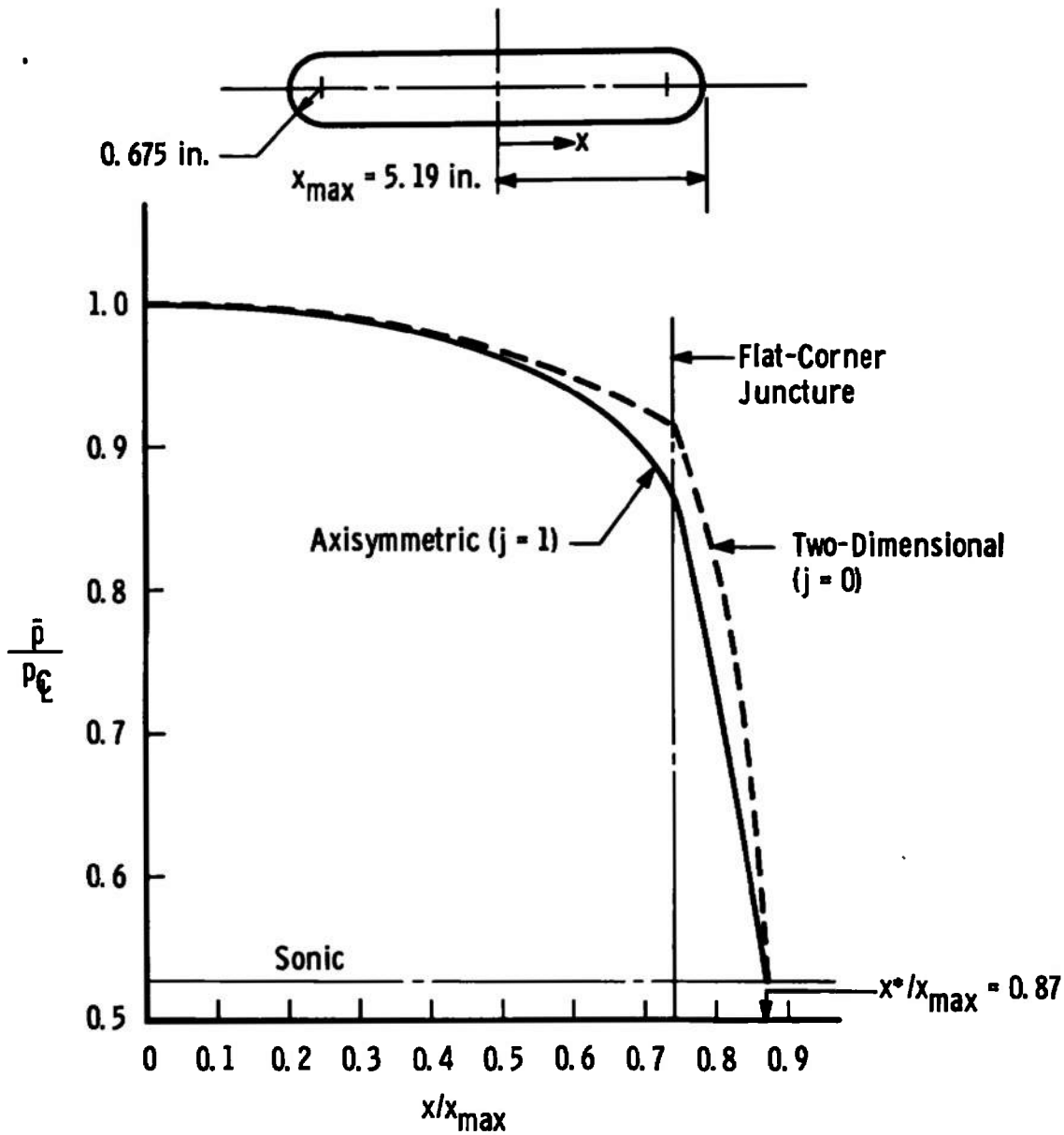

Fig. 35 Effects of Body Type on Spanwise Pressure Distribution

NASA LRC-SB Delta Wing at α = 60 deg
AEDC VKF Tunnel F Run No. 3648 from
NASA CR-120,036 (Ref. 96)

	Time, msec	M_∞	Re_∞/ft	$\dot{q}_{ref}$ (Btu/ft^2-sec)
△	60	10.77	10.16×10^6	105.9
□	136	10.68	5.11×10^6	70.4

—— Present Three-Dimensional Turbulent Boundary-Layer Theory Using Newtonian Surface Pressure

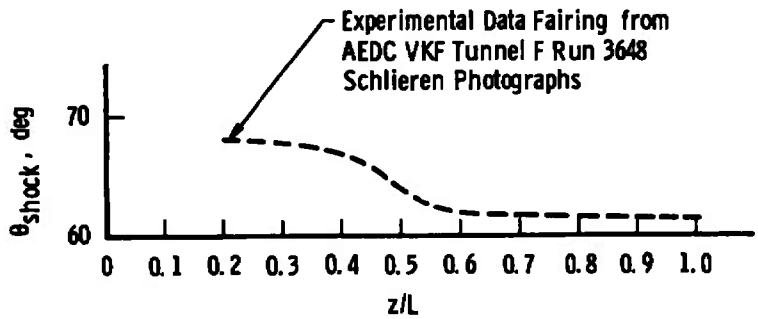

a. Centerline Shock Angle Distribution

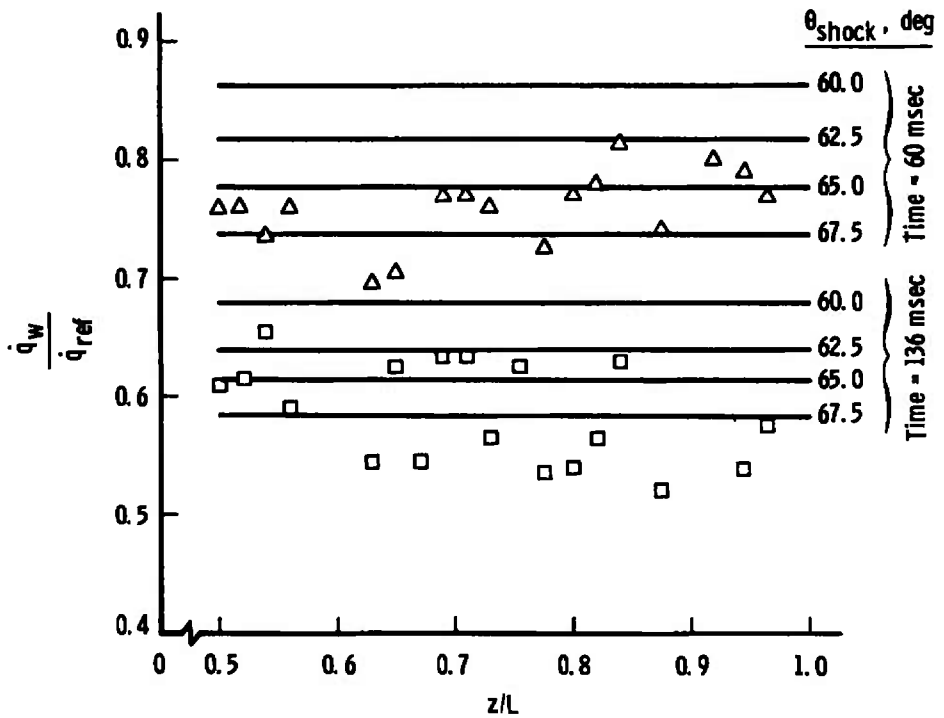

b. Centerline Heat-Transfer-Rate Distribution

Fig. 36 Centerline Shock Angle and Heat-Transfer Distributions on the NASA LRC-SB at High Incidence

NASA LRC-SB Delta Wing at α = 60 deg

AEDC VKF Tunnel F Run No. 3648 from
NASA CR-120,036 (Ref. 96)

	Time, msec	M_∞	Re_∞/ft	$\dot{q}_{ref}$ (Btu/ft^2-sec)
◊	60	10.77	10.16×10^6	105.9

═══ Present Three-Dimensional Turbulent Boundary-Layer Theory Based on θ_{shock} = 65.0 deg and Newtonian Surface Pressure

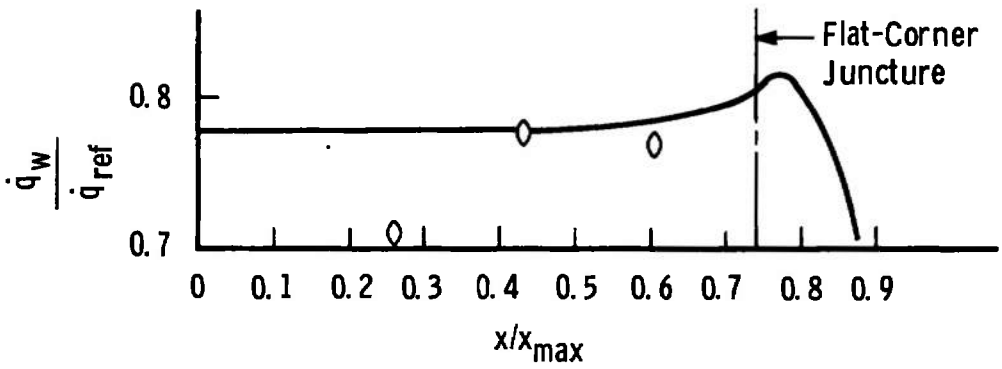

a. Spanwise Heat-Transfer Distribution for Body Location z/L = 0.74

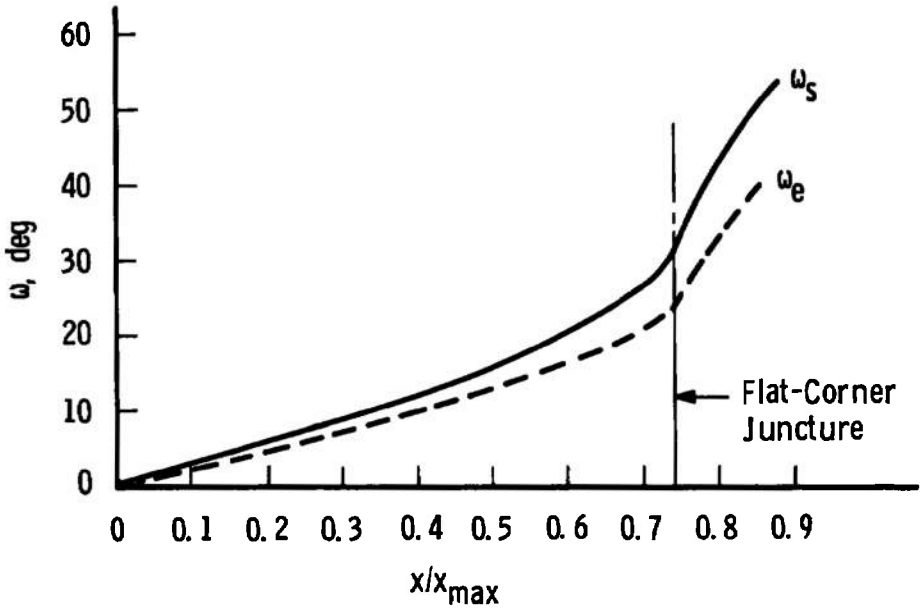

b. Spanwise Surface and Edge Flow Directions

Fig. 37 Spanwise Heat-Transfer and Flow Angle Distributions on the NASA LRC-SB at High Incidence

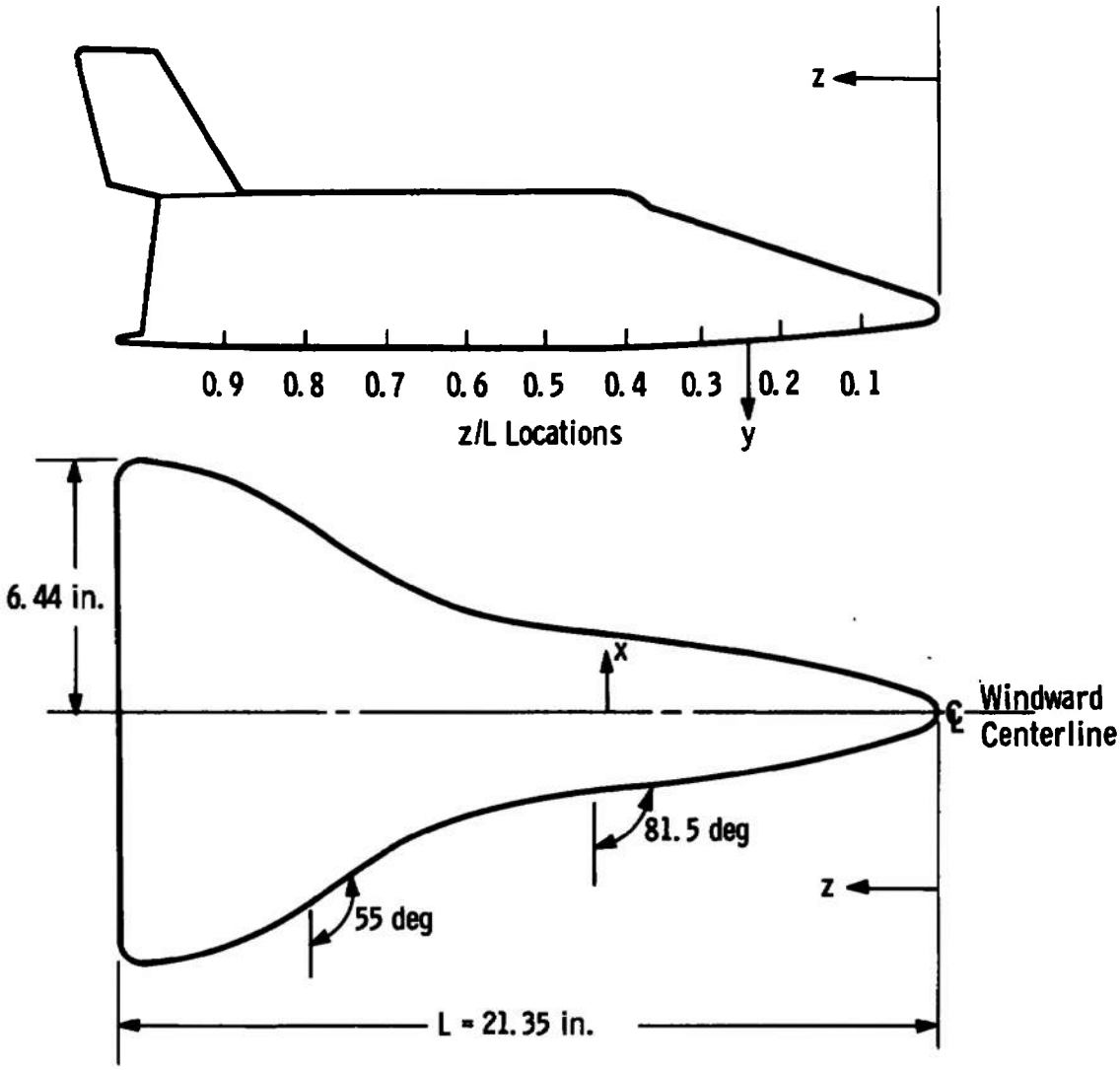

Fig. 38 McDonnell-Douglas (MDAC) Delta Wing Orbiter Configuration (0.011-Scale)

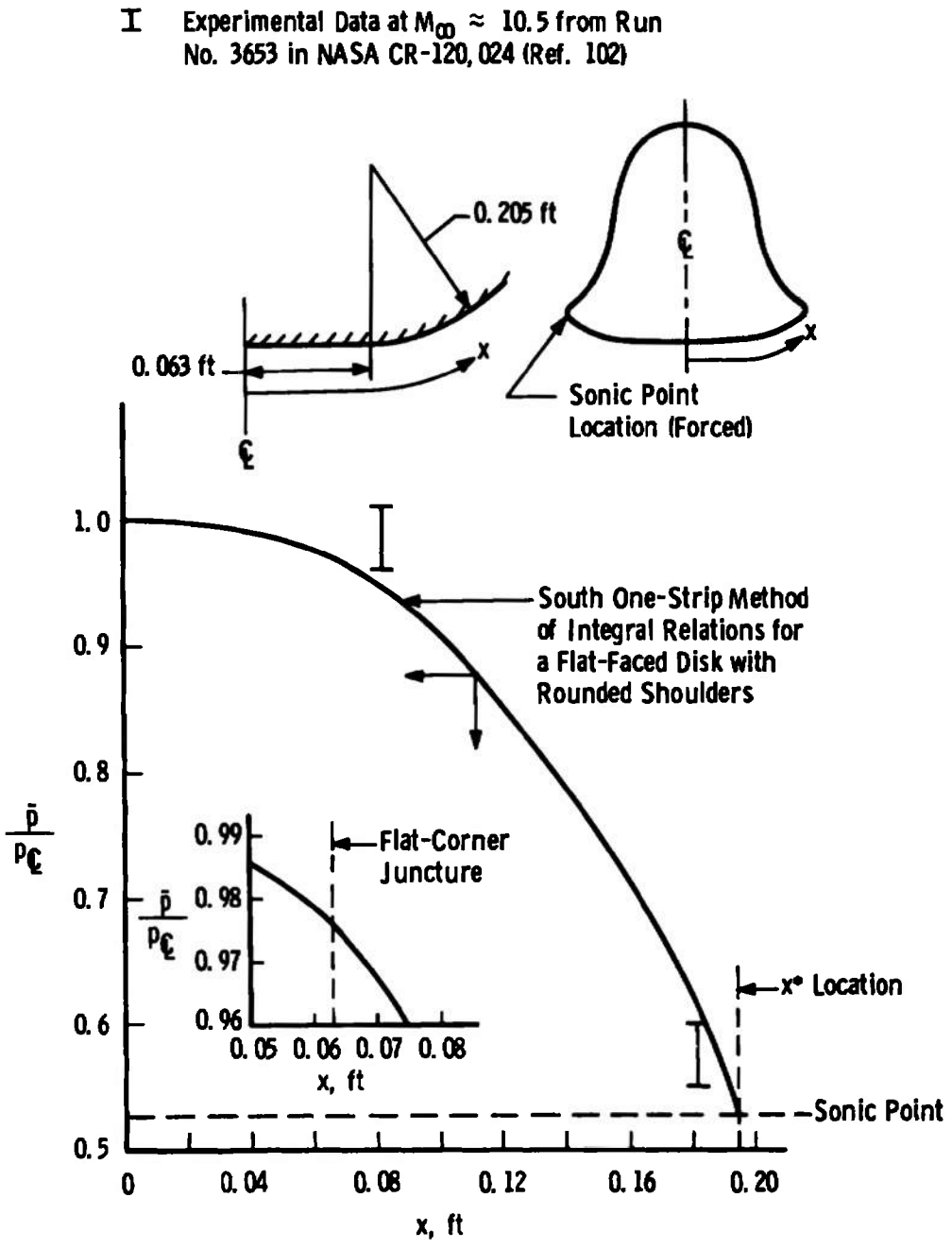

Fig. 39 Spanwise Pressure Distribution on the MDAC Orbiter at Incidence

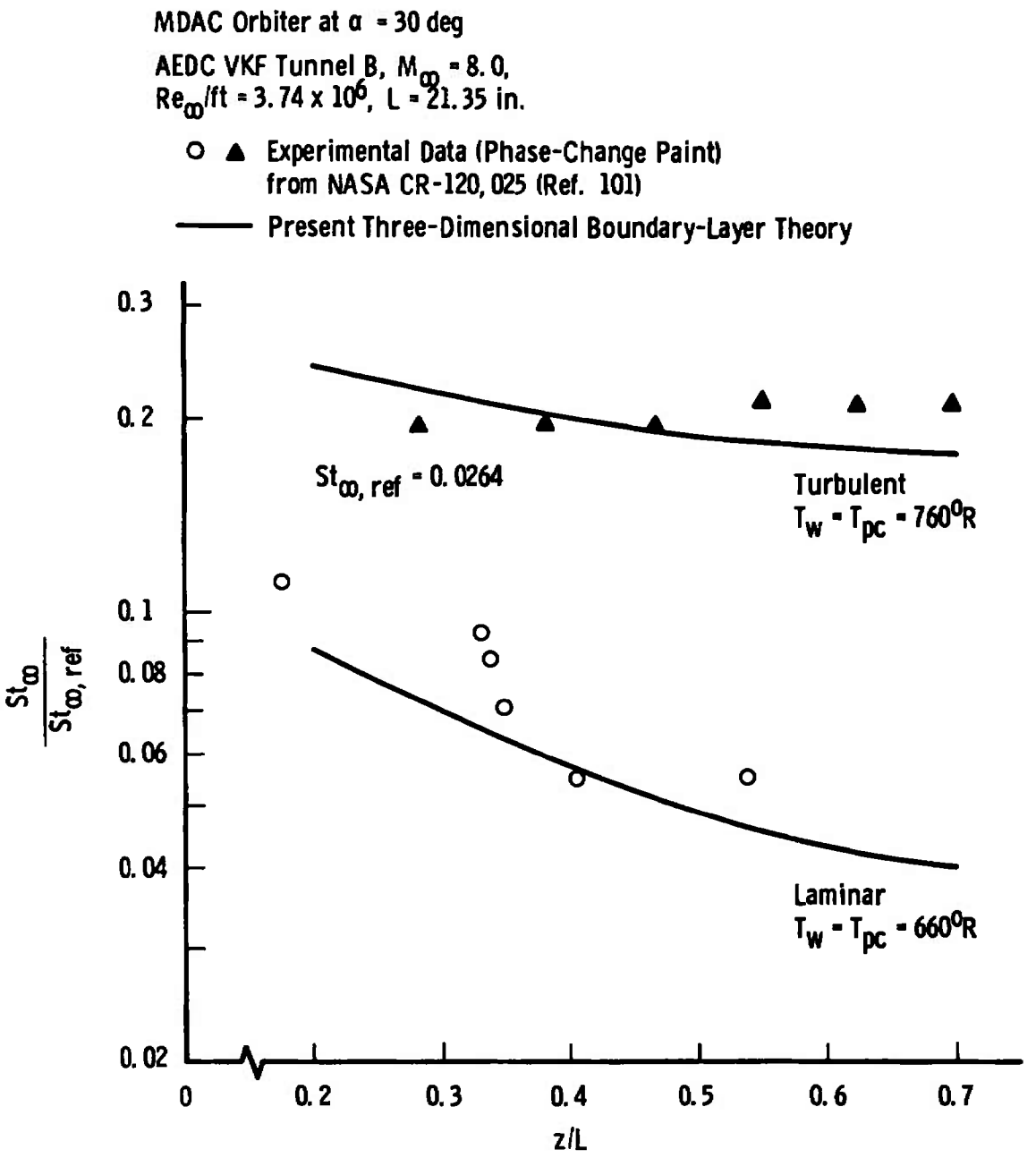

a. 30-deg Angle of Attack

Fig. 40 Windward Centerline Stanton Number Distributions on the MDAC Orbiter under AEDC-VKF Tunnel B Conditions

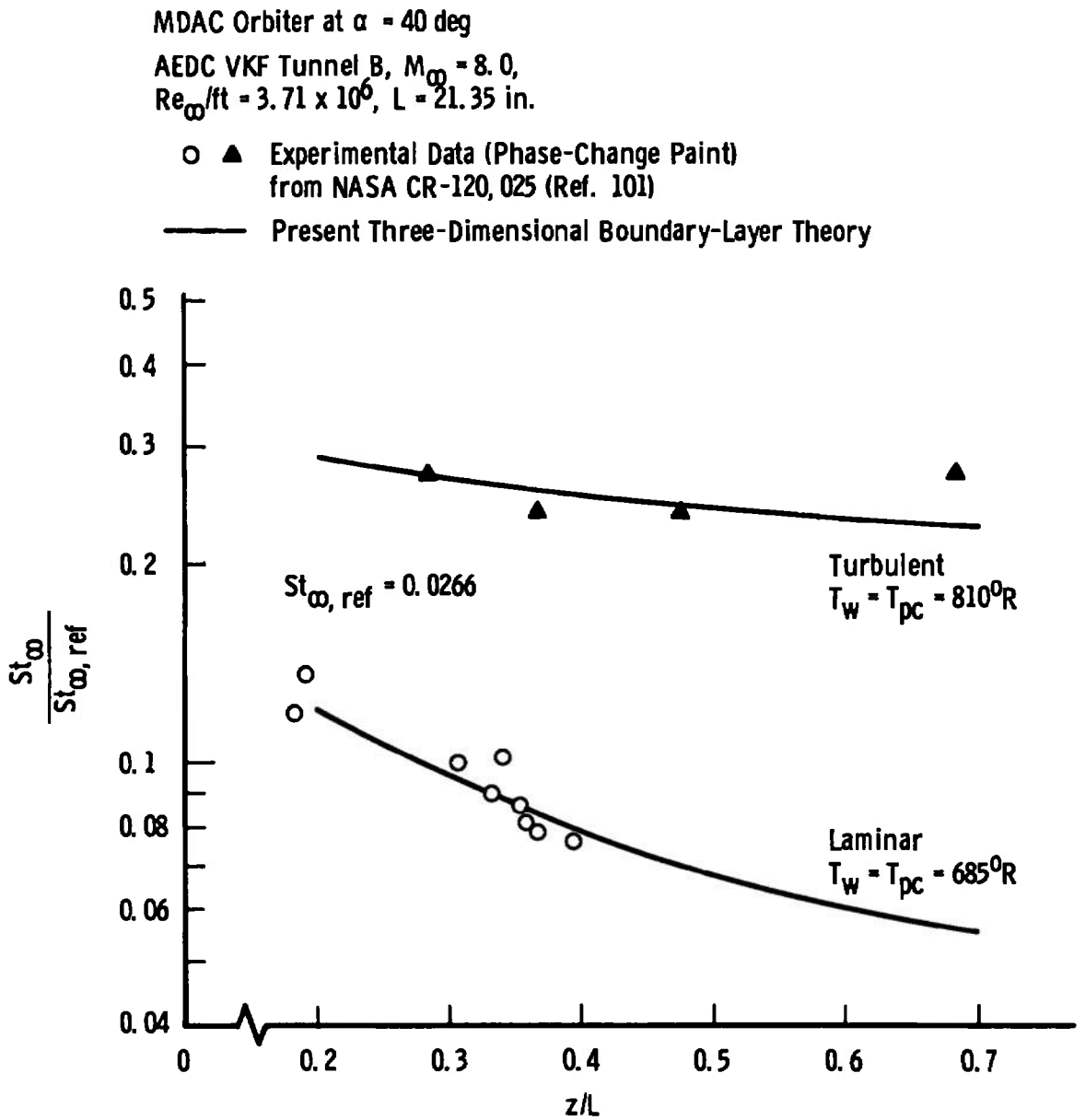

b. 40-deg Angle of Attack
Fig. 40 Continued

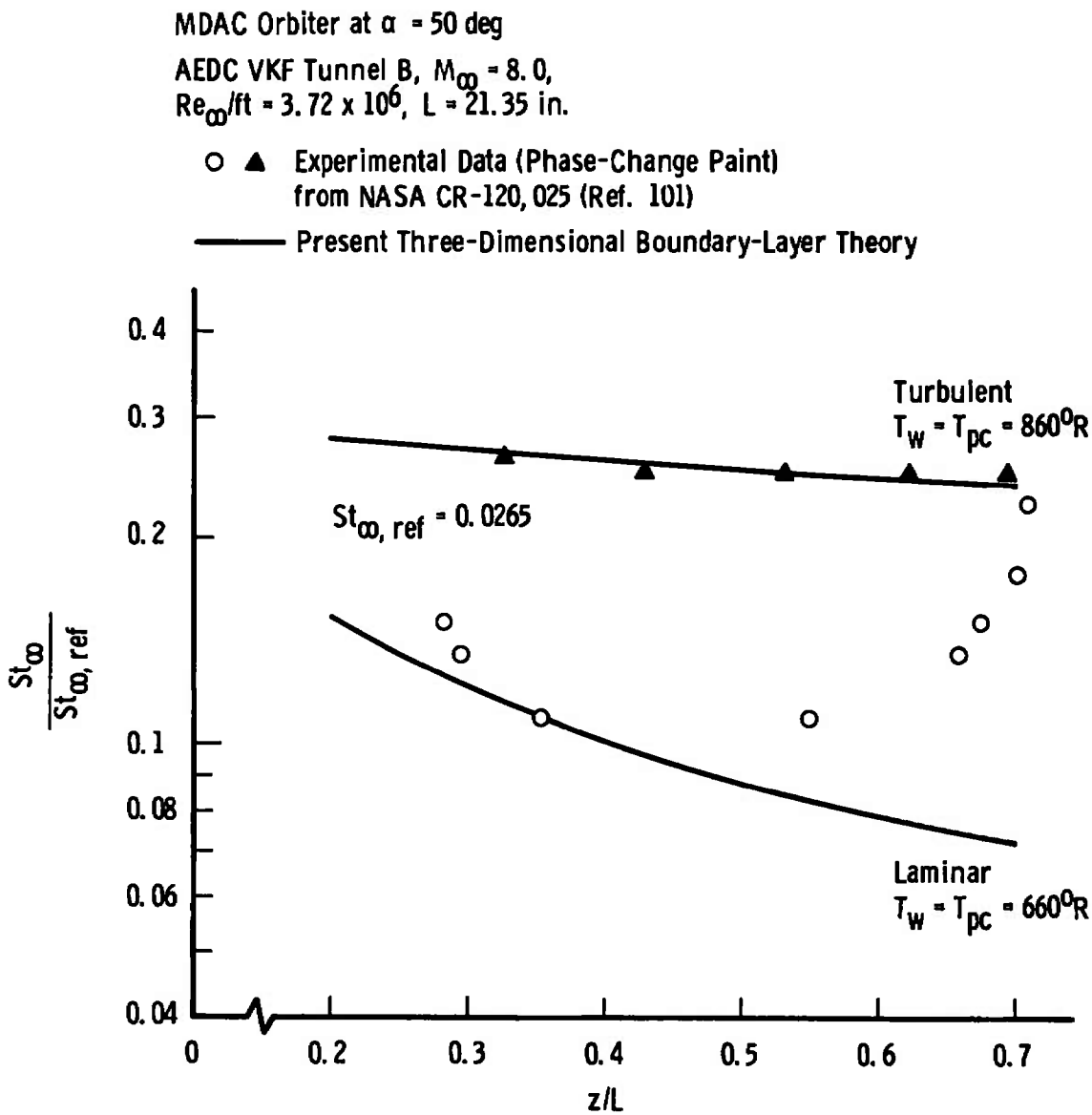

c. 50-deg Angle of Attack
Fig. 40 Concluded

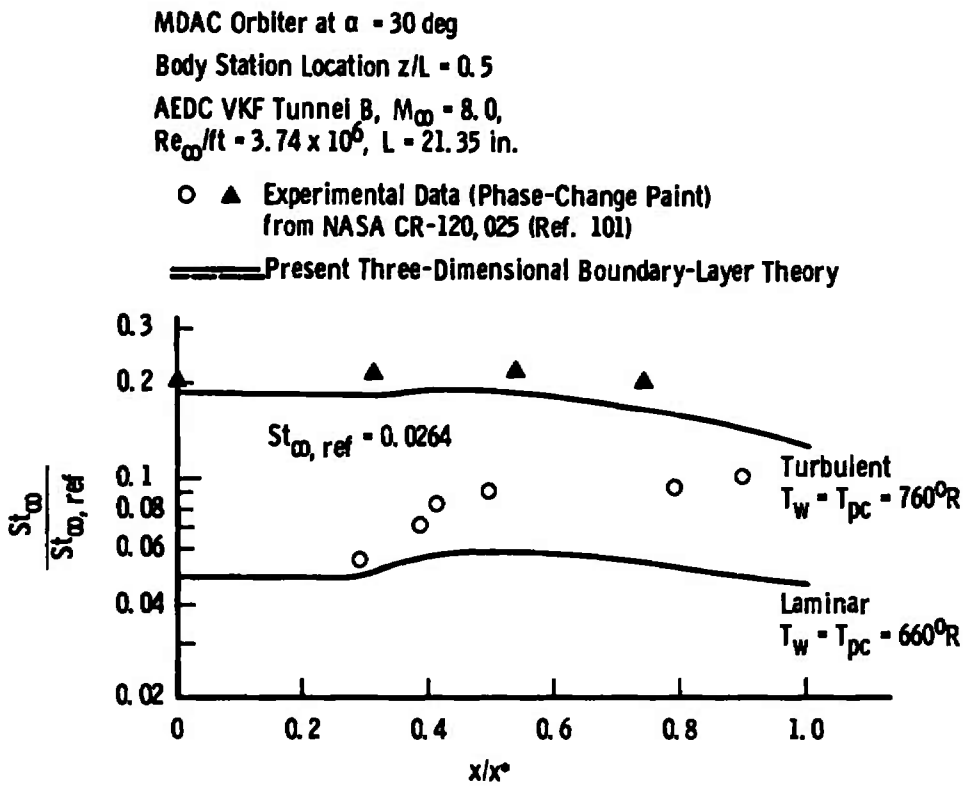

a. Spanwise Stanton Number Distribution

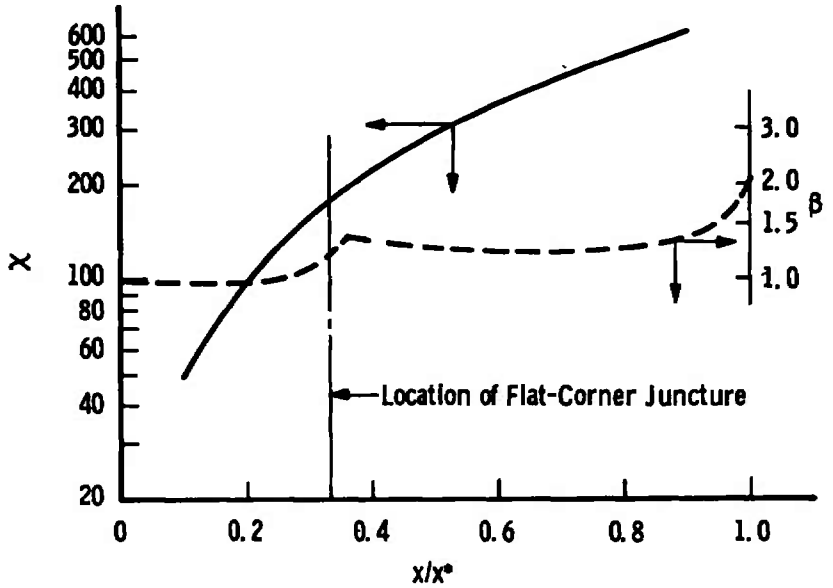

b. Spanwise Crossflow Reynolds Number and Inviscid Velocity Gradient Parameter Distributions

Fig. 41 Spanwise Stanton Number, Crossflow Reynolds Number, and Inviscid Velocity Gradient Parameter Distributions on the MDAC Orbiter under AEDC-VKF Tunnel B Conditions

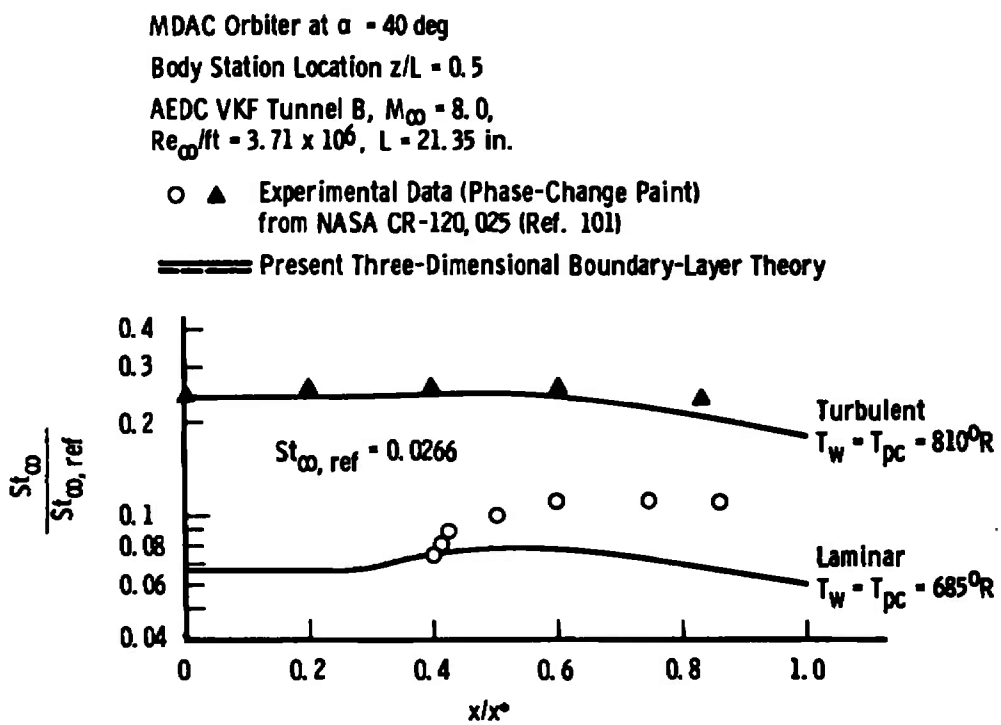

c. Spanwise Stanton Number Distribution

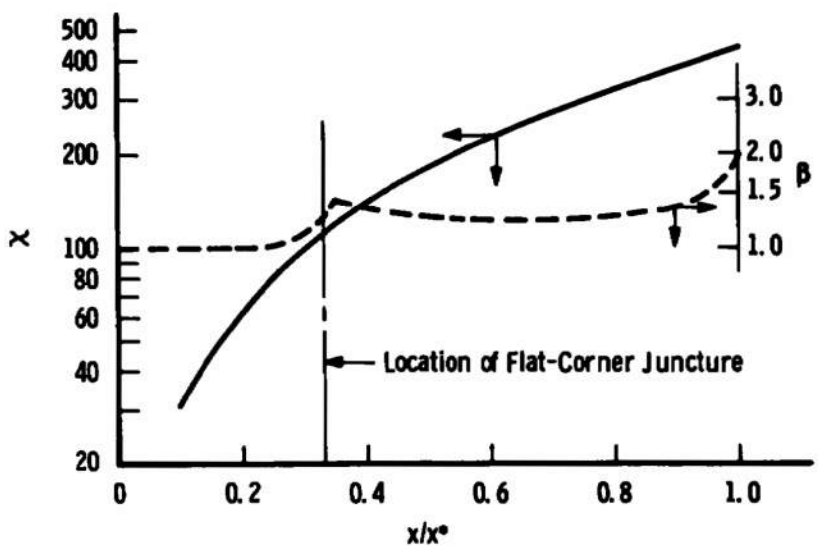

d. Spanwise Crossflow Reynolds Number and Inviscid Velocity Gradient Parameter Distributions

Fig. 41 Continued

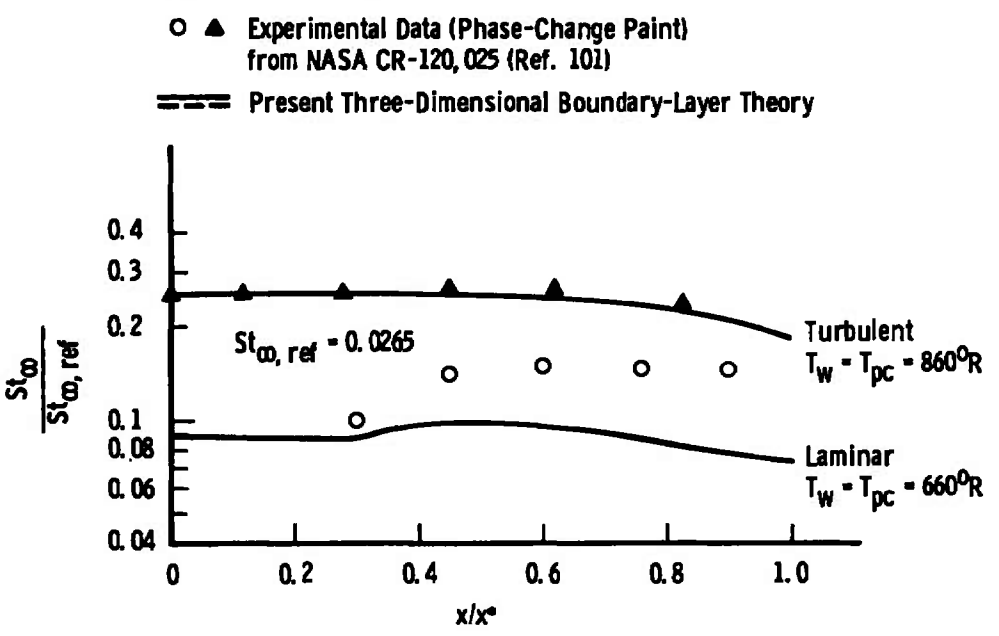

e. Spanwise Stanton Number Distribution

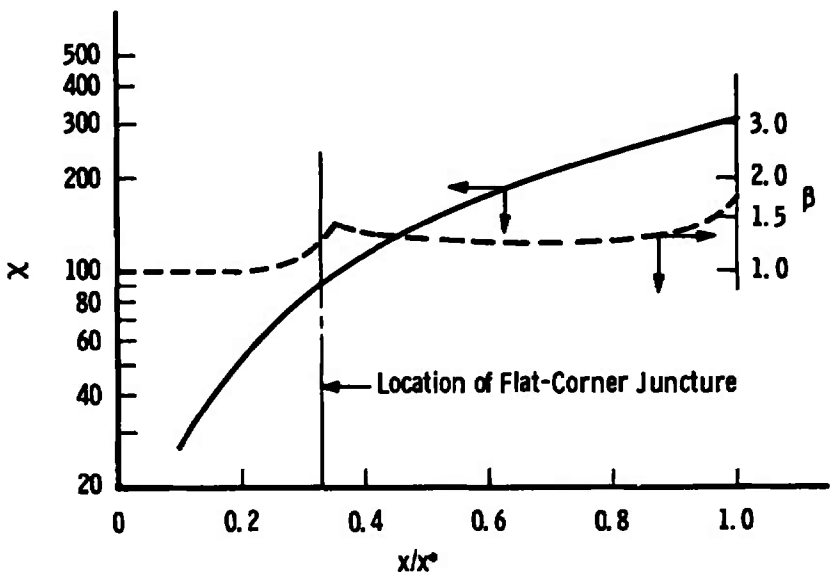

f. Spanwise Crossflow Reynolds Number and Inviscid Velocity Gradient Parameter Distributions

Fig. 41 Concluded

MDAC Orbiter at α = 50 deg

Data Symbol	AEDC VKF Tunnel	Time, msec	M_∞	Re_∞/ft	$T_w/T_{0,\infty}$	$St_{\infty, ref}$
▲	B	-	8.0	3.73×10^6	0.64	2.65×10^{-2}
■	F Run 3659	61	10.70	12.65×10^6	0.24	1.72×10^{-2}
●	F Run 3659	135	10.53	4.16×10^6	0.20	2.92×10^{-2}

——— Present Three-Dimensional Turbulent Boundary-Layer Theory

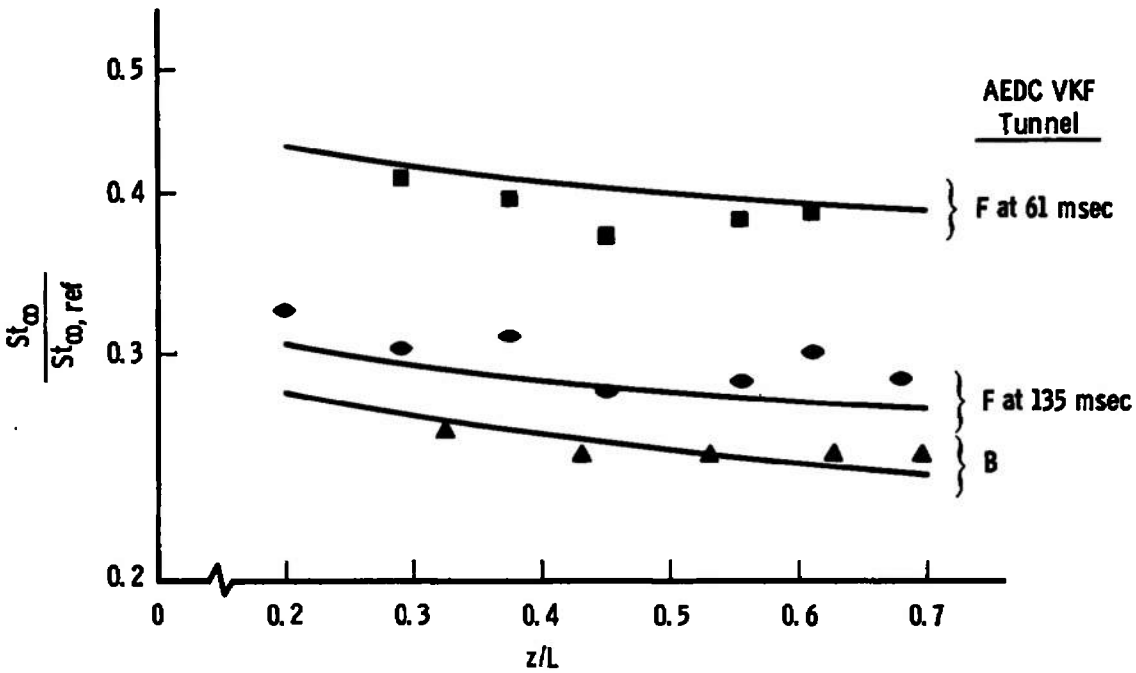

Fig. 42 Effects of Mach Number, Reynolds Number, and Wall Temperature Ratio on MDAC Orbiter Windward Centerline Turbulent Heat Transfer under High Angle-of-Attack Conditions

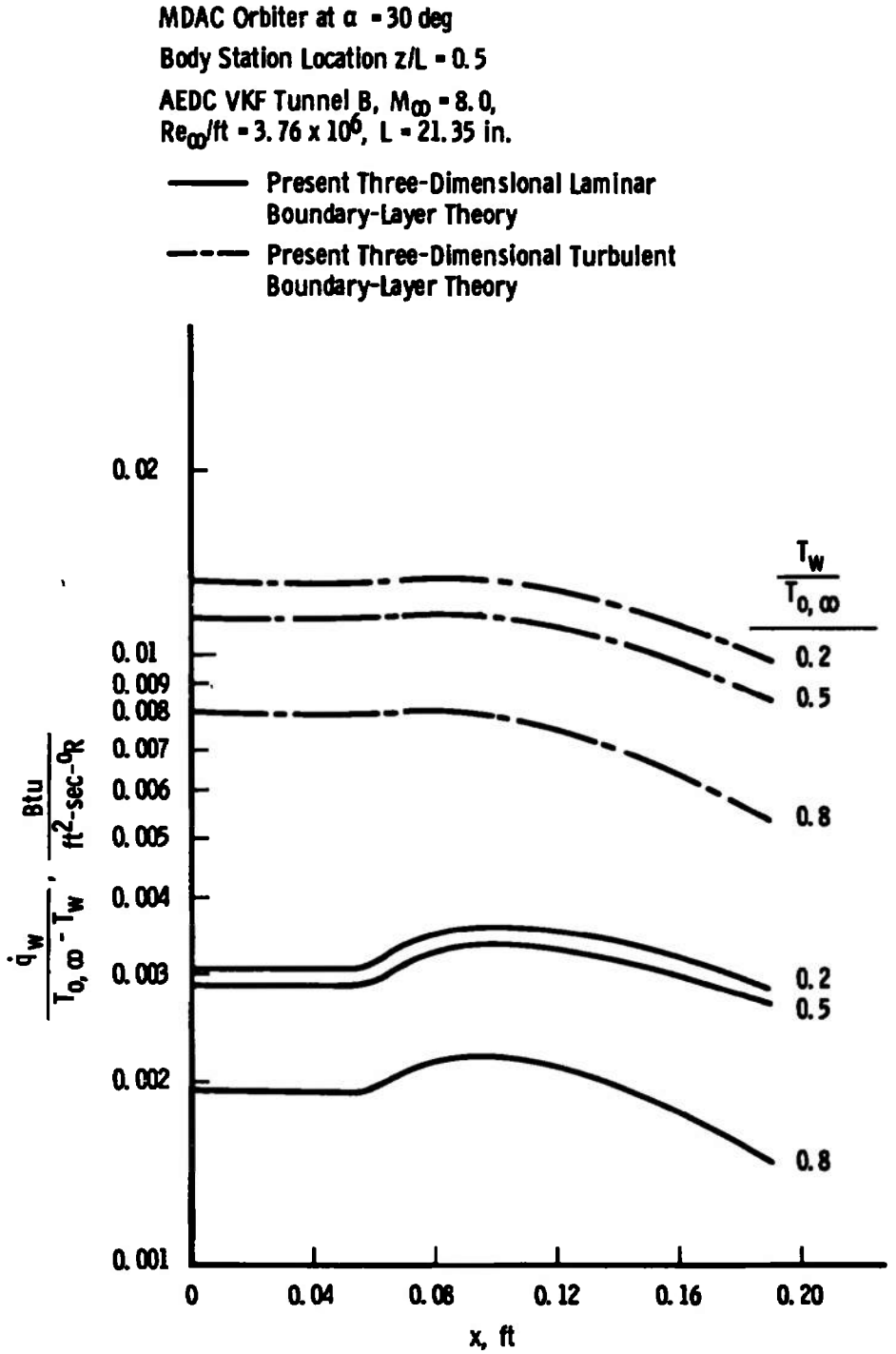

Fig. 43 Wall Temperature Effects on Spanwise Laminar and Turbulent Heat-Transfer Distributions

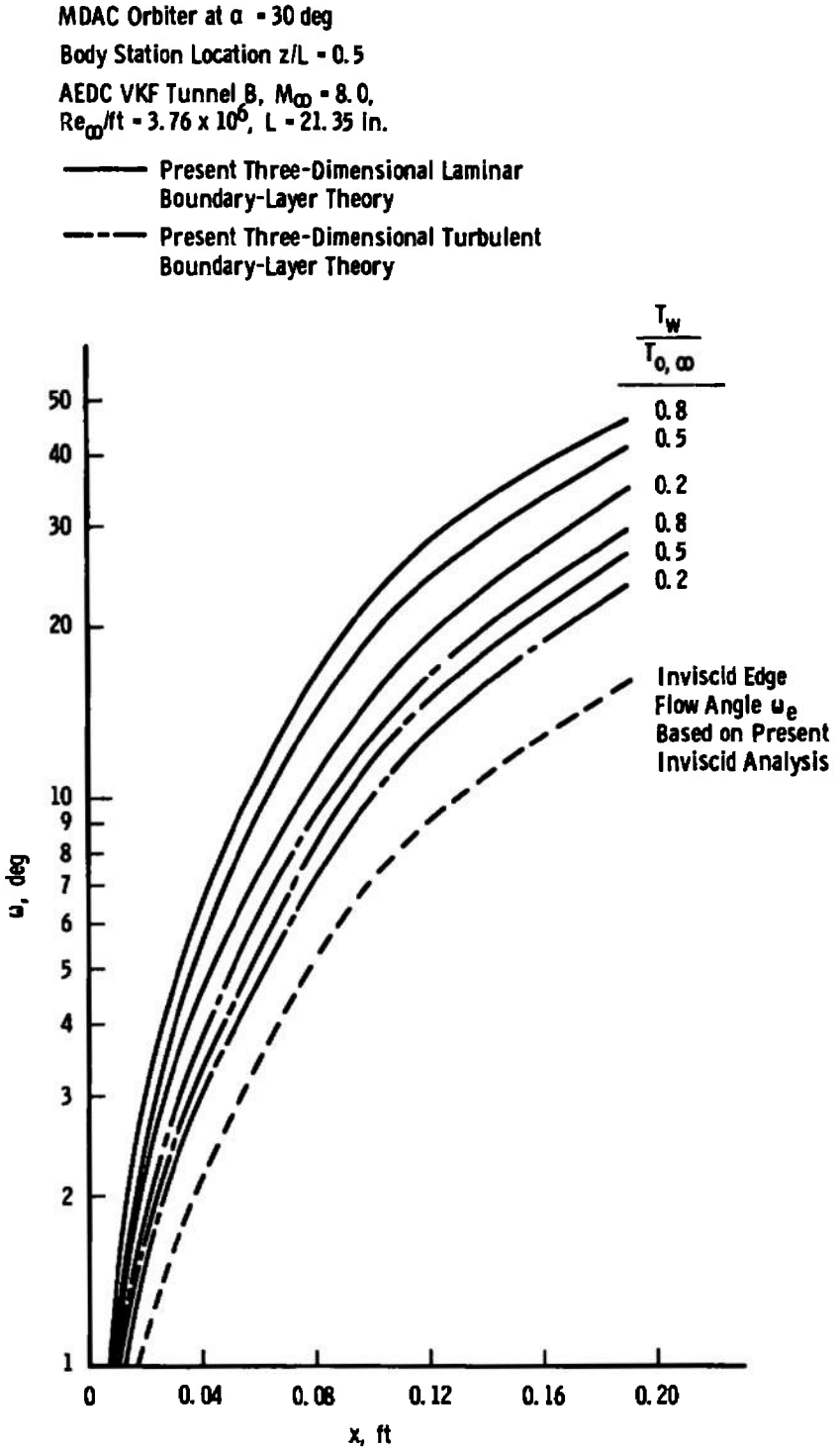

Fig. 44 Wall Temperature Effects on Spanwise Laminar and Turbulent Surface Flow Angle Distributions

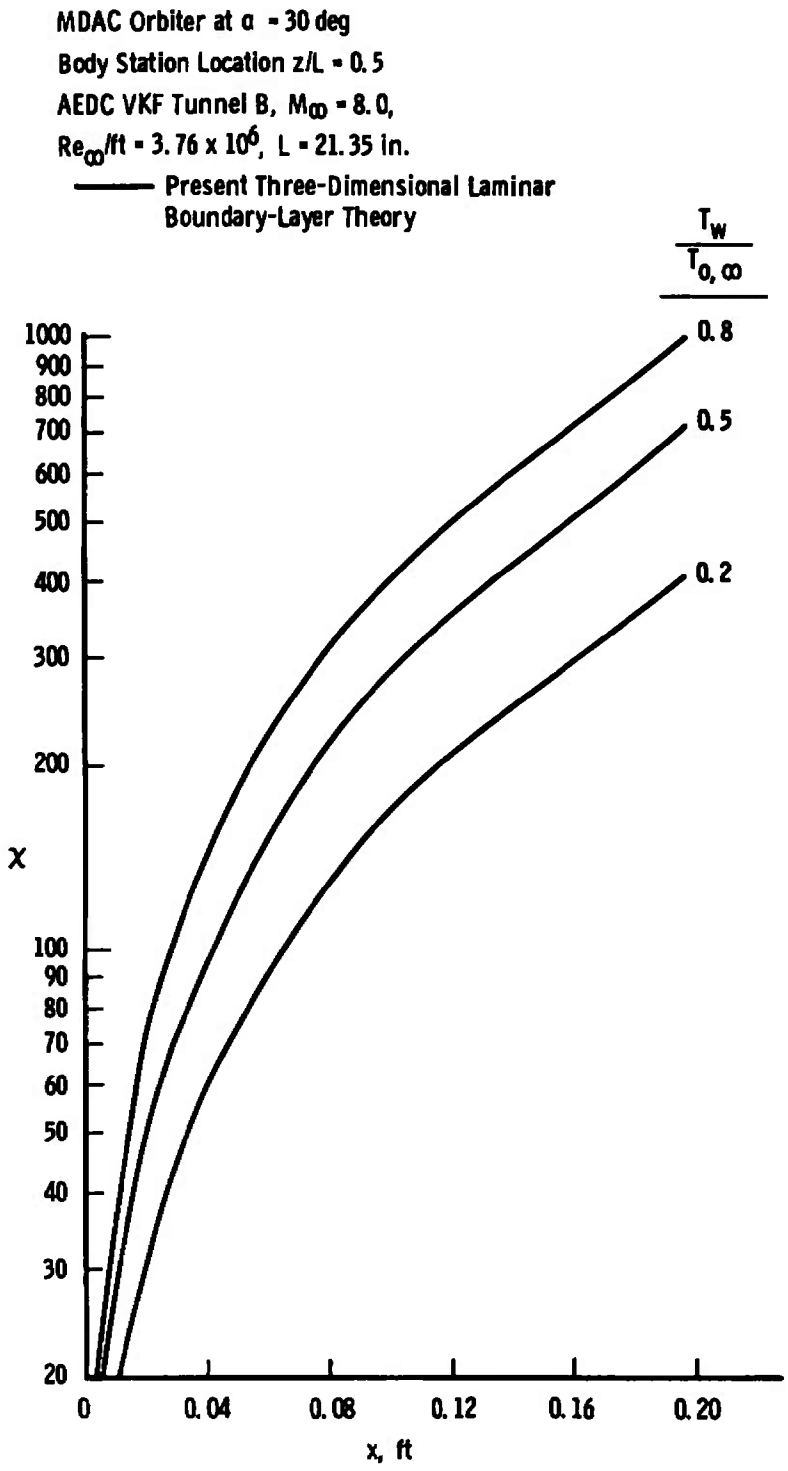

Fig. 45 Wall Temperature Effects on Spanwise Crossflow Reynolds Number Distributions

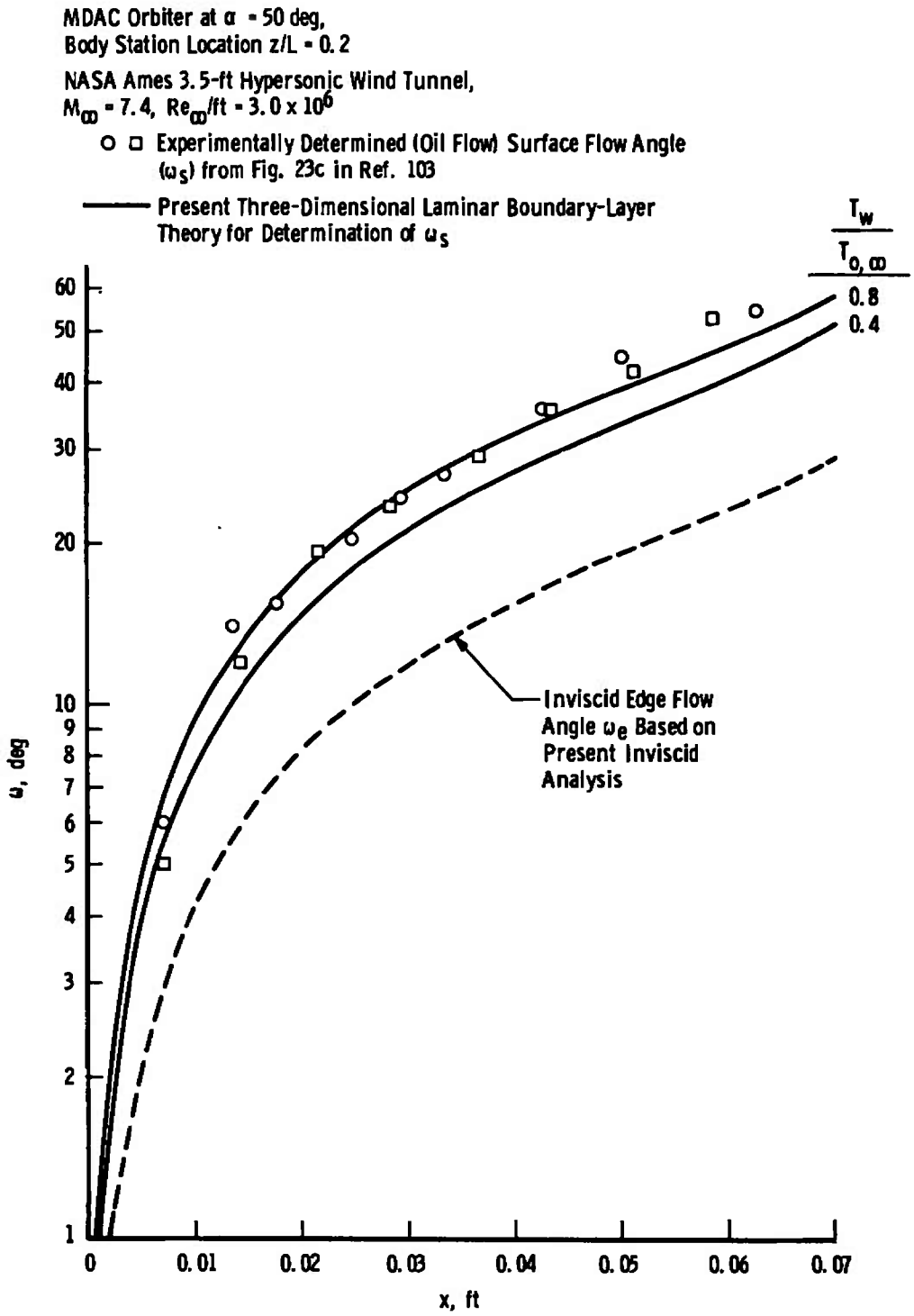

Fig. 46 Spanwise Surface Flow Angle Distribution in the Nose Region of the MDAC Orbiter under High Angle-of-Attack Conditions

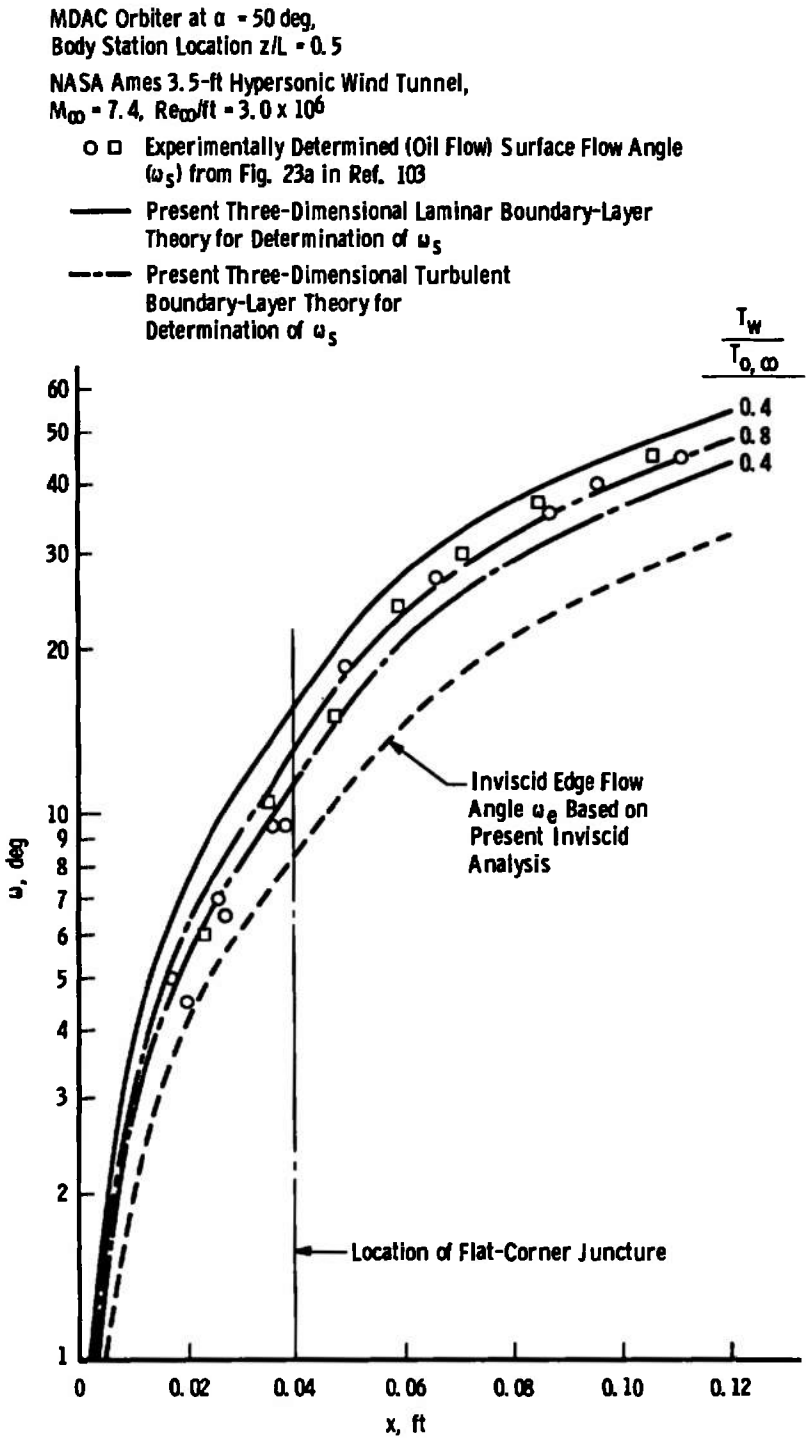

Fig. 47 Spanwise Surface Flow Angle Distribution at Mid-Body on the MDAC Orbiter under High Angle-of-Attack Conditions

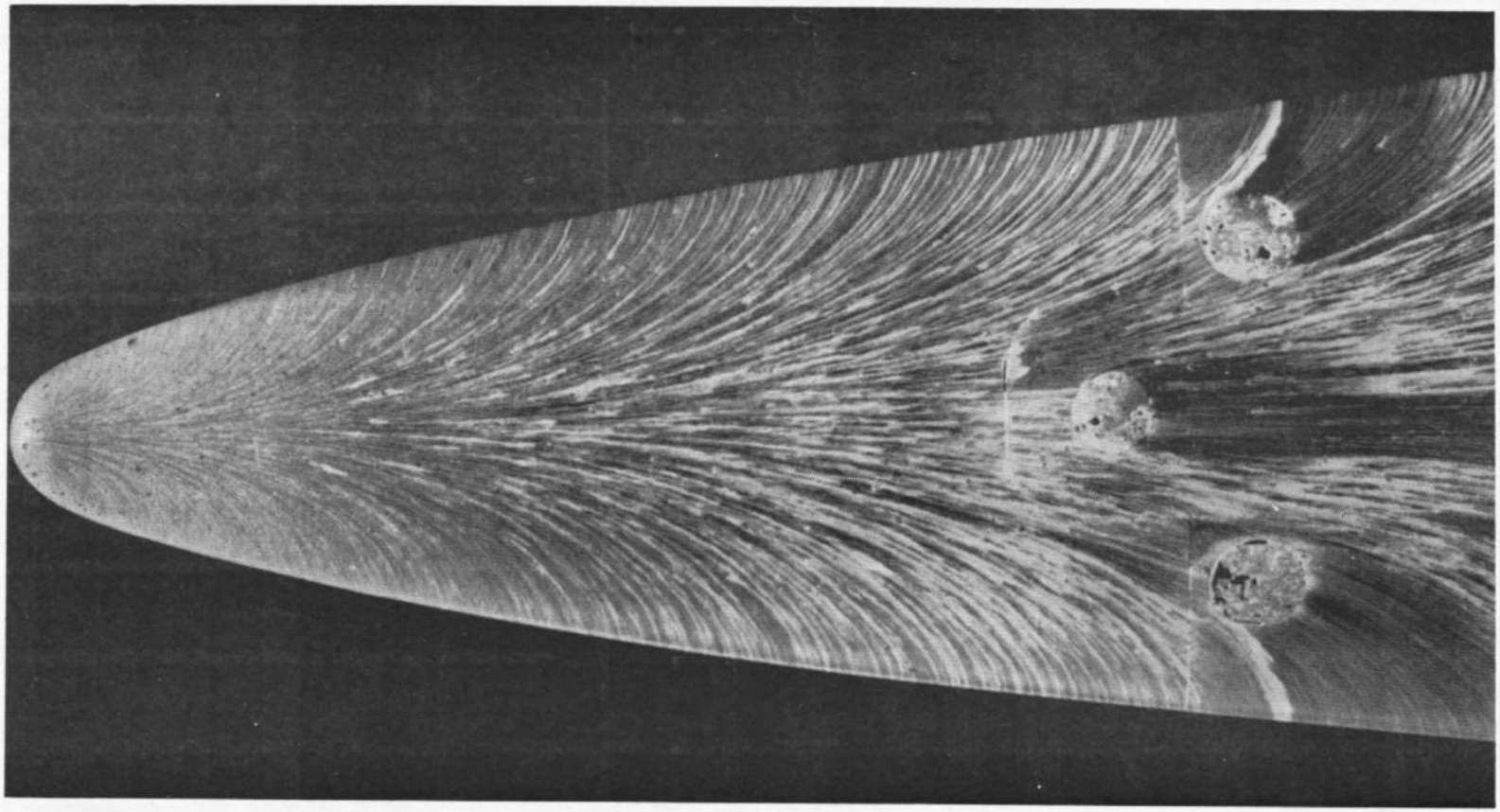

Fig. 48 Nose Region Windward Surface Flow Visualization Photograph of the MDAC Delta Wing Orbiter at 50-deg Angle of Attack as Taken from Fig. 23c in Mellenthin, Hamilton, and Zoerner (Ref. 103)

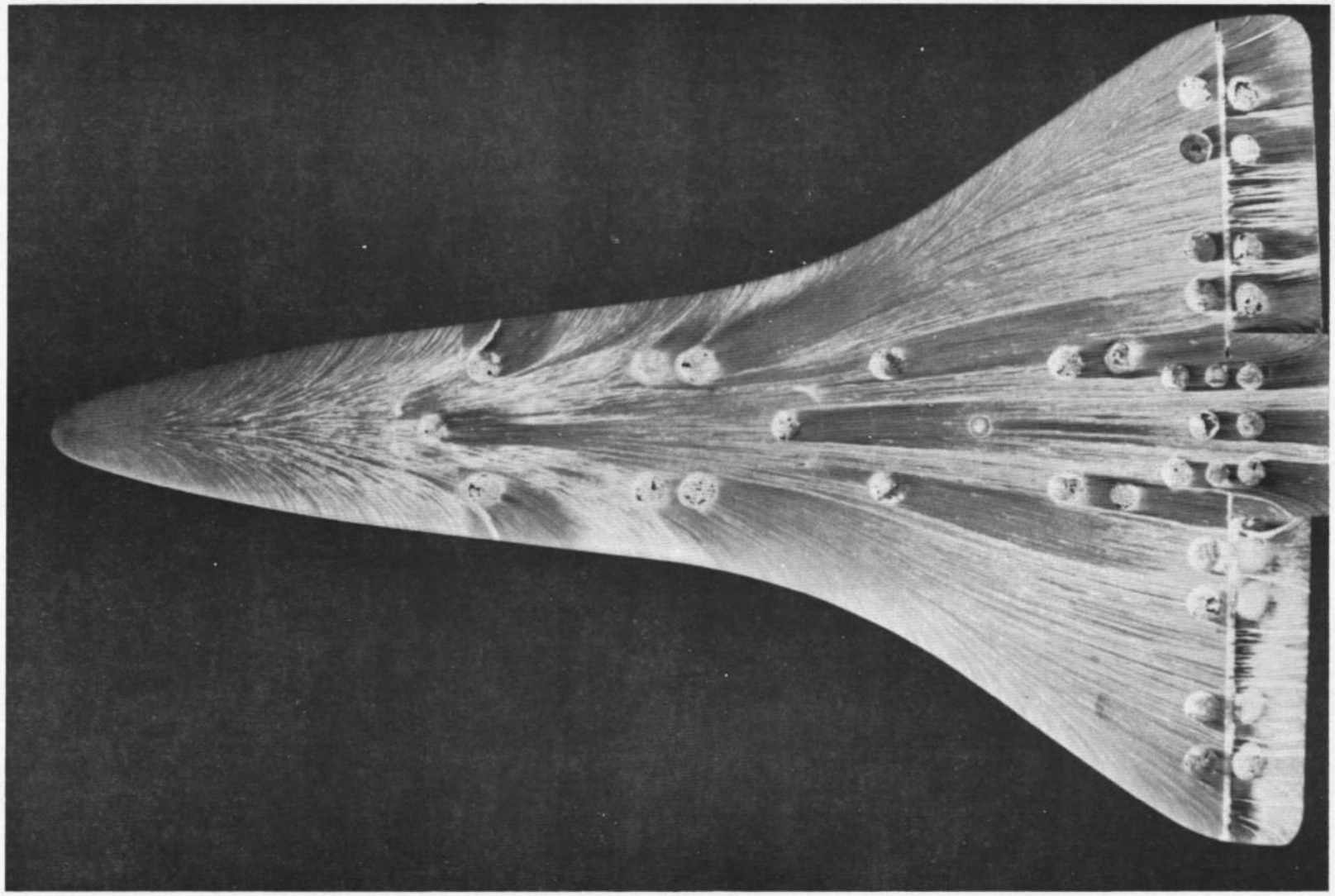

Fig. 49 Windward Surface Flow Visualization Photograph of the MDAC Delta Wing Orbiter at 50-deg Angle of Attack as Taken from Fig. 23a in Mellenthin, Hamilton, and Zoerner (Ref. 103)

TABLE I
COMPARISON OF INVISCID CONICAL FLOW PARAMETERS ON A 30-DEG HALF-ANGLE SHARP CONE

	p_s/p_∞		T_s/T_∞		M_s		θ_{shock}, deg	
M_∞	Sims	HSD	Sims	HSD	Sims	HSD	Sims	HSD
4.0	7.190	7.152	2.097	2.096	2.239	2.240	36.937	37.019
6.0	14.529	14.492	3.285	3.286	2.735	2.734	34.872	34.926
8.0	24.801	24.756	4.941	4.944	2.994	2.993	34.138	34.181
10.0	38.007	37.950	7.069	7.074	3.139	3.138	33.795	33.833
12.0	54.147	54.074	9.668	9.675	3.227	3.225	33.609	33.644
20.0	148.054	147.884	24.787	24.807	3.367	3.365	33.336	33.367

Notes: Sims = Sims Tables (Ref. 56)
HSD = Rasmussen Hypersonic Small-Disturbance Theory (Ref. 54)

TABLE II
EFFECTS OF SHOCK ANGLE ON INVISCID CENTERLINE PARAMETERS FOR THE NASA LRC-SB DELTA WING AT 60-DEG ANGLE OF ATTACK UNDER AEDC-VKF TUNNEL F RUN NO. 3648 CONDITIONS

Time, msec	θ_{shock}, deg	Newtonian $p_{\mathfrak{L}} \times 10^{-3}$, lb_f/ft^2	$T_e \times 10^{-3}$, °R	$\rho_e \times 10^4$, slugs/ft^3	$W_e \times 10^{-3}$, ft/sec	$\frac{dU_e}{dx} \times 10^{-3}$, 1/sec
60	60.0	3.3722	1.9187	9.8960	2.5965	4.5995
↓	62.5	↓	1.9805	9.5871	2.4440	4.6730
↓	65.0	↓	2.0380	9.3168	2.2932	4.7403
↓	67.5	↓	2.0908	9.0814	2.1452	4.8013
136	60.0	1.6434	1.8588	4.9780	2.5543	4.5271
↓	62.5	↓	1.9187	4.8228	2.4043	4.5994
↓	65.0	↓	1.9743	4.6870	2.2560	4.6656
↓	67.5	↓	2.0254	4.5687	2.1104	4.7256

TABLE III
EFFECTS OF SHOCK ANGLE ON TURBULENT BOUNDARY-LAYER PARAMETERS AT THE CENTERLINE LOCATION z/L = 0.74 FOR THE NASA LRC-SB DELTA WING AT 60-DEG ANGLE OF ATTACK UNDER AEDC-VKF TUNNEL F RUN NO. 3648 CONDITIONS

Time, msec	θ_{shock}, deg	$\dot{q}_w$, Btu/ft^2 - sec	$g'(\eta = 0)$	$C_{f_\infty, z} \times 10^3$	$f''(\eta = 0)$	$\delta_z^* \times 10^3$, in.	$\theta_{m,z} \times 10^3$, in.
60	60.0	91.3562	1.0885	6.1057	2.1083	6.0180	11.9098
↓	62.5	86.5869	1.0169	5.4284	1.9642	5.3675	11.7502
↓	65.0	82.3012	0.9541	4.8261	1.8342	4.6092	11.1022
↓	67.5	77.9435	0.8931	4.2626	1.7136	4.0188	10.7180
136	60.0	47.9264	0.8567	6.7142	1.6999	7.0165	13.2571
↓	62.5	45.0974	0.7947	5.9332	1.5790	5.9233	12.4617
↓	65.0	43.3032	0.7532	5.3215	1.4859	5.4051	12.3122
↓	67.5	41.1089	0.7068	4.7111	1.3923	4.7122	11.7949

TABLE IV
EFFECTS OF WALL TEMPERATURE RATIO ON WINDWARD CENTERLINE LAMINAR BOUNDARY-LAYER PARAMETERS

$T_w/T_{o,\infty}$	$\dot{q}_w$, Btu/ft^2 - sec	$St_\infty \times 10^3$	$C_{f\infty,z} \times 10^3$	δ_z, in.	δ^*_z, in.	$\theta_{m,z}$, in.
0.10	3.693	1.350	2.046	0.0204	0.00556	0.00270
0.20	3.280	1.349	2.075	0.0220	0.00754	0.00260
0.30	2.842	1.336	2.095	0.0234	0.00936	0.00251
0.40	2.389	1.310	2.109	0.0252	0.0110	0.00244
0.50	1.927	1.268	2.119	0.0264	0.0126	0.00237
0.60	1.459	1.201	2.128	0.0276	0.0141	0.00231
0.70	0.987	1.082	2.134	0.0288	0.0155	0.00225
0.80	0.511	0.840	2.140	0.0299	0.0168	0.00219
0.90	0.0322	0.106	2.144	0.0312	0.0181	0.00214

MDAC Orbiter at α = 30 deg and Body Station z/L = 0.5
AEDC-VKF Tunnel B, M_∞ = 8.0, Re_∞/ft = 3.74 x 10^6, L = 21.35 in.
Conical Inviscid Edge Conditions

TABLE V
EFFECTS OF WALL TEMPERATURE RATIO ON WINDWARD CENTERLINE TURBULENT BOUNDARY-LAYER PARAMETERS

$T_w/T_{o,\infty}$	$\dot{q}_w$, Btu/ft^2 - sec	$St_\infty \times 10^3$	$C_{f_\infty, z} \times 10^3$	δ_z, in.	δ_z^*, in.	$\theta_{m,z}$, in.
0.10	16.446	6.014	9.164	0.133	0.0255	0.0136
0.20	14.505	5.967	9.180	0.136	0.0313	0.0134
0.30	12.188	5.730	8.928	0.139	0.0350	0.0127
0.40	10.003	5.486	8.695	0.141	0.0394	0.0123
0.50	7.905	5.203	8.456	0.143	0.0437	0.0119
0.60	5.854	4.817	8.137	0.145	0.0477	0.0115
0.70	3.947	4.330	7.866	0.146	0.0487	0.0106
0.80	2.173	3.576	7.680	0.146	0.0510	0.0102
0.90	0.476	1.567	7.509	0.147	0.0534	0.00977

MDAC Orbiter at α = 30 deg and Body Station z/L = 0.5
AEDC-VKF Tunnel B, M_∞ = 8.0, Re_∞/ft = 3.74 x 10^6, L = 21.35 in.
Conical Inviscid Edge Conditions

TABLE VI
EFFECTS OF WALL TEMPERATURE RATIO ON MDAC TRANSITION PARAMETER

$T_w/T_{o,\infty}$	$TP = \frac{Re_{e,\theta_{m,z}}/M_{e,z}}{[Re_{e,z}/ft]^{0.2}}$
0.10	12.826
0.20	12.365
0.30	11.950
0.40	11.580
0.50	11.251
0.60	10.961
0.70	10.685
0.80	10.420
0.90	10.187

MDAC Orbiter at α = 30 deg and Body Station z/L = 0.5
AEDC-VKF Tunnel B, M_∞ = 8.0, $Re_\infty/ft = 3.74 \times 10^6$, L = 21.35 in.
Conical Inviscid Edge Conditions
$M_{e,z}$ = 3.021, $Re_{e,z}/ft = 3.511 \times 10^6$

APPENDIX III
IMPLICIT FINITE-DIFFERENCE SOLUTION OF GOVERNING BOUNDARY-LAYER EQUATIONS

The governing turbulent boundary-layer equations for flow over an infinite extent body as derived in Section 2.6 of the present report form a set of coupled, nonlinear, parabolic, partial differential equations with the transformed coordinates ξ and η as the independent variables. For completeness, these governing equations (Eqs. (38), (39), and (40)) are repeated below with primes denoting partial differentiation with respect to the η-coordinate:

x - MOMENTUM

$$\ell^* f''' + \left[\frac{\partial \ell^*}{\partial \eta} + f\right] f'' + \beta[\theta - (f')^2] = 2\xi\left[f' \frac{\partial f'}{\partial \xi} - f'' \frac{\partial f}{\partial \xi}\right] \tag{III-1}$$

z - MOMENTUM

$$\ell^* c'' + \left[\frac{\partial \ell^*}{\partial \eta} + f\right] c' = 2\xi\left[f' \frac{\partial c}{\partial \xi} - c' \frac{\partial f}{\partial \xi}\right] \tag{III-2}$$

ENERGY

$$\left(\frac{\ell^{**}}{Pr}\right) g'' + \left[\frac{\partial}{\partial \eta}\left(\frac{\ell^{**}}{Pr}\right) + f\right] g' + \Omega' = 2\xi\left[f' \frac{\partial g}{\partial \xi} - g' \frac{\partial f}{\partial \xi}\right] \tag{III-3}$$

with the definitions

$$f' = \frac{\bar{u}}{U_e} \tag{III-4}$$

$$c = \frac{\bar{w}}{W_e} \tag{III-5}$$

$$g = \frac{\bar{H}}{H_e} \tag{III-6}$$

$$\theta = \frac{\rho_e}{\bar{\rho}} = \frac{\bar{T}}{T_e} \tag{III-7}$$

$$\ell = \frac{\bar{\rho}\mu}{\rho_e \mu_e} \tag{III-8}$$

$$\ell^* = \ell\left[1 + \frac{\epsilon}{\mu}\right] \tag{III-9}$$

$$\ell^{**} = \ell\left[1 + \frac{\epsilon}{\mu}\,\frac{Pr}{Pr_t}\right] \tag{III-10}$$

$$\beta = \frac{2\xi}{U_e}\,\frac{dU_e}{d\xi} \tag{III-11}$$

$$\Omega = \ell\left[\frac{\epsilon}{\mu}\left(1 - \frac{1}{Pr_t}\right) + \left(1 - \frac{1}{Pr}\right)\right]\left[\frac{U_e^2}{H_e}\, f'f'' + \frac{W_e^2}{H_e}\, cc'\right] \tag{III-12}$$

The boundary conditions are:

MOMENTUM

$$\left.\begin{aligned} f(\xi,\eta = 0) &= 0 \\ f'(\xi,\eta = 0) &= 0 \\ \lim_{\eta\to\infty} f'(\xi,\eta) &= 1 \end{aligned}\right\} \tag{III-13}$$

$$\left.\begin{aligned} c(\xi,\eta = 0) &= 0 \\ \lim_{\eta\to\infty} c(\xi,\eta) &= 1 \end{aligned}\right\} \tag{III-14}$$

ENERGY

$$\left.\begin{aligned} g(\xi,\eta = 0) &= \frac{H_w}{H_e} = \frac{h_w}{H_e} = g_w \\ \lim_{\eta\to\infty} g(\xi,\eta) &= 1 \end{aligned}\right\} \tag{III-15}$$

Following the approach by Blottner (Ref. 106) and Davis (Ref. 107) the momentum and energy equations (III-1, -2, and -3) are rewritten in "standard" form for a parabolic partial differential equation as

$$\frac{\partial^2 W}{\partial \eta^2} + a_1 \frac{\partial W}{\partial \eta} + a_2 W + a_3 + a_4 \frac{\partial W}{\partial \xi} = 0 \qquad \text{(III-16)}$$

where W = f′ for the x-momentum equation, W = c for the z-momentum equation, and W = g for the energy equation. Using Eqs. (III-1, -2, and -3), one finds the coefficients a_1 through a_4 in linearized form:

x-MOMENTUM

$$a_1 = \frac{\frac{\partial \ell^*}{\partial \eta} + f + 2\xi \frac{\partial f}{\partial \xi}}{\ell^*} \qquad \text{(III-17)}$$

$$a_2 = \frac{-\beta f'}{\ell^*} \qquad \text{(III-18)}$$

$$a_3 = \frac{\beta \theta}{\ell^*} \qquad \text{(III-19)}$$

$$a_4 = \frac{-2\xi f'}{\ell^*} \qquad \text{(III-20)}$$

z-MOMENTUM

$$a_1 = \frac{\frac{\partial \ell^*}{\partial \eta} + f + 2\xi \frac{\partial f}{\partial \xi}}{\ell^*} \qquad \text{(III-21)}$$

$$a_2 = 0 \qquad \text{(III-22)}$$

$$a_3 = 0 \qquad \text{(III-23)}$$

$$a_4 = \frac{-2\xi f'}{\ell^*} \qquad \text{(III-24)}$$

ENERGY

$$a_1 = \frac{\frac{\partial}{\partial \eta}\left(\frac{\ell^{**}}{Pr}\right) + f + 2\xi \frac{\partial f}{\partial \xi}}{\left(\frac{\ell^{**}}{Pr}\right)} \qquad \text{(III-25)}$$

$$a_2 = 0 \tag{III-26}$$

$$a_3 = \frac{\Omega'}{\left(\frac{\ell^{**}}{Pr}\right)} \tag{III-27}$$

$$a_4 = \frac{-2\xi f'}{\left(\frac{\ell^{**}}{Pr}\right)} \tag{III-28}$$

The η derivatives in Eq. (III-16) are replaced with finite-difference quotients which allow variable grid spacing in the η direction in order to concentrate grid points in the region near the body surface where the dependent variables change most rapidly. The derivative in the ξ direction in Eq. (III-16) is handled in the usual manner as a two-point backward difference between points (m+1, n) and (m, n), whereas all η derivatives are evaluated at point (m+1, n) according to the grid mesh shown below.

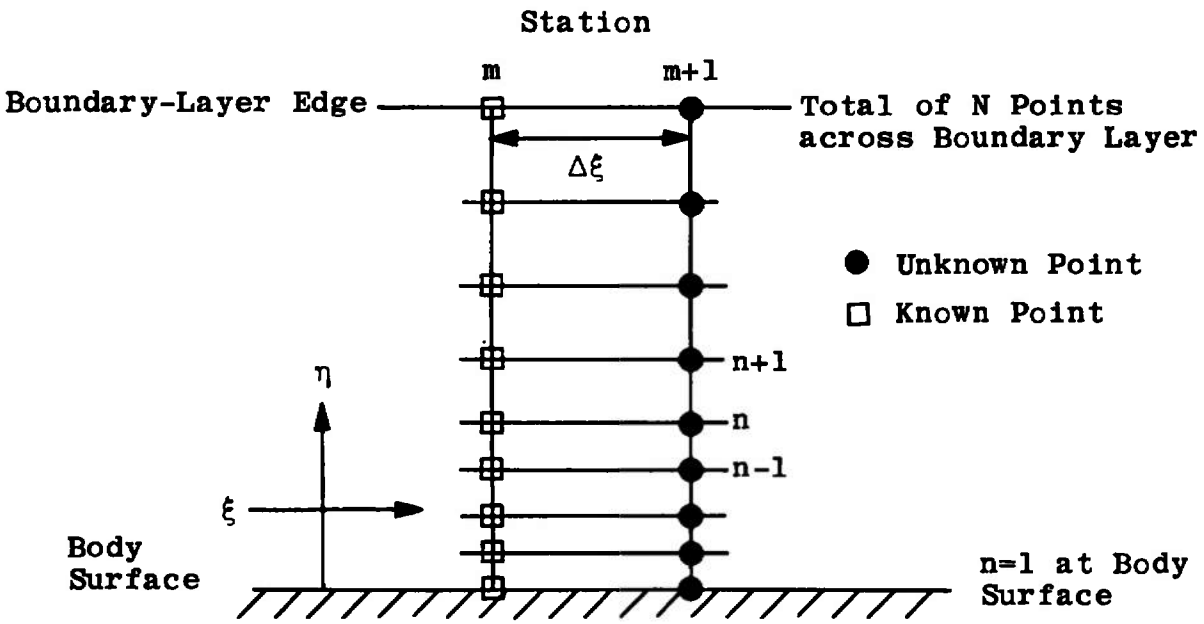

The solution is assumed to be known at point (m, n) and unknown at point (m+1, n) so that the finite-difference scheme to be constructed will be implicit in nature. The finite-difference replacements for the derivatives are as follows (see Appendix IV of Ref. 34 for derivation):

$$\left[\frac{\partial^2 W}{\partial \eta^2}\right]_{m+1,n} = \frac{2[W_{n+1} + KW_{n-1} - (1+K)W_n]_{m+1}}{D_2} \tag{III-29}$$

$$\left[\frac{\partial W}{\partial \eta}\right]_{m+1,n} = \frac{[W_{n+1} - K^2 W_{n-1} - (1-K^2)W_n]_{m+1}}{D_1} \tag{III-30}$$

$$\left[\frac{\partial W}{\partial \xi}\right]_{m+1,n} = \frac{W_{m+1,n} - W_{m,n}}{\Delta \xi} \tag{III-31}$$

where

$$D_1 = (\eta_{n+1} - \eta_n) + K^2(\eta_n - \eta_{n-1}) \tag{III-32}$$

$$D_2 = (\eta_{n+1} - \eta_n)^2 + K(\eta_n - \eta_{n-1})^2 \tag{III-33}$$

$$K = \frac{\eta_{n+1} - \eta_n}{\eta_n - \eta_{n-1}} \text{ (constant)} \tag{III-34}$$

$$\zeta = \eta_2 - \eta_1 \text{ (constant)} \tag{III-35}$$

The finite-difference form of Eq. (III-16) becomes, upon substitution of Eqs. (III-29, -30, and -31),

$$\bar{A}_n W_{m+1,n+1} + \bar{B}_n W_{m+1,n} + \bar{C}_n W_{m+1,n-1} = \bar{D}_n \tag{III-36}$$

where

$$\bar{A}_n = \frac{2}{D_2} + \frac{a_1}{D_1} \tag{III-37}$$

$$\bar{B}_n = \frac{-2(1+K)}{D_2} - \frac{a_1(1-K^2)}{D_1} + a_2 + \frac{a_4}{\Delta \xi} \tag{III-38}$$

$$\bar{C}_n = \frac{2K}{D_2} - \frac{K^2 a_1}{D_1} \tag{III-39}$$

$$\bar{D}_n = -a_3 + \frac{a_4 W_{m,n}}{\Delta \xi} \tag{III-40}$$

For Eq. (III-36) to be linear, the coefficients $\bar{A}_n$, $\bar{B}_n$, $\bar{C}_n$, and $\bar{D}_n$ must be treated as known quantities at point n; more will follow on this subject later. The important point is that Eq. (III-36) represents a set of simultaneous linear algebraic equations under this restriction.

Since the simultaneous linear algebraic equations resulting from Eq. (III-36) are of a special form (tridiagonal), an efficient method of solution on a digital computer is available from Richtmyer and Morton (Ref. 108, pp. 198-201 and 274-282). For this procedure the boundary conditions at the wall (n = 1) and the outer edge (n = N) must have specified values $W_{m+1,1}$ and $W_{m+1,N}$. Because of the special form of the Eq. (III-36), the relation

$$W_{m+1,n} = E_n W_{m+1,n+1} + e_n, \quad 2 \leq n \leq N-1 \tag{III-41}$$

exists where

$$E_2 = \frac{-\bar{A}_2}{\bar{B}_2} \tag{III-42}$$

$$e_2 = \frac{\bar{D}_2 - \bar{C}_2 W_{m+1,1}}{\bar{B}_2} \tag{III-43}$$

$$\left.\begin{aligned} E_n &= \frac{-\bar{A}_n}{\bar{B}_n + \bar{C}_n E_{n-1}} \qquad \text{(III-44)} \\ e_n &= \frac{\bar{D}_n - \bar{C}_n e_{n-1}}{\bar{B}_n + \bar{C}_n E_{n-1}} \qquad \text{(III-45)} \end{aligned}\right\} \quad 3 \leq n \leq N-1$$

The quantities E_n and e_n are computed from Eqs. (III-42) through (III-45) starting with n = 2 and progressing to n = N-1. The solution $W_{m+1,n}$ is then obtained by evaluating Eq. (III-41) from n = N-1 to n = 2. Knowing the distribution of f' and θ across the boundary layer from the above procedure, the transformed stream function f is evaluated from

$$f(\xi,\eta) = \int_0^{\eta} f'(\xi,\eta)\, d\eta \tag{III-46}$$

where the integral is numerically integrated using the well-known trapezoidal rule, viz.,

$$f(\xi,\eta = \eta_n) = \sum_{i=2}^{n} [f'(\xi,\eta = \eta_i) + f'(\xi,\eta = \eta_{i-1})] D_i \tag{III-47}$$

with

$$D_i = \frac{\eta_i - \eta_{i-1}}{2} \tag{III-48}$$

Inversion from the transformed (ξ, η) plane to the physical (x, y) plane is, from Eq. (63),

$$y = \frac{\sqrt{2\xi}}{\rho_e U_e} \int_0^{\eta} \frac{\rho_e}{\bar{\rho}} \, d\eta \tag{III-49}$$

where

$$\frac{\rho_e}{\bar{\rho}} = \frac{\bar{T}}{T_e} = \theta \tag{III-50}$$

because of the constancy of static pressure across the boundary layer. Again using the trapezoidal rule method of numerical integration yields

$$y_n = \frac{\sqrt{2\xi}}{\rho_e U_e} \sum_{i=2}^{n} [\theta(\xi,\eta = \eta_i) + \theta(\xi,\eta = \eta_{i-1})] D_i \tag{III-51}$$

with D_i given by Eq. (III-48). The relationship between ξ and x is determined from integration of Eq. (31)

$$\xi = \int_0^x \rho_e \mu_e U_e \, dx \tag{III-52}$$

using trapezoidal rule numerical integration to advance from station m to station m+1, i. e.,

$$\xi_{m+1} = \xi_m + [(\rho_e \mu_e U_e)_m + (\rho_e \mu_e U_e)_{m+1}] \frac{\Delta x}{2} \tag{III-53}$$

where Δx is the x-direction step size integration increment. For the present work the x-direction step size was determined by dividing the total x-distance into 40 equally spaced Δx increments. Experience with varying this increment has indicated that the above choice is adequate under the present flow conditions.

The mathematical basis of the above tridiagonal matrix procedure applied to the solution of boundary-layer problems is from Flügge-Lotz and Blottner (Ref. 109). The present application differs from their original work in one important aspect: the linearized difference equations herein are uncoupled and solved separately. In Flügge-Lotz and Blottner's approach, the difference equations remain coupled and require additional machine storage and manipulations for solution. With the present uncoupled approach, the difference equations are iterated to

convergence at each station along the body so that one must pay the price of iteration; this procedure is how the linearizing coefficients α_1 through α_4 are evaluated at each station using the results of the previous iteration. Iteration at a given station is continued until successive values of f , c, and g differ by less than 0.10 percent from the corresponding value of the preceding cycle. Typically, about three to eight iterations per station are required for both laminar and turbulent cases with the number of iterations per station increasing as the pressure gradient parameter β increases. By use of the above procedure the final solution obtained at each station is exact in the sense that it represents a converged iterated solution to the governing nonlinear partial differential equations written in finite-difference form.

The variable grid mesh used in the present work is taken from Smith and Cebeci (Ref. 110). The various constants used herein are as follows:

$$N = 96$$

$$K = 1.063$$

$$\zeta = 0.010$$

Experience with varying these constants and observing their influence on the resultant numerical solution has indicated that the above choices are adequate under the present flow conditions. These values may not be satisfactory, however, for other body geometries and flow conditions; thus, the influence of the variable grid mesh constants should be ascertained for each new investigation.

Evaluation of heat-transfer rate and shear stress at the body surface requires numerical determination of the wall derivatives $g'(\xi,\eta = 0)$, $c'(\xi,\eta = 0)$, and $f''(\xi,\eta = 0)$, since

$$\dot{q}_w \propto g'(\xi,\eta = 0)$$

$$\tau_{w,x} \propto f''(\xi,\eta=0)$$

$$\tau_{w,z} \propto c'(\xi,\eta=0)$$

from Eqs. (59), (61), and (62). Because of the variable grid spacing in the η-direction discussed previously, the wall derivatives are evaluated in the present work by application of the three-point Lagrangian interpolation formula (Ref. 111, pp. 71-77) evaluated according to the following diagram:

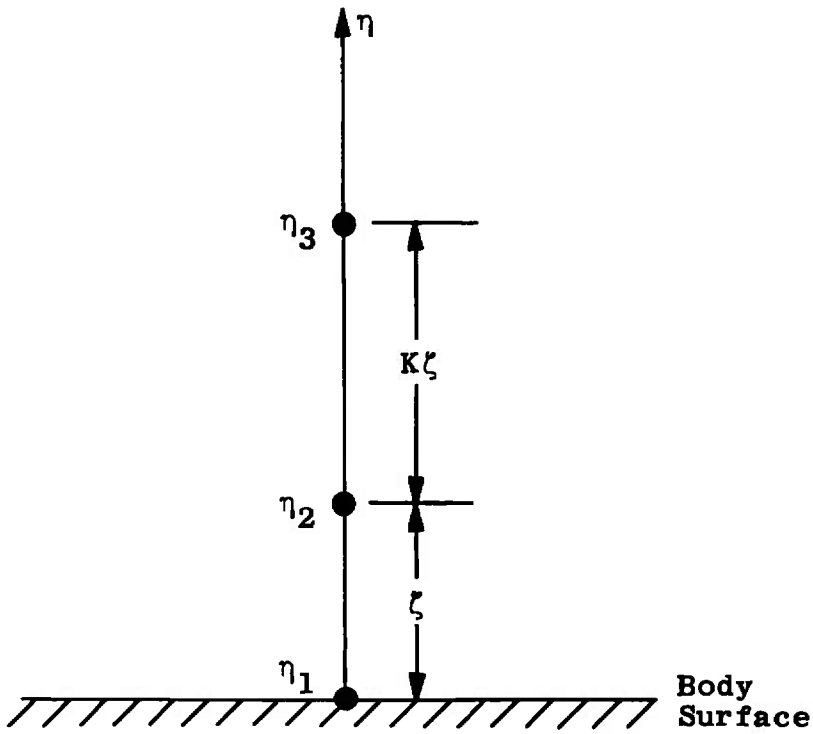

which yields, at station m+1,

$$f''(\eta=0) = \zeta[B_1(2+K)f'_{\eta_1} + B_2(1+K)f'_{\eta_2} + B_3 f'_{\eta_3}] \quad \text{(III-54)}$$

$$c'(\eta=0) = \zeta[B_1(2+K)c_{\eta_1} + B_2(1+K)c_{\eta_2} + B_3 c_{\eta_3}] \quad \text{(III-55)}$$

$$g'(\eta=0) = \zeta[B_1(2+K)g_{\eta_1} - B_2(1+K)g_{\eta_2} + B_3 g_{\eta_3}] \quad \text{(III-56)}$$

where

$$B_1 = \frac{-1}{\zeta^2(1+K)} \quad \text{(III-57)}$$

$$B_2 = \frac{+1}{K\zeta^2} \quad \text{(III-58)}$$

$$B_3 = \frac{-1}{\zeta^2 K(1+K)} \quad \text{(III-59)}$$

and

$$f'_{\eta_i} = f'(\eta=\eta_i) \quad \text{(III-60)}$$

$$c_{\eta_i} = c(\eta = \eta_i) \tag{III-61}$$

$$g_{\eta_i} = g(\eta = \eta_i) \tag{III-62}$$

with i = 1, 2, 3. The parameters K and ξ are defined by Eqs. (III-34) and III-35), respectively. The use of the three-point Lagrangian interpolation formula for the wall derivatives is consistent with the formulation of the variable grid spacing derivatives discussed in Appendix IV of Ref. 34 and follows the work of Smith and Cebeci (Ref. 110, Appendix C).

Along the centerline of the body where $\xi = 0$ since x = 0, the governing boundary-layer equations (III-1), (III-2), and (III-3) reduce to the following ordinary, nonlinear, differential equations:

x-MOMENTUM

$$\ell^* f''' + \left[\frac{\partial \ell^*}{\partial \eta} + f\right] f'' + \beta[\theta - (f')^2] = 0 \tag{III-63}$$

z-MOMENTUM

$$\ell^* c'' + \left[\frac{\partial \ell^*}{\partial \eta} + f\right] c' = 0 \tag{III-64}$$

ENERGY

$$\left(\frac{\ell^{**}}{Pr}\right) g'' + \left[\frac{\partial}{\partial \eta}\left(\frac{\ell^{**}}{Pr}\right) + f\right] g' + \Omega' = 0 \tag{III-65}$$

with the boundary conditions (III-13) through (III-15). In order to obtain starting profiles for the finite-difference scheme to march downstream, Eqs. (III-63), (III-64), and (III-65) are solved in the following manner by using the tridiagonal matrix procedure described previously. Along the centerline of the body, $\xi = 0$ so that $\alpha_4 = 0$ in both of the momentum equations, as well as the energy equation; in addition, the term containing ξ in α_1 of both the momentum and energy equations vanishes. Furthermore, $\beta = 1$ at $\xi = 0$ under the restriction that

$$U_e \approx \left[\frac{dU_e}{dx}\right]_{x=0} x$$

near x = 0. Initial guesses for f', c, and g are input to the analysis as

$$f_I' = 1 - \exp(-\eta) \tag{III-66}$$

$$c_I = f_I' \tag{III-67}$$

$$g_I = g_w + (1 - g_w) f_I' \tag{III-68}$$

where the subscript I denotes the initial approximation. The equations are then iterated to convergence in the same manner described previously; an averaging scheme is used to speed convergence. Typically, about 10 to 20 iterations are required to generate a converged initial solution for a laminar boundary layer. On the order of approximately 60 iterations are required for a converged turbulent boundary-layer solution.

By the use of the above procedures the numerical solution of any two-point boundary-value problem governed by either linear or nonlinear ordinary differential equations, as well as sets of coupled parabolic partial differential equations (either linear or nonlinear) is reduced to subroutine status on a digital computer in that only the coefficients α_1 through α_4 must be defined in conjunction with the required boundary conditions for each new problem. Based on experience with analyses of this type, the use of the iterative tridiagonal matrix approach where applicable is highly recommended.

APPENDIX IV
FORTRAN 63 SOURCE DECK LISTING OF STAGNATION LINE YAWED BLUNT-BODY COMPRESSIBLE BOUNDARY-LAYER PROGRAM SLYBBCBL

```
      PROGRAM SLYBBCBL
C * * * * * * * * * * * * * * * * * * * * * * * * * * * * * * * * * * * * *
C *                              STAGNATION LINE                           *
C *    INFINITE YAWED BLUNT-BODY COMPRESSIBLE BOUNDARY-LAYER PROGRAM       *
C *    WRITTEN IN FORTRAN 63 FOR USE ON A CDC 1604-B DIGITAL COMPUTER      *
C *                                   BY                                   *
C *    DR. JOHN C. ADAMS, JR., ARO, INC., SUPERVISOR, PROJECT SUPPORT      *
C *    AND SPECIAL STUDIES SECTION, AERODYNAMICS PROJECTS BRANCH,          *
C *    AERODYNAMICS DIVISION, VON KARMAN GAS DYNAMICS FACILITY, AEDC.      *
C * * * * * * * * * * * * * * * * * * * * * * * * * * * * * * * * * * * * *
C *                                REFERENCES                              *
C *         (1)  KALPS, K. AND KELTNER, G.  LAMINAR COMPRESSIBLE BOUNDARY  *
C *    LAYER ON A YAWED INFINITE WING.  DOUGLAS AIRCRAFT DIVISION REPORT    *
C *    NO. LB 32706, MARCH 1967.                                           *
C *         (2)  HUNT, J.L., BUSHNELL, D.M., AND BECKWITH, I.E.  FINITE-   *
C *    DIFFERENCE ANALYSIS OF THE COMPRESSIBLE TURBULENT BOUNDARY LAYER     *
C *    ON A BLUNT SWEPT SLAB WITH LEADING-EDGE BLOWING.  PAPER NO. 19 IN    *
C *    ANALYTIC METHODS IN AIRCRAFT AERODYNAMICS, NASA SP-228, 1970.       *
C *    SEE ALSO NASA TN D-6203, MARCH 1971.                                *
C *         (3)  ADAMS, J.C., JR.  IMPLICIT FINITE-DIFFERENCE ANALYSIS     *
C *    OF COMPRESSIBLE LAMINAR, TRANSITIONAL, AND TURBULENT BOUNDARY       *
C *    LAYERS ALONG THE WINDWARD STREAMLINE OF A SHARP CONE AT INCIDENCE.   *
C *    AEDC-TR-71-235, DECEMBER 1971.                                      *
C * * * * * * * * * * * * * * * * * * * * * * * * * * * * * * * * * * * * *
C *    GENERALIZED ITERATIVE IMPLICIT FINITE-DIFFERENCE METHOD OF INTEGRATION *
C *    FOR COUPLED NONLINEAR ORDINARY DIFFERENTIAL EQUATIONS OF SECOND ORDER *
C *    WITH TWO-POINT (SPLIT-END) PRESCRIBED BOUNDARY CONDITIONS           *
C * * * * * * * * * * * * * * * * * * * * * * * * * * * * * * * * * * * * *
      COMMON N,NEQ,W(300, 5),WOLD(300, 5),CAPE(300, 5),SMALLE(300, 5),
     1       A(10),B(10),C(10),D(10),WALLBC(10),F(10),H(10),OEBC(10),
     2       DETA,BETA
      COMMON /DISMCH/ DSTARINT,THMOMINT
      COMMON /DIST/ XDIST(505),PEDIST(505),UEDIST(505),XMAX,X,POP,TOP,R,
     1              GAMMA,TERMQDOT,TERMY,PE,RHOE,PEPOPX,DX,RNOSE,VISMUE,
     2              DUEDX,RHOINF,VELINF,TERMCFX,TERMCFZ,TERMEV
      COMMON /EDDYVIS/ EV(300),ELM(300),ELE(300),OELM(300),DELE(300)
      COMMON /STORE/ FINT(300),WO(300, 5),ANGLE(300),THETAINT(300)
      COMMON/TRANS/ TWALL,TE,SUTHER,TSTAG,UE,WE,CP,PR,XI,DELXI,NEND,NPTS
      COMMON /VARGS/ ETA(300),AK,AK2,TURB,KML,LAMBDA,ASTAR,PRT,VISCON
      COMMON /VIS/ THETA(300),EL(300),ETERM(300),DEL(300),DETERM(300)
      DIMENSION HEADER(12)
      TYPE INTEGER HEADER
      TYPE REAL KML,LAMBDA
C           INPUT PRESENT CASE DATA, THEN SET INITIAL CONSTANTS
C           AND INTEGRATION DATA
  999 X = 0.0
      XI = 0.0
      DX = 0.0
      ITURB = 0  $  TURB = 0.0
      PI = 3.1415926535
      READ(5,800) (HEADER(I), I=1,10)
      READ(5,801) FSMACH,PINF,TINF,TWALL,YAWANGLE,XSTAR,RNOSE
      IF ( EOF,5 ) 9999,5
    5 READ(5,801) XTRANS,POP,WE,DUEDX,VISCON
      READ(5,801) GAMMA,PR,CP,SUTHER,KML,LAMBDA,ASTAR,PRT
      R = CP*(GAMMA-1.0)/GAMMA
```

```
      POPIN = POP  $  DUEDXIN = DUEDX
C           MAXIMUM NUMBER OF ALLOWED ITERATION CYCLES
      ITERMAX = 150
C           TOTAL NUMBER OF DIFFERENTIAL EQUATIONS TO BE SOLVED
      NEQ = 3
C           PRINT EVERY POINT IN N-ARRAY PROFILES
      NPRINT = 1
C           TOTAL NUMBER OF N-POINTS ACROSS BOUNDARY LAYER
      NPTS = 96
      NENC = NPTS - 1
C           INITIAL ETA STEP-SIZE INCREMENT
      DETA1 = 0.0100
C           ETA GRID STEP-SIZE MULTIPLICATION FACTOR
      AK = 1.0630  $  AK2 = AK*AK
C           SOLUTION CONVERGENCE CRITERION
      EPS = 0.0010
C           SOLUTION WEIGHING FACTOR
      RELAXF = 0.50
C           COMPUTE FREE-STREAM QUANTITIES
      RHOINF = PINF/(R*TINF)
      VELINF = FSMACH*SQRTF(GAMMA*R*TINF)
      TSTAG = TINF*(1.0+((GAMMA-1.0)/2.0)*FSMACH*FSMACH)
      HSTAG = CP*TSTAG
      FSRFF = (((GAMMA+1.0)*FSMACH*FSMACH/2.0)**(GAMMA/(GAMMA-1.0)))
     1 *(((GAMMA+1.0)/(2.0*GAMMA*FSMACH*FSMACH-GAMMA+1.0))
     2 **(1.0/(GAMMA-1.0)))
      ALPHA = 90.0 - YAWANGLE
      THETASK = 90.0 - YAWANGLE
      GWALL = TWALL/TSTAG
C           HYPERSONIC SIMILARITY PARAMETER
      HSP = FSMACH*COSF(YAWANGLE*PI/180.0)  $  XK = HSP
      IF ( POP ) 8,10,20
C           CONICAL INVISCID FLOW FOLLOWING
C           HYPERSONIC SMALL-DISTURBANCE THEORY
    8 TERMK = ((GAMMA+1.0)*XK*XK+2.0)/((GAMMA-1.0)*XK*XK+2.0)
      CPM = 1.0 + TERMK*LOGF(((GAMMA+1.0)/2.0) + (1.0/(XK*XK)))
      PEOPINF = 1.0 + (GAMMA*CPM*XK*XK/2.0)
      XMN = XK*SQRTF(((GAMMA+1.0)/2.0) + (1.0/(XK*XK)))
      THETASK = ASINF(COSF(YAWANGLE*PI/180.0)*XMN/XK)*180.0/PI
      PSOPINF = (2.0*GAMMA*XMN*XMN-GAMMA+1.0)/(GAMMA+1.0)
      TSOTINF = ((2.0*GAMMA*XMN*XMN-GAMMA+1.0)*((GAMMA-1.0)*XMN*XMN+2.0)
     1          )/((GAMMA+1.0)*(GAMMA+1.0)*XMN*XMN)
      TEOTINF = TSOTINF*((PEOPINF/PSOPINF)**((GAMMA-1.0)/GAMMA))
      POP = PEOPINF*PINF  $  TOP = TEOTINF*TINF
      WE = SQRTF(2.0*CP*(TSTAG-TOP))
      GO TO 22
C           YAWED CYLINDER WITH PARALLEL SHOCK INVISCID FLOW
   10 FSMN = FSMACH*COSF(YAWANGLE*PI/180.0)
      POP = PINF*(((GAMMA+1.0)*FSMN*FSMN/2.0)**(GAMMA/(GAMMA-1.0)))
     1 *(((GAMMA+1.0)/(2.0*GAMMA*FSMN*FSMN-GAMMA+1.0))**(1.0/(GAMMA-1.0)
     2 ))
      WE = VELINF*SINF(YAWANGLE*PI/180.0)
      THETASK = 90.0 - YAWANGLE
   20 CONTINUE
      TOP = TSTAG - (WE*WE/(2.0*CP))
   22 CONTINUE
```

```
C            COMPUTE INVISCID EDGE QUANTITIES
      BETA = 1.0  $  PEPOPX = 1.0
      PE = POP  $  TE = TOP  $  UE = 0.0  $  RHOE = PE/(R*TE)
      VISMUE = VISCON*(TE**1.50)/(TE+SUTHER)
      IF ( DUEDX ) 24,25,26
C            FLAT-FACED DISK STAGNATION POINT VELOCITY GRADIENT
   24 DUEDX = 0.78*SQRTF(GAMMA*R*TOP)/(2.0*XSTAR)
      GO TO 26
C            NEWTONIAN STAGNATION POINT VELOCITY GRADIENT
   25 DUEDX = SQRTF(2.0*(POP-PINF)/RHOE)/RNOSE
   26 CONTINUE
      TERMQDOT = SQRTF(RHOE*VISMUE*DUEDX)
      TERMY = SQRTF(VISMUE/(RHOE*DUEDX))
      TERMEV = SQRTF(DUEDX/(RHOE*VISMUE))
      TERMCFX = 0.0
      TERMCFZ = 2.0*SQRTF(RHOE*VISMUE*DUEDX)*WE/(RHOINF*VELINF*VELINF)
C            PRINT INPUT DATA FOR PRESENT CASE
      WRITE(6,911) (HEADER(I), I=1,10)
      IF ( X - XTRANS ) 28,27,27
   27 WRITE(6,905)
      GO TO 29
   28 WRITE(6,906)
   29 WRITE(6,913) FSMACH,PINF,TINF,TWALL,YAWANGLE,POP,TOP,TSTAG,WE,
     1             RNOSE,XSTAR,DUEDX,GWALL,ALPHA,THETASK
      WRITE(6,910)
      WRITE(6,914) CP,H,GAMMA,PR,SUTHER,VISCON,KML,LAMBDA,ASTAR,PRT
      IF ( POPIN ) 30,31,32
   30 WRITE(6,916)
      GO TO 33
   31 WRITE(6,917)
      GO TO 33
   32 WRITE(6,918)
   33 IF ( DUEDXIN ) 34,35,36
   34 WRITE(6,919)
      GO TO 37
   35 WRITE(6,920)
      GO TO 37
   36 WRITE(6,921)
C            SET BOUNDARY CONDITIONS
   37 DO 38 I=1,NEQ
      F(I) = 0.0
   38 H(I) = 0.0
      WALLBC(1) = 0.0                                                    WALL
      WALLBC(2) = 0.0                                                    WALL
      WALLBC(3) = GWALL                                                  WALL
      QEBC(1) = 1.0                                                      EDGE
      QEBC(2) = 1.0                                                      EDGE
      QEBC(3) = 1.0                                                      EDGE
      ETA(1) = 0.0                                                       WALL
C            NOMENCLATURE FOR PRESENT W-ARRAY STORAGE WITH N=1 TO N=NPTS
C            W(N,1) = U/UE      ( X-MOMENTUM EQUATION SOLUTION )
C            W(N,2) = W/WE      ( Z-MOMENTUM EQUATION SOLUTION )
C            W(N,3) = H/HE      ( ENERGY EQUATION SOLUTION )
      W(1,1) = WALLBC(1)  $  WOLD(1,1) = W(1,1)                          WALL
      W(1,2) = WALLBC(2)  $  WOLD(1,2) = W(1,2)                          WALL
      W(1,3) = WALLBC(3)  $  WOLD(1,3) = W(1,3)                          WALL
```

```
      W(NPTS,I) = CEBC(1)  $  WOLD(NPTS,1) = W(NPTS,I)                    EDGE
      W(NPTS,2) = CEBC(2)  $  WOLD(NPTS,2) = W(NPTS,2)                    EDGE
      W(NPTS,3) = CEBC(3)  $  WOLD(NPTS,3) = W(NPTS,3)                    EDGE
C           INITIAL PROFILE GUESS
      DETA = DETA1
      DO 40 I=2,NEND
      ETA(I) = ETA(I-1) + DETA
      DETA = AK*DETA
      W(I,1) = 1.0 - EXPF(-ETA(I))                                        U/UE
      W(I,2) = W(I,I)                                                     W/WE
      W(I,3) = WALLBC(3) + (1.0-WALLBC(3))*W(I,1)                         H/HE
C           INITIALIZE INITIAL PROFILES
      WOLD(I,1) = W(I,1)
      WOLD(I,2) = W(I,2)
      WOLD(I,3) = W(I,3)
      EV(I) = 0.0
      THETAINT(I) = 0.0
   40 CONTINUE
      ETA(NPTS) = ETA(NEND) + DETA
      ITER = I
C           CALCULATE MATRIX COEFFICIENTS FOR EACH N-POINT
C           ACROSS BOUNDARY LAYER
   50 N = I
      CALL VISC
   60 N = N + 1
      CALL ABCD
      IF ( N - NENC ) 60,70,70
C           CALCULATE NEW W-ARRAY PROFILES
   70 CALL SOLVE
C           TEST FOR CONVERGENCE OF SUCCESSIVE PROFILES
      DO 90 I=2,NEND
   77 DO 80 J=1,NEQ
      IF ( (ABSF(1.0-(WOLD(I,J)/W(I,J)))) - EPS ) 80,80,100
   80 CONTINUE
   90 CONTINUE
C           CONVERGENCE ATTAINED, CHECK FOR ONSET OF TURBULENT SOLUTION
      IF ( X - XTRANS ) 130,95,95
   95 IF ( ITURB ) 96,96,130
   96 TURB = 0.0050
      ITURB = 1  $  ITER = 1
C           CONVERGENCE NOT ATTAINED, WEIGH SOLUTION AND ITERATE
  100 ITER = ITER + 1
      DO 120 I=1,NPTS
      DO 110 J=I,NEQ
  110 WOLD(I,J) = (1.0-RELAXF)*WOLD(I,J) + RELAXF*W(I,J)
  120 CONTINUE
      IF ( ITER - ITERMAX ) 125,128,128
  125 GO TO 50
C           SOLUTION DID  N O T  CONVERGE IN ITERMAX CYCLES
  128 WRITE(6,904) ITERMAX
C           PRINT PRESENT CASE CONVERGED SOLUTION
  130 CONTINUE
      WRITE(6,911) (HEADER(I), I=1,10)
C           THREE-POINT NUMERICAL DERIVATIVE AT WALL
      DY1 = ETA(2)-ETA(1)
      B1 = -1.0/(DY1*DY1*(1.0+AK))
```

```
      B2 = +1.0/(DY1*DY1*AK)
      B3 = -1.0/(DY1*DY1*AK*(1.0+AK))
      FPPW = DY1*((B1*(2.0+AK)*W(1,1))+(B2*(1.0+AK)*W(2,1))+(B3*W(3,1)))
      CPW  = DY1*((B1*(2.0+AK)*W(1,2))+(B2*(1.0+AK)*W(2,2))+(B3*W(3,2)))
      GPW  = DY1*((B1*(2.0+AK)*W(1,3))+(B2*(1.0+AK)*W(2,3))+(B3*W(3,3)))
C           COMPUTE BOUNDARY-LAYER PARAMETERS
      QDOT = -HSTAG*TERMQDOT*EL(1)*GPW/(PR*778.26)
      STINF = -QDOT*778.26/(RHOINF*VELINF*CP*(TSTAG-TWALL))
      CFINFX = TERMCFX*EL(1)*FPPW  $  CFINFZ = TERMCFZ*EL(1)*CPW
      DSTARZ = TERMY*DSTARINT  $  THMOMZ = TERMY*THMOMINT
      REYFT = RHOE*WE/VISMUE  $  REYTHZ = REYFT*THMOMZ
      EDGEME = WE/SQRTF(GAMMA*R*TE)
      TRANSP = (REYTHZ/EDGEME)/(REYFT**0.20)
      HEATTC = -QDOT/(TSTAG-TWALL)
      THETAINT(NPTS) = THETAINT(NEND) + 0.50*(THETA(NPTS)+THETA(NEND))
     1                 * (ETA(NPTS)-ETA(NEND))
      SRN = X/RNOSE
C           PRINT PRESENT CASE INVISCID EDGE QUANTITIES
C           AND BOUNDARY-LAYER PARAMETERS
      IF ( X - XTRANS ) 132,131,131
  131 WRITE(6,905)
      GO TO 133
  132 WRITE(6,906)
  133 WRITE(6,903) X,XI,BETA,PEPOPX,SRN,UE,WE,PE,TE,RHOE,VISMUE,DUEDX,
     1             ITER
      WRITE(6,912) FPPW,CPW,GPW,QDOT,STINF,CFINFX,CFINFZ,HSP
      WRITE(6,915) DSTARZ,THMOMZ,REYFT,REYTHZ,EDGEME,TRANSP,HEATTC
      WRITE(6,901)
C           PRINT PRESENT CASE BOUNDARY-LAYER PROFILES
      DO 140 I=1,NPTS,NPRINT
      YFT = TERMY*THETAINT(I)
      BLMACH = WE*W(I,2)/SQRTF(GAMMA*R*TE*THETA(I))
      IF ( BLMACH - 1.010 ) 134,135,135
  134 BLRPF = (1.0+0.50*(GAMMA-1.0)*BLMACH*BLMACH)**(GAMMA/(GAMMA-1.0))
      GO TO 136
  135 BLRPF = (((GAMMA+1.0)*BLMACH*BLMACH/2.0)**(GAMMA/(GAMMA-1.0)))
     1 *(((GAMMA+1.0)/(2.0*GAMMA*BLMACH*BLMACH-GAMMA+1.0))
     2 **(1.0/(GAMMA-1.0)))
  136 PITOT = BLRPF*PE/(FSRPF*PINF)
      WRITE(6,902) ETA(I),YFT,W(I,1),W(I,2),W(I,3),THETA(I),BLMACH,
     1             PITOT,EV(I)
  140 CONTINUE
C           PRESENT CASE COMPLETED, READ IN NEXT CASE
      GO TO 999
  800 FORMAT(10A8)
  801 FORMAT(8E10.2)
  901 FORMAT(1H0,//,6X,3HETA,7X,5HY(FT),10X,4HU/UE,8X,4HW/WE,7X,5H M/ME,
     18X,4HT/TE,7X,5H MACH,7X,5HPITOT,7X,5HEV/MU, /)
  902 FORMAT(1F10.3,2X,1E12.5,8F12.5)
  903 FORMAT(2X,8HX (FT) =1E14.6,5X,4HXI =1E14.6,10X,6HBETA =1E14.6,5X,
     18HPE/POP =1E14.6,5X,6HS/RN =1E14.6,//,2X,13HUE (FT/SEC) =1E14.6,
     25X,13HWE (FT/SEC) =1E14.6,5X,14HPE (LBF/FT2) =1E14.6,5X,12HTE (DEG
     3 R) =1E14.6,//,2X,17HRHOE (SLUG/FT3) =1E14.6,5X,19HMUE (LBF-SEC/FT
     42) =1E14.6,5X,16HDUE/DX (1/SEC) =1E14.6,5X,12HITERATIONS =14, /)
  904 FORMAT(1H0,//,20X,57H*** WARNING *** THE ITERATION PROCESS DID NOT
     1 CONVERGE IN, I5, 2X,10HCYCLES ***, //)
```

```
  905 FORMAT(2X, 88HINFINITE YAWED BLUNT-BODY STAGNATION LINE COMPRESSIB
     1LE TURBULENT BOUNDARY-LAYER ANALYSIS, /)
  906 FORMAT(2X, 86HINFINITE YAWED BLUNT-BODY STAGNATION LINE COMPRESSIB
     1LE LAMINAR BOUNDARY-LAYER ANALYSIS, /)
  910 FORMAT(2X,43HTHERMALLY AND CALORICALLY PERFECT GAS MODEL, /)
  911 FORMAT(1H1,///,30X,10A8,////)
  912 FORMAT(2X,8HFPP(0) =1E14.6,5X,7HCP(0) =1E14.6,5X,7HGP(0) =1E14.6,
     110X, 6HQDOT =1E14.6,2X,13HBTU/(FT2-SEC),//,2X, 9HST(INF) =1E14.6,
     210X,10HCFX(INF) =1E14.6,10X,10HCFZ(INF) =1E14.6,10X,5HHSP =1E14.6,
     3 /)
  913 FORMAT(2X,25HFREE-STREAM MACH NUMBER =1E14.6,5X,16HPINF (LBF/FT2)
     1=1E14.6,5X,14HTINF (DEG R) =1E14.6,//,2X,15HTWALL (DEG R) =1E14.6,
     25X,17HYAW ANGLE (DEG) =1E14.6,5X,15HPOP (LBF/FT2) =1E14.6,//,2X,
     313HTOP (DEG R) =1E14.6,5X,15HTSTAG (DEG R) =1E14.6,5X,13HWE (FT/SE
     4C) =1E14.6,//,2X,18HNOSE RADIUS (FT) =1E14.6,5X,11H  X* (FT) =1E14
     5.6,5X,16HDUE/DX (1/SEC) =1E14.6,//,2X, 13HTWALL/TSTAG =1E14.6,5X,
     623HANGLE OF ATTACK (DEG) =1E14.6,5X, 19HSHOCK ANGLE (DEG) =1E14.6,
     7 ////)
  914 FORMAT(2X,3HCP=F8.2,1X,16HFT2/(SEC2-DEG R),3X,2HR=F8.2,1X,16HFT2/(
     1SEC2-DEG R),3X,6HGAMMA=1F7.4,3X,3HPR=1F7.4,3X,6HCSTAR=F8.2,1X,
     2 5HDEG R, // ,2X,19HVISCOSITY CONSTANT=1E12.4,1X, 25HLBF-SEC/(FT2-
     3SQRT(DEG R)), 3X,4HKML=1F7.4,3X,7HLAMBDA=1F7.4,3X,6HASTAR=1F7.3,
     4 3X,4HPHT=1F7.4, ////)
  915 FORMAT(2X,13HDELTA* (FT) =1E14.6,5X,15HTHETAMOM (FT) =1E14.6,5X,
     113HEDGE REY/FT =1E14.6,5X,18HEDGE REYTHETAMOM =1E14.6,//,
     22X,14HEDGE MACH NO =1E14.6,5X,40HMCDONNELL-DOUGLAS TRANSITION PARA
     3METER =1E14.6,5X,21H-QDOT/(TSTAG-TWALL) =1E14.6, /)
  916 FORMAT(2X, 67HCONICAL INVISCID FLOW FOLLOWING HYPERSONIC SMALL-DIS
     1TURBANCE THEORY, /)
  917 FORMAT(2X, 48HYAWED CYLINDER WITH PARALLEL SHOCK INVISCID FLOW, /)
  918 FORMAT(2X, 70HINVISCID CENTERLINE PRESSURE (POP) AND VELOCITY (WE)
     1 INPUT TO ANALYSIS, /)
  919 FORMAT(2X, 50HFLAT-FACED DISK STAGNATION POINT VELOCITY GRADIENT )
  920 FORMAT(2X, 44HNEWTONIAN STAGNATION POINT VELOCITY GRADIENT )
  921 FORMAT(2X, 60HSTAGNATION POINT VELOCITY GRADIENT (DUEDX) INPUT TO
     1ANALYSIS )
 9999 STOP
      END
```

```
      SUBROUTINE ABCD
CABCD       COMPUTES A, B, C, AND D MATRIX COEFFICIENTS WHICH ARE USED TO
C           COMPUTE RECURSION COEFFICIENTS FOR TRIDIAGONAL MATRIX SYSTEMS
      COMMON N,NEQ,W(300, 5),WOLD(300, 5),CAPE(300, 5),SMALLE(300, 5),
     1       A(10),B(10),C(10),D(10),WALLBC(10),F(10),H(10),OEBC(10),
     2       DETA,BETA
      COMMON /DISMOM/ USTARINT,THMOMINT
      COMMON /EDDYVIS/ EV(300),ELM(300),ELE(300),DELM(300),DELE(300)
      COMMON /STORE/ FINT(300),WO(300, 5),ANGLE(300),THETAINT(300)
      COMMON/TRANS/ TWALL,TE,SUTHER,TSTAG,UE,WE,CP,PR,XI,DELXI,NEND,NPTS
      COMMON /VARGS/ ETA(300),AK,AK2,TURB,KML,LAMBDA,ASTAR,PRT,VISCON
      COMMON /VIS/ THETA(300),EL(300),ETERM(300),DEL(300),DETERM(300)
      DIMENSION ALPHA(4,10)
      DA = ETA(N+1)-ETA(N)  $  DB = ETA(N)-ETA(N-1)
      DI = DA + AK2*DB  $  D2 = DA*DA + AK*DB*DB
      FP = WOLD(N,1)
C           NUMERICALLY INTEGRATE FPRIME AND THETA
C           USING TRAPEZOIDAL-RULE FORMULA
      IF ( N - 2 ) 10,10,20
   10 FINT(1) = 0.0  $  THETAINT(1) = 0.0
      DSTARINT = 0.0  $  THMOMINT = 0.0
   20 FINT(N) = FINT(N-1) + 0.50*(WOLD(N,1)+WOLD(N-1,1))*DB
      THETAINT(N) = THETAINT(N-1) + 0.50*(THETA(N)+THETA(N-1))*DB
      DSTARINT = DSTARINT + 0.50*(THETA(N)-WOLD(N,2)+THETA(N-1)
     1           -WOLD(N-1,2))*DB
      THMOMINT = THMOMINT + 0.50*(WOLD(N,2)-WOLD(N,2)*WOLD(N,2)
     1           +WOLD(N-1,2)-WOLD(N-1,2)*WOLD(N-1,2))*DB
C           ALPHAS FOR X-MOMENTUM EQUATION
      ALPHA(1,1) = (DELM(N) + FINT(N))/ELM(N)
      ALPHA(2,1) = -BETA*FP/ELM(N)
      ALPHA(3,1) = BETA*THETA(N)/ELM(N)
C           ALPHAS FOR Z-MOMENTUM EQUATION
      ALPHA(1,2) = ALPHA(1,1)
      ALPHA(2,2) = 0.0
      ALPHA(3,2) = 0.0
C           ALPHAS FOR ENERGY EQUATION
      ALPHA(1,3) = (DELE(N) + PR*FINT(N))/ELE(N)
      ALPHA(2,3) = 0.0
      ALPHA(3,3) = PR*DETERM(N)/ELE(N)
C           COMPUTE TRIDIAGONAL MATRIX COEFFICIENTS FOR EACH EQUATION
      DO 30 I=1,NEQ
      A(I) = 2.0/D2 + ALPHA(1,I)/DI
      B(I) = -2.0*(1.0+AK)/D2 - ALPHA(1,I)*(1.0-AK2)/DI + ALPHA(2,I)
      C(I) = 2.0*AK/D2 - AK2*ALPHA(1,I)/DI
   30 D(I) = -ALPHA(3,1)
C           COMPUTE RECURSION COEFFICIENTS FOR EACH EQUATION
      IF ( N - 2 ) 100,100,300
  100 DO 200 I=1,NEQ
      CAPE(2,I) = -(A(I)+C(I)*F(I))/(B(I)+C(I)*H(I))
  200 SMALLE(2,I) = (D(I)-C(I)*WALLBC(I))/(B(I)+C(I)*H(I))
      GO TO 9999
  300 DO 400 I=1,NEQ
      CAPE(N,I) = -A(I)/(B(I)+C(I)*CAPE(N-1,I))
  400 SMALLE(N,I) = (D(I)-C(I)*SMALLE(N-1,I))/(B(I)+C(I)*CAPE(N-1,I))
 9999 RETURN
      END
```

```
      SUBROUTINE VISC
CVISC       CALCULATES RHO*MU RATIO, T/TE, AND ENERGY EQUATION TERM
C           USING SUTHERLAND VISCOSITY LAW FOR LAMINAR TRANSPORT
C           AND TWO-LAYER (INNER-OUTER) EDDY VISCOSITY MODEL
C           FOR TURBULENT TRANSPORT
      COMMON N,NEQ,W(300, 5),WOLD(300, 5),CAPE(300, 5),SMALLE(300, 5),
     1       A(10),B(10),C(10),D(10),WALLBC(10),F(10),H(10),OEBC(10),
     2       DETA,BETA
      COMMON /DIST/ XDIST(505),PEDIST(505),UEDIST(505),XMAX,X,POP,TOP,R,
     1              GAMMA,TERMQDOT,TERMY,PE,RHOE,PEPOPX,OX,RNOSE,VISMUE,
     2              DUEOX,RHOINF,VELINF,TERMCFX,TERMCFZ,TERMEV
      COMMON /EDDYVIS/ EV(300),ELM(300),ELE(300),DELM(300),DELE(300)
      COMMON /STORE/ FINT(300),WO(300, 5),ANGLE(300),THETAINT(300)
      COMMON/TRANS/ TWALL,TE,SUTHER,TSTAG,UE,WE,CP,PR,XI,CELXI,NENO,NPTS
      COMMON /VARGS/ ETA(300),AK,AK2,TURB,KML,LAMBDA,ASTAR,PRT,VISCON
      COMMON /VIS/ THETA(300),EL(300),ETERM(300),OEL(300),DETERM(300)
      TYPE REAL KML,LAMBDA,MLI,MLO
C           SET WALL AND OUTER EDGE VALUES
      THETA(I) = TWALL/TE  $  THETA(NPTS) = 1.0
      EL(I) = ((1.0+SUTHER/TE)/(THETA(1)+SUTHER/TE))*SQRTF(THETA(1))
      EL(NPTS) = 1.0
      ETERM(1) = 0.0  $  ETERM(NPTS) = 0.0
      ELM(1) = EL(I)  $  ELM(NPTS) = EL(NPTS)
      ELE(1) = EL(1)  $  ELE(NPTS) = EL(NPTS)
      EV(1) = 0.0  $  EV(NPTS) = 0.0
      TURB = TURB*1.10
      IF ( TURB - 1.0 ) 525,525,520
  520 TURB = 1.0
C           DEFINE VARIOUS CONVENIENT TERMS FOR LATER USE
  525 TERM1 = TSTAG/TE
      TERM2 = UE*UE/(2.0*CP*TE)
      TERM3 = WE*WE/(2.0*CP*TE)
      TERM4 = SUTHER/TE
      TERM5 = 1.0 - 1.0/PR
      TERM6 = UE*UE/(CP*TSTAG)
      TERM7 = WE*WE/(CP*TSTAG)
      TERM8 = 1.0 - 1.0/PRT
C           LOCATE EDGE OF BOUNDARY LAYER
      VELE = SQRTF(UE*UE + WE*WE)
      DO 610 K=40,NENO
      VEL = SQRTF(UE*UE*WOLD(K,1)*WOLD(K,1)+WE*WE*WOLD(K,2)*WOLD(K,2))
      TEST = VEL/VELE
      IF ( TEST - 0.990 ) 605,605,615
  605 KEDGE = K
  610 CONTINUE
C           FAILED TO LOCATE EDGE, SOLUTION HAS BLOWN-UP,  S T O P  *****
      WRITE(6,901)
      STOP
  615 YL = TERMY*THETAINT(KEDGE)
C           CALCULATE RHO*MU RATIO, STATIC TEMPERATURE RATIO,
C           AND ENERGY EQUATION TERM ACROSS BOUNDARY LAYER
      DO 10 I=2,NENO
      DA = ETA(I+1)-ETA(I)  $  DB = ETA(I)-ETA(I-1)  $  D1 = DA+AK2*DB
C           STATIC TEMPERATURE RATIO (T/TE)
      THETA(I) = TERM1*WOLD(I,3) - TERM2*WOLD(I,1)*WOLD(I,1)
     1         - TERM3*WOLD(I,2)*WOLD(I,2)
```

```
C            RHO*MU RATIO FOR LAMINAR FLOW BASED ON SUTHERLAND VISCOSITY LAW
      EL(I) = ((1.0+TERM4)/(THETA(1)+TERM4))*SQRTF(THETA(I))
C            TWO-LAYER (INNER-OUTER) EDDY VISCOSITY MODEL
C            USING INVARIANT TURBULENCE APPROACH FOR GENERAL
C            THREE-DIMENSIONAL TURBULENT BOUNDARY-LAYER FLOWS
      FPP = (WOLD(I+1,1)-AK2*WOLD(I-1,1)-(1.0-AK2)*WOLD(I,1))/D1
      CPRIME = (WOLD(I+1,2)-AK2*WOLD(I-1,2)-(1.0-AK2)*WOLD(I,2))/D1
      VELGRAD = SQRTF(UE*UE*FPP*FPP + WE*WE*CPRIME*CPRIME)
      RHO = PE/(R*TE*THETA(I))
      VIS = VISCON*((TE*THETA(I))**1.50)/(TE*THETA(I)+SUTHER)
      Y = TERMY*THETAINT(I)
C            VAN DRIEST WALL DAMPING TERM EVALUATED USING
C            L O C A L  BOUNDARY-LAYER PROPERTIES
      DAMP = 1.0 - EXPF(-Y*SQRTF(RHO*RHO*VIS*TERMEV*(1.0+EV(1))*VELGRAD)
     1     / (VIS*ASTAR))
C            INNER LAYER MIXING LENGTH AND EDDY VISCOSITY RATIO
      ML1 = KML*Y*DAMP  $  EVI = RHO*RHO*ML1*ML1*TERMEV*VELGRAD/VIS
C            OUTER LAYER MIXING LENGTH AND EDDY VISCOSITY RATIO
      MLO = LAMBDA*YL  $  EVO = RHO*RHO*MLO*MLO*TERMEV*VELGRAD/VIS
      EV(I) = EVI*TURB
      IF ( EVI - EVO ) 630,630,620
  620 EV(I) = EVO*TURB
  630 CONTINUE
C            RHO*MU RATIO FOR MOMENTUM EQUATIONS
      ELM(I) = EL(I)*(1.0 + EV(I))
C            RHO*MU RATIO FOR ENERGY EQUATION
      ELE(I) = EL(I)*(1.0 + EV(I)*PR/PRT)
C            ENERGY EQUATION TERM
      ETERM(I) = EL(I)*(TERM8*EV(I)+TERM5)*(TERM6*WOLD(I,1)*FPP
     1         + TERM7*WOLD(I,2)*CPRIME)
   10 CONTINUE
C            CALCULATE FIRST DERIVATIVE OF RHO*MU RATIO AND ENERGY EQUATION
C            TERM WITH RESPECT TO ETA ACROSS BOUNDARY LAYER
      DO 20 I=2,NEND
      DA = ETA(I+1)-ETA(I)  $  DB = ETA(I)-ETA(I-1)  $  D1 = DA+AK2*DB
      DELM(I) = (ELM(I+1)-AK2*ELM(I-1)-(1.0-AK2)*ELM(I))/D1
      DELE(I) = (ELE(I+1)-AK2*ELE(I-1)-(1.0-AK2)*ELE(I))/D1
      DETERM(I) = (ETERM(I+1)-AK2*ETERM(I-1)-(1.0-AK2)*ETERM(1))/D1
   20 CONTINUE
  901 FORMAT(1H0,30X, 61H*****  PANIC STOP AT 0.990 TEST IN SUBROUTINE
     1V I S C  *****  )
 9999 RETURN
      END
```

```
      SUBROUTINE SOLVE
CSOLVE      SOLVES TRIDIAGONAL MATRIX SYSTEMS BY BACK-SUBSTITUTION
      COMMON N,NEQ,W(300, 5),WOLD(300, 5),CAPE(300, 5),SMALLE(300, 5),
     1        A(10),B(10),C(10),D(10),WALLBC(10),F(10),H(10),OEBC(10),
     2        DETA,BETA
C           SET OUTER-EDGE CONDITIONS AT N=NPTS
      N = N + 1
      DO 10 I=1,NEQ
   10 W(N,I) = OEBC(I)
C           BACK-SUBSTITUTE ACROSS LAYER FROM N=NPTS-1 TO N=2
   20 N = N - 1
      DO 30 I=1,NEQ
   30 W(N,I) = CAPE(N,I)*W(N+I,I) + SMALLE(N,I)
      IF ( N - 2 ) 40,40,20
C           SET WALL CONDITIONS AT N=1
   40 DO 50 I=1,NEQ
   50 W(1,I) = WALLBC(I) + H(I)*W(2,I) + F(I)*W(3,I)
 9999 RETURN
      END
```

APPENDIX V
SAMPLE INPUT-OUTPUT DATA FOR PROGRAM SLYBBCBL

DESCRIPTION OF INPUT DATA

In the following description of the input data, a card number is given first, followed by the list of variables on that card and the FORTRAN FORMAT under which the card is read into the program. Each variable in the list is then described relative to its physical meaning, including units if applicable.

Card 1. HEADER (10A8)

Alphameric Data for Identification of the Case.

Card 2. FSMACH, PINF, TINF, TWALL, YAWANGLE, XSTAR, RNOSE (8E10.2)

FSMACH	Free-Stream Mach Number.
PINF	Free-Stream Static Pressure in lb_f/ft^2.
TINF	Free-Stream Static Temperature in °R.
TWALL	Wall Temperature in °R.
YAWANGLE	Body Yaw Angle Relative to Free-Stream Direction in degrees.
XSTAR	x-Distance from Centerline to Sonic Line Location in ft. If Yawed Cylinder or DUEDX Input Analysis, Set XSTAR = 0.0.
RNOSE	Radius of Cylinder in ft. If Lifting Body or DUEDX Input Analysis, Set RNOSE = 0.0.

Card 3. XTRANS, POP, WE, DUEDX, VISCON (8E10.2)

XTRANS	Type Boundary Layer Indicator. If Laminar, Set XTRANS to Any Number Greater than Zero. If Turbulent, Set XTRANS to Any Number Less than Zero.
POP	Body Surface Pressure in lb_f/ft^2. If POP Set to Any Number Less Than Zero, All Inviscid Flow Parameters are Internally Calculated from Conical Flow Hypersonic Small-Disturbance

Theory Based on the Local Flow Deflection Angle. If POP Set Identically Equal to Zero, All Inviscid Flow Parameters are Internally Calculated from Yawed Cylinder with Parallel Shock Theory Based on the Local Flow Deflection Angle.

WE — Inviscid Centerline z-Direction Velocity in ft/sec. If POP Set Either Zero or Less than Zero, Input WE as Zero Since WE Will be Internally Calculated from the Appropriate POP-Controlled Inviscid Theory.

DUEDX — Inviscid Crossflow Velocity Gradient at the Body Centerline in 1/sec. If DUEDX Set to Any Number Less Than Zero, DUEDX Will be Internally Calculated Based on the Flat-Faced Disk Expression and the Input Value for XSTAR. If DUEDX Set Identically Equal to Zero, DUEDX Will be Internally Calculated Based on Newtonian Theory for a Cylinder and the Input Value for RNOSE.

VISCON — Numerical Factor for Sutherland's Viscosity Law in lb_f-sec/ft^2. For Air: VISCON = 2.27E-08. For Nitrogen: VISCON = 2.1996E-08.

Card 4. GAMMA, PR, CP, SUTHER, KML, LAMBDA, ASTAR, PRT (8E10.2)

GAMMA — Ratio of Specific Heats. For Perfect Gas Air and Nitrogen: GAMMA = 1.40.

PR — Prandtl Number. For Perfect Gas Air and Nitrogen: PR = 0.71.

CP — Specific Heat at Constant Pressure in ft^2/sec^2 -°R. For Perfect Gas Air: CP = 6006.0. For Perfect Gas Nitrogen: CP = 6216.0.

SUTHER — Sutherland Viscosity Law Constant in °R. For Air and Nitrogen: SUTHER = 198.6.

KML — Inner Layer Mixing-Length Constant. For Fully Turbulent Flows, Suggest KML = 0.435.

LAMBDA — Outer Layer Mixing Length Constant. For Fully Turbulent Flows, Suggest LAMBDA = 0.090.

ASTAR	Van Driest Wall Damping Term Constant. For Fully Turbulent Flows, Suggest ASTAR = 26.0.
PRT	Turbulent Prandtl Number. For Air and Nitrogen, Suggest PRT = 0.90.

Data input sets (Cards 1 through 4) can be stacked for program execution as shown in the following sample data set. The last card in the data set must be either a header-type card or a blank card followed by an end-of-file (EOF) card which terminates the run on the AEDC-VKF CDC 1604-B monitor system.

SAMPLE INPUT DATA SET

```
 NASA TN C-3094 * FIG 12 * 60-DEG SWEPT CYLINDER AT RE(INF-D)=2.55E+05
7.93        10.98       102.5       555.0       60.0        0.0         0.041667
12345.6     0.0         0.0         0.0         2.2722E-08
1.40        0.710       6006.0      198.60      0.4350      0.0900      26.0        0.90
 NASA TN C-3094 * FIG 12 * 60-DEG SWEPT CYLINDER * NOTE THAT LAMBDA=0.050
7.93        10.98       102.5       555.0       60.0        0.0         0.041667
-12345.6    0.0         0.0         0.0         2.2722E-08
1.40        0.710       6006.0      198.60      0.4350      0.0500      26.0        0.90
 NASA TN C-2302 * FIG 6A * 70-DEG SWEEP DELTA WING LEADING EDGE * ALPHA=0 DEG
9.86        2.27        81.68       540.0       70.0        0.0         0.041667
 12345.6    0.0         0.0         0.0         2.2722E-08
1.40        0.710       6006.0      198.60      0.4350      0.0900      26.0        0.90
 NASA CR-535 * FIG 51 * TEST AD461M-1 MODEL W3+NOSE * ALPHA=40 DEG * Z/D=12.5
7.0         48.7        97.3        500.0       50.0        0.1058      0.0
-12345.6    -12345.6    0.0         -12345.6    2.2722E-08
1.40        0.710       6006.0      198.60      0.4350      0.0900      26.0        0.90
 NAR-ORBITER CENTERLINE * STATION 840 * ALPHA=40 DEG * REINF/FT=3.76E+06 * VKF B
8.0         12.2        97.0        540.0       50.0        0.0         0.0
12345.6     481.41      2748.38     9418.03     2.2722E-08
1.40        0.710       6006.0      198.60      0.4350      0.0900      26.0        0.90
 NAR-ORBITER CENTERLINE * STATION 840 * ALPHA=40 DEG * REINF/FT=3.76E+06 * VKF B
8.0         12.2        97.0        540.0       50.0        0.0         0.0
-12345.6    481.41      2748.38     9418.03     2.2722E-08
1.40        0.710       6006.0      198.60      0.4350      0.0900      26.0        0.90
 NASA LRC 75-DEG SWEEP DELTA WING * Z/L=0.2 * REINF/FT=3.77E+06 * VKF B
8.0         12.816      97.3        860.0       30.0        0.0         0.0
12345.6     874.05      1513.33     5506.30     2.2722E-08
1.40        0.710       6006.0      198.60      0.4350      0.0900      26.0        0.90
 NASA LRC 75-DEG SWEEP DELTA WING * Z/L=0.5 * REINF/FT=3.77E+06 * VKF B
8.0         12.816      97.3        860.0       50.0        0.0         0.0
-12345.6    505.71      2752.62     1726.89     2.2722E-08
1.40        0.710       6006.0      198.60      0.4350      0.0900      26.0        0.90
 MDAC-ORBITER CENTERLINE * STATION 800 * VKF F RUN 3828 TIME 85 MSEC * N2 GAS
10.75       11.98       81.5        540.0       47.0        0.0803      0.0
12345.6     -12345.6    0.0         -12345.6    2.1996E-08
1.40        0.710       6216.0      198.60      0.4350      0.0900      26.0        0.90
 MDAC-ORBITER CENTERLINE * STATION 800 * VKF F RUN 3828 TIME 85 MSEC * N2 GAS
10.75       11.98       81.5        540.0       47.0        0.0803      0.0
-12345.6    -12345.6    0.0         -12345.6    2.1996E-08
1.40        0.710       6216.0      198.60      0.4350      0.0900      26.0        0.90
 MDAC-ORBITER CENTERLINE * STATION 800 * VKF F RUN 3828 TIME 152 MSEC * N2 GAS
10.87       6.16        80.0        540.0       47.0        0.0803      0.0
12345.6     -12345.6    0.0         -12345.6    2.1996E-08
1.40        0.710       6216.0      198.60      0.4350      0.0900      26.0        0.90
 MDAC-ORBITER CENTERLINE * STATION 800 * VKF F RUN 3828 TIME 152 MSEC * N2 GAS
10.87       6.16        80.0        540.0       47.0        0.0803      0.0
-12345.6    -12345.6    0.0         -12345.6    2.1996E-08
1.40        0.710       6216.0      198.60      0.4350      0.0900      26.0        0.90
 * * * * *  N O T E  * * * * THIS CARD GOES LAST * * * *  N O T E  * * * * *
```

SAMPLE OUTPUT DATA CORRESPONDING TO SAMPLE INPUT DATA SET

```
                NASA TN D-3094 * FIG 12 * 60-DEG SWEPT CYLINDER AT RE(INF-D)=2.55E+05


INFINITE YAWED BLUNT-BODY STAGNATION LINE COMPRESSIBLE LAMINAR BOUNDARY-LAYER ANALYSIS
FREE-STREAM MACH NUMBER =  7.930000E 00     PINF (LBF/FT2) =  1.098000E 01     TINF (DEG R) =  1.025000E 02
TWALL (DEG R) =  5.550000E 02     YAW ANGLE (DEG) =  6.000000E 01     PDP (LBF/FT2) =  2.273878E 02
TDP (DEG R) =  4.247851E 02     TSTAG (DEG R) =  1.391640E 03     WE (FT/SEC) =  3.407912E 03
NOSE RADIUS (FT) =  4.166700E-02     X* (FT) =  0     DUE/DX (1/SEC) =  2.826955E 04
TWALL/TSTAG =  3.988099E-01     ANGLE OF ATTACK (DEG) =  3.000000E 01     SHOCK ANGLE (DEG) =  3.000000E 01


THERMALLY AND CALORICALLY PERFECT GAS MODEL
CP= 6006.00 FT2/(SEC2-DEG R)   R= 1716.00 FT2/(SEC2-DEG R)   GAMMA= 1.4000   PR=  .7100   CSTAR=  198.60 DEG R
VISCOSITY CONSTANT=  2.2722E-08 LBF-SEC/(FT2-SQRT(DEG R))   KPL=  .4350   LAMBDA=  .0900   ASTAR= 26.000   PRT=  .9000


YAWED CYLINDER WITH PARALLEL SHOCK INVISCID FLOW
NEWTONIAN STAGNATION POINT VELOCITY GRADIENT
```

INFINITE YAWED BLUNT-BODY STAGNATION LINE COMPRESSIBLE LAMINAR BOUNDARY-LAYER ANALYSIS

X (FT) = 0 X1 = 0 BETA = 1.000000E 00 PE/POP = 1.000000E 00 S/RN = 0

UE (FT/SEC) = 0 WE (FT/SEC) = 3.407912E 03 PE (LBF/FT2) = 2.273878E 02 TE (DEG R) = 4.247851E 02

RHOE (SLUG/FT3) = 3.119469E-04 MUE (LBF-SEC/FT2) = 3.191127E-07 DUE/DX (1/SEC) = 2.826955E 04 ITERATIONS = 10

FPP(0) = 1.646438E 00 CP(0) = 6.262588E-01 GP(0) = 2.735562E-01 QDOT = -6.563343E 00 BTU/(FT2-SEC)

ST(INF) = 4.138154E-03 CFX(INF) = 0 CFZ(INF) = 7.003977E-03 HSP = 3.965000E 00

DELTA* (FT) = 3.701393E-04 THETAMOM (FT) = 6.816854E-05 EDGE REY/FT = 3.331386E 06 EDGE REYTHETAMOM = 2.270957E 02

EDGE MACH NO = 3.373503E 00 MCDONNELL-DOUGLAS TRANSITION PARAMETER = 3.338896E 00 -QDOT/(TSTAG-TWALL) = 7.844879E-03

ETA	Y(FT)	U/UE	W/WE	H/HE	T/TE	MACH	PITOT	EV/MU
0	0	0	0	.39881	1.30654	0	.25432	0
.010	2.49389E-06	.01641	.00627	.40156	1.31547	.01843	.25438	0
.021	5.16339E-06	.03373	.01294	.40450	1.32484	.03793	.25458	0
.032	8.02169E-06	.05199	.02005	.40765	1.33465	.05854	.25493	0
.044	1.10830E-05	.07124	.02761	.41103	1.34493	.08033	.25547	0
.057	1.43627E-05	.09152	.03567	.41465	1.35567	.10336	.25623	0
.070	1.78774E-05	.11286	.04426	.41854	1.36687	.12770	.25724	0
.085	2.16448E-05	.13530	.05340	.42271	1.37854	.15343	.25854	0
.100	2.56844E-05	.15887	.06314	.42719	1.39068	.18062	.26018	0
.116	3.00168E-05	.18360	.07351	.43201	1.40327	.20935	.26221	0
.134	3.46644E-05	.20950	.08456	.43719	1.41630	.23971	.26470	0
.152	3.96511E-05	.23661	.09633	.44276	1.42975	.27179	.26772	0
.172	4.50028E-05	.26494	.10887	.44876	1.44358	.30568	.27135	0
.193	5.07472E-05	.29448	.12223	.45522	1.45776	.34151	.27570	0
.215	5.69137E-05	.32523	.13645	.46218	1.47222	.37937	.28088	0
.238	6.35339E-05	.35717	.15159	.46968	1.48690	.41938	.28703	0
.263	7.06413E-05	.39028	.16771	.47776	1.50171	.46168	.29433	0
.290	7.82714E-05	.42449	.18486	.48649	1.51656	.50641	.30298	0
.318	8.64618E-05	.45975	.20311	.49590	1.53131	.55371	.31321	0
.348	9.52518E-05	.49596	.22251	.50605	1.54587	.60374	.32534	0
.380	1.04682E-04	.53301	.24312	.51701	1.55991	.65667	.33972	0
.414	1.14796E-04	.57076	.26499	.52883	1.57337	.71268	.35681	0
.450	1.25636E-04	.60903	.28818	.54158	1.58596	.77196	.37717	0
.488	1.37247E-04	.64763	.31273	.55532	1.59740	.83472	.40150	0
.529	1.49672E-04	.68632	.33868	.57012	1.60739	.90116	.43068	0
.572	1.62955E-04	.72483	.36605	.58603	1.61558	.97152	.46583	0
.618	1.77137E-04	.76286	.39484	.60310	1.62159	1.04601	.50831	0
.667	1.92257E-04	.80006	.42506	.62137	1.62502	1.12486	.55901	0
.719	2.08348E-04	.83609	.45664	.64087	1.62544	1.20828	.61843	0
.775	2.25439E-04	.87054	.48952	.66160	1.62243	1.29648	.68726	0
.834	2.43552E-04	.90303	.52358	.68351	1.61557	1.38963	.76629	0
.896	2.62699E-04	.93315	.55865	.70655	1.60450	1.48783	.85642	0
.963	2.82884E-04	.96052	.59454	.73059	1.58891	1.59110	.95859	0
1.033	3.04099E-04	.98480	.63097	.75545	1.56860	1.69955	1.07371	0
1.108	3.26327E-04	1.00569	.66762	.78091	1.54351	1.81282	1.20257	0
1.188	3.49539E-04	1.02298	.70411	.80665	1.51376	1.93062	1.34578	0

1.273	3.73697E-04	1.03654	.74004	.83232	1.47965	2.05237	1.50356	0
1.363	3.98760E-04	1.04636	.77493	.85750	1.44171	2.17724	1.67565	0
1.459	4.24681E-04	1.05258	.80833	.88174	1.40068	2.30408	1.86106	0
1.561	4.51419E-04	1.05542	.83975	.90455	1.35751	2.43143	2.05794	0
1.669	4.78541E-04	1.05528	.86878	.92550	1.31326	2.55750	2.26338	0
1.784	5.07228E-04	1.05262	.89503	.94417	1.26912	2.68021	2.47340	0
1.907	5.36285E-04	1.04801	.91821	.96026	1.22627	2.79726	2.68300	0
2.037	5.66141E-04	1.04206	.93815	.97358	1.18581	2.90633	2.88642	0
2.175	5.96857E-04	1.03537	.95478	.98407	1.14870	3.00525	3.07767	0
2.322	6.28528E-04	1.02852	.96819	.99185	1.11568	3.09222	3.25113	0
2.479	6.61279E-04	1.02200	.97858	.99718	1.08723	3.16606	3.40230	0
2.645	6.95271E-04	1.01617	.98629	1.00043	1.06354	3.22634	3.52837	0
2.822	7.30686E-04	1.01129	.99172	1.00205	1.04453	3.27349	3.62863	0
3.009	7.67731E-04	1.00743	.99533	1.00254	1.02989	3.30865	3.70435	0
3.209	8.06629E-04	1.00459	.99756	1.00234	1.01912	3.33356	3.75849	0
3.421	8.47607E-04	1.00264	.99884	1.00181	1.01158	3.35024	3.79498	0
3.647	8.90898E-04	1.00140	.99950	1.00122	1.00660	3.36076	3.81806	0
3.886	9.36733E-04	1.00068	.99981	1.00073	1.00352	3.36695	3.83171	0
4.141	9.85237E-04	1.00030	.99994	1.00038	1.00175	3.37035	3.83920	0
4.412	1.03693E-03	1.00012	.99998	1.00018	1.00082	3.37208	3.84300	0
4.700	1.09174E-03	1.00004	1.00000	1.00007	1.00036	3.37288	3.84478	0
5.006	1.14599E-03	1.00002	1.00000	1.00002	1.00016	3.37322	3.84554	0
5.331	1.21189E-03	1.00001	1.00000	1.00001	1.00008	3.37337	3.84585	0
5.677	1.27769E-03	1.00000	1.00000	1.00000	1.00005	3.37343	3.84598	0
6.045	1.34764E-03	1.00000	1.00000	1.00000	1.00003	3.37345	3.84605	0
6.436	1.42199E-03	1.00000	1.00000	1.00000	1.00002	3.37347	3.84609	0
6.851	1.50102E-03	1.00000	1.00000	1.00000	1.00001	3.37348	3.84611	0
7.293	1.58503E-03	1.00000	1.00000	1.00000	1.00001	3.37349	3.84613	0
7.762	1.67433E-03	1.00000	1.00000	1.00000	1.00000	3.37350	3.84614	0
8.261	1.76926E-03	1.00000	1.00000	1.00000	1.00000	3.37350	3.84614	0
8.792	1.87017E-03	1.00000	1.00000	1.00000	1.00000	3.37350	3.84615	0
9.356	1.97744E-03	1.00000	1.00000	1.00000	1.00000	3.37350	3.84615	0
9.955	2.09147E-03	1.00000	1.00000	1.00000	1.00000	3.37350	3.84615	0
10.592	2.21268E-03	1.00000	1.00000	1.00000	1.00000	3.37350	3.84615	0
11.270	2.34152E-03	1.00000	1.00000	1.00000	1.00000	3.37350	3.84615	0
11.990	2.47848E-03	1.00000	1.00000	1.00000	1.00000	3.37350	3.84615	0
12.755	2.62407E-03	1.00000	1.00000	1.00000	1.00000	3.37350	3.84615	0
13.569	2.77884E-03	1.00000	1.00000	1.00000	1.00000	3.37350	3.84615	0
14.433	2.94335E-03	1.00000	1.00000	1.00000	1.00000	3.37350	3.84615	0
15.353	3.11823E-03	1.00000	1.00000	1.00000	1.00000	3.37350	3.84615	0
16.330	3.30412E-03	1.00000	1.00000	1.00000	1.00000	3.37350	3.84615	0
17.369	3.50173E-03	1.00000	1.00000	1.00000	1.00000	3.37350	3.84615	0
18.473	3.71178E-03	1.00000	1.00000	1.00000	1.00000	3.37350	3.84615	0
19.647	3.93507E-03	1.00000	1.00000	1.00000	1.00000	3.37350	3.84615	0
20.895	4.17243E-03	1.00000	1.00000	1.00000	1.00000	3.37350	3.84615	0
22.221	4.42474E-03	1.00000	1.00000	1.00000	1.00000	3.37350	3.84615	0
23.631	4.69294E-03	1.00000	1.00000	1.00000	1.00000	3.37350	3.84615	0
25.130	4.97805E-03	1.00000	1.00000	1.00000	1.00000	3.37350	3.84615	0
26.723	5.28111E-03	1.00000	1.00000	1.00000	1.00000	3.37350	3.84615	0
28.416	5.60326E-03	1.00000	1.00000	1.00000	1.00000	3.37350	3.84615	0
30.217	5.94572E-03	1.00000	1.00000	1.00000	1.00000	3.37350	3.84615	0
32.130	6.30974E-03	1.00000	1.00000	1.00000	1.00000	3.37350	3.84615	0
34.164	6.69670E-03	1.00000	1.00000	1.00000	1.00000	3.37350	3.84615	0
36.327	7.10804E-03	1.00000	1.00000	1.00000	1.00000	3.37350	3.84615	0
38.625	7.54530E-03	1.00000	1.00000	1.00000	1.00000	3.37350	3.84615	0
41.069	8.01010E-03	1.00000	1.00000	1.00000	1.00000	3.37350	3.84615	0
43.666	8.50418E-03	1.00000	1.00000	1.00000	1.00000	3.37350	3.84615	0
46.427	9.02939E-03	1.00000	1.00000	1.00000	1.00000	3.37350	3.84615	0
49.362	9.58768E-03	1.00000	1.00000	1.00000	1.00000	3.37350	3.84615	0
52.482	1.01812E-02	1.00000	1.00000	1.00000	1.00000	3.37350	3.84615	0

NASA TN D-3094 * FIG 12 * 60-DEG SWEPT CYLINDER * NOTE THAT LAMBDA=0.050

INFINITE YAWED BLUNT-BODY STAGNATION LINE COMPRESSIBLE TURBULENT BOUNDARY-LAYER ANALYSIS

FREE-STREAM MACH NUMBER = 7.930000E 00 PINF (LBF/FT2) = 1.098000E 01 TINF (DEG R) = 1.025000E 02

TWALL (DEG R) = 5.550000E 02 YAW ANGLE (DEG) = 6.000000E 01 POP (LBF/FT2) = 2.273878E 02

TOP (DEG R) = 4.247851E 02 TSTAG (DEG R) = 1.391640E 03 UE (FT/SEC) = 3.407912E 03

NOSE RADIUS (FT) = 4.166700E-02 X* (FT) = 0 DUE/DX (1/SEC) = 2.826955E 04

TWALL/TSTAG = 3.988099E-01 ANGLE OF ATTACK (DEG) = 3.000000E 01 SHOCK ANGLE (DEG) = 3.000000E 01

THERMALLY AND CALORICALLY PERFECT GAS MODEL

CP= 6006.00 FT2/(SEC2-DEG R) R= 1716.00 FT2/(SEC2-DEG R) GAMMA= 1.4000 PR= .7100 CSTAR= 198.60 DEG R

VISCOSITY CONSTANT= 2.2722E-08 LBF-SEC/(FT2-SQRT(DEG R)) KPL= .4350 LAMBDA= .0500 ASTAR= 26.000 PRT= .9000

YAWED CYLINDER WITH PARALLEL SHOCK INVISCID FLOW

NEWTONIAN STAGNATION POINT VELOCITY GRADIENT

NASA TN D-3094 * FIG 12 * 60-DEG SWEPT CYLINDER * NOTE THAT LAMBDA=0.050

INFINITE YAWED BLUNT-BODY STAGNATION LINE COMPRESSIBLE TURBULENT BOUNDARY-LAYER ANALYSIS

X (FT) = 0 X_1 = 0 BETA = 1.000000E 00 PE/POP = 1.000000E 00 S/RN = 0

UE (FT/SEC) = 0 WE (FT/SEC) = 3.407912E 03 PE (LBF/FT2) = 2.273878E 02 TE (DEG R) = 4.247851E 02

RHOE (SLUG/FT3) = 3.119469E-04 MUE (LBF-SEC/FT2) = 3.191127E-07 DUE/DX (1/SEC) = 2.826955E 04 ITERATIONS = 63

FPP(0) = 2.080685E 00 CP(0) = 9.912251E-01 GP(0) = 4.417628E-01 QDOT = -1.059907E 01 BTU/(FT2-SEC)

ST(INF) = 6.682657E-03 CFX(INF) = 0 CFZ(INF) = 1.108570E-02 HSP = 3.965000E 00

DELTA* (FT) = 5.434393E-04 THETAMOM (FT) = 1.189687E-04 EDGE REY/FT = 3.331386E 06 EDGE REYTHETAMOM = 3.963307E 02

EDGE MACH NO = 3.373503E 00 MCDONNELL-DOUGLAS TRANSITION PARAMETER = 5.827088E 00 -QDOT/(TSTAG-TWALL) = 1.266860E-02

ETA	Y(FT)	U/UE	W/WE	H/HE	T/TE	MACH	P1TOT	EV/MU
0	0	0	0	.39881	1.30654	0	.25432	0
.010	2.49902E-06	.02076	.00992	.40325	1.32086	.02913	.25447	.00000
.021	5.18503E-06	.04274	.02050	.40803	1.33577	.05985	.25496	.00001
.032	8.07294E-06	.06599	.03178	.41318	1.35127	.09222	.25584	.00007
.044	1.11788E-05	.09057	.04380	.41871	1.36733	.12635	.25717	.00023
.057	1.45201E-05	.11653	.05660	.42468	1.38394	.16232	.25904	.00060
.070	1.81153E-05	.14394	.07025	.43112	1.40104	.20023	.26153	.00135
.085	2.19847E-05	.17283	.08479	.43805	1.41861	.24016	.26474	.00272
.100	2.61496E-05	.20323	.10026	.44553	1.43656	.28220	.26878	.00504
.116	3.06330E-05	.23517	.11671	.45358	1.45480	.32643	.27380	.00877
.134	3.54593E-05	.26862	.13417	.46226	1.47321	.37290	.27995	.01451
.152	4.06543E-05	.30355	.15265	.47158	1.49166	.42163	.28740	.02304
.172	4.62450E-05	.33984	.17215	.48158	1.50997	.47260	.29635	.03534
.193	5.22597E-05	.37737	.19264	.49227	1.52793	.52574	.30702	.05261
.215	5.87277E-05	.41589	.21405	.50364	1.54531	.58088	.31963	.07625
.238	6.56791E-05	.45515	.23628	.51566	1.56185	.63780	.33441	.10790
.263	7.31445E-05	.49477	.25918	.52827	1.57731	.69618	.35157	.14934
.290	8.11550E-05	.53438	.28257	.54139	1.59143	.75563	.37132	.20251
.318	8.97419E-05	.57353	.30623	.55491	1.60399	.81569	.39380	.26942
.348	9.89366E-05	.61180	.32993	.56870	1.61481	.87587	.41913	.35215
.380	1.08771E-04	.64880	.35345	.58261	1.62379	.93572	.44736	.45284
.414	1.19276E-04	.68417	.37657	.59649	1.63086	.99476	.47848	.57367
.450	1.30485E-04	.71765	.39911	.61022	1.63605	1.05263	.51235	.71689
.488	1.42432E-04	.74903	.42091	.62367	1.63942	1.10899	.54836	.88481
.529	1.55151E-04	.77821	.44187	.63674	1.64110	1.16360	.58589	1.07981
.572	1.68679E-04	.80513	.46189	.64936	1.64123	1.21630	.62443	1.30424
.618	1.83054E-04	.82981	.48096	.66146	1.63999	1.26697	.66356	1.56124
.667	1.98317E-04	.85230	.49904	.67303	1.63755	1.31558	.70294	1.85111
.719	2.14513E-04	.87269	.51615	.68404	1.63410	1.36213	.74230	2.18089
.775	2.31688E-04	.89108	.53231	.69449	1.62977	1.40663	.78141	2.55098
.834	2.49894E-04	.90762	.54758	.70440	1.62473	1.44922	.82017	2.95282
.896	2.69183E-04	.92239	.56196	.71379	1.61921	1.48982	.85832	3.43047
.963	2.89612E-04	.93638	.57637	.72323	1.61286	1.53102	.89822	3.35430
1.033	3.11234E-04	.95028	.59162	.73324	1.60515	1.57531	.94244	3.36582
1.108	3.34098E-04	.96385	.60758	.74376	1.59612	1.62239	.99093	3.36450
1.188	3.58255E-04	.97700	.62428	.75482	1.58561	1.67247	1.04420	3.36490

1.273	3.83751E-04	.98959	.64168	.76639	1.57348	1.72570	1.10270	3.36503
1.363	4.10630E-04	1.00150	.65976	.77848	1.55959	1.78221	1.16690	3.36480
1.459	4.38932E-04	1.01259	.67848	.79105	1.54383	1.84212	1.23732	3.36387
1.561	4.68691E-04	1.02272	.69779	.80407	1.52608	1.90553	1.31450	3.36177
1.669	4.99939E-04	1.03177	.71761	.81749	1.50627	1.97251	1.39895	3.35787
1.784	5.32698E-04	1.03961	.73787	.83126	1.48434	2.04312	1.49123	3.35133
1.907	5.66986E-04	1.04614	.75845	.84529	1.46028	2.11734	1.59181	3.34108
2.037	6.02812E-04	1.05127	.77924	.85950	1.43412	2.19512	1.70114	3.32571
2.175	6.40180E-04	1.05492	.80009	.87378	1.40596	2.27632	1.81958	3.30345
2.322	6.79089E-04	1.05707	.82086	.88800	1.37596	2.36074	1.94733	3.27207
2.479	7.19533E-04	1.05771	.84138	.90204	1.34433	2.44805	2.08442	3.22883
2.645	7.61504E-04	1.05687	.86147	.91575	1.31136	2.53782	2.23062	3.17037
2.822	8.04995E-04	1.05462	.88095	.92898	1.27741	2.62946	2.38534	3.09265
3.009	8.50004E-04	1.05109	.89962	.94156	1.24291	2.72220	2.54756	2.99093
3.209	8.96536E-04	1.04642	.91729	.95333	1.20834	2.81510	2.71573	2.85977
3.421	9.44615E-04	1.04080	.93376	.96413	1.17424	2.90695	2.88760	2.69310
3.647	9.94283E-04	1.03450	.94884	.97380	1.14121	2.99632	3.06015	2.48454
3.886	1.04561E-03	1.02777	.96232	.98217	1.10991	3.08145	3.22938	2.22792
4.141	1.09872E-03	1.02097	.97400	.98911	1.08103	3.16025	3.39026	1.91839
4.412	1.15376E-03	1.01447	.98368	.99448	1.05534	3.23026	3.53664	1.55474
4.700	1.21098E-03	1.00871	.99115	.99818	1.03369	3.28873	3.66135	1.14315
5.006	1.27068E-03	1.00418	.99628	1.00022	1.01701	3.33273	3.75669	.70609
5.331	1.33330E-03	1.00132	.99905	1.00078	1.00631	3.35973	3.81580	.31309
5.677	1.39936E-03	1.00019	.99993	1.00047	1.00158	3.37061	3.83976	.07516
6.045	1.46936E-03	1.00001	1.00000	1.00012	1.00029	3.37303	3.84510	.00234
6.436	1.54372E-03	1.00000	1.00000	1.00001	1.00002	3.37346	3.84607	.00001
6.851	1.62276E-03	1.00000	1.00000	1.00000	1.00000	3.37351	3.84616	.00000
7.293	1.70677E-03	1.00000	1.00000	1.00000	1.00000	3.37350	3.84615	.00000
7.762	1.79607E-03	1.00000	1.00000	1.00000	1.00000	3.37350	3.84615	.00000
8.261	1.89100E-03	1.00000	1.00000	1.00000	1.00000	3.37350	3.84615	.00000
8.792	1.99191E-03	1.00000	1.00000	1.00000	1.00000	3.37350	3.84615	0
9.356	2.09918E-03	1.00000	1.00000	1.00000	1.00000	3.37350	3.84615	0
9.955	2.21320E-03	1.00000	1.00000	1.00000	1.00000	3.37350	3.84615	0
10.592	2.33441E-03	1.00000	1.00000	1.00000	1.00000	3.37350	3.84615	0
11.270	2.46326E-03	1.00000	1.00000	1.00000	1.00000	3.37350	3.84615	0
11.990	2.60022E-03	1.00000	1.00000	1.00000	1.00000	3.37350	3.84615	0
12.755	2.74581E-03	1.00000	1.00000	1.00000	1.00000	3.37350	3.84615	0
13.569	2.90057E-03	1.00000	1.00000	1.00000	1.00000	3.37350	3.84615	0
14.433	3.06508E-03	1.00000	1.00000	1.00000	1.00000	3.37350	3.84615	0
15.353	3.23996E-03	1.00000	1.00000	1.00000	1.00000	3.37350	3.84615	0
16.330	3.42586E-03	1.00000	1.00000	1.00000	1.00000	3.37350	3.84615	0
17.369	3.62346E-03	1.00000	1.00000	1.00000	1.00000	3.37350	3.84615	0
18.473	3.83352E-03	1.00000	1.00000	1.00000	1.00000	3.37350	3.84615	0
19.647	4.05681E-03	1.00000	1.00000	1.00000	1.00000	3.37350	3.84615	0
20.895	4.29416E-03	1.00000	1.00000	1.00000	1.00000	3.37350	3.84615	0
22.221	4.54647E-03	1.00000	1.00000	1.00000	1.00000	3.37350	3.84615	0
23.631	4.81468E-03	1.00000	1.00000	1.00000	1.00000	3.37350	3.84615	0
25.130	5.09978E-03	1.00000	1.00000	1.00000	1.00000	3.37350	3.84615	0
26.723	5.40284E-03	1.00000	1.00000	1.00000	1.00000	3.37350	3.84615	0
28.416	5.72500E-03	1.00000	1.00000	1.00000	1.00000	3.37350	3.84615	0
30.217	6.06745E-03	1.00000	1.00000	1.00000	1.00000	3.37350	3.84615	0
32.130	6.43148E-03	1.00000	1.00000	1.00000	1.00000	3.37350	3.84615	0
34.164	6.81844E-03	1.00000	1.00000	1.00000	1.00000	3.37350	3.84615	0
36.327	7.22978E-03	1.00000	1.00000	1.00000	1.00000	3.37350	3.84615	0
38.625	7.66703E-03	1.00000	1.00000	1.00000	1.00000	3.37350	3.84615	0
41.069	8.13183E-03	1.00000	1.00000	1.00000	1.00000	3.37350	3.84615	0
43.666	8.62591E-03	1.00000	1.00000	1.00000	1.00000	3.37350	3.84615	0
46.427	9.15112E-03	1.00000	1.00000	1.00000	1.00000	3.37350	3.84615	0
49.362	9.70942E-03	1.00000	1.00000	1.00000	1.00000	3.37350	3.84615	0
52.482	1.03029E-02	1.00000	1.00000	1.00000	1.00000	3.37350	3.84615	0

NASA TN D-2302 • FIG 6A • 70-DEG SWEEP DELTA WING LEADING EDGE • ALPHA=0 DEG

INFINITE YAWED BLUNT-BODY STAGNATION LINE COMPRESSIBLE LAMINAR BOUNDARY-LAYER ANALYSIS

FREE-STREAM MACH NUMBER = 9.860000E 00 PINF (LBF/FT2) = 2.270000E 00 TINF (DEG R) = 8.168000E 01

TWALL (DEG R) = 5.400000E 02 YAW ANGLE (DEG) = 7.000000E 01 POP (LBF/FT2) = 3.430642E 01

TOP (DEG R) = 2.674617E 02 TSTAG (DEG R) = 1.069859E 03 UE (FT/SEC) = 4.104339E 03

NOSE RADIUS (FT) = 4.166700E-02 X• (FT) = 0 DUE/DX (1/SEC) = 2.222012E 04

TWALL/TSTAG = 3.233805E-01 ANGLE OF ATTACK (DEG) = 2.000000E 01 SHOCK ANGLE (DEG) = 2.000000E 01

THERMALLY AND CALORICALLY PERFECT GAS MODEL

CP= 6006.00 FT2/(SEC2-DEG R) R= 1716.00 FT2/(SEC2-DEG R) GAMMA= 1.4000 PR= .7100 CSTAR= 198.60 DEG R

VISCOSITY CONSTANT= 2.2722E-08 LBF-SEC/(FT2-SQRT(DEG R)) KPL= .4350 LAMBDA= .0900 ASTAR= 26.000 PRT= .9000

YAWED CYLINDER WITH PARALLEL SHOCK INVISCID FLOW

NEWTONIAN STAGNATION POINT VELOCITY GRADIENT

INFINITE YAWED BLUNT-BODY STAGNATION LINE COMPRESSIBLE LAMINAR BOUNDARY-LAYER ANALYSIS

X (FT) = 0 X1 = 0 BETA = 1.000000E 00 PE/POP = 1.000000E 00 S/RN = 0

UE (FT/SEC) = 0 WE (FT/SEC) = 4.104339E 03 PE (LBF/FT2) = 3.430642E 01 TE (DEG R) = 2.674617E 02

RHOE (SLUG/FT3) = 7.474748E-05 MUE (LBF-SEC/FT2) = 2.132532E-07 DUE/DX (1/SEC) = 2.222012E 04 ITERATIONS = 10

FPP(0) = 2.320460E 00 CP(0) = 7.039805E-01 GP(0) = 3.414006E-01 QDOT = -3.306480E 00 BTU/(FT2-SEC)

ST(INF) = 5.360813E-03 CFX(INF) = 0 CFZ(INF) = 9.980347E-03 HSP = 3.372319E 00

DELTA* (FT) = 1.170467E-03 THETAMOM (FT) = 1.156853E-04 EDGE REY/FT = 1.438614E 06 EDGE REYTHETAMOM = 1.664264E 02

EDGE MACH NO = 5.120234E 00 MCDONNELL-DOUGLAS TRANSITION PARAMETER = 1.906969E 00 -QDOT/(TSTAG-TWALL) = 2.926453E-03

ETA	Y(FT)	U/UE	W/WE	H/HE	T/TE	MACH	PITOT	EV/MU
0	0	0	0	.32338	2.01898	0	.12029	0
.010	7.27248E-06	.02312	.00705	.32681	2.04018	.02527	.12034	0
.021	1.50858E-05	.04750	.01456	.33049	2.06237	.05191	.12052	0
.032	2.34831E-05	.07321	.02256	.33445	2.08555	.08000	.12083	0
.044	3.25115E-05	.10027	.03110	.33870	2.10974	.10962	.12131	0
.057	4.22216E-05	.12875	.04019	.34327	2.13492	.14084	.12197	0
.070	5.26682E-05	.15868	.04989	.34818	2.16109	.17375	.12285	0
.085	6.39108E-05	.19010	.06022	.35347	2.18822	.20845	.12399	0
.100	7.60133E-05	.22304	.07124	.35917	2.21626	.24503	.12542	0
.116	8.90445E-05	.25752	.08299	.36531	2.24517	.28360	.12720	0
.134	1.03079E-04	.29355	.09552	.37193	2.27485	.32427	.12938	0
.152	1.18195E-04	.33114	.10887	.37908	2.30522	.36717	.13203	0
.172	1.34479E-04	.37027	.12311	.38679	2.33612	.41242	.13523	0
.193	1.52021E-04	.41091	.13829	.39512	2.36740	.46019	.13909	0
.215	1.70916E-04	.45299	.15446	.40412	2.39885	.51062	.14371	0
.238	1.91266E-04	.49646	.17169	.41385	2.43022	.56390	.14926	0
.263	2.13178E-04	.54119	.19003	.42438	2.46119	.62020	.15592	0
.290	2.36762E-04	.58705	.20955	.43576	2.49141	.67975	.16390	0
.318	2.62131E-04	.63385	.23030	.44807	2.52044	.74276	.17351	0
.348	2.89402E-04	.68139	.25235	.46138	2.54778	.80950	.18511	0
.380	3.18691E-04	.72940	.27575	.47577	2.57285	.88024	.19917	0
.414	3.50112E-04	.77757	.30054	.49132	2.59498	.95527	.21629	0
.450	3.83775E-04	.82553	.32676	.50809	2.61343	1.03493	.23727	0
.488	4.19781E-04	.87287	.35443	.52616	2.62735	1.11959	.26272	0
.529	4.58219E-04	.91912	.38355	.54559	2.63586	1.20962	.29298	0
.572	4.99161E-04	.96377	.41410	.56642	2.63798	1.30545	.32853	0
.618	5.42657E-04	1.00628	.44604	.58868	2.63273	1.40752	.36997	0
.667	5.88728E-04	1.04605	.47927	.61236	2.61912	1.51631	.41804	0
.719	6.37360E-04	1.08251	.51366	.63741	2.59622	1.63229	.47362	0
.775	6.88502E-04	1.11506	.54905	.66376	2.56320	1.75596	.53769	0
.834	7.42057E-04	1.14316	.58521	.69124	2.51942	1.88779	.61140	0
.896	7.97881E-04	1.16635	.62186	.71965	2.46453	2.02822	.69599	0
.963	8.55782E-04	1.18422	.65867	.74870	2.39850	2.17763	.79283	0
1.033	9.15523E-04	1.19655	.69525	.77804	2.32171	2.33629	.90334	0
1.108	9.76827E-04	1.20325	.73120	.80726	2.23500	2.50430	1.02894	0
1.188	1.03939E-03	1.20441	.76607	.83587	2.13971	2.68153	1.17099	0

1.273	1.10290E-03	1.20033	.79943	.86338	2.03760	2.86755	1.33060	0
1.363	1.16703E-03	1.19150	.83084	.88928	1.93083	3.06149	1.50849	0
1.459	1.23149E-03	1.17861	.85991	.91309	1.82184	3.26201	1.70469	0
1.561	1.29604E-03	1.16247	.88631	.93440	1.71321	3.46714	1.91832	0
1.669	1.36050E-03	1.14401	.90981	.95287	1.60750	3.67421	2.14722	0
1.784	1.42476E-03	1.12422	.93024	.96831	1.50708	3.87985	2.38772	0
1.907	1.48884E-03	1.10409	.94756	.98067	1.41403	4.08005	2.63443	0
2.037	1.55281E-03	1.08453	.96183	.99004	1.33001	4.27031	2.88043	0
2.175	1.61691E-03	1.06635	.97321	.99666	1.25616	4.44605	3.11762	0
2.322	1.68144E-03	1.05015	.98197	1.00089	1.19312	4.60306	3.33763	0
2.479	1.74680E-03	1.03637	.98843	1.00317	1.14094	4.73809	3.53295	0
2.645	1.81349E-03	1.02518	.99297	1.00401	1.09922	4.84935	3.69813	0
2.822	1.88205E-03	1.01655	.99599	1.00389	1.06710	4.93677	3.83061	0
3.009	1.95304E-03	1.01027	.99788	1.00323	1.04339	5.00199	3.93099	0
3.209	2.02707E-03	1.00597	.99897	1.00238	1.02670	5.04800	4.00260	0
3.421	2.10469E-03	1.00323	.99954	1.00158	1.01555	5.07856	4.05052	0
3.647	2.18648E-03	1.00161	.99982	1.00094	1.00855	5.09759	4.08051	0
3.886	2.27294E-03	1.00074	.99994	1.00050	1.00443	5.10863	4.09797	0
4.141	2.36455E-03	1.00031	.99998	1.00024	1.00218	5.11459	4.10739	0
4.412	2.46178E-03	1.00012	1.00000	1.00010	1.00104	5.11756	4.11209	0
4.700	2.56504E-03	1.00005	1.00000	1.00004	1.00051	5.11894	4.11428	0
5.006	2.67476E-03	1.00002	1.00000	1.00001	1.00027	5.11955	4.11526	0
5.331	2.79138E-03	1.00001	1.00000	1.00000	1.00016	5.11984	4.11571	0
5.677	2.91534E-03	1.00001	1.00000	1.00000	1.00010	5.11998	4.11594	0
6.045	3.04709E-03	1.00000	1.00000	1.00000	1.00006	5.12007	4.11608	0
6.436	3.18715E-03	1.00000	1.00000	1.00000	1.00004	5.12013	4.11617	0
6.851	3.33602E-03	1.00000	1.00000	1.00000	1.00003	5.12017	4.11623	0
7.293	3.49427E-03	1.00000	1.00000	1.00000	1.00002	5.12019	4.11627	0
7.762	3.66249E-03	1.00000	1.00000	1.00000	1.00001	5.12021	4.11630	0
8.261	3.84131E-03	1.00000	1.00000	1.00000	1.00001	5.12022	4.11632	0
8.792	4.03139E-03	1.00000	1.00000	1.00000	1.00000	5.12023	4.11633	0
9.356	4.23345E-03	1.00000	1.00000	1.00000	1.00000	5.12023	4.11633	0
9.955	4.44823E-03	1.00000	1.00000	1.00000	1.00000	5.12023	4.11634	0
10.597	4.67655E-03	1.00000	1.00000	1.00000	1.00000	5.12023	4.11634	0
11.270	4.91925E-03	1.00000	1.00000	1.00000	1.00000	5.12023	4.11634	0
11.990	5.17724E-03	1.00000	1.00000	1.00000	1.00000	5.12023	4.11634	0
12.755	5.45149E-03	1.00000	1.00000	1.00000	1.00000	5.12023	4.11634	0
13.569	5.74301E-03	1.00000	1.00000	1.00000	1.00000	5.12023	4.11634	0
14.433	6.05290E-03	1.00000	1.00000	1.00000	1.00000	5.12023	4.11634	0
15.353	6.38231E-03	1.00000	1.00000	1.00000	1.00000	5.12023	4.11634	0
16.330	6.73247E-03	1.00000	1.00000	1.00000	1.00000	5.12023	4.11634	0
17.369	7.10470E-03	1.00000	1.00000	1.00000	1.00000	5.12023	4.11634	0
18.473	7.50037E-03	1.00000	1.00000	1.00000	1.00000	5.12023	4.11634	0
19.647	7.92097E-03	1.00000	1.00000	1.00000	1.00000	5.12023	4.11634	0
20.895	8.36807E-03	1.00000	1.00000	1.00000	1.00000	5.12023	4.11634	0
22.221	8.84334E-03	1.00000	1.00000	1.00000	1.00000	5.12023	4.11634	0
23.631	9.34855E-03	1.00000	1.00000	1.00000	1.00000	5.12023	4.11634	0
25.130	9.88558E-03	1.00000	1.00000	1.00000	1.00000	5.12023	4.11634	0
26.723	1.04565E-02	1.00000	1.00000	1.00000	1.00000	5.12023	4.11634	0
28.416	1.10633E-02	1.00000	1.00000	1.00000	1.00000	5.12023	4.11634	0
30.217	1.17084E-02	1.00000	1.00000	1.00000	1.00000	5.12023	4.11634	0
32.130	1.23941E-02	1.00000	1.00000	1.00000	1.00000	5.12023	4.11634	0
34.164	1.31230E-02	1.00000	1.00000	1.00000	1.00000	5.12023	4.11634	0
36.327	1.38978E-02	1.00000	1.00000	1.00000	1.00000	5.12023	4.11634	0
38.625	1.47214E-02	1.00000	1.00000	1.00000	1.00000	5.12023	4.11634	0
41.069	1.55970E-02	1.00000	1.00000	1.00000	1.00000	5.12023	4.11634	0
43.666	1.65276E-02	1.00000	1.00000	1.00000	1.00000	5.12023	4.11634	0
46.427	1.75170E-02	1.00000	1.00000	1.00000	1.00000	5.12023	4.11634	0
49.362	1.85686E-02	1.00000	1.00000	1.00000	1.00000	5.12023	4.11634	0
52.482	1.96865E-02	1.00000	1.00000	1.00000	1.00000	5.12023	4.11634	0

NASA CR-535 * FIG 51 * TEST AD461M-1 MODEL W3+NOSE * ALPHA=40 DEG * Z/D=12.5

INFINITE YAWED BLUNT-BODY STAGNATION LINE COMPRESSIBLE TURBULENT BOUNDARY-LAYER ANALYSIS

FREE-STREAM MACH NUMBER = 7.000000E 00 PINF (LBF/FT2) = 4.870000E 01 TINF (DEG R) = 9.730000E 01

TWALL (DEG R) = 5.000000E 02 YAW ANGLE (DEG) = 5.000000E 01 POP (LBF/FT2) = 1.508732E 03

TOP (DEG R) = 5.788273E 02 TSTAG (DEG R) = 1.050840E 03 WE (FT/SEC) = 2.381138E 03

NOSE RADIUS (FT) = 0 X* (FT) = 1.058000E-01 DUE/DX (1/SEC) = 4.346864E 03

TWALL/TSTAG = 4.758098E-01 ANGLE OF ATTACK (DEG) = 4.000000E 01 SHOCK ANGLE (DEG) = 4.592946E 01

THERMALLY AND CALORICALLY PERFECT GAS MODEL

CP= 6006.00 FT2/(SEC2-DEG R) R= 1716.00 FT2/(SEC2-DEG R) GAMMA= 1.4000 PR= .7100 CSTAR= 198.60 DEG R

VISCOSITY CONSTANT= 2.2722E-08 LBF-SEC/(FT2-SQRT(DEG R)) KPL= .4350 LAMBDA= .0900 ASTAR= 26.000 PHI= .9000

CONICAL INVISCIC FLOW FOLLOWING HYPERSONIC SMALL-DISTURBANCE THEORY

FLAT-FACED DISK STAGNATION POINT VELOCITY GRADIENT

INFINITE YAWED BLUNT-BODY STAGNATION LINE COMPRESSIBLE TURBULENT BOUNDARY-LAYER ANALYSIS

X (FT) = 0 X1 = 0 BETA = 1.000000E 00 PE/POP = 1.000000E 00 S/RN = 0

UE (FT/SEC) = 0 WE (FT/SEC) = 2.381138E 03 PE (LBF/FT2) = 1.508732E 03 TE (DEG R) = 5.788273E 02

RHOE (SLUG/FT3) = 1.518558E-03 MUE (LBF-SEC/FT2) = 4.070149E-07 DUE/DX (1/SEC) = 4.346864E 03 ITERATIONS = 68

FPP(0) = 3.988116E 00 CP(0) = 2.971383E 00 GP(0) = 1.192103E 00 QDOT = -2.308662E 01 BTU/(FT2-SEC)

ST(INF) = 5.501717E-03 CFX(INF) = 0 CFZ(INF) = 7.181710E-03 HSP = 4.499513E 00

DELTA* (FT) = 1.216904E-03 THETAMOM (FT) = 6.463167E-04 EDGE REY/FT = 8.886279E 06 EDGE REYTHETAMOM = 5.743350E 03

EDGE MACH NO = 2.019237E 00 MCDONNELL-DOUGLAS TRANSITION PARAMETER = 1.159402E 02 -QDOT/(TSTAG-TWALL) = 4.191166E-02

ETA	Y(FT)	U/UE	W/WE	H/HE	T/TE	MACH	PITOT	EV/MU
0	0	0	0	.47581	.86382	0	.48747	0
.010	2.17096E-06	.03992	.02978	.48787	.88498	.06391	.48887	.00013
.021	4.53495E-06	.08245	.06156	.50101	.90644	.13057	.49331	.00219
.032	7.10620E-06	.12754	.09536	.51527	.92799	.19988	.50124	.01120
.044	9.90749E-06	.17485	.13089	.53063	.94930	.27127	.51305	.03544
.057	1.29496E-05	.22351	.16756	.54689	.96990	.34355	.52895	.08534
.070	1.62505E-05	.27224	.20438	.56370	.98923	.41493	.54879	.17128
.085	1.98257E-05	.31957	.24026	.58057	1.00684	.48349	.57201	.30146
.100	2.36892E-05	.36429	.27427	.59702	1.02244	.54771	.59775	.48122
.116	2.78551E-05	.40565	.30585	.61269	1.03594	.60677	.62509	.71412
.134	3.23372E-05	.44338	.33475	.62734	1.04746	.66045	.65326	1.00343
.152	3.71503E-05	.47752	.36100	.64090	1.05718	.70896	.68163	1.35283
.172	4.23101E-05	.50830	.38477	.65336	1.06534	.75274	.70978	1.76651
.193	4.78338E-05	.53604	.40628	.66476	1.07218	.79228	.73742	2.24902
.215	5.37399E-05	.56109	.42579	.67521	1.07792	.82810	.76439	2.80514
.238	6.00490E-05	.58376	.44352	.68479	1.08274	.86068	.79059	3.43973
.263	6.67831E-05	.60437	.45972	.69359	1.08679	.89045	.81600	4.15763
.290	7.39660E-05	.62318	.47457	.70170	1.09021	.91777	.84062	4.96361
.318	8.16237E-05	.64042	.48825	.70921	1.09310	.94298	.86448	5.86221
.348	8.97837E-05	.65629	.50092	.71619	1.09556	.96636	.88763	6.85778
.380	9.84758E-05	.67098	.51270	.72270	1.09765	.98814	.91012	7.95432
.414	1.07732E-04	.68462	.52371	.72880	1.09943	1.00854	.93202	9.15549
.450	1.17586E-04	.69736	.53404	.73455	1.10094	1.02774	.95336	10.46457
.488	1.28074E-04	.70929	.54379	.73998	1.10224	1.04588	.97416	11.88444
.529	1.39235E-04	.72052	.55302	.74513	1.10334	1.06311	.99447	13.41760
.572	1.51110E-04	.73113	.56181	.75004	1.10428	1.07953	1.01431	15.06619
.618	1.63743E-04	.74120	.57019	.75474	1.10507	1.09525	1.03375	16.83207
.667	1.77181E-04	.75077	.57823	.75925	1.10573	1.11036	1.05282	18.71689
.719	1.91473E-04	.75991	.58596	.76360	1.10628	1.12493	1.07157	20.72222
.775	2.06672E-04	.76867	.59343	.76780	1.10673	1.13903	1.09005	22.84969
.834	2.22835E-04	.77707	.60066	.77187	1.10709	1.15272	1.10830	25.10112
.896	2.40022E-04	.78517	.60768	.77584	1.10737	1.16606	1.12637	27.47875
.963	2.58294E-04	.79298	.61453	.77970	1.10757	1.17908	1.14428	29.98540
1.033	2.77721E-04	.80054	.62121	.78348	1.10769	1.19184	1.16208	32.62465
1.108	2.98374E-04	.80787	.62776	.78719	1.10776	1.20437	1.17979	35.40103
1.188	3.20328E-04	.81498	.63418	.79083	1.10776	1.21669	1.19746	38.32015

1.273	3.43665E-04	.82190	.64050	.79441	1.10770	1.22884	1.21509	41.38885
1.363	3.68470E-04	.82863	.64672	.79794	1.10759	1.24084	1.23273	44.61527
1.459	3.94835E-04	.83519	.65286	.80143	1.10742	1.25270	1.25039	48.00892
1.561	4.22855E-04	.84158	.65892	.80488	1.10720	1.26446	1.26808	51.58062
1.669	4.52635E-04	.84782	.66491	.80830	1.10693	1.27612	1.28583	55.34250
1.784	4.84282E-04	.85391	.67085	.81168	1.10661	1.28770	1.30365	59.30792
1.907	5.17912E-04	.85986	.67673	.81503	1.10624	1.29920	1.32155	63.49132
2.037	5.53649E-04	.86565	.68256	.81836	1.10583	1.31064	1.33953	67.90809
2.175	5.91621E-04	.87131	.68834	.82167	1.10537	1.32202	1.35761	72.57448
2.322	6.31969E-04	.87683	.69408	.82495	1.10486	1.33334	1.37579	77.50739
2.479	6.74838E-04	.88220	.69978	.82822	1.10431	1.34462	1.39407	82.72433
2.645	7.20384E-04	.88744	.70543	.83146	1.10372	1.35586	1.41246	88.24326
2.822	7.68772E-04	.89253	.71105	.83468	1.10308	1.36705	1.43096	94.08249
3.009	8.20178E-04	.89748	.71664	.83789	1.10240	1.37821	1.44957	100.26138
3.209	8.74788E-04	.90228	.72218	.84107	1.10168	1.38933	1.46829	106.79408
3.421	9.32800E-04	.90694	.72769	.84424	1.10092	1.40041	1.48711	113.71667
3.647	9.94422E-04	.91145	.73316	.84739	1.10012	1.41145	1.50605	121.05125
3.886	1.05988E-03	.91581	.73860	.85052	1.09928	1.42247	1.52510	128.54728
4.141	1.12940E-03	.91999	.74398	.85362	1.09842	1.43340	1.54417	138.07004
4.412	1.20325E-03	.92413	.74946	.85679	1.09750	1.44456	1.56381	138.09829
4.700	1.28160E-03	.92835	.75525	.86013	1.09648	1.45640	1.58482	137.62266
5.006	1.36497E-03	.93265	.76137	.86366	1.09534	1.46896	1.60733	137.19244
5.331	1.45340E-03	.93703	.76783	.86739	1.09408	1.48228	1.63143	136.66438
5.677	1.54730E-03	.94146	.77465	.87134	1.09268	1.49640	1.65724	136.06124
6.045	1.64698E-03	.94593	.78183	.87550	1.09113	1.51135	1.68487	135.36683
6.436	1.75277E-03	.95042	.78940	.87988	1.08941	1.52717	1.71444	134.56720
6.851	1.86505E-03	.95490	.79735	.88449	1.08751	1.54391	1.74607	133.64673
7.293	1.98418E-03	.95936	.80570	.88934	1.08541	1.56158	1.77989	132.58735
7.762	2.11056E-03	.96376	.81446	.89442	1.08310	1.58023	1.81601	131.36826
8.261	2.24460E-03	.96809	.82361	.89974	1.08055	1.59987	1.85457	129.96544
8.792	2.38673E-03	.97229	.83316	.90530	1.07775	1.62053	1.89567	128.35119
9.356	2.53740E-03	.97635	.84311	.91109	1.07469	1.64221	1.93940	126.49351
9.955	2.69709E-03	.98023	.85343	.91710	1.07134	1.66491	1.98585	124.35548
10.592	2.86629E-03	.98390	.86410	.92331	1.06769	1.68861	2.03507	121.89444
11.270	3.04551E-03	.98731	.87509	.92972	1.06374	1.71326	2.08707	119.06119
11.990	3.23528E-03	.99043	.88637	.93628	1.05948	1.73882	2.14179	115.79894
12.755	3.43617E-03	.99323	.89786	.94296	1.05491	1.76517	2.19911	112.04236
13.569	3.64877E-03	.99569	.90950	.94972	1.05004	1.79219	2.25883	107.71631
14.433	3.87368E-03	.99776	.92119	.95650	1.04489	1.81970	2.32059	102.73484
15.353	4.11156E-03	.99945	.93282	.96322	1.03951	1.84745	2.38388	96.99975
16.330	4.36310E-03	1.00072	.94426	.96980	1.03394	1.87513	2.44800	90.40016
17.369	4.62903E-03	1.00160	.95532	.97612	1.02826	1.90233	2.51199	82.80938
18.473	4.91016E-03	1.00208	.96581	.98206	1.02258	1.92854	2.57454	74.09350
19.647	5.20737E-03	1.00221	.97547	.98746	1.01705	1.95312	2.63401	64.10901
20.895	5.52163E-03	1.00205	.98401	.99215	1.01183	1.97529	2.68829	52.51391
22.221	5.85408E-03	1.00169	.99103	.99589	1.00724	1.99392	2.73442	39.90544
23.631	6.20600E-03	1.00125	.99617	.99850	1.00337	2.00813	2.76988	24.25755
25.130	6.57895E-03	1.00090	.99925	.99986	1.00118	2.01654	2.79101	1.70822
26.723	6.97528E-03	1.00122	.99701	.99855	1.00270	2.01049	2.77580	.73847
28.416	7.39655E-03	1.00084	.99915	.99974	1.00110	2.01642	2.79069	.58714
30.217	7.84438E-03	1.00125	.99704	.99861	1.00280	2.01045	2.77569	.47738
32.130	8.32040E-03	1.00075	.99918	.99972	1.00099	2.01659	2.79112	.40190
34.164	8.82645E-03	1.00130	.99697	.99861	1.00293	2.01018	2.77501	.34017
36.327	9.36433E-03	1.00062	.99928	.99974	1.00083	2.01695	2.79203	.29601
38.625	9.93615E-03	1.00137	.99684	.99857	1.00311	2.00973	2.77388	.25696
41.069	1.05439E-02	1.00047	.99945	.99979	1.00063	2.01750	2.79341	.22873
43.666	1.11901E-02	1.00146	.99664	.99850	1.00335	2.00909	2.77228	.20190
46.427	1.18768E-02	1.00026	.99969	.99988	1.00035	2.01825	2.79529	.18274
49.362	1.26070E-02	1.00158	.99636	.99839	1.00366	2.00823	2.77013	.16318
52.482	1.33830E-02	1.00000	1.00000	1.00000	1.00000	2.01924	2.79779	0

NAR-ORBITER CENTERLINE * STATION 840 * ALPHA=40 DEG * REINF/FT=3.76E+06 * VKF B

INFINITE YAWED BLUNT-BODY STAGNATION LINE COMPRESSIBLE LAMINAR BOUNDARY-LAYER ANALYSIS

FREE-STREAM MACH NUMBER = 8.000000E 00 PINF (LBF/FT2) = 1.220000E 01 TINF (DEG R) = 9.700000E 01

TWALL (DEG R) = 5.400000E 02 YAW ANGLE (DEG) = 5.000000E 01 POP (LBF/FT2) = 4.814100E 02

TOP (DEG R) = 7.097628E 02 TSTAG (DEG R) = 1.338600E 03 WE (FT/SEC) = 2.748380E 03

NOSE RADIUS (FT) = 0 X* (FT) = 0 DUE/DX (1/SEC) = 9.418030E 03

TWALL/TSTAG = 4.034065E-01 ANGLE OF ATTACK (DEG) = 4.000000E 01 SHOCK ANGLE (DEG) = 4.000000E 01

THERMALLY AND CALORICALLY PERFECT GAS MODEL

CP= 6006.00 FT2/(SEC2-DEG R) R= 1716.00 FT2/(SEC2-DEG R) GAMMA= 1.4000 PR= .7100 CSTAR= 198.60 DEG R

VISCOSITY CONSTANT= 2.2722E-08 LBF-SEC/(FT2-SQRT(DEG R)) KPL= .4350 LAMBDA= .0900 ASTAR= 26.000 PRT= .9000

INVISCID CENTERLINE PRESSURE (POP) AND VELOCITY (WE) INPUT TO ANALYSIS

STAGNATION POINT VELOCITY GRADIENT (DUEDX) INPUT TO ANALYSIS

NAR-ORBITER CENTERLINE = STATION 840 = ALPHA=40 DEG = RE1NF/FT=3.76E+06 = VKF H

INFINITE YAWED BLUNT-BODY STAGNATION LINE COMPRESSIBLE LAMINAR BOUNDARY-LAYER ANALYSIS

X (FT) = 0 X1 = 0 BETA = 1.000000E 00 PE/POP = 1.000000E 00 S/RN = 0

UE (FT/SEC) = 0 WE (FT/SEC) = 2.748380E 03 PE (LBF/FT2) = 4.814100E 02 TE (DEG R) = 7.097628E 02

RHOE (SLUG/FT3) = 3.952616E-04 MUE (LBF-SEC/FT2) = 4.729956E-07 DUE/DX (1/SEC) = 9.418030E 03 ITERATIONS = 12

FPP(0) = 1.123676E 00 CP(0) = 5.344535E-01 HP(0) = 2.465192E-01 QDOT = -5.105579E 00 BTU/(FT2-SEC)

ST(INF) = 2.926751E-03 CFX(INF) = 0 CFZ(INF) = 3.825516E-03 RSP = 5.142301E 00

DELTA* (FT) = 3.774188E-04 THETAMOM (FT) = 1.423912E-04 EDGE REY/FT = 2.296700E 06 EDGE REYTHETAMOM = 3.270300E 02

EDGE MACH NO = 2.104735E 00 MCDONNELL-DOUGLAS TRANSITION PARAMETER = 8.301742E 00 -QDOT/(TSTAG-TWALL) = 6.393162E-03

ETA	Y(FT)	U/UE	W/WE	H/HE	T/TE	MACH	PITOT	EV/MU
0	0	0	0	.40341	.76082	0	.47619	0
.010	2.72025E-06	.01121	.00535	.40588	.76546	.01287	.47625	0
.021	5.62594E-06	.02306	.01104	.40852	.77035	.02648	.47643	0
.032	8.74322E-06	.03559	.01710	.41134	.77552	.04088	.47675	0
.044	1.20754E-05	.04883	.02356	.41435	.78098	.05610	.47724	0
.057	1.56430E-05	.06282	.03043	.41757	.78673	.07220	.47793	0
.070	1.94639E-05	.07757	.03775	.42101	.79279	.08923	.47885	0
.085	2.35575E-05	.09314	.04554	.42469	.79916	.10722	.48003	0
.100	2.79447E-05	.10955	.05384	.42864	.80587	.12623	.48152	0
.116	3.26483E-05	.12683	.06268	.43285	.81292	.14632	.48337	0
.134	3.76929E-05	.14502	.07209	.43737	.82032	.16754	.48561	0
.152	4.31051E-05	.16415	.08213	.44221	.82808	.18995	.48833	0
.172	4.89137E-05	.18424	.09281	.44739	.83621	.21362	.49158	0
.193	5.51500E-05	.20532	.10419	.45295	.84472	.23861	.49544	0
.215	6.18477E-05	.22741	.11632	.45891	.85360	.26499	.50001	0
.238	6.90434E-05	.25054	.12924	.46531	.86286	.29284	.50539	0
.263	7.67767E-05	.27470	.14300	.47217	.87249	.32222	.51171	0
.290	8.50501E-05	.29991	.15766	.47954	.88249	.35323	.51910	0
.318	9.40298E-05	.32616	.17327	.48745	.89285	.38594	.52772	0
.348	1.03645E-04	.35344	.18988	.49595	.90354	.42045	.53777	0
.380	1.13990E-04	.38173	.20757	.50508	.91455	.45683	.54946	0
.414	1.25122E-04	.41098	.22639	.51489	.92583	.49520	.56307	0
.450	1.37101E-04	.44115	.24639	.52544	.93735	.53564	.57889	0
.488	1.49994E-04	.47217	.26765	.53677	.94905	.57826	.59728	0
.529	1.63869E-04	.50394	.29022	.54894	.96087	.62314	.61868	0
.572	1.78802E-04	.53636	.31414	.56201	.97271	.67040	.64360	0
.618	1.94869E-04	.56928	.33948	.57603	.98449	.72012	.67263	0
.667	2.12153E-04	.60256	.36626	.59106	.99610	.77238	.70650	0
.719	2.30738E-04	.63601	.39450	.60714	1.00740	.82727	.74606	0
.775	2.50712E-04	.66941	.42422	.62432	1.01824	.88483	.79232	0
.834	2.72166E-04	.70252	.45538	.64262	1.02847	.94510	.84644	0
.896	2.95190E-04	.73510	.48794	.66205	1.03790	1.00806	.90993	0
.963	3.19876E-04	.76684	.52180	.68260	1.04636	1.07366	.98385	0
1.033	3.46316E-04	.79747	.55684	.70423	1.05365	1.14177	1.06837	0
1.108	3.74599E-04	.82667	.59285	.72685	1.05961	1.21220	1.16343	0
1.188	4.04812E-04	.85415	.62960	.75033	1.06406	1.28464	1.26886	0

1.273	4.37039E-04	.87962	.66677	.77448	1.06690	1.35866	1.38428	0
1.363	4.71360E-04	.90282	.70397	.79906	1.06803	1.43371	1.50897	0
1.459	5.07652E-04	.92355	.74077	.82374	1.06744	1.50907	1.64175	0
1.561	5.46592E-04	.94166	.77667	.84816	1.06521	1.58386	1.78091	0
1.669	5.87657E-04	.95707	.81113	.87190	1.06146	1.65706	1.92413	0
1.784	6.31129E-04	.96979	.84361	.89450	1.05644	1.72750	2.06846	0
1.907	6.77099E-04	.97993	.87358	.91551	1.05043	1.79398	2.21046	0
2.037	7.25672E-04	.98767	.90057	.93449	1.04379	1.85528	2.34634	0
2.175	7.76972E-04	.99327	.92421	.95110	1.03690	1.91029	2.47233	0
2.322	8.31145E-04	.99706	.94426	.96510	1.03012	1.95815	2.58502	0
2.479	8.88365E-04	.99939	.96065	.97640	1.02376	1.99832	2.68184	0
2.645	9.48833E-04	1.00064	.97351	.98506	1.01808	2.03070	2.76135	0
2.822	1.01278E-03	1.00113	.98311	.99130	1.01323	2.05563	2.82344	0
3.009	1.08046E-03	1.00116	.98989	.99548	1.00928	2.07385	2.86932	0
3.209	1.15215E-03	1.00095	.99437	.99802	1.00621	2.08642	2.90123	0
3.421	1.22816E-03	1.00068	.99713	.99939	1.00396	2.09456	2.92198	0
3.647	1.30881E-03	1.00043	.99867	1.00000	1.00236	2.09947	2.93453	0
3.886	1.39442E-03	1.00024	.99946	1.00018	1.00132	2.10221	2.94156	0
4.141	1.48535E-03	1.00012	.99981	1.00017	1.00068	2.10361	2.94517	0
4.412	1.58196E-03	1.00005	.99994	1.00011	1.00032	2.10428	2.94687	0
4.700	1.68463E-03	1.00002	.99999	1.00005	1.00014	2.10456	2.94760	0
5.006	1.79375E-03	1.00001	1.00000	1.00002	1.00005	2.10468	2.94789	0
5.331	1.90974E-03	1.00000	1.00000	1.00001	1.00002	2.10472	2.94799	0
5.677	2.03303E-03	1.00000	1.00000	1.00000	1.00001	2.10473	2.94803	0
6.045	2.16409E-03	1.00000	1.00000	1.00000	1.00000	2.10473	2.94804	0
6.436	2.30341E-03	1.00000	1.00000	1.00000	1.00000	2.10473	2.94804	0
6.851	2.45150E-03	1.00000	1.00000	1.00000	1.00000	2.10473	2.94804	0
7.293	2.60892E-03	1.00000	1.00000	1.00000	1.00000	2.10473	2.94804	0
7.762	2.77627E-03	1.00000	1.00000	1.00000	1.00000	2.10473	2.94804	0
8.261	2.95415E-03	1.00000	1.00000	1.00000	1.00000	2.10474	2.94805	0
8.792	3.14324E-03	1.00000	1.00000	1.00000	1.00000	2.10474	2.94805	0
9.356	3.34424E-03	1.00000	1.00000	1.00000	1.00000	2.10474	2.94805	0
9.955	3.55791E-03	1.00000	1.00000	1.00000	1.00000	2.10474	2.94805	0
10.592	3.78503E-03	1.00000	1.00000	1.00000	1.00000	2.10474	2.94805	0
11.270	4.02647E-03	1.00000	1.00000	1.00000	1.00000	2.10474	2.94805	0
11.990	4.28312E-03	1.00000	1.00000	1.00000	1.00000	2.10474	2.94805	0
12.755	4.55593E-03	1.00000	1.00000	1.00000	1.00000	2.10474	2.94805	0
13.569	4.84593E-03	1.00000	1.00000	1.00000	1.00000	2.10474	2.94805	0
14.433	5.15420E-03	1.00000	1.00000	1.00000	1.00000	2.10474	2.94805	0
15.353	5.48190E-03	1.00000	1.00000	1.00000	1.00000	2.10474	2.94805	0
16.330	5.83024E-03	1.00000	1.00000	1.00000	1.00000	2.10474	2.94805	0
17.369	6.20052E-03	1.00000	1.00000	1.00000	1.00000	2.10474	2.94805	0
18.473	6.59413E-03	1.00000	1.00000	1.00000	1.00000	2.10474	2.94805	0
19.647	7.01254E-03	1.00000	1.00000	1.00000	1.00000	2.10474	2.94805	0
20.895	7.45731E-03	1.00000	1.00000	1.00000	1.00000	2.10474	2.94805	0
22.221	7.93010E-03	1.00000	1.00000	1.00000	1.00000	2.10474	2.94805	0
23.631	8.43267E-03	1.00000	1.00000	1.00000	1.00000	2.10474	2.94805	0
25.130	8.96691E-03	1.00000	1.00000	1.00000	1.00000	2.10474	2.94805	0
26.723	9.53480E-03	1.00000	1.00000	1.00000	1.00000	2.10474	2.94805	0
28.416	1.01385E-02	1.00000	1.00000	1.00000	1.00000	2.10474	2.94805	0
30.217	1.07802E-02	1.00000	1.00000	1.00000	1.00000	2.10474	2.94805	0
32.130	1.14623E-02	1.00000	1.00000	1.00000	1.00000	2.10474	2.94805	0
34.164	1.21874E-02	1.00000	1.00000	1.00000	1.00000	2.10474	2.94805	0
36.327	1.29582E-02	1.00000	1.00000	1.00000	1.00000	2.10474	2.94805	0
38.625	1.37775E-02	1.00000	1.00000	1.00000	1.00000	2.10474	2.94805	0
41.069	1.46485E-02	1.00000	1.00000	1.00000	1.00000	2.10474	2.94805	0
43.666	1.55743E-02	1.00000	1.00000	1.00000	1.00000	2.10474	2.94805	0
46.427	1.65585E-02	1.00000	1.00000	1.00000	1.00000	2.10474	2.94805	0
49.362	1.76047E-02	1.00000	1.00000	1.00000	1.00000	2.10474	2.94805	0
52.482	1.87167E-02	1.00000	1.00000	1.00000	1.00000	2.10474	2.94805	0

NAR-ORBITER CENTERLINE * STATION 840 * ALPHA=40 DEG * REINF/FT=3.76E+06 * VKF R

INFINITE YAWED BLUNT-BODY STAGNATION LINE COMPRESSIBLE TURBULENT BOUNDARY-LAYER ANALYSIS

FREE-STREAM MACH NUMBER = 8.000000E 00 PINF (LBF/FT2) = 1.220000E 01 TINF (DEG R) = 9.700000E 01

TWALL (DEG R) = 5.400000E 02 YAW ANGLE (DEG) = 5.000000E 01 POP (LBF/FT2) = 4.814100E 02

TOP (DEG R) = 7.097628E 02 TSTAG (DEG R) = 1.338600E 03 WE (FT/SEC) = 2.748380E 03

NOSE RADIUS (FT) = 0 X* (FT) = 0 DUE/DX (1/SEC) = 9.418030E 03

TWALL/TSTAG = 4.03406SE-01 ANGLE OF ATTACK (DEG) = 4.000000E 01 SHOCK ANGLE (DEG) = 4.000000E 01

THERMALLY AND CALORICALLY PERFECT GAS MODEL

CP= 6006.00 FT2/(SEC2-DEG R) R= 1716.00 FT2/(SEC2-DEG R) GAMMA= 1.4000 PR= .7100 CSTAR= 198.60 DEG R

VISCOSITY CONSTANT= 2.2722E-08 LBF-SEC/(FT2-SQRT(DEG R)) KPL= .4350 LAMBDA= .0900 ASTAR= 26.000 PWT= .9000

INVISCID CENTERLINE PRESSURE (POP) AND VELOCITY (WE) INPUT TO ANALYSIS

STAGNATION POINT VELOCITY GRADIENT (DUEDX) INPUT TO ANALYSIS

NAR-OHHITER CENTERLINE • STATION 840 • ALPHA=40 DEG • RE1NF/FT=3.76E+06 • VKF 8

INFINITE YAWED BLUNT-BODY STAGNATION LINE COMPRESSIBLE TURBULENT BOUNDARY-LAYER ANALYSIS

X (FT) = 0 X1 = 0 BETA = 1.000000E 00 PE/POP = 1.000000E 00 S/RN = 0

UE (FT/SEC) = 0 WE (FT/SEC) = 2.748380E 03 PE (LBF/FT2) = 4.814100E 02 TE (DEG R) = 7.097628E 02

RHOE (SLUG/FT3) = 3.952616E-04 MUE (LBF-SEC/FT2) = 4.729956E-07 DUE/DX (1/SEC) = 9.418030E 03 ITERATIONS = 68

FPP(0) = 2.128431E 00 CP(0) = 1.473314E 00 GP(0) = 6.808752E-01 QDOT = -1.410138E 01 BTU/(FT2-SEC)

ST(1NF) = 8.083557E-03 CFX(1NF) = 0 CFZ(1NF) = 1.054570E-02 HSP = 5.142301E 00

DELTA* (FT) = 8.677825E-04 THETAMOM (FT) = 4.608428E-04 EDGE REY/FT = 2.296700E 06 EDGE REYTHETAMOM = 1.058418E 03

EDGE MACH NO = 2.104735E 00 MCDONNELL-DOUGLAS TRANSITION PARAMETER = 2.686821E 01 -QDOT/(TSTAG-TWALL) = 1.765763E-02

ETA	Y(FT)	U/UE	W/WE	H/HE	T/TE	MACH	P1TOT	EV/MU.
0	0	0	0	.40341	.76082	0	.47619	0
.010	2.73466E-06	.02129	.01476	.41026	.77354	.03532	.47661	.00001
.021	5.69086E-06	.04393	.03051	.41764	.78682	.07240	.47794	.00010
.032	8.88788E-06	.06799	.04732	.42558	.80064	.11131	.48033	.00052
.044	1.23466E-05	.09356	.06525	.43414	.81499	.15213	.48395	.00174
.057	1.60897E-05	.12068	.08436	.44337	.82985	.19490	.48897	.00449
.070	2.01416E-05	.14938	.10468	.45329	.84516	.23965	.49561	.00984
.085	2.45285E-05	.17966	.12622	.46395	.86084	.28633	.50408	.01920
.100	2.92782E-05	.21143	.14895	.47536	.87679	.33481	.51462	.03438
.116	3.44202E-05	.24455	.17279	.48749	.89288	.38487	.52742	.05753
.134	3.99855E-05	.27876	.19757	.50032	.90893	.43618	.54268	.09107
.152	4.60060E-05	.31374	.22309	.51376	.92475	.48828	.56051	.13757
.172	5.25147E-05	.34909	.24906	.52768	.94014	.54065	.58095	.19962
.193	5.95453E-05	.38438	.27519	.54195	.95490	.59273	.60395	.27974
.215	6.71321E-05	.41918	.30117	.55640	.96887	.64400	.62937	.38039
.238	7.53102E-05	.45310	.32672	.57085	.98191	.69397	.65699	.50395
.263	8.41152E-05	.48583	.35160	.58515	.99394	.74227	.68656	.65287
.290	9.35838E-05	.51713	.37561	.59918	1.00491	.78863	.71777	.82970
.318	1.03754E-04	.54684	.39864	.61280	1.01482	.83287	.75035	1.03714
.348	1.14666E-04	.57488	.42059	.62596	1.02369	.87492	.78399	1.27811
.380	1.26360E-04	.60120	.44142	.63858	1.03158	.91475	.81845	1.55570
.414	1.38881E-04	.62584	.46115	.65064	1.03855	.95241	.85348	1.87321
.450	1.52275E-04	.64883	.47977	.66213	1.04469	.98796	.88888	2.23410
.488	1.66592E-04	.67026	.49734	.67304	1.05006	1.02152	.92447	2.64200
.529	1.81883E-04	.69021	.51391	.68339	1.05474	1.05320	.95998	3.10061
.572	1.98206E-04	.70877	.52953	.69321	1.05881	1.08312	.99515	3.61376
.618	2.15619E-04	.72604	.54427	.70251	1.06234	1.11142	1.02978	4.18530
.667	2.34187E-04	.74213	.55819	.71134	1.06540	1.13821	1.06377	4.81910
.719	2.53977E-04	.75711	.57135	.71972	1.06802	1.16361	1.09705	5.51900
.775	2.75062E-04	.77109	.58382	.72768	1.07028	1.18775	1.12958	6.28877
.834	2.97520E-04	.78414	.59565	.73526	1.07221	1.21073	1.16137	7.13205
.896	3.21432E-04	.79634	.60689	.74248	1.07385	1.23265	1.19243	8.05232
.963	3.46886E-04	.80776	.61761	.74937	1.07523	1.25360	1.22277	9.05288
1.033	3.73976E-04	.81847	.62784	.75597	1.07639	1.27368	1.25244	10.13676
1.108	4.02800E-04	.82852	.63763	.76230	1.07735	1.29296	1.28146	11.30672
1.188	4.33466E-04	.83796	.64701	.76838	1.07813	1.31152	1.30990	12.56524

1.273	4.66085E-04	.84686	.65603	.77423	1.07875	1.32942	1.33779	13.91453
1.363	5.00776E-04	.85523	.66472	.77987	1.07923	1.34673	1.36517	15.35635
1.459	5.37667E-04	.86313	.67311	.78533	1.07958	1.36351	1.39210	16.89222
1.561	5.76893E-04	.87059	.68123	.79062	1.07981	1.37980	1.41863	18.52435
1.669	6.18597E-04	.87764	.68910	.79575	1.07994	1.39565	1.44479	20.25052
1.784	6.62931E-04	.88431	.69674	.80074	1.07997	1.41112	1.47063	22.07544
1.907	7.10058E-04	.89061	.70418	.80561	1.07991	1.42622	1.49618	24.02225
2.037	7.60149E-04	.89658	.71144	.81036	1.07977	1.44103	1.52153	25.94763
2.175	8.13388E-04	.90218	.71849	.81499	1.07956	1.45545	1.54650	28.52160
2.322	8.69967E-04	.90765	.72561	.81966	1.07927	1.47006	1.57207	28.37566
2.479	9.30092E-04	.91323	.73314	.82460	1.07887	1.48559	1.59957	28.25081
2.645	9.93978E-04	.91890	.74109	.82983	1.07835	1.50207	1.62910	28.10361
2.822	1.06185E-03	.92463	.74949	.83535	1.07769	1.51955	1.66081	27.93696
3.009	1.13395E-03	.93040	.75834	.84118	1.07688	1.53808	1.69487	27.74796
3.209	1.21053E-03	.93619	.76766	.84733	1.07588	1.55771	1.73142	27.53288
3.421	1.29185E-03	.94197	.77746	.85380	1.07468	1.57847	1.77063	27.28795
3.647	1.37818E-03	.94770	.78774	.86060	1.07326	1.60040	1.81267	27.00878
3.886	1.46983E-03	.95335	.79851	.86773	1.07159	1.62354	1.85769	26.69030
4.141	1.56708E-03	.95887	.80976	.87519	1.06964	1.64791	1.90585	26.32659
4.412	1.67026E-03	.96423	.82147	.88297	1.06739	1.67352	1.95728	25.91083
4.700	1.77969E-03	.96938	.83364	.89106	1.06481	1.70036	2.01210	25.43509
5.006	1.89571E-03	.97428	.84624	.89944	1.06189	1.72842	2.07038	24.89017
5.331	2.01868E-03	.97888	.85920	.90807	1.05859	1.75764	2.13213	24.26540
5.677	2.14897E-03	.98313	.87250	.91693	1.05491	1.78794	2.19731	23.54843
6.045	2.28696E-03	.98699	.88604	.92596	1.05085	1.81919	2.26576	22.72497
6.436	2.43305E-03	.99042	.89973	.93508	1.04641	1.85122	2.33719	21.77853
6.851	2.58766E-03	.99338	.91345	.94423	1.04161	1.88378	2.41115	20.69015
7.293	2.75123E-03	.99584	.92706	.95328	1.03648	1.91657	2.48694	19.43823
7.762	2.92423E-03	.99780	.94037	.96211	1.03111	1.94915	2.56361	17.99830
8.261	3.10715E-03	.99925	.95317	.97056	1.02557	1.98100	2.63985	16.34304
8.792	3.30055E-03	1.00020	.96518	.97844	1.02000	2.01145	2.71391	14.44345
9.356	3.50503E-03	1.00069	.97610	.98554	1.01457	2.03964	2.78352	12.26801
9.955	3.72126E-03	1.00080	.98555	.99158	1.00950	2.06453	2.84582	9.78055
10.592	3.95005E-03	1.00063	.99306	.99627	1.00511	2.08481	2.89711	7.01888
11.270	4.19231E-03	1.00034	.99819	.99931	1.00168	2.09916	2.93374	3.74531
11.990	4.44918E-03	1.00013	1.00032	1.00038	1.00010	2.10530	2.94949	.52663
12.755	4.72210E-03	1.00024	.99944	.99977	1.00064	2.10288	2.94329	.16826
13.569	5.01221E-03	1.00015	1.00003	1.00009	1.00011	2.10469	2.94792	.09595
14.433	5.32059E-03	1.00023	.99959	.99989	1.00059	2.10325	2.94424	.05814
15.353	5.64840E-03	1.00015	.99994	1.00003	1.00016	2.10444	2.94729	.03324
16.330	5.99687E-03	1.00024	.99965	.99993	1.00055	2.10342	2.94466	.02095
17.369	6.36729E-03	1.00015	.99990	1.00000	1.00019	2.10433	2.94700	.01433
18.473	6.76104E-03	1.00024	.99967	.99994	1.00052	2.10350	2.94486	.01041
19.647	7.17960E-03	1.00014	.99989	.99999	1.00021	2.10428	2.94687	.00801
20.895	7.62453E-03	1.00024	.99968	.99995	1.00052	2.10353	2.94495	.00643
22.221	8.09749E-03	1.00014	.99988	.99999	1.00021	2.10426	2.94682	.00539
23.631	8.60025E-03	1.00025	.99969	.99995	1.00052	2.10353	2.94496	.00466
25.130	9.13468E-03	1.00013	.99988	.99999	1.00021	2.10426	2.94683	.00418
26.723	9.70279E-03	1.00026	.99968	.99995	1.00052	2.10352	2.94492	.00383
28.416	1.03067E-02	1.00012	.99989	.99999	1.00020	2.10429	2.94690	.00361
30.217	1.09486E-02	1.00027	.99968	.99995	1.00054	2.10349	2.94484	.00341
32.130	1.16310E-02	1.00011	.99990	.99999	1.00018	2.10433	2.94700	.00299
34.164	1.23564E-02	1.00028	.99966	.99995	1.00056	2.10343	2.94471	.00264
36.327	1.31274E-02	1.00009	.99991	.99999	1.00015	2.10439	2.94716	.00235
38.625	1.39471E-02	1.00030	.99964	.99995	1.00060	2.10336	2.94452	.00210
41.069	1.48183E-02	1.00007	.99993	.99999	1.00011	2.10448	2.94738	.00189
43.666	1.57445E-02	1.00032	.99962	.99995	1.00064	2.10326	2.94427	.00171
46.427	1.67290E-02	1.00004	.99996	1.00000	1.00006	2.10459	2.94767	.00156
49.362	1.77756E-02	1.00035	.99959	.99994	1.00069	2.10314	2.94394	.00142
52.482	1.88881E-02	1.00000	1.00000	1.00000	1.00000	2.10474	2.94805	0

NASA LRC 75-OEG SWEEP DELTA WING • Z/L=0.2 • REINF/FT=3.77E+06 • VKF B

INFINITE YAWED BLUNT-BODY STAGNATION LINE COMPRESSIBLE LAMINAR BOUNDARY-LAYER ANALYSIS

FREE-STREAM MACH NUMBER = 8.000000E 00 PINF (LBF/FT2) = 1.281600E 01 TINF (OEG R) = 9.730000E 01

TWALL (OEG R) = 8.600000E 02 YAW ANGLE (OEG) = 3.000000E 01 POP (LBF/FT2) = 8.740500E 02

TOP (DEG R) = 1.152083E 03 TSTAG (OEG R) = 1.342740E 03 WE (FT/SEC) = 1.513330E 03

NOSE RADIUS (FT) = 0 X• (FT) = 0 DUE/DX (1/SEC) = 5.506300E 03

TWALL/TSTAG = 6.404814E-01 ANGLE OF ATTACK (OEG) = 6.000000E 01 SHOCK ANGLE (DEG) = 6.000000E 01

THERMALLY AND CALORICALLY PERFECT GAS MODEL

CP= 6006.00 FT2/(SEC2-DEG R) R= 1716.00 FT2/(SEC2-DEG R) GAMMA= 1.4000 PR= .7100 CSTAR= 198.60 DEG R

VISCOSITY CONSTANT= 2.2722E-08 LBF-SEC/(FT2-SQRT(DEG R)) KNL= .4350 LAMBDA= .0900 ASTAR= 26.000 PRT= .9000

INVISCID CENTERLINE PRESSURE (POP) AND VELOCITY (WE) INPUT TO ANALYSIS

STAGNATION POINT VELOCITY GRADIENT (DUEDX) INPUT TO ANALYSIS

NASA LRC 75-DEG SWEEP DELTA WING • Z/L=0.2 • RE1NF/FT=3.77E+06 • VKF A

INFINITE YAWED BLUNT-BODY STAGNATION LINE COMPRESSIBLE LAMINAR BOUNDARY-LAYER ANALYSIS

X (FT) = 0 XI = 0 BETA = 1.000000E 00 PE/POP = 1.000000E 00 S/RN = 0

UE (FT/SEC) = 0 WE (FT/SEC) = 1.513330E 03 PE (LBF/FT2) = 8.740500E 02 TE (DEG R) = 1.152083E 03

RHOE (SLUG/FT3) = 4.421148E-04 MUE (LBF-SEC/FT2) = 6.578379E-07 DUE/DX (1/SEC) = 5.506300E 03 ITERATIONS = 12

FPP(0) = 1.035546E 00 CP(0) = 5.188135E-01 QP(0) = 1.535884E-01 QDOT = -3.127076E 00 BTU/(FT2-SEC)

ST(INF) = 2.827308E-03 CFX(INF) = 0 CFZ(INF) = 1.907657E-03 HSP = 6.928203E 00

DELTA* (FT) = 4.293572E-04 THETAMOM (FT) = 2.166028E-04 EDGE REY/FT = 1.017068E 06 EDGE REYTHETAMOM = 2.202997E 02

EDGE MACH NO = 9.096389E-01 MCDONNELL-DOUGLAS TRANSITION PARAMETER = 1.522912E 01 -QDOT/(TSTAG-TWALL) = 6.477764E-03

ETA	Y(FT)	U/UE	W/WE	H/HE	T/TE	MACH	PITOT	EV/MU
0	0	0	0	.64048	.74647	0	.82302	0
.010	3.88505E-06	.01033	.00519	.64202	.74826	.00546	.82304	0
.021	8.02504E-06	.02124	.01071	.64366	.75016	.01125	.82309	0
.032	1.24373E-05	.03276	.01659	.64540	.75217	.01740	.82319	0
.044	1.71405E-05	.04492	.02283	.64726	.75430	.02392	.82335	0
.057	2.21545E-05	.05775	.02948	.64925	.75655	.03083	.82357	0
.070	2.75008E-05	.07128	.03656	.65136	.75894	.03817	.82386	0
.085	3.32023E-05	.08554	.04409	.65361	.76147	.04596	.82424	0
.100	3.92838E-05	.10056	.05210	.65602	.76414	.05421	.82471	0
.116	4.57717E-05	.11636	.06062	.65858	.76697	.06296	.82531	0
.134	5.26946E-05	.13297	.06969	.66131	.76997	.07225	.82603	0
.152	6.00831E-05	.15043	.07934	.66423	.77313	.08208	.82691	0
.172	6.79702E-05	.16874	.08962	.66734	.77647	.09251	.82796	0
.193	7.63915E-05	.18795	.10055	.67067	.78001	.10356	.82922	0
.215	8.53850E-05	.20806	.11218	.67421	.78373	.11527	.83070	0
.238	9.49919E-05	.22909	.12456	.67800	.78767	.12767	.83245	0
.263	1.05257E-04	.25106	.13774	.68205	.79181	.14080	.83450	0
.290	1.16227E-04	.27398	.15176	.68637	.79618	.15471	.83689	0
.318	1.27954E-04	.29784	.16667	.69098	.80077	.16942	.83967	0
.348	1.40493E-04	.32264	.18253	.69591	.80561	.18498	.84290	0
.380	1.53905E-04	.34837	.19939	.70118	.81068	.20144	.84664	0
.414	1.68253E-04	.37499	.21732	.70681	.81601	.21883	.85094	0
.450	1.83608E-04	.40249	.23636	.71282	.82159	.23720	.85589	0
.488	2.00043E-04	.43081	.25659	.71924	.82743	.25659	.86158	0
.529	2.17641E-04	.45989	.27805	.72610	.83352	.27703	.86809	0
.572	2.36488E-04	.48965	.30080	.73342	.83988	.29857	.87553	0
.618	2.56677E-04	.52001	.32490	.74123	.84649	.32122	.88401	0
.667	2.78309E-04	.55086	.35038	.74955	.85334	.34502	.89367	0
.719	3.81492E-04	.58206	.37728	.75841	.86043	.36998	.90462	0
.775	3.26344E-04	.61347	.40563	.76783	.86774	.39610	.91701	0
.834	3.52988E-04	.64491	.43542	.77783	.87526	.42336	.93099	0
.896	3.81557E-04	.67621	.46663	.78843	.88294	.45172	.94670	0
.963	4.12194E-04	.70715	.49921	.79961	.89077	.48114	.96429	0
1.033	4.45050E-04	.73751	.53308	.81138	.89869	.51151	.98388	0
1.108	4.80287E-04	.76705	.56810	.82371	.90668	.54270	1.00557	0
1.188	5.18075E-04	.79554	.60407	.83655	.91467	.57455	1.02942	0

1.273	5.58595E-04	.82271	.64077	.84985	.92261	.60682	1.05542	0
1.363	6.02038E-04	.84835	.67786	.86352	.93043	.63924	1.08348	0
1.459	6.48603E-04	.87221	.71496	.87742	.93808	.67147	1.11339	0
1.561	6.98500E-04	.89410	.75162	.89142	.94549	.70314	1.14482	0
1.669	7.51949E-04	.91385	.78733	.90531	.95258	.73379	1.17726	0
1.784	8.09180E-04	.93135	.82152	.91891	.95931	.76297	1.21008	0
1.907	8.70430E-04	.94655	.85362	.93196	.96561	.79019	1.24246	0
2.037	9.35950E-04	.95943	.88308	.94423	.97144	.81501	1.27353	0
2.175	1.00600E-03	.97008	.90940	.95548	.97675	.83702	1.30238	0
2.322	1.08084E-03	.97863	.93220	.96553	.98150	.85592	1.32815	0
2.479	1.16077E-03	.98527	.95126	.97421	.98567	.87157	1.35020	0
2.645	1.24606E-03	.99025	.96654	.98144	.98925	.88397	1.36814	0
2.822	1.33702E-03	.99383	.97823	.98721	.99222	.89332	1.38195	0
3.009	1.43398E-03	.99629	.98668	.99162	.99461	.89995	1.39190	0
3.209	1.53727E-03	.99789	.99242	.99481	.99645	.90435	1.39856	0
3.421	1.64724E-03	.99888	.99603	.99698	.99780	.90703	1.40265	0
3.647	1.76427E-03	.99944	.99812	.99837	.99872	.90851	1.40492	0
3.886	1.88877E-03	.99975	.99921	.99919	.99932	.90923	1.40602	0
4.141	2.02118E-03	.99990	.99971	.99963	.99967	.90952	1.40648	0
4.412	2.16196E-03	.99996	.99991	.99985	.99986	.90962	1.40663	0
4.700	2.31164E-03	.99999	.99998	.99995	.99995	.90964	1.40666	0
5.006	2.47075E-03	1.00000	1.00000	.99998	.99998	.90964	1.40666	0
5.331	2.63989E-03	1.00000	1.00000	1.00000	1.00000	.90964	1.40666	0
5.677	2.81969E-03	1.00000	1.00000	1.00000	1.00000	.90964	1.40666	0
6.045	3.01082E-03	1.00000	1.00000	1.00000	1.00000	.90964	1.40666	0
6.436	3.21399E-03	1.00000	1.00000	1.00000	1.00000	.90964	1.40666	0
6.851	3.42996E-03	1.00000	1.00000	1.00000	1.00000	.90964	1.40666	0
7.293	3.65953E-03	1.00000	1.00000	1.00000	1.00000	.90964	1.40666	0
7.762	3.90357E-03	1.00000	1.00000	1.00000	1.00000	.90964	1.40666	0
8.261	4.16299E-03	1.00000	1.00000	1.00000	1.00000	.90964	1.40666	0
8.792	4.43874E-03	1.00000	1.00000	1.00000	1.00000	.90964	1.40666	0
9.356	4.73187E-03	1.00000	1.00000	1.00000	1.00000	.90964	1.40666	0
9.955	5.04346E-03	1.00000	1.00000	1.00000	1.00000	.90964	1.40666	0
10.592	5.37469E-03	1.00000	1.00000	1.00000	1.00000	.90964	1.40666	0
11.270	5.72678E-03	1.00000	1.00000	1.00000	1.00000	.90964	1.40666	0
11.990	6.10106E-03	1.00000	1.00000	1.00000	1.00000	.90964	1.40666	0
12.755	6.49891E-03	1.00000	1.00000	1.00000	1.00000	.90964	1.40666	0
13.569	6.92183E-03	1.00000	1.00000	1.00000	1.00000	.90964	1.40666	0
14.433	7.37139E-03	1.00000	1.00000	1.00000	1.00000	.90964	1.40666	0
15.353	7.84928E-03	1.00000	1.00000	1.00000	1.00000	.90964	1.40666	0
16.330	8.35727E-03	1.00000	1.00000	1.00000	1.00000	.90964	1.40666	0
17.369	8.89727E-03	1.00000	1.00000	1.00000	1.00000	.90964	1.40666	0
18.473	9.47128E-03	1.00000	1.00000	1.00000	1.00000	.90964	1.40666	0
19.647	1.00815E-02	1.00000	1.00000	1.00000	1.00000	.90964	1.40666	0
20.895	1.07301E-02	1.00000	1.00000	1.00000	1.00000	.90964	1.40666	0
22.221	1.14196E-02	1.00000	1.00000	1.00000	1.00000	.90964	1.40666	0
23.631	1.21525E-02	1.00000	1.00000	1.00000	1.00000	.90964	1.40666	0
25.130	1.29316E-02	1.00000	1.00000	1.00000	1.00000	.90964	1.40666	0
26.723	1.37597E-02	1.00000	1.00000	1.00000	1.00000	.90964	1.40666	0
28.416	1.46401E-02	1.00000	1.00000	1.00000	1.00000	.90964	1.40666	0
30.217	1.55759E-02	1.00000	1.00000	1.00000	1.00000	.90964	1.40666	0
32.130	1.65707E-02	1.00000	1.00000	1.00000	1.00000	.90964	1.40666	0
34.164	1.76281E-02	1.00000	1.00000	1.00000	1.00000	.90964	1.40666	0
36.327	1.87522E-02	1.00000	1.00000	1.00000	1.00000	.90964	1.40666	0
38.625	1.99471E-02	1.00000	1.00000	1.00000	1.00000	.90964	1.40666	0
41.069	2.12172E-02	1.00000	1.00000	1.00000	1.00000	.90964	1.40666	0
43.666	2.25674E-02	1.00000	1.00000	1.00000	1.00000	.90964	1.40666	0
46.427	2.40026E-02	1.00000	1.00000	1.00000	1.00000	.90964	1.40666	0
49.362	2.55283E-02	1.00000	1.00000	1.00000	1.00000	.90964	1.40666	0
52.482	2.71500E-02	1.00000	1.00000	1.00000	1.00000	.90964	1.40666	0

NASA LRC 75-DEG SWEEP DELTA WING • Z/L=0.5 • REINF/FT=3.77E+06 • VKF B

INFINITE YAWED BLUNT-BODY STAGNATION LINE COMPRESSIBLE TURBULENT BOUNDARY-LAYER ANALYSIS

FREE-STREAM MACH NUMBER = 8.000000E 00 PINF (LBF/FT2) = 1.281600E 01 TINF (DEG R) = 9.730000E 01

TWALL (DEG R) = 8.600000E 02 YAW ANGLE (DEG) = 5.000000E 01 POP (LBF/FT2) = 5.057100E 02

TOP (DEG R) = 7.119610E 02 TSTAG (DEG R) = 1.342740E 03 UE (FT/SEC) = 2.752620E 03

NOSE RADIUS (FT) = 0 X* (FT) = 0 DUE/DX (1/SEC) = 1.726890E 03

TWALL/TSTAG = 6.404814E-01 ANGLE OF ATTACK (DEG) = 4.000000E 01 SHOCK ANGLE (DEG) = 4.000000E 01

THERMALLY AND CALORICALLY PERFECT GAS MODEL

CP= 6006.00 FT2/(SEC2-DEG R) R= 1716.00 FT2/(SEC2-DEG R) GAMMA= 1.4000 PR= .7100 CSTAR= 198.60 DEG R

VISCOSITY CONSTANT= 2.2722E-08 LBF-SEC/(FT2-SQRT(DEG R)) KPL= .4350 LAMBDA= .0900 ASTAR= 26.000 PRT= .9000

INVISCID CENTERLINE PRESSURE (POP) AND VELOCITY (UE) INPUT TO ANALYSIS

STAGNATION POINT VELOCITY GRADIENT (DUEDX) INPUT TO ANALYSIS

NASA LRC 75-DEG SWEEP DELTA WING • Z/L=0.5 • RE1NF/FT=3.77E+06 • VKF B

INFINITE YAWED BLUNT-BODY STAGNATION LINE COMPRESSIBLE TURBULENT BOUNDARY-LAYER ANALYSIS

X (FT) = 0 X1 = 0 BETA = 1.000000E 00 PE/POP = 1.000000E 00 S/RN = 0

UE (FT/SEC) = 0 WE (FT/SEC) = 2.752620E 03 PE (LBF/FT2) = 5.057100E 02 TE (DEG R) = 7.119610E 02

RHOE (SLUG/FT3) = 4.139311E-04 MUE (LBF-SEC/FT2) = 4.740475E-07 DUE/DX (1/SEC) = 1.726890E 03 ITERATIONS = 68

FPP(0) = 3.957732E 00 GP(0) = 2.786526E 00 GP(0) = 7.311136E-01 QDOT = -5.871981E 00 BTU/(FT2-SEC)

ST(INF) = 5.309080E-03 CFX(1NF) = 0 CFZ(1NF) = 7.351643E-03 MSP = 5.142301E 00

DELTA* (FT) = 4.331421E-03 THETAMOM (FT) = 1.732181E-03 EDGE REY/FT = 2.403546E 06 EDGE REYTHETAMOM = 4.163377E 03

EDGE MACH NO = 2.104726E 00 MCDONNELL-DOUGLAS TRANSITION PARAMETER = 1.047321E 02 -QDOT/(TSTAG-TWALL) = 1.216386E-02

ETA	Y(FT)	U/UE	W/WE	H/HE	T/TE	MACH	P1TOT	EV/MU
0	0	0	0	.64048	1.20793	0	.47618	0
.010	9.89114E-06	.03957	.02790	.64791	1.22126	.05315	.47713	.00006
.021	2.05199E-05	.08161	.05765	.65606	1.23439	.10922	.48017	.00103
.032	3.19374E-05	.12617	.08930	.66501	1.24714	.16830	.48569	.00557
.044	4.41959E-05	.17310	.12276	.67477	1.25927	.23024	.49409	.01865
.057	5.73479E-05	.22193	.15772	.68531	1.27047	.29450	.50573	.04766
.070	7.14455E-05	.27176	.19355	.69651	1.28043	.36000	.52080	.10167
.085	8.65391E-05	.32134	.22936	.70809	1.28885	.42522	.53923	.18978
.100	1.02678E-04	.36931	.26419	.71973	1.29557	.48852	.56060	.31940
.116	1.19912E-04	.41458	.29722	.73110	1.30058	.54854	.58425	.49556
.134	1.38291E-04	.45646	.32794	.74195	1.30401	.60444	.60950	.72174
.152	1.57869E-04	.49470	.35615	.75211	1.30608	.65592	.63569	1.00097
.172	1.78705E-04	.52936	.38187	.76153	1.30702	.70302	.66230	1.33655
.193	2.00861E-04	.56066	.40523	.77020	1.30707	.74602	.68896	1.73215
.215	2.24409E-04	.58891	.42645	.77814	1.30642	.78527	.71540	2.19177
.238	2.49422E-04	.61445	.44574	.78543	1.30524	.82118	.74145	2.71962
.263	2.75982E-04	.63759	.46335	.79212	1.30367	.85412	.76700	3.32005
.290	3.04179E-04	.65864	.47947	.79827	1.30180	.88447	.79200	3.99741
.318	3.34107E-04	.67785	.49428	.80395	1.29973	.91252	.81644	4.75607
.348	3.65868E-04	.69545	.50796	.80921	1.29750	.93858	.84032	5.60028
.380	3.99571E-04	.71166	.52065	.81411	1.29516	.96289	.86366	6.53414
.414	4.35331E-04	.72663	.53247	.81868	1.29275	.98567	.88651	7.56153
.450	4.73273E-04	.74053	.54353	.82297	1.29029	1.00710	.90890	8.68610
.488	5.13527E-04	.75349	.55392	.82701	1.28780	1.02736	.93086	9.91118
.529	5.56235E-04	.76560	.56373	.83082	1.28528	1.04657	.95239	11.23979
.572	6.01544E-04	.77697	.57303	.83445	1.28275	1.06488	.97351	12.67466
.618	6.49612E-04	.78769	.58187	.83790	1.28022	1.08239	.99425	14.21816
.667	7.00607E-04	.79782	.59032	.84121	1.27767	1.09919	1.01463	15.87244
.719	7.54708E-04	.80743	.59841	.84438	1.27513	1.11537	1.03471	17.63940
.775	8.12101E-04	.81656	.60620	.84743	1.27257	1.13101	1.05451	19.52081
.834	8.72989E-04	.82528	.61371	.85038	1.27002	1.14618	1.07409	21.51841
.896	9.37581E-04	.83361	.62098	.85324	1.26746	1.16093	1.09347	23.63404
.963	1.00610E-03	.84160	.62804	.85602	1.26489	1.17531	1.11269	25.86979
1.033	1.07680E-03	.84927	.63490	.85873	1.26231	1.18938	1.13180	28.22814
1.108	1.15591E-03	.85665	.64161	.86137	1.25972	1.20317	1.15082	30.71212
1.188	1.23771E-03	.86376	.64816	.86397	1.25711	1.21673	1.16978	33.32553

1.273	1.32449E-03	.87062	.65459	.86651	1.25449	1.23007	1.18873	36.07301
1.363	1.41654E-03	.87726	.66090	.86901	1.25185	1.24324	1.20767	38.96023
1.459	1.51418E-03	.88367	.66711	.87147	1.24918	1.25626	1.22665	41.99398
1.561	1.61775E-03	.88988	.67323	.87390	1.24650	1.26915	1.24567	45.18223
1.669	1.72761E-03	.89589	.67927	.87630	1.24379	1.28193	1.26477	48.53416
1.784	1.84413E-03	.90171	.68523	.87867	1.24105	1.29461	1.28395	52.06014
1.907	1.96772E-03	.90734	.69113	.88102	1.23829	1.30721	1.30323	55.77170
2.037	2.09881E-03	.91279	.69697	.88335	1.23550	1.31973	1.32262	59.68141
2.175	2.23783E-03	.91806	.70275	.88566	1.23268	1.33220	1.34213	63.80273
2.322	2.38527E-03	.92315	.70848	.88795	1.22983	1.34462	1.36178	68.14998
2.479	2.54164E-03	.92807	.71415	.89022	1.22695	1.35696	1.38156	72.73835
2.645	2.70747E-03	.93281	.71979	.89247	1.22405	1.36930	1.40148	77.58016
2.822	2.88333E-03	.93737	.72537	.89471	1.22111	1.38159	1.42154	82.71400
3.009	3.06981E-03	.94175	.73092	.89693	1.21815	1.39384	1.44176	88.00458
3.209	3.26756E-03	.94593	.73640	.89913	1.21517	1.40601	1.46204	94.45911
3.421	3.47724E-03	.95002	.74195	.90136	1.21211	1.41840	1.48290	95.57802
3.647	3.69956E-03	.95414	.74778	.90370	1.20883	1.43148	1.50513	95.32427
3.886	3.93521E-03	.95831	.75393	.90617	1.20531	1.44536	1.52898	95.28773
4.141	4.18495E-03	.96250	.76040	.90878	1.20153	1.46007	1.55453	95.17547
4.412	4.44957E-03	.96670	.76722	.91152	1.19747	1.47565	1.58191	95.03361
4.700	4.72986E-03	.97088	.77439	.91441	1.19313	1.49214	1.61124	94.84551
5.006	5.02670E-03	.97502	.78191	.91744	1.18847	1.50959	1.64266	94.60485
5.331	5.34096E-03	.97909	.78980	.92062	1.18348	1.52802	1.67630	94.30190
5.677	5.67356E-03	.98307	.79806	.92395	1.17815	1.54749	1.71231	93.92572
6.045	6.02547E-03	.98692	.80668	.92743	1.17245	1.56802	1.75081	93.46353
6.436	6.39766E-03	.99062	.81568	.93107	1.16636	1.58965	1.79197	92.90046
6.851	6.79118E-03	.99412	.82505	.93485	1.15987	1.61240	1.83590	92.21924
7.293	7.20708E-03	.99739	.83477	.93877	1.15296	1.63628	1.88275	91.39978
7.762	7.64646E-03	1.00040	.84484	.94282	1.14563	1.66130	1.93262	90.41872
8.261	8.11046E-03	1.00312	.85523	.94700	1.13786	1.68746	1.98561	89.26895
8.792	8.60023E-03	1.00550	.86591	.95129	1.12965	1.71473	2.04178	87.85899
9.356	9.11700E-03	1.00752	.87685	.95567	1.12102	1.74306	2.10115	86.21234
9.955	9.66200E-03	1.00915	.88799	.96012	1.11197	1.77239	2.16368	84.26674
10.592	1.02365E-02	1.01036	.89929	.96460	1.10253	1.80261	2.22925	81.97336
11.270	1.08420E-02	1.01114	.91067	.96909	1.09274	1.83357	2.29765	79.27588
11.990	1.14797E-02	1.01147	.92204	.97353	1.08265	1.86510	2.36852	76.10957
12.755	1.21513E-02	1.01137	.93330	.97788	1.07233	1.89694	2.44136	72.40040
13.569	1.28583E-02	1.01084	.94433	.98208	1.06190	1.92877	2.51546	68.06401
14.433	1.36025E-02	1.00991	.95499	.98606	1.05146	1.96018	2.58983	63.00525
15.353	1.43858E-02	1.00864	.96509	.98974	1.04120	1.99066	2.66318	57.11656
16.330	1.52105E-02	1.00709	.97444	.99303	1.03130	2.01957	2.73383	50.28627
17.369	1.60790E-02	1.00538	.98280	.99582	1.02204	2.04611	2.79959	42.38426
18.473	1.69943E-02	1.00363	.98989	.99801	1.01375	2.06928	2.85775	33.18988
19.647	1.79601E-02	1.00205	.99534	.99947	1.00691	2.08771	2.90445	23.20489
20.895	1.89806E-02	1.00087	.99883	1.00016	1.00176	2.10042	2.93694	10.26822
22.221	2.00619E-02	1.00056	.99959	1.00000	1.00050	2.10334	2.94442	.14920
23.631	2.12113E-02	1.00088	.99888	.99999	1.00146	2.10084	2.93801	.09602
25.130	2.24330E-02	1.00053	.99959	1.00000	1.00052	2.10331	2.94435	.08277
26.723	2.37317E-02	1.00090	.99888	.99999	1.00146	2.10083	2.93797	.07114
28.416	2.51122E-02	1.00048	.99960	1.00000	1.00050	2.10336	2.94448	.06195
30.217	2.65796E-02	1.00093	.99885	1.00000	1.00149	2.10074	2.93775	.05402
32.130	2.81396E-02	1.00043	.99964	1.00000	1.00046	2.10348	2.94479	.04776
34.164	2.97978E-02	1.00097	.99881	1.00000	1.00155	2.10059	2.93737	.04224
36.327	3.15604E-02	1.00036	.99969	1.00000	1.00039	2.10367	2.94526	.03786
38.625	3.34342E-02	1.00103	.99874	.99999	1.00163	2.10037	2.93680	.03387
41.069	3.54259E-02	1.00027	.99977	1.00000	1.00030	2.10393	2.94593	.03071
43.666	3.75432E-02	1.00110	.99865	.99999	1.00174	2.10007	2.93603	.02774
46.427	3.97937E-02	1.00015	.99987	1.00000	1.00017	2.10427	2.94681	.02539
49.362	4.21863E-02	1.00119	.99854	.99999	1.00189	2.09967	2.93502	.02307
52.482	4.47293E-02	1.00000	1.00000	1.00000	1.00000	2.10473	2.94798	0

MDAC-ORBITER CENTERLINE * STATION 900 * VKF F RUN 3828 TIME 85 MSEC * N2 GAS

INFINITE YAWED BLUNT-BODY STAGNATION LINE COMPRESSIBLE LAMINAR BOUNDARY-LAYER ANALYSIS

FREE-STREAM MACH NUMBER = 1.075000E 01 PINF (LBF/FT2) = 1.198000E 01 TINF (DEG R) = 8.150000E 01

TWALL (DEG R) = 5.400000E 02 YAW ANGLE (DEG) = 4.700000E 01 POP (LBF/FT2) = 9.595113E 02

TOP (DEG R) = 1.170572E 03 TSTAG (DEG R) = 1.965169E 03 UE (FT/SEC) = 3.221134E 03

NOSE RADIUS (FT) = 0 X* (FT) = 8.030000E-02 DUE/DX (1/SEC) = 8.142986E 03

TWALL/TSTAG = 2.747856E-01 ANGLE OF ATTACK (DEG) = 4.300000E 01 SHOCK ANGLE (DEG) = 4.883880E 01

THERMALLY AND CALORICALLY PERFECT GAS MODEL

CP= 6216.00 FT2/(SEC2-DEG R) R= 1776.00 FT2/(SEC2-DEG R) GAMMA= 1.4000 PR= .7100 CSTAR= 198.60 DEG R

VISCOSITY CONSTANT= 2.1596E-08 LBF-SEC/(FT2-SQRT(DEG R)) KPL= .4350 LAMBDA= .0900 ASTAR= 26.000 PRT= .9000

CONICAL INVISCIC FLOW FOLLOWING HYPERSONIC SMALL-DISTURBANCE THEORY

FLAT-FACED DISK STAGNATION POINT VELOCITY GRADIENT

MDAC-ORBITER CENTERLINE * STATION 800 * VKF F RUN 3828 TIME 85 MSEC * N2 GAS

INFINITE YAWED BLUNT-BODY STAGNATION LINE COMPRESSIBLE LAMINAR BOUNDARY-LAYER ANALYSIS

X (FT) = 0 X1 = 0 BETA = 1.000000E 00 PE/POP = 1.000000E 00 S/RN = 0

UE (FT/SEC) = 0 WE (FT/SEC) = 3.221134E 03 PE (LBF/FT2) = 9.595113E 02 TE (DEG R) = 1.130572E 03

RHOE (SLUG/FT3) = 4.778690E-04 MUE (LBF-SEC/FT2) = 6.290858E-07 DUE/DX (1/SEC) = 8.142986E 03 ITERATIONS = 13

FPP(0) = 8.596026E-01 CP(0) = 4.610575E-01 GP(0) = 2.670783E-01 QDOT = -1.148913E 01 BTU/(FT2-SEC)

ST(INF) = 2.520030E-03 CFX(INF) = 0 CFZ(INF) = 2.982037E-03 MSP = 7.331482E 00

DELTA* (FT) = 2.921720E-04 THETAMOM (FT) = 1.702606E-04 EDGE REY/FT = 2.446853E 06 EDGE REYTHETAMOM = 4.166026E 02

EDGE MACH NO = 1.921207E 00 MCDONNELL-DOUGLAS TRANSITION PARAMETER = 1.144000E 01 -QDOT/(TSTAG-TWALL) = 8.061594E-03

ETA	Y(FT)	U/UE	W/WE	H/HE	T/TE	MACH	PITOT	EV/MU
0	0	0	0	.27479	.47763	0	.53662	0
.010	1.92578E-06	.00859	.00462	.27746	.48227	.01277	.53668	0
.021	4.00157E-06	.01769	.00953	.28032	.48719	.02624	.53688	0
.032	6.22689E-06	.02735	.01477	.28337	.49241	.04045	.53729	0
.044	8.61835E-06	.03758	.02036	.28663	.49793	.05543	.53777	0
.057	1.11897E-05	.04842	.02631	.29011	.50378	.07122	.53853	0
.070	1.39559E-05	.05991	.03266	.29384	.50998	.08786	.53952	0
.085	1.69334E-05	.07207	.03943	.29782	.51655	.10539	.54080	0
.100	2.01401E-05	.08495	.04664	.30207	.52349	.12385	.54240	0
.116	2.35957E-05	.09857	.05434	.30663	.53084	.14328	.54437	0
.134	2.73216E-05	.11298	.06255	.31150	.53861	.16373	.54676	0
.152	3.13416E-05	.12820	.07131	.31672	.54683	.18526	.54962	0
.172	3.56812E-05	.14429	.08065	.32231	.55550	.20790	.55303	0
.193	4.03689F-05	.16126	.09063	.32830	.56466	.23170	.55706	0
.215	4.54356E-05	.17917	.10127	.33472	.57432	.25674	.56179	0
.238	5.09154E-05	.19804	.11264	.34161	.58450	.28305	.56732	0
.263	5.68455E-05	.21790	.12477	.34899	.59523	.31070	.57376	0
.290	6.32668E-05	.23879	.13773	.35692	.60651	.33976	.58125	0
.318	7.02240E-05	.26073	.15156	.36543	.61837	.37028	.58991	0
.348	7.77662E-05	.28374	.16633	.37458	.63081	.40233	.59992	0
.380	8.59471E-05	.30783	.18209	.38440	.64384	.43599	.61148	0
.414	9.48254E-05	.33302	.19892	.39496	.65748	.47133	.62480	0
.450	1.04465E-04	.35929	.21689	.40631	.67171	.50841	.64015	0
.488	1.14936E-04	.38664	.23605	.41851	.68653	.54733	.65783	0
.529	1.26314E-04	.41504	.25648	.43164	.70193	.58815	.67819	0
.572	1.38682E-04	.44443	.27826	.44574	.71787	.63096	.70164	0
.618	1.52130E-04	.47477	.30144	.46091	.73432	.67582	.72860	0
.667	1.66752E-04	.50596	.32609	.47719	.75123	.72282	.75986	0
.719	1.82655F-04	.53790	.35227	.49468	.76853	.77200	.79586	0
.775	1.99947E-04	.57044	.38001	.51342	.78613	.82343	.83746	0
.834	2.18747E-04	.60344	.40935	.53349	.80393	.87712	.88555	0
.896	2.39179E-04	.63668	.44029	.55492	.82180	.93310	.94119	0
.963	2.61376E-04	.66996	.47279	.57776	.83959	.99131	1.00557	0
1.033	2.85472E-04	.70300	.50680	.60199	.85713	1.05169	1.07984	0
1.108	3.11610E-04	.73553	.54220	.62760	.87423	1.11408	1.16421	0
1.188	3.39933E-04	.76724	.57881	.65452	.89071	1.17827	1.25840	0

1.273	3.70588E-04	.79781	.61641	.68260	.90635	1.24393	1.36206	0
1.363	4.03723E-04	.82690	.65467	.71167	.92096	1.31062	1.47456	0
1.459	4.39485E-04	.85419	.69320	.74145	.93435	1.37778	1.59492	0
1.561	4.78022E-04	.87939	.73153	.77159	.94639	1.44467	1.72169	0
1.669	5.19479E-04	.90223	.76910	.80165	.95698	1.51045	1.85290	0
1.784	5.64004E-04	.92252	.80532	.83112	.96608	1.57411	1.98599	0
1.907	6.11745E-04	.94014	.83954	.85944	.97370	1.63456	2.11787	0
2.037	6.62857E-04	.95503	.87115	.88602	.97995	1.69069	2.24505	0
2.175	7.17502E-04	.96728	.89958	.91030	.98496	1.74142	2.36391	0
2.322	7.75854E-04	.97702	.92437	.93180	.98890	1.78586	2.47106	0
2.479	8.38103E-04	.98449	.94525	.95015	.99195	1.82338	2.56372	0
2.645	9.04453E-04	.99000	.96213	.96519	.99431	1.85374	2.64017	0
2.822	9.75131E-04	.99387	.97515	.97693	.99610	1.87712	2.69995	0
3.009	1.05038E-03	.99644	.98465	.98562	.99745	1.89414	2.74394	0
3.209	1.13046E-03	.99809	.99117	.99165	.99843	1.90574	2.77415	0
3.421	1.21566E-03	.99905	.99532	.99554	.99911	1.91307	2.79335	0
3.647	1.30628E-03	.99957	.99775	.99785	.99955	1.91732	2.80450	0
3.886	1.40264E-03	.99983	.99904	.99908	.99981	1.91954	2.81034	0
4.141	1.50509E-03	.99994	.99964	.99967	.99995	1.92057	2.81307	0
4.412	1.61401E-03	.99998	.99989	.99990	1.00000	1.92099	2.81418	0
4.700	1.72979E-03	1.00000	.99997	.99998	1.00001	1.92114	2.81457	0
5.006	1.85287E-03	1.00000	.99999	1.00000	1.00001	1.92119	2.81469	0
5.331	1.98370E-03	1.00000	1.00000	1.00000	1.00001	1.92120	2.81473	0
5.677	2.12277E-03	1.00000	1.00000	1.00000	1.00000	1.92120	2.81474	0
6.045	2.27060E-03	1.00000	1.00000	1.00000	1.00000	1.92121	2.81474	0
6.436	2.42775E-03	1.00000	1.00000	1.00000	1.00000	1.92121	2.81474	0
6.851	2.59480E-03	1.00000	1.00000	1.00000	1.00000	1.92121	2.81474	0
7.293	2.77237E-03	1.00000	1.00000	1.00000	1.00000	1.92121	2.81474	0
7.762	2.96113E-03	1.00000	1.00000	1.00000	1.00000	1.92121	2.81474	0
8.261	3.16178E-03	1.00000	1.00000	1.00000	1.00000	1.92121	2.81474	0
8.792	3.37507E-03	1.00000	1.00000	1.00000	1.00000	1.92121	2.81474	0
9.356	3.60179E-03	1.00000	1.00000	1.00000	1.00000	1.92121	2.81474	0
9.955	3.84280E-03	1.00000	1.00000	1.00000	1.00000	1.92121	2.81474	0
10.592	4.09900E-03	1.00000	1.00000	1.00000	1.00000	1.92121	2.81474	0
11.270	4.37133E-03	1.00000	1.00000	1.00000	1.00000	1.92121	2.81474	0
11.990	4.66083E-03	1.00000	1.00000	1.00000	1.00000	1.92121	2.81474	0
12.755	4.96856E-03	1.00000	1.00000	1.00000	1.00000	1.92121	2.81474	0
13.569	5.29567E-03	1.00000	1.00000	1.00000	1.00000	1.92121	2.81474	0
14.433	5.64340E-03	1.00000	1.00000	1.00000	1.00000	1.92121	2.81474	0
15.353	6.01303E-03	1.00000	1.00000	1.00000	1.00000	1.92121	2.81474	0
16.330	6.40595E-03	1.00000	1.00000	1.00000	1.00000	1.92121	2.81474	0
17.369	6.82363E-03	1.00000	1.00000	1.00000	1.00000	1.92121	2.81474	0
18.473	7.26761E-03	1.00000	1.00000	1.00000	1.00000	1.92121	2.81474	0
19.647	7.73957E-03	1.00000	1.00000	1.00000	1.00000	1.92121	2.81474	0
20.895	8.24126E-03	1.00000	1.00000	1.00000	1.00000	1.92121	2.81474	0
22.221	8.77456E-03	1.00000	1.00000	1.00000	1.00000	1.92121	2.81474	0
23.631	9.34146E-03	1.00000	1.00000	1.00000	1.00000	1.92121	2.81474	0
25.130	9.94407E-03	1.00000	1.00000	1.00000	1.00000	1.92121	2.81474	0
26.723	1.05846E-02	1.00000	1.00000	1.00000	1.00000	1.92121	2.81474	0
28.416	1.12656E-02	1.00000	1.00000	1.00000	1.00000	1.92121	2.81474	0
30.217	1.19894E-02	1.00000	1.00000	1.00000	1.00000	1.92121	2.81474	0
32.130	1.27588E-02	1.00000	1.00000	1.00000	1.00000	1.92121	2.81474	0
34.164	1.35767E-02	1.00000	1.00000	1.00000	1.00000	1.92121	2.81474	0
36.327	1.44462E-02	1.00000	1.00000	1.00000	1.00000	1.92121	2.81474	0
38.625	1.53704E-02	1.00000	1.00000	1.00000	1.00000	1.92121	2.81474	0
41.069	1.63528E-02	1.00000	1.00000	1.00000	1.00000	1.92121	2.81474	0
43.666	1.73971E-02	1.00000	1.00000	1.00000	1.00000	1.92121	2.81474	0
46.427	1.85072E-02	1.00000	1.00000	1.00000	1.00000	1.92121	2.81474	0
49.362	1.96873E-02	1.00000	1.00000	1.00000	1.00000	1.92121	2.81474	0
52.482	2.09417E-02	1.00000	1.00000	1.00000	1.00000	1.92121	2.81474	0

MDAC-ORBITER CENTERLINE * STATION 800 * VKF F RUN 3828 TIME 85 MSEC * N2 GAS

INFINITE YAWED BLUNT-BODY STAGNATION LINE COMPRESSIBLE TURBULENT BOUNDARY-LAYER ANALYSIS

FREE-STREAM MACH NUMBER = 1.075000E 01 PINF (LBF/FT2) = 1.198000E 01 TINF (DEG R) = 8.150000E 0)

TWALL (DEG R) = 5.400000E 02 YAW ANGLE (DEG) = 4.700000E 01 POP (LBF/FT2) = 9.595113E 02

TOP (DEG R) = 1.130572E 03 TSTAG (DEG R) = 1.965169E 03 UE (FT/SEC) = 3.221134E 03

NOSE RADIUS (FT) = 0 X* (FT) = 8.030000E-02 DUE/DX (1/SEC) = 8.142986E 03

TWALL/TSTAG = 2.747856E-01 ANGLE OF ATTACK (DEG) = 4.300000E 01 SHOCK ANGLE (DEG) = 4.883800E 01

THERMALLY AND CALORICALLY PERFECT GAS MODEL

CP= 6216.00 FT2/(SEC2-DEG R) R= 1776.00 FT2/(SEC2-DEG R) GAMMA= 1.4000 PR= .7100 CSTAR= 198.60 UFG R

VISCOSITY CONSTANT= 2.1596E-08 LBF-SEC/(FT2-SQRT(DEG R)) KML= .4350 LAMBDA= .0900 ASTAR= 26.000 PRT= .9000

CONICAL INVISCIC FLOW FOLLOWING HYPERSONIC SMALL-DISTURBANCE THEORY

FLAT-FACED DISK STAGNATION POINT VELOCITY GRADIENT

MDAC-ORBITER CENTERLINE * STATION 800 * VKF F RUN 3828 TIME 85 MSEC * N2 GAS

INFINITE YAWED BLUNT-BODY STAGNATION LINE COMPRESSIBLE TURBULENT BOUNDARY-LAYER ANALYSIS

X (FT) = 0 X1 = 0 BETA = 1.000000F 00 PE/POP = 1.000000E 00 S/RN = 0

UE (FT/SEC) = 0 WE (FT/SEC) = 3.221134E 03 PE (LBF/FT2) = 9.595113E 02 TE (DEG R) = 1.130572E 03

RHOF (SLUG/FT3) = 4.778690E-04 MUF (LBF-SEC/FT2) = 6.290858E-07 DUE/DX (1/SEC) = 8.142986E 03 ITERATIONS = 68

FPP(0) = 2.040197E 00 CP(0) = 1.532844E 00 GP(0) = 8.764925E-01 QDOT = -3.770482E 01 BTU/(FT2-SEC)

ST(INF) = 8.270186E-03 CFX(INF) = 0 CFZ(INF) = 9.914157E-03 HSP = 7.331482E 00

DELTA* (FT) = 7.747558F-04 THETAMOM (FT) = 6.306542E-04 EDGE REY/FT = 2.446853E 06 EDGE REYTHETAMOM = 1.543118E 03

EDGE MACH NO = 1.921207E 00 MCDONNELL-DOUGLAS TRANSITION PARAMETER = 4.237438E 01 -QDOT/(TSTAG-TWALL) = 2.645639E-02

ETA	Y(FT)	U/UE	W/WE	H/HE	T/TE	MACH	P1TOT	EV/MU
0	0	0	0	.27479	.47763	0	.53662	0
.010	1.95094E-06	.02046	.01538	.28361	.49280	.04210	.53728	.00002
.021	4.09131E-06	.04232	.03186	.29313	.50876	.08581	.53939	.00026
.032	6.44089E-06	.06567	.04950	.30339	.52554	.13117	.54311	.00133
.044	9.02149E-06	.09059	.06836	.31446	.54313	.17821	.54864	.00424
.057	1.18570E-05	.11717	.08850	.32638	.56151	.22690	.55621	.01043
.070	1.49734E-05	.14524	.10991	.33918	.58061	.27711	.56602	.02178
.085	1.83988E-05	.17488	.13254	.35287	.60034	.32863	.57829	.04051
.100	2.21632E-05	.20585	.15627	.36741	.62055	.38112	.59319	.06909
.116	2.62581E-05	.23791	.18092	.38273	.64104	.43413	.61081	.11013
.134	3.08364E-05	.27069	.20624	.39872	.66159	.48714	.63117	.16625
.152	3.58122E-05	.30382	.23193	.41521	.68194	.53957	.65417	.24000
.172	4.12600E-05	.33687	.25767	.43203	.70187	.59090	.67963	.33385
.193	4.72151E-05	.36944	.28317	.44898	.72115	.64064	.70726	.45030
.215	5.37132E-05	.40121	.30817	.46587	.73960	.68843	.73675	.59195
.238	6.07907E-05	.43187	.33243	.48254	.75710	.73401	.76775	.76157
.263	6.84847E-05	.46124	.35580	.49883	.77354	.77722	.79990	.96218
.290	7.68333E-05	.48916	.37817	.51463	.78889	.81799	.83286	1.19704
.318	8.58759E-05	.51557	.39945	.52985	.80314	.85634	.86634	1.46971
.348	9.56537E-05	.54045	.41963	.54444	.81630	.89231	.90008	1.78396
.380	1.06210E-04	.56380	.43871	.55837	.82843	.92603	.93384	2.14379
.414	1.17590E-04	.58567	.45671	.57163	.83957	.95761	.96745	2.55339
.450	1.29842E-04	.60613	.47368	.58422	.84981	.98719	1.00078	3.01707
.488	1.43017E-04	.62525	.48967	.59616	.85919	1.01492	1.03370	3.53925
.529	1.57169E-04	.64313	.50474	.60748	.86781	1.04095	1.06609	4.12442
.572	1.72358E-04	.65985	.51896	.61821	.87573	1.06542	1.09778	4.77703
.618	1.88644E-04	.67549	.53238	.62839	.88300	1.08847	1.12868	5.50152
.667	2.06093E-04	.69015	.54508	.63806	.88971	1.11022	1.15877	6.30221
.719	2.24777E-04	.70391	.55711	.64725	.89590	1.13080	1.18804	7.18327
.775	2.44770E-04	.71683	.56853	.65601	.90163	1.15032	1.21649	8.14865
.834	2.66154E-04	.72900	.57940	.66436	.90694	1.16887	1.24416	9.20207
.896	2.89013E-04	.74048	.58977	.67235	.91188	1.18656	1.27108	10.34693
.963	3.13440E-04	.75133	.59968	.68000	.91648	1.20346	1.29732	11.58634
1.033	3.39532E-04	.76159	.60917	.68735	.92078	1.21966	1.32291	12.92303
1.108	3.67394E-04	.77134	.61830	.69442	.92481	1.23522	1.34791	14.35942
1.188	3.97137E-04	.78059	.62708	.70125	.92860	1.25022	1.37237	15.89758

1.273	4.28879E-04	.78941	.63557	.70785	.93216	1.26471	1.39634	17.53929
1.363	4.62746E-04	.79782	.64378	.71424	.93553	1.27874	1.41988	19.28608
1.459	4.98873E-04	.80585	.65174	.72046	.93871	1.29236	1.44304	21.13933
1.561	5.37404E-04	.81354	.65948	.72651	.94174	1.30561	1.46586	23.10032
1.669	5.78490E-04	.82091	.66703	.73241	.94461	1.31854	1.48838	25.17036
1.784	6.22295E-04	.82797	.67440	.73818	.94735	1.33118	1.51065	27.35084
1.907	6.68591E-04	.83476	.68161	.74384	.94996	1.34355	1.53271	29.64370
2.037	7.18762E-04	.84129	.68867	.74938	.95245	1.35570	1.55458	32.05070
2.175	7.71805E-04	.84757	.69561	.75484	.95484	1.36764	1.57631	34.57271
2.322	8.28328E-04	.85361	.70243	.76020	.95713	1.37940	1.59792	37.22613
2.479	8.88553E-04	.85942	.70915	.76550	.95933	1.39100	1.61944	39.94199
2.645	9.52716E-04	.86500	.71576	.77071	.96144	1.40242	1.64083	43.14505
2.822	1.02107E-03	.87046	.72238	.77594	.96350	1.41389	1.66251	44.30775
3.009	1.09389E-03	.87602	.72933	.78143	.96560	1.42593	1.68548	43.72929
3.209	1.17146E-03	.88178	.73671	.78727	.96776	1.43876	1.71022	43.44200
3.421	1.25411E-03	.88769	.74454	.79346	.96997	1.45240	1.73676	43.05913
3.647	1.34217E-03	.89376	.75284	.80004	.97223	1.46688	1.76527	42.64777
3.886	1.43599E-03	.89996	.76163	.80701	.97453	1.48225	1.79586	42.19136
4.141	1.53597E-03	.90629	.77093	.81440	.97685	1.49855	1.82870	41.68593
4.412	1.64249E-03	.91270	.78074	.82221	.97919	1.51582	1.86391	41.12528
4.704	1.75600E-03	.91920	.79109	.83045	.98152	1.53410	1.90165	40.50241
5.006	1.87694E-03	.92574	.80199	.83915	.98382	1.55340	1.94204	39.80930
5.331	2.00580E-03	.93230	.81343	.84829	.98608	1.57375	1.98522	39.03676
5.677	2.14309E-03	.93882	.82541	.85789	.98827	1.59516	2.03130	38.17425
6.045	2.28934E-03	.94529	.83791	.86792	.99037	1.61761	2.08035	37.20964
6.436	2.44513E-03	.95163	.85092	.87838	.99234	1.64108	2.13241	36.12896
6.851	2.61105E-03	.95782	.86437	.88922	.99415	1.66552	2.18745	34.91613
7.293	2.78773E-03	.96379	.87823	.90041	.99578	1.69083	2.24537	33.55260
7.762	2.97582E-03	.96949	.89239	.91187	.99720	1.71687	2.30592	32.01702
8.261	3.17603E-03	.97486	.90674	.92352	.99838	1.74345	2.36875	30.28479
8.792	3.38907E-03	.97987	.92114	.93522	.99930	1.77032	2.43327	28.32781
9.356	3.61572E-03	.98436	.93539	.94683	.99996	1.79711	2.49864	26.11366
9.955	3.85676E-03	.98838	.94924	.95815	1.00035	1.82338	2.56372	23.60639
10.592	4.11307E-03	.99184	.96240	.96892	1.00049	1.84852	2.62695	20.76573
11.270	4.38553E-03	.99471	.97449	.97882	1.00042	1.87180	2.68627	17.54658
11.990	4.67511E-03	.99694	.98504	.98748	1.00020	1.89228	2.73910	13.88618
12.755	4.98286E-03	.99851	.99347	.99440	.99991	1.90874	2.78200	9.89714
13.569	5.30989E-03	.99945	.99920	.99911	.99961	1.92005	2.81170	5.06887
14.433	5.65746E-03	.99976	1.00138	1.00088	.99949	1.92435	2.82302	.46714
15.353	6.02691E-03	.99959	1.00010	.99977	.99948	1.92189	2.81655	.19523
16.334	6.41959E-03	.99970	1.00111	1.00052	.99932	1.92399	2.82208	.12893
17.369	6.83703E-03	.99963	1.00026	.99996	.99956	1.92212	2.81716	.09078
18.473	7.28076E-03	.99966	1.00100	1.00041	.99927	1.92384	2.82167	.06688
19.647	7.75245E-03	.99966	1.00033	1.00003	.99960	1.92222	2.81742	.05090
20.895	8.25385E-03	.99964	1.00096	1.00036	.99925	1.92377	2.82151	.03991
22.221	8.78684E-03	.99968	1.00035	1.00007	.99961	1.92225	2.81750	.03197
23.631	9.35341E-03	.99962	1.00095	1.00033	.99923	1.92377	2.82150	.02617
25.130	9.95567E-03	.99971	1.00035	1.00008	.99964	1.92224	2.81746	.02175
26.723	1.05959E-02	.99960	1.00095	1.00033	.99920	1.92380	2.82159	.01839
28.414	1.12764E-02	.99973	1.00034	1.00009	.99966	1.92218	2.81731	.01571
30.217	1.19998E-02	.99958	1.00098	1.00033	.99917	1.92388	2.82179	.01361
32.130	1.27688E-02	.99977	1.00031	1.00008	.99970	1.92209	2.81706	.01187
34.164	1.35862E-02	.99956	1.00101	1.00033	.99913	1.92399	2.82209	.01048
36.327	1.44552E-02	.99981	1.00026	1.00007	.99975	1.92195	2.81671	.00929
38.625	1.53789E-02	.99953	1.00107	1.00035	.99907	1.92415	2.82251	.00832
41.069	1.63607E-02	.99986	1.00020	1.00005	.99981	1.92177	2.81622	.00746
43.666	1.74044E-02	.99949	1.00114	1.00037	.99900	1.92437	2.82307	.00676
46.427	1.85139E-02	.99992	1.00011	1.00003	.99989	1.92152	2.81558	.00612
49.362	1.96933E-02	.99945	1.00124	1.00039	.99891	1.92464	2.82381	.00560
52.482	2.09470E-02	1.00000	1.00000	1.00000	1.00000	1.92121	2.81474	0

MDAC-ORBITER CENTERLINE * STATION 800 * VKF F RUN 3028 TIME 152 MSEC * N_2 GAS

INFINITE YAWED BLUNT-BODY STAGNATION LINE COMPRESSIBLE LAMINAR BOUNDARY-LAYER ANALYSIS

FREE-STREAM MACH NUMBER = 1.087000E 01 PINF (LBF/FT2) = 6.160000E 00 TINF (DEG R) = 8.000000E 01

TWALL (DEG R) = 5.400000E 02 YAW ANGLE (DEG) = 4.700000E 01 POP (LBF/FT2) = 5.042670E 02

TOP (DEG R) = 1.132589E 03 TSTAG (DEG R) = 1.970510E 03 WE (FT/SEC) = 3.227544E 03

NOSE RADIUS (FT) = 0 X* (FT) = 8.030000E-02 DUE/DX (1/SEC) = 8.150246E 03

TWALL/TSTAG = 2.740407E-01 ANGLE OF ATTACK (DEG) = 4.300000E 01 SHOCK ANGLE (DEG) = 4.882782E 01

THERMALLY AND CALORICALLY PERFECT GAS MODEL

CP= 6214.00 FT2/(SEC2-DEG R) R= 1776.00 FT2/(SEC2-DEG R) GAMMA= 1.4000 PR= .7100 CSTAR= 198.60 DEG R

VISCOSITY CONSTANT= 2.1996E-08 LBF-SEC/(FT2-SQRT(DEG R)) KML= .4350 LAMBDA= .0900 ASTAR= 26.000 PRT= .9000

CONICAL INVISCIC FLOW FOLLOWING HYPERSONIC SMALL-DISTURBANCE THEORY

FLAT-FACED DISK STAGNATION POINT VELOCITY GRADIENT

INFINITE YAWED BLUNT-BODY STAGNATION LINE COMPRESSIBLE LAMINAR BOUNDARY-LAYER ANALYSIS

X (FT) = 0 XI = 0 BETA = 1.000000E 00 PE/POP = 1.000000E 00 S/RN = 0

UE (FT/SEC) = 0 WE (FT/SEC) = 3.227544E 03 PE (LBF/FT2) = 5.042670E 02 TE (DEG R) = 1.132589E 03

RHOE (SLUG/FT3) = 2.506948E-04 MUE (LBF-SEC/FT2) = 6.298142E-07 DUE/DX (1/SEC) = 8.150246E 03 ITERATIONS = 13

FPP(0) = 8.588658F-01 CP(0) = 4.607866E-01 GP(01 = 2.671889E-01 QDOT = -8.361429E 00 BTU/(FT2-SEC)

ST(INF) = 3.481733E-03 CFX(INF) = 0 CFZ(INF) = 4.120876E-03 HSP = 7.413322E 00

DELTA* (FT) = 4.032369F-04 THETAMOM (FT) = 2.351210E-04 EDGE REY/FT = 1.284710E 06 EDGE REYTHETAMOM = 3.020623E 02

EDGE MACH NO = 1.923315E 00 MCDONNELL-DOUGLAS TRANSITION PARAMETER = 9.425078E 00 -QDOT/(TSTAG-TWALL) = 5.845067E-03

ETA	Y(FT)	U/UE	W/WE	H/HE	T/TE	MACH	PITOT	EV/MU
0	0	0	0	.27404	.47678	0	.53646	0
.010	2.65999E-06	.00858	.00461	.27672	.48143	.01279	.53652	0
.021	5.51581E-06	.01768	.00953	.27958	.48636	.02628	.53672	0
.032	8.58337E-06	.02732	.01477	.28263	.49158	.04050	.53708	0
.044	1.18800E-05	.03755	.02035	.28589	.49711	.05551	.53762	0
.057	1.54248E-05	.04838	.02630	.28937	.50297	.07132	.53838	0
.070	1.92383E-05	.05986	.03264	.29310	.50918	.08798	.53938	0
.085	2.33433E-05	.07202	.03940	.29708	.51575	.10553	.54066	0
.100	2.77645E-05	.08488	.04662	.30134	.52271	.12401	.54226	0
.116	3.25290E-05	.09850	.05431	.30590	.53007	.14346	.54423	0
.134	3.76665E-05	.11290	.06251	.31077	.53785	.16394	.54662	0
.152	4.32096E-05	.12811	.07127	.31599	.54607	.18549	.54949	0
.172	4.91938E-05	.14419	.08061	.32159	.55476	.20815	.55291	0
.193	5.56582E-05	.16115	.09058	.32758	.56393	.23199	.55695	0
.215	6.26456E-05	.17905	.10122	.33400	.57361	.25705	.56169	0
.239	7.02030E-05	.19791	.11258	.34089	.58381	.28339	.56723	0
.263	7.83819E-05	.21776	.12471	.34828	.59455	.31107	.57369	0
.290	8.72387E-05	.23864	.13766	.35622	.60585	.34015	.58118	0
.318	9.68352E-05	.26057	.15148	.36474	.61772	.37070	.58986	0
.348	1.07239E-04	.28357	.16625	.37388	.63018	.40278	.59990	0
.381	1.18525E-04	.30765	.18201	.38371	.64324	.43647	.61148	0
.414	1.30773E-04	.33283	.19883	.39428	.65690	.47184	.62482	0
.451	1.44072E-04	.35910	.21679	.40564	.67115	.50896	.64020	0
.488	1.58519E-04	.38644	.23595	.41785	.68600	.54791	.65791	0
.529	1.74219E-04	.41484	.25638	.43098	.70142	.58877	.67831	0
.572	1.91286E-04	.44423	.27815	.44510	.71739	.63161	.70181	0
.618	2.09842E-04	.47456	.30133	.46028	.73388	.67651	.72890	0
.667	2.30022E-04	.50575	.32597	.47658	.75082	.72354	.76015	0
.719	2.51969E-04	.53769	.35214	.49407	.76815	.77277	.79622	0
.775	2.75835E-04	.57024	.37989	.51284	.78578	.82424	.83790	0
.834	3.01783E-04	.60324	.40922	.53292	.80361	.87798	.88610	0
.896	3.29987E-04	.63649	.44015	.55437	.82152	.93400	.94186	0
.963	3.60626E-04	.66977	.47266	.57723	.83934	.99226	1.00639	0
1.033	3.93890E-04	.70283	.50666	.60149	.85691	1.05270	1.08083	0
1.109	4.29973E-04	.73537	.54206	.62712	.87405	1.11515	1.16537	0
1.188	4.69075E-04	.76709	.57868	.65406	.89056	1.17940	1.25976	0

1.273	5.11394E-04	.79767	.61628	.68218	.90623	1.24512	1.36361	0
1.363	5.57147E-04	.82678	.65455	.71179	.92086	1.31188	1.47633	0
1.459	6.06524E-04	.85409	.69309	.74110	.93428	1.37911	1.59691	0
1.561	6.59733E-04	.87930	.73142	.77127	.94635	1.44608	1.72394	0
1.669	7.16976E-04	.90214	.76900	.80137	.95695	1.51194	1.85541	0
1.786	7.78456E-04	.92246	.80523	.83088	.96606	1.57568	1.98877	0
1.907	8.44378E-04	.94009	.83946	.85923	.97370	1.63621	2.12092	0
2.037	9.14954E-04	.95500	.87108	.88585	.97995	1.69241	2.24838	0
2.175	9.90410E-04	.96725	.89952	.91017	.98496	1.74322	2.36751	0
2.322	1.07098E-03	.97700	.92433	.93169	.98890	1.78773	2.47491	0
2.479	1.15894E-03	.98448	.94522	.95008	.99196	1.82531	2.56780	0
2.645	1.24856E-03	.98999	.96211	.96513	.99431	1.85572	2.64444	0
2.822	1.34615E-03	.99387	.97513	.97690	.99611	1.87915	2.70437	0
3.009	1.45006E-03	.99646	.98464	.98559	.99745	1.89619	2.74847	0
3.209	1.56064E-03	.99809	.99116	.99163	.99843	1.90782	2.77877	0
3.421	1.67829E-03	.99905	.99532	.99553	.99911	1.91516	2.79802	0
3.647	1.80342E-03	.99957	.99775	.99784	.99956	1.91941	2.80920	0
3.886	1.93647E-03	.99987	.99904	.99908	.99982	1.92164	2.81507	0
4.141	2.07794E-03	.99996	.99964	.99967	.99995	1.92268	2.81780	0
4.412	2.22834E-03	.99998	.99989	.99990	1.00000	1.92310	2.81892	0
4.700	2.38821E-03	1.00000	.99997	.99998	1.00001	1.92325	2.81931	0
5.008	2.55816E-03	1.00000	.99999	1.00000	1.00001	1.92330	2.81943	0
5.338	2.73881E-03	1.00000	1.00000	1.00000	1.00001	1.92331	2.81947	0
5.692	2.93085E-03	1.00000	1.00000	1.00000	1.00000	1.92331	2.81948	0
6.070	3.1349AE-03	1.00000	1.00000	1.00000	1.00000	1.92331	2.81948	0
6.476	3.35197E-03	1.00000	1.00000	1.00000	1.00000	1.92331	2.81948	0
6.911	3.58264E-03	1.00000	1.00000	1.00000	1.00000	1.92332	2.81948	0
7.378	3.82703E-03	1.00000	1.00000	1.00000	1.00000	1.92332	2.81948	0
7.876	4.08647E-03	1.00000	1.00000	1.00000	1.00000	1.92332	2.81948	0
8.408	4.36153E-03	1.00000	1.00000	1.00000	1.00000	1.92332	2.81948	0
8.975	4.66005E-03	1.00000	1.00000	1.00000	1.00000	1.92332	2.81948	0
9.578	4.97312E-03	1.00000	1.00000	1.00000	1.00000	1.92332	2.81948	0
9.955	5.30592E-03	1.00000	1.00000	1.00000	1.00000	1.92332	2.81948	0
10.599	5.65968E-03	1.00000	1.00000	1.00000	1.00000	1.92332	2.81948	0
11.274	6.03573E-03	1.00000	1.00000	1.00000	1.00000	1.92332	2.81948	0
11.990	6.43547E-03	1.00000	1.00000	1.00000	1.00000	1.92332	2.81948	0
12.755	6.86039E-03	1.00000	1.00000	1.00000	1.00000	1.92332	2.81948	0
13.569	7.31208E-03	1.00000	1.00000	1.00000	1.00000	1.92332	2.81948	0
14.433	7.79223E-03	1.00000	1.00000	1.00000	1.00000	1.92332	2.81948	0
15.353	8.30263E-03	1.00000	1.00000	1.00000	1.00000	1.92332	2.81948	0
16.330	8.84518E-03	1.00000	1.00000	1.00000	1.00000	1.92332	2.81948	0
17.369	9.42192E-03	1.00000	1.00000	1.00000	1.00000	1.92332	2.81948	0
18.473	1.00350E-02	1.00000	1.00000	1.00000	1.00000	1.92332	2.81948	0
19.647	1.06867E-02	1.00000	1.00000	1.00000	1.00000	1.92332	2.81948	0
20.895	1.13794E-02	1.00000	1.00000	1.00000	1.00000	1.92332	2.81948	0
22.221	1.21158E-02	1.00000	1.00000	1.00000	1.00000	1.92332	2.81948	0
23.631	1.28586E-02	1.00000	1.00000	1.00000	1.00000	1.92332	2.81948	0
25.130	1.37307E-02	1.00000	1.00000	1.00000	1.00000	1.92332	2.81948	0
26.723	1.46152E-02	1.00000	1.00000	1.00000	1.00000	1.92332	2.81948	0
28.414	1.55555E-02	1.00000	1.00000	1.00000	1.00000	1.92332	2.81948	0
30.217	1.65550E-02	1.00000	1.00000	1.00000	1.00000	1.92332	2.81948	0
32.134	1.76174E-02	1.00000	1.00000	1.00000	1.00000	1.92332	2.81948	0
34.164	1.87468E-02	1.00000	1.00000	1.00000	1.00000	1.92332	2.81948	0
36.327	1.99473E-02	1.00000	1.00000	1.00000	1.00000	1.92332	2.81948	0
38.625	2.12235E-02	1.00000	1.00000	1.00000	1.00000	1.92332	2.81948	0
41.069	2.25801E-02	1.00000	1.00000	1.00000	1.00000	1.92332	2.81948	0
43.664	2.40221E-02	1.00000	1.00000	1.00000	1.00000	1.92332	2.81948	0
46.427	2.55550E-02	1.00000	1.00000	1.00000	1.00000	1.92332	2.81948	0
49.362	2.71844E-02	1.00000	1.00000	1.00000	1.00000	1.92332	2.81948	0
52.482	2.89166E-02	1.00000	1.00000	1.00000	1.00000	1.92332	2.81948	0

MOAC-ORBITER CENTERLINE * STATION 800 * VKF F RUN 3828 TIME 152 MSEC * N_2 GAS

INFINITE YAWED BLUNT-BODY STAGNATION LINE COMPRESSIBLE TURBULENT BOUNDARY-LAYER ANALYSIS

FREE-STREAM MACH NUMBER = 1.087000E 01 PINF (LBF/FT2) = 6.160000E 00 TINF (DEG R) = 8.000000E 01

TWALL (DEG R) = 5.400000E 02 YAW ANGLE (DEG) = 4.700000E 01 POP (LBF/FT2) = 5.042670E 02

TOP (DEG R) = 1.132589E 03 TSTAG (DEG R) = 1.970510E 03 WE (FT/SEC) = 3.227544E 03

NOSE RADIUS (FT) = 0 X* (FT) = 8.030000E-02 DUE/DX (1/SEC) = 8.150246E 03

TWALL/TSTAG = 2.740407E-01 ANGLE OF ATTACK (DEG) = 4.300000E 01 SHOCK ANGLE (DEG) = 4.882782E 01

THERMALLY AND CALORICALLY PERFECT GAS MODEL

CP= 6214.00 FT2/(SEC2-DEG R) R= 1776.00 FT2/(SEC2-DEG R) GAMMA= 1.4000 PR= .7100 CSTAR= 198.60 DEG R

VISCOSITY CONSTANT= 2.1996E-08 LBF-SEC/(FT2-SQRT(DEG R)) KM1= .4350 LAMBDA= .0900 ASTAR= 26.000 PRT= .9000

CONICAL INVISCIC FLOW FOLLOWING HYPERSONIC SMALL-DISTURBANCE THEORY

FLAT-FACED DISK STAGNATION POINT VELOCITY GRADIENT

MDAC-ORBITER CENTERLINE * STATION P00 * VKF F RUN 382A TIME 152 MSEC * N2 GAS

INFINITE YAWED BLUNT-BODY STAGNATION LINE COMPRESSIBLE TURBULENT BOUNDARY-LAYER ANALYSIS

X (FT) = 0 XI = 0 BETA = 1.000000E 00 PE/POP = 1.000000E 00 S/RN = 0

UE (FT/SEC) = 0 WE (FT/SEC) = 3.227544E 03 PE (LBF/FT2) = 5.042670E 02 TE (DEG R) = 1.132589E 03

RHOE (SLUG/FT3) = 2.506848E-04 MUE (LBF-SEC/FT2) = 6.298142E-07 DUE/DX (1/SEC) = 8.150246E 03 ITERATIONS = 66

FPP(0) = 1.690808E 00 CP(0) = 1.231764E 00 GP(0) = 7.067571E-01 QDOT = -2.211731E 01 BTU/(FT2-SEC)

ST(INF) = 9.209734E-03 CFX(INF) = 0 CFZ(INF) = 1.101583E-02 HSP = 7.413322E 00

DELTA* (FT) = 8.912251E-04 THETAMOM (FT) = 7.043334E-04 EDGE REY/FT = 1.284710E 06 EDGE REYTHETAMOM = 9.048640E 02

EDGE MACH NO = 1.923319E 00 MCDONNELL-DOUGLAS TRANSITION PARAMETER = 2.823396E 01 -QDOT/(TSTAG-TWALL) = 1.546113E-02

ETA	Y(FT)	U/UE	W/WE	H/HE	T/TE	MACH	PITOT	EV/MU
0	0	0	0	.27404	.47678	0	.53646	0
.013	2.68109E-06	.01694	.01235	.28115	.48903	.03398	.53690	.00001
.021	5.60534E-06	.03501	.02557	.28879	.50195	.06940	.53827	.00009
.032	8.79705E-06	.05429	.03970	.29701	.51556	.10633	.54072	.00048
.044	1.22830E-05	.07484	.05481	.30586	.52989	.14481	.54438	.00157
.057	1.60927E-05	.09674	.07095	.31538	.54494	.18486	.54941	.00395
.074	2.02585E-05	.12002	.08818	.32562	.56070	.22650	.55598	.00842
.095	2.48158E-05	.14472	.10653	.33661	.57717	.26969	.56428	.01604
.100	2.98032E-05	.17083	.12599	.34838	.59428	.31434	.57450	.02807
.114	3.52624E-05	.19828	.14655	.36094	.61198	.36031	.58682	.04600
.134	4.12380E-05	.22695	.16813	.37428	.63015	.40736	.60141	.07150
.152	4.77777E-05	.25668	.19062	.38836	.64866	.45520	.61839	.10634
.172	5.49316E-05	.28723	.21385	.40311	.66736	.50348	.63784	.15242
.193	6.27524E-05	.31832	.23764	.41843	.68606	.55180	.65977	.21165
.215	7.12945E-05	.34965	.26175	.43421	.70459	.59975	.68419	.28600
.238	8.06145E-05	.38089	.28597	.45030	.72276	.64695	.71078	.37747
.263	9.07702E-05	.41175	.31006	.46655	.74040	.69304	.73954	.48819
.294	1.01821E-04	.44195	.33381	.48282	.75739	.73772	.77017	.62042
.318	1.13829E-04	.47126	.35705	.49896	.77360	.78076	.80242	.77659
.348	1.26856E-04	.49949	.37962	.51485	.78895	.82201	.83601	.95933
.380	1.40968E-04	.52651	.40142	.53039	.80339	.86136	.87066	1.17150
.414	1.56232E-04	.55223	.42236	.54549	.81690	.89877	.90611	1.41617
.450	1.72719E-04	.57660	.44239	.56008	.82948	.93424	.94211	1.69661
.488	1.90503E-04	.59961	.46150	.57413	.84115	.96781	.97845	2.01630
.529	2.09662E-04	.62126	.47968	.58761	.85194	.99954	1.01494	2.37888
.572	2.30277E-04	.64161	.49695	.60050	.86190	1.02951	1.05138	2.78814
.619	2.52435E-04	.66069	.51333	.61281	.87109	1.05783	1.08750	3.24798
.667	2.76230E-04	.67857	.52886	.62456	.87955	1.08458	1.12308	3.76237
.719	3.01759E-04	.69531	.54359	.63575	.88734	1.10989	1.15797	4.33531
.775	3.29125E-04	.71099	.55757	.64642	.89452	1.13384	1.19208	4.97080
.834	3.58442E-04	.72568	.57084	.65659	.90115	1.15655	1.22536	5.67278
.898	3.89826E-04	.73945	.58345	.66630	.90726	1.17811	1.25780	6.44508
.967	4.23405E-04	.75236	.59546	.67557	.91292	1.19862	1.28939	7.29141
1.037	4.59313E-04	.76449	.60690	.68443	.91816	1.21817	1.32016	8.21527
1.108	4.97693E-04	.77588	.61783	.69291	.92302	1.23684	1.35013	9.21987
1.188	5.38700E-04	.78660	.62828	.70105	.92754	1.25470	1.37934	10.30823

1.273	5.82495E-04	.79670	.63830	.70886	.93175	1.27183	1.40784	11.48304
1.369	6.29254E-04	.80623	.64793	.71638	.93568	1.28829	1.43568	12.74654
1.459	6.79160E-04	.81522	.65719	.72364	.93936	1.30415	1.46290	14.10063
1.561	7.32413E-04	.82372	.66612	.73064	.94280	1.31946	1.48956	15.54734
1.669	7.89221E-04	.83177	.67476	.73743	.94604	1.33427	1.51569	17.08871
1.784	8.49809E-04	.83939	.68312	.74401	.94909	1.34862	1.54136	18.71941
1.907	9.14416E-04	.84662	.69123	.75040	.95196	1.36257	1.56660	20.45432
2.037	9.83294E-04	.85347	.69911	.75662	.95468	1.37615	1.59146	22.28495
2.175	1.05672E-03	.85997	.70678	.76269	.95725	1.38939	1.61597	24.20306
2.322	1.13497E-03	.86615	.71428	.76862	.95971	1.40233	1.64018	26.18963
2.479	1.21836E-03	.87230	.72196	.77471	.96214	1.41561	1.66530	25.58281
2.645	1.30724E-03	.87868	.73017	.78122	.96465	1.42984	1.69251	25.42982
2.822	1.40196E-03	.88522	.73886	.78812	.96722	1.44495	1.72173	25.17115
3.009	1.50292E-03	.89191	.74808	.79544	.96984	1.46099	1.75313	24.89803
3.209	1.61054E-03	.89873	.75783	.80321	.97249	1.47802	1.78688	24.59499
3.421	1.72525E-03	.90566	.76813	.81142	.97516	1.49606	1.82313	24.25929
3.647	1.84751E-03	.91268	.77901	.82011	.97783	1.51517	1.86202	23.88680
3.886	1.97784E-03	.91975	.79046	.82927	.98049	1.53536	1.90373	23.47280
4.141	2.11675E-03	.92684	.80250	.83892	.98310	1.55667	1.94837	23.01186
4.412	2.26480E-03	.93391	.81512	.84905	.98565	1.57910	1.99609	22.49775
4.704	2.42257E-03	.94090	.82829	.85965	.98809	1.60264	2.04696	21.92329
5.004	2.59069E-03	.94778	.84200	.87071	.99041	1.62726	2.10105	21.28024
5.331	2.76981E-03	.95449	.85620	.88219	.99256	1.65291	2.15831	20.55905
5.677	2.96060E-03	.96096	.87082	.89404	.99450	1.67949	2.21866	19.74875
6.045	3.16378E-03	.96714	.88578	.90619	.99622	1.70685	2.28186	18.83671
6.436	3.38011E-03	.97296	.90094	.91854	.99768	1.73480	2.34751	17.80843
6.851	3.61038E-03	.97836	.91614	.93096	.99885	1.76305	2.41501	16.64734
7.293	3.85539E-03	.98327	.93119	.94328	.99972	1.79122	2.48347	15.33463
7.762	4.11604E-03	.98763	.94582	.95528	1.00029	1.81884	2.55166	13.84964
8.261	4.39322E-03	.99139	.95969	.96670	1.00058	1.84526	2.61792	12.16965
8.792	4.68791E-03	.99449	.97242	.97719	1.00062	1.86969	2.68008	10.26807
9.356	5.00116E-03	.99690	.98350	.98634	1.00048	1.89114	2.73534	8.12588
9.955	5.33407E-03	.99860	.99234	.99365	1.00023	1.90836	2.78018	5.78144
10.592	5.68786E-03	.99961	.99836	.99862	.99994	1.92022	2.81132	2.95996
11.270	6.06387E-03	.99997	1.00074	1.00057	.99987	1.92487	2.82359	.38417
11.990	6.46356E-03	.99984	.99980	.99978	.99989	1.92304	2.81875	.12295
12.755	6.88840E-03	.99990	1.00040	1.00016	.99969	1.92438	2.82230	.06139
13.569	7.34000E-03	.99988	.99998	.99994	.99992	1.92334	2.81956	.02903
14.433	7.82006F-03	.99988	1.00030	1.00008	.99970	1.92418	2.82176	.01569
15.353	8.33036E-03	.99989	1.00004	.99998	.99991	1.92348	2.81992	.00934
16.330	8.87281E-03	.99987	1.00026	1.00005	.99971	1.92408	2.82151	.00604
17.369	9.44943E-03	.99990	1.00007	1.00000	.99989	1.92355	2.82010	.00418
18.473	1.00624F-02	.99986	1.00024	1.00004	.99972	1.92404	2.82139	.00307
19.647	1.07139E-02	.99990	1.00008	1.00000	.99989	1.92358	2.82018	.00237
20.895	1.14066E-02	.99986	1.00023	1.00004	.99973	1.92402	2.82134	.00192
22.221	1.21428E-02	.99991	1.00009	1.00001	.99989	1.92359	2.82021	.00161
23.631	1.29254E-02	.99985	1.00023	1.00003	.99973	1.92401	2.82133	.00141
25.130	1.37574E-02	.99991	1.00009	1.00001	.99989	1.92359	2.82020	.00126
26.723	1.46417F-02	.99985	1.00023	1.00003	.99972	1.92402	2.82135	.00117
28.414	1.55818E-02	.99992	1.00008	1.00001	.99989	1.92358	2.82017	.00110
30.217	1.65811E-02	.99984	1.00023	1.00003	.99971	1.92404	2.82140	.00106
32.130	1.76433E-02	.99993	1.00007	1.00001	.99990	1.92355	2.82010	.00104
34.164	1.87725F-02	.99983	1.00024	1.00003	.99970	1.92407	2.82148	.00104
36.327	1.99728F-02	.99994	1.00006	1.00001	.99992	1.92351	2.82001	.00101
38.625	2.12487E-02	.99982	1.00026	1.00004	.99968	1.92411	2.82159	.00091
41.069	2.26050F-02	.99996	1.00005	1.00001	.99994	1.92347	2.81988	.00082
43.666	2.40468F-02	.99981	1.00028	1.00004	.99966	1.92417	2.82174	.00074
46.427	2.55794E-02	.99998	1.00003	1.00000	.99997	1.92340	2.81971	.00067
49.362	2.72085E-02	.99979	1.00030	1.00004	.99963	1.92425	2.82194	.00061
52.482	2.89403E-02	1.00000	1.00000	1.00000	1.00000	1.92332	2.81948	0

UNCLASSIFIED

Security Classification

DOCUMENT CONTROL DATA - R & D

(Security classification of title, body of abstract and indexing annotation must be entered when the overall report is classified)

1 ORIGINATING ACTIVITY (Corporate author)	2a. REPORT SECURITY CLASSIFICATION
Arnold Engineering Development Center Arnold Air Force Station, Tennessee 37389	UNCLASSIFIED
	2b. GROUP N/A

3 REPORT TITLE

HYPERSONIC LIFTING BODY WINDWARD SURFACE FLOW-FIELD ANALYSIS FOR HIGH ANGLES OF INCIDENCE

4 DESCRIPTIVE NOTES (Type of report and inclusive dates)

Final Report -- July 1971 through July 1972

5. AUTHOR(S) (First name, middle initial, last name)

John C. Adams, Jr., and William R. Martindale, ARO, Inc.

6 REPORT DATE	7a. TOTAL NO OF PAGES	7b. NO. OF REFS
February 1973	233	111

8a. CONTRACT OR GRANT NO	9a. ORIGINATOR'S REPORT NUMBER(S)
b. PROJECT NO	AEDC-TR-73-2
c. Program Element 65802F	9b. OTHER REPORT NO(S) (Any other numbers that may be assigned this report)
d	ARO-VKF-TR-72-128

10 DISTRIBUTION STATEMENT

Approved for public release; distribution unlimited.

11 SUPPLEMENTARY NOTES	12. SPONSORING MILITARY ACTIVITY
Available in DDC.	Arnold Engineering Development Center, Air Force Systems Command, Arnold Air Force Station, TN 37389

13 ABSTRACT

Formulation and application of a windward surface flow-field (inviscid and viscous) analysis is presented for general lifting body configurations at high angles of incidence under hypersonic perfect gas conditions. Primary emphasis is placed on development of an approach which is accurate and easy to use while requiring only modest digital computing facilities. Basically the present technique applies the "strip theory" concept, leading to an infinite extent yawed body treatment applied in the windward surface crossflow plane for both the inviscid and viscous (boundary layer) flow fields. A one-strip integral relations approach is used to determine the spanwise surface pressure distribution at a given body location with all inviscid centerline quantities determined via an inviscid conical flow approach or some alternate technique. The boundary-layer analysis is based on implicit finite-difference integration of the governing equations for infinite-extent, yawed, blunt body boundary layers. Both laminar and turbulent flows are considered using a three-dimensional eddy viscosity-mixing length model of turbulence. Comparisons of the present "strip theory" approach with experimental data on various lifting body configurations (including several NASA Phase B Space Shuttle configurations) are presented in order to ascertain the validity and applicability of the current technique.

DD FORM 1 NOV 65 1473

UNCLASSIFIED

Security Classification

14. KEY WORDS	LINK A		LINK B		LINK C	
	ROLE	WT	ROLE	WT	ROLE	WT
lifting reentry vehicles						
delta wings						
hypersonic flow						
pressure distribution						
heat transfer						
laminar boundary layer						
turbulent boundary layer						
boundary layer transition						
boundary layer stability						

AFSC
Arnold AFS Tenn